Downloaded from orbit.dtu.dk on: May 06, 2023

DTU Library

High Temperature PEM Fuel Cells and Organic Fuels

Vassiliev, Anton

Publication date:
2014

Document Version
Publisher's PDF, also known as Version of record

Link back to DTU Orbit

Citation (APA):
Vassiliev, A. (2014). *High Temperature PEM Fuel Cells and Organic Fuels*. Department of Energy Conversion and Storage, Technical University of Denmark.

General rights
Copyright and moral rights for the publications made accessible in the public portal are retained by the authors and/or other copyright owners and it is a condition of accessing publications that users recognise and abide by the legal requirements associated with these rights.

- Users may download and print one copy of any publication from the public portal for the purpose of private study or research.
- You may not further distribute the material or use it for any profit-making activity or commercial gain
- You may freely distribute the URL identifying the publication in the public portal

If you believe that this document breaches copyright please contact us providing details, and we will remove access to the work immediately and investigate your claim.

Technical University of Denmark

High Temperature PEM Fuel Cells and Organic Fuels

Anton Vassiliev

Department of Energy Conversion and Storage

Ph.D. Thesis, June 2014

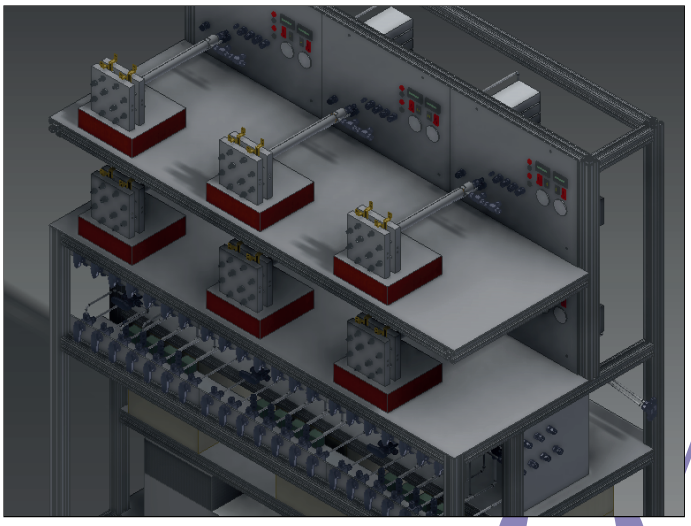

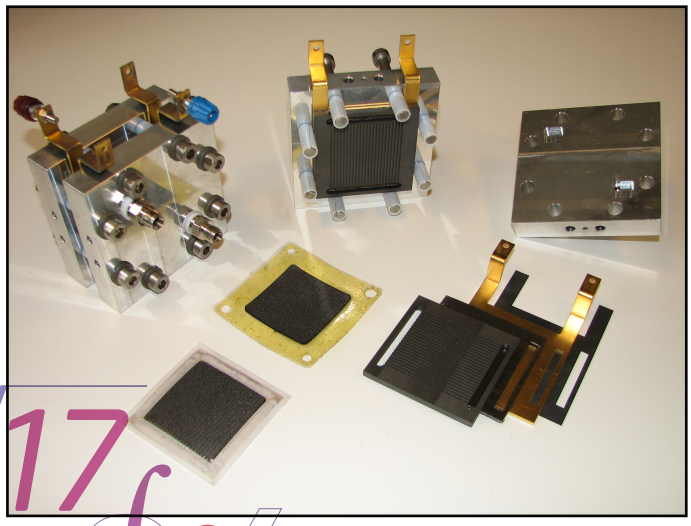

$$f(x+\Delta x)=\sum_{i=0}^{\infty}\frac{(\Delta x)^i}{i!}f^{(i)}(x) \qquad \int_a^b \varepsilon \qquad e^{i\pi}=-1 \qquad \{2.7182818284\}$$

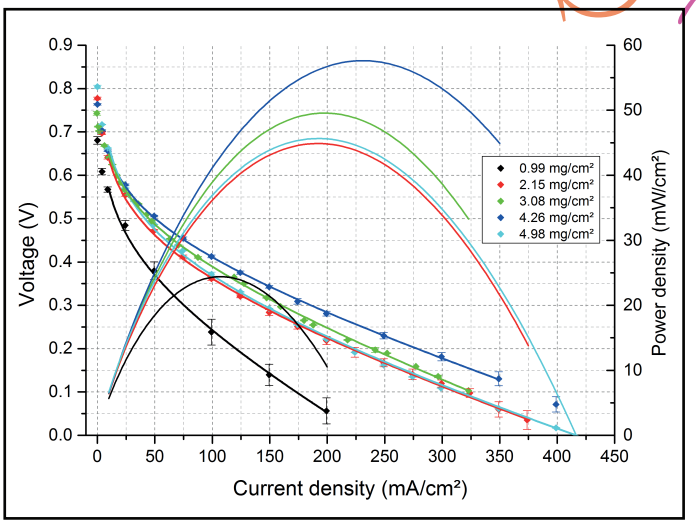

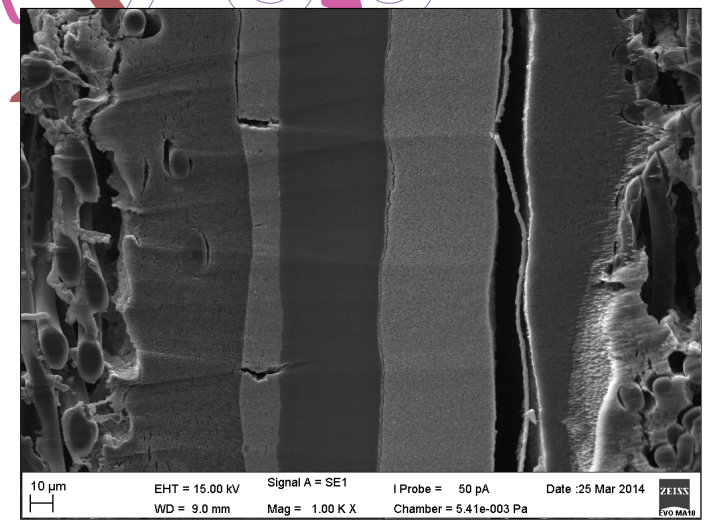

DTU Energy Conversion
Department of Energy Conversion and Storage

High Temperature PEM Fuel Cells and Organic Fuels

Ph.D. Thesis

Anton Vassiliev

Technical University of Denmark, DK

June 2014

Author:

Anton Vassiliev

Supervisor:

Professor Niels J. Bjerrum

Co-supervisors:

Associate Professor Jens Oluf Jensen

Associate Professor Qingfeng Li

Proton Conductors Group

Department of Energy Conversion and Storage

Technical University of Denmark

Kemitorvet building 207

DK-2800 Kgs. Lyngby

www.pro.ecs.dtu.dk

Tel: (+45) 45 25 23 13

Fax: (+45) 45 88 31 36

E-mail: anvas@dtu.dk

All rights reserved. No parts of this publication may be reproduced or transmitted, in any form or by any means, without written permission.

ISBN 978-87-92986-18-4

Abstract

Modern way of life demands enormous amounts of energy, which so far has been mainly produced by combustion of various types of fossil fuel. Increased amounts of atmospheric CO_2 and global warming leading to severe climate changes are the consequence. There is a need to make the energy production sustainable and break the dependency on fossil fuels. Hydrogen economy provides such a solution, where hydrogen produced by renewables, such as wind and solar power, becomes the energy carrier. The storage, handling and transportation of hydrogen are the main obstacles on the route to a sustainable future when it comes to powering small and medium sized applications, transportation sector in particular. This is mainly due to the gravimetric energy density being immensely inferior to the liquid fuels gasoline and diesel.

Dimethyl ether has already been identified as an excellent renewable fuel and a diesel substitute, which possesses energy density not much less than those of conventional diesel and gasoline. With its predicted widespread, there is an interest in harvesting electricity from dimethyl ether directly, rather than using it solely for combustion. High temperature PEM fuel cells provide such an opportunity. Some knowledge about the electrooxidation of DME is available, together with its limited use in low temperature PEM fuel cells, where the low temperature poses an obstacle in the form of phase separation in the fuel supply, making the cells less effective and reducing the amount of power harvested from the cells. This is completely avoided at the elevated temperatures with the additional benefit of increased kinetics.

In the presented work an experimental setup for testing direct dimethyl ether high temperature fuel cells is described, proposing a novel design of an evaporator for a burst-free supply of a fuel and steam mixture. Based on the knowledge gathered with the construction and operation of the single cell setup a more versatile and flexible setup was designed and commissioned for independent testing of up to 6 cells, enabling fuel cell experiments with up to 3 gasses and a single evaporated liquid stream supply to either of the electrodes.

A large number of MEAs with different component compositions have been prepared and tested in different conditions using the constructed setups to obtain a basic understanding of the nature of direct DME HT-PEM FC, to map the processes occurring inside the cells and to determine the lifetime. Additionally, comparison was made with methanol as fuel, which is the main competitor to DME in direct oxidation of organic fuels in fuel cells. For the reference, measurements have also been done with conventional hydrogen/air operation. All the experiments have been conducted at atmospheric pressure.

Experiments with varying amounts of PBI in the cathode catalyst layer has shown that there is a minimum content limit for the preparation of a well dispersed catalyst

ink of 15 carbon to PBI weight ratio in the currently used ink formulation. On the other hand, for the MEA operation it has been shown that too much PBI has a negative effect with large mass transport limitations as a consequence. The amount of catalyst in the electrode has also shown an effect on the performance, with the optimum being between 3 and 4 mg/cm² of a 60 wt% $Pt_{50}Ru_{50}$ catalyst on 40 wt% carbon support.

Catalysts with varying Pt, Ru and Sn content on carbon support has been synthesised and used for MEA testing, with the outcome of other operation and MEA composition parameters, such as reliable fuel supply, MEA assembly and operation and the characteristics of the electrolyte membrane having a much more pronounced effect on the final performance than the catalyst composition.

The increased operating temperature showed improved performances for all 3 investigated fuels, hydrogen, DME and methanol, with the additional energy supplied in terms of heat helping to overcome the kinetic barriers of the oxidation of the fuels. The resistance of the electrolyte was also found to be decreasing until 200 °C, passing which would result in a rapid membrane dryout and supposed polymerisation of the phosphoric acid, irreversibly lowering the conductivity of the membrane. By increasing the partial pressure of oxygen on the cathode side from 0.21 bar to 1 bar an overall increase in cell voltages was observed for all 3 fuels, with peak power densities increasing by 25 % and 35 % for DME and MeOH operation respectively, thereby also indirectly confirming the larger fuel crossover effect of the latter.

Gas chromatography study of the anode exhaust gas at open circuit voltage revealed a small degree of internal fuel reforming with different products when operated on dimethyl ether or methanol. While methanol seemed to reform to syngas, the DME yielded methane rather than CO as one of the products. The observation of internal reforming was indirectly confirmed by electrochemical impedance spectroscopy, where the best fits were obtained when a Gerischer element describing preceding chemical reaction and diffusion was included in the equivalent circuit of a methanol/air operated cell. In general it has been shown that EIS is a powerful tool for studying MEAs and making reference electrodes unnecessary.

Finally, durability studies have shown that the average lifetimes of the cells are between 300 – 600 hours, depending on the operating temperature and water content in the anode fuel supply. However, a potential to operate past 1500 hours has been demonstrated. Post-mortem analyses of the MEAs have shown that one of the reasons for the cell death was formation of pinholes in the membrane, rather than an overall thinning.

Resumé

Moderne livsstil kræver enorme mængder energi, som hidtil har hovedsagelig været produceret ved forbrænding af forskellige typer af fossile brændstoffer. Dette har ført til øgede mængder af atmosfærisk CO_2, global temperaturstigning og alvorlige klimaændringer. Der er behov for at gøre energiproduktionen bæredygtig og mindske afhængigheden af fossile brændstoffer. Hydrogen økonomi giver en sådan løsning, hvor brint produceres vha. vedvarende energikilder, såsom vind -og solenergi, og bliver en energibærer. Opbevaring, håndtering og transport af brint er de vigtigste forhindringer på ruten til en bæredygtig fremtid, transportsektoren i særdeleshed. Dette primært skyldes den gravimetriske energitæthed af hydrogen, som er meget lille i forhold til de flydende brændstoffer benzin og diesel.

Dimethyl æter er allerede blevet identificeret som et fremragende vedvarende brændstof og en diesel- erstatning. Den besidder en energitæthed ikke meget mindre end for konventionelle benzin og diesel. Med dens forventede udbredelse, er der en interesse i at producere elektricitet fra dimethyl æter direkte, i stedet for at bruge det udelukkende til forbrænding. Høj temperatur PEM brændselsceller giver en sådan mulighed. Elektrooxidation af DME og dens begrænsede brug i lave temperaturer PEM brændselsceller er blevet studeret i et begrænset omfang. De lave temperaturer er en hindring, som fører til fase adskillelse i brændstofforsyningen, hvilket gør cellerne mindre effektive og reducerer mængden af strøm man kan trække fra cellerne. Dette problem undgås fuldstændigt ved at køre ved temperaturer over 100 °C, med den yderligere fordel af øget kinetik.

Det præsenterede arbejde beskriver opbygning af en forsøgsopstilling til test af direkte dimethyl æter højtemperatur brændselscelle og foreslår et nyt design af en fordamper til en pulseringsfri levering af brændstof og damp blanding. Baseret på den indsamlede viden med konstruktion og drift af enkelt celle opstillingen, en mere fleksibel opstilling til tests af op til 6 celler er blevet designet og bygget. Den er konstrueret således at det er muligt at forsyne med op til 3 gasser og en enkelt fordampet væske til en af elektroderne på brændselscellen samtidigt, som åbner for mange forskellige HT PEM brændselscelle forsøg.

Et stort antal af MEA'er med forskellige komponenter er blevet fremstillet og testet under forskellige forhold ved hjælp af de byggede opstillinger for at opnå en grundlæggende forståelse af direkte DME HT-PEM brændselscellers natur, at kortlægge de processer, der forekommer inde i cellerne og til at bestemme levetiden. Desuden blev resultaterne sammenlignet med metanol som brændsel, som er den største konkurrent til DME i direkte oxidation af organiske brændstoffer i brændselsceller. Som reference er målingerne også blevet gjort med konventionel brint/luft operation. Alle forsøg er gennemført ved atmosfærisk tryk.

Forsøg med varierende mængder af PBI i katodens katalysatorlag har vist, at der findes en nedre grænse på 15 C til PBI repeating unit for at opnå en god dispergering af katalysator partikler i et katalysator blæk til fremstilling af elektroder. For MEA drift er det blevet vist, at for meget PBI har en negativ virkning med store massetransport begrænsninger til følge. Mængden af katalysator i elektroden har også vist en effekt på performance, med optimum mellem 3 og 4 mg/cm² af en 60 vægt% $Pt_{50}Ru_{50}$ katalysator på 40 vægt% kulstof support.

Katalysatorer med varierende Pt, Ru og Sn forhold på kulstof support er blevet syntetiseret og anvendt til MEA test. Det har vist sig, at drift og MEA sammensætning parametre, såsom pålidelig brændstofforsyning, MEA samling og egenskaberne af elektrolyt membranen har en langt mere udtalt påvirkning på det samlede ydeevne end katalysatorsammensætningen.

Den øgede driftstemperatur viste forbedringer for alle 3 undersøgte brændstoffer, brint, DME og metanol. Den ekstra energi, der leveres i form af varme, bidrager til at overkomme de kinetiske barrierer for oxidation af brændstofferne. Modstanden af elektrolytten viste sig at være faldende indtil 200 °C, hvorefter irreversibelt tab af protonledningsevne skete som følge af en hurtig membran udtørring og formodet polymerisation af fosforsyre. Ved at øge partialtrykket af ilt på katodesiden fra 0,21 bar til 1 bar blev en samlet stigning i cellespændinger observeret for alle 3 brændstoffer. Effekttæthedsstigninger på 25 % og 35 % for henholdsvis DME og MeOH drift blev opnået, som indirekte bekræfter større brændstof crossover hos den sidstnævnte.

Gaskromatografi undersøgelser af anodens udstødningsgas ved OCV afslørede en lille grad af intern brændstof reformering med forskellige produkter ved drift med enten dimethyl æter eller metanol. Mens metanol reformerede til syntesegas, DME blev omdannet til metan i stedet for CO som et af produkterne. Observationen af den interne reformering blev indirekte bekræftet ved elektrokemisk impedans spektroskopi, hvor de bedste fit blev opnået med en Gerischer element, som beskriver foregående kemisk reaktion og diffusion, inkluderet i det ækvivalente kredsløb for en metanol/luft dreven celle. Generelt har det vist sig, at EIS er et kraftfuldt værktøj til at studere MEA og gøre referenceelektroder unødvendig.

Levetidsstudie har vist, at den gennemsnitlige levetid for direkte DME HT-PEM brændselsceller er mellem 300 til 600 timer, afhængigt af vandindholdet i anode brændstofforsyningen og driftstemperaturen. Imidlertid var der en celle med en levetid på over 1500 timer. Post-mortem analyse af MEA'er har vist, at dannelsen af pinholes i membranen var en af grundene til celledød, snarere end en samlet udtynding af elektrolytten.

Preface

The presented work covers the research conducted during a Ph.D. study from August 2010 to June 2014 in the Proton Conductors group at the Department of Energy Conversion and Storage, Technical University of Denmark. The thesis was written as a partial fulfillment of the requirements for obtaining the Doctor of Philosophy degree. The study was financed by the Danish Agency for Science, Technology and Innovation under the Innovation Consortium "Vedvarende Energiteknologier" and the durability study by Copenhagen Cleantech Cluster as a GAP project administered by DTU.

First I would like to thank and acknowledge all my supervisors. Professor Niels J. Bjerrum for giving me the opportunity to study in this group, Associate Professor Qingfeng Li for his invaluable feedback on the conducted work and proposals of interesting working directions. Especially I would like to thank Associate Professor Jens Oluf Jensen for the inspiration and enthusiasm in the daily work, for showing me the path when I was at a loss and always finding the time for a discussion, scientific or otherwise.

I would like to thank the VETEK project partners, Jens Christiansen, Rasmus M. Nielsen and Morten Ø. Andersen from Danish Technological Institute for their scientific support and Jens Hinke from SP Group A/S for many interesting ideas. Without the staff of Danish Power Systems the work would not be possible. Especially to Thomas Steenberg and Mayte R. Sanchez I express my gratitude.

Thanks to all the former and present members of the Proton Conductors (previously Energy and Materials Science) group for all the practical and scientific support and a pleasant working atmosphere, Chao Pan, Larisa Seerup, Aleksey Nikiforov, Yang Hu, David Aili, Erik Christensen, Irina Petrushina, Steen Blichfeldt, Kirsten M. Thomsen, Tonny D. Jakobsen, Stine Søndergaard, Carsten B. Prag, Tatiana Anfimova, Annemette H. Jensen and Santiago M. Fernandez.

Special thanks to Lars N. Cleemann, for the astonishing ability to resolve any technical or practical issue. Thanks to Claus B. Mortensen and Magnus M. Gudnason for their great technical expertise. Thanks to James A. Mugabi for the existential talks. Special thanks to my friends Anastasia A. Permyakova and Antonio L. T. García for the coffee breaks and all beyond.

Finally, but most importantly, I thank my family, whose continuous care and support never ceased despite my frequent neglect, without anything asked in return. I thank my wife, for accepting me as I am and forgiving my mistakes. I thank my daughter, for being a beacon of joy and happiness and giving my life a purpose. To her I dedicate this work.

Contents

List of Figures

List of Tables

1 Introduction

1.1 Energy

For the major part of the human history the technology development went hand in hand with the consumption of fuel. In fact, most of the technological breakthroughs were achieved when a more efficient fuel have been discovered. Charcoal led to the Bronze Age, the depletion of the woodland and later on outcrop coal led to development of shaft mining and invention of steam engine, sparking the Industrial Revolution, which only intensified the use of coal. The petroleum brought us the life we have today, with mass production, overseas travel, personal transportation and all the commodity goods we now take for granted. The self-perpetuating effect of the increasing population combined with the increasing amount of energy consumed per person led to the energy demand rocketing within last 60 years, as seen from Figure 1.1 on the left. The annual consumption of energy was $12.5 \cdot 10^9$ metric tons of oil equivalent (toe), which corresponds to app. 2 m^3 oil equivalent consumed per person. The value is predicted to rise further, due to progress in developing countries, where an increasing amount of people can afford luxury goods and commodities.

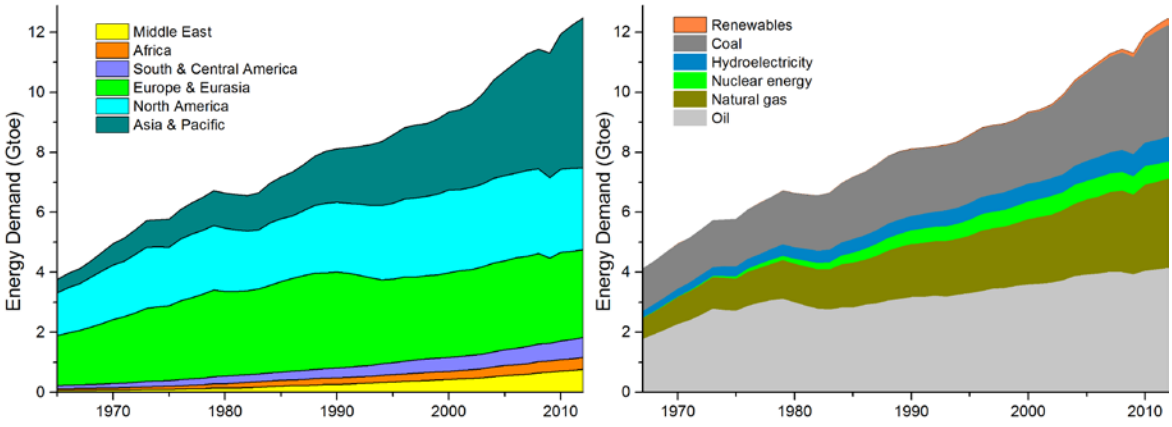

Figure 1.1: Energy demand in Gtoe by region (left) and fuel type (right) [1, 2].

Most of the energy demand is covered by consumption of fossil fuels – coal, oil and natural gas. They contribute by $^2/_3$ to the total energy produced – see Figure 1.1 on the right. Taking into account that it took nature over 300 million years to produce the vast deposits of the fossil fuels, they will inevitably be depleted within the foreseeable future with our current consumption rate. Another aspect is the enormous amounts of greenhouse gasses released into the atmosphere, which is predicted to lead to sudden climate changes, sea level rise and possibly mass extinctions. This puts an enormous strain on our civilization to break the dependency on carbonaceous fuels to secure the energy supply for the future and minimize the climate effect mankind has on the planet.

The answer to this is renewable energy, such as wind, solar, hydro and geothermal power and biomass. The energy produced by those sources is however not always usable in its form or production location. Another problem with renewables is that they are a non-constant resource, where the demand at some points can exceed the supply. The big advantage of the fossil fuels is that the energy is stored as chemical bonds that can be broken to release the energy again. This makes it possible to use the fuels where and when needed. In order to make the renewable energy sources viable there is a need for an energy currency.

Hydrogen economy, utilizing hydrogen in energy delivery, presents such a solution. Energy in form of electricity produced by wind turbines, solar cells and hydropower plants can be converted into chemical energy by splitting water into its constituents, thus binding the energy in hydrogen by means of electrolysis. The process can then be reverted utilizing fuel cells, recombining hydrogen and oxygen into water and releasing the stored chemical energy in the form of electricity and heat.

1.2 Historical Review of Fuel Cells

The decomposition of water into hydrogen and oxygen was observed in the end of 18th century, when two Dutchmen, Adriaan Paets van Troostwijk and his friend Johan Rudolph Deiman performed a simple experiment back in 1789, submerging 2 gold wires in water and passing electric current trough them [3, 4]. Gas was evolved on both wires, which would recombine explosively upon an electric discharge to form water.

The concept of extracting electric current from recombination of hydrogen and oxygen was developed in 1839 by a Welshman, Sir William R. Grove. He constructed a device with hydrogen and oxygen in separate containers with a platinized platinum electrode in each container. Submerging it in sulphuric acid he observed that a constant current flowed between the electrodes [5]. He called the device "Gaseous Voltaic Battery", which in fact was the first fuel cell. Later on he connected 50 of his batteries in series, with the effect of, in authors own words, "*A shock was given which could be felt by five persons joining hands, and which when taken by a single person was painful*" [6]. He continued his investigation, summarizing it in his book, where he describes fuel cells operating on many different fuels [7].

The invention has been modified and developed further by two British scientists Ludwig Mond and Carl Langer. They refined Grove's gas battery by making the electrodes three-dimensional and also introducing a matrix that soaked the electrolyte, preventing the electrodes from flooding [8]. The phosphoric acid fuel cells (PAFCs) of today are in principle a modern version of Mond and Langer cell [9]. Last but not least they should be remembered for the introduction of the term "fuel cell".

A lot of work in the field of fuel cells has been done in late 19th century, leading to fundamental understandings of the working principle, discovery of different types of electrode and electrolyte materials and designs. At the same time there was also a

desire among researches to generate continuous electric energy from a "battery". A German Professor for Physical Chemistry, Wilhelm Ostwald, had a vision that 20th century would be the Age of Electrochemical Combustion, with fuel cells providing a much more efficient, noise and pollution free energy, opposite to the steam engine with its only 10% efficiency at the time [10]. A student of Ostwald, Walter Hermann Nernst, worked with electrode potentials of ions, which was presented in his Habil thesis from 1889 [11]. Soon after he derived one of the building blocks in electrochemistry, the equilibrium equation. Nernst also discovered that certain oxides conducted oxygen ions at high temperatures, which laid the foundation for solid oxide fuel cells (SOFC) [12].

Emil Baur conducted wide-ranged investigations in different kinds of fuel cells in early 20th century [13-17]. He built the first molten carbonate fuel cell (MCFC) in 1921, and the first SOFC with a solid oxide electrolyte of zirconium type in 1937, which could electrochemically convert carbon via integrated gasification step inside the cell [18, 19]. A comprehensive study of more than 200 literature citations on state of the art of the whole fuel cell field was published together with his co-worker Jakob Tobler in 1933, classifying groups of fuel cells and electrodes by type [17]. The authors came to the conclusion that the most viable cell type at the time would be one with aqueous alkaline electrolyte and a carbon/air cathode and metal anode.

The fuel cells, however, remained without a practical application, a curiosity, until Sir Francis T. Bacon constructed the first prototype of a fuel cell in kW range in 1953. Bacon started research on alkali electrolytes in late 1930'ies, eventually settling on potassium hydroxide, which proved to be successful. Based on his results the US space agency (NASA) chose to use alkaline fuel cells as a power source on their Apollo missions [20, 21]. Although acid-based proton exchange membrane (PEM) fuel cells were used for their first manned mission – the Gemini in 1964, it was the alkaline fuel cell that took man to the moon. The choice was made mostly due to power generating efficiencies close to 70 %. Another big advantage was the water management – at zero gravity it was possible to use wicks to transport water out of the cell by capillary forces. Pressure differential across a porous ceramic used as a sealing forced the liquid water through the pores into storage container. The water was pure enough to drink for the astronauts, who thus used the fuel cell not only as a power, but also as a drinking water source [22].

The Apollo missions were the most remarkable, but not the only early use of fuel cells. Prior to space exploration, Bacon developed fuel cells for the submarines of the Royal Navy during WWII. He also ran a number of demonstrations in 1959, powering a forklift and other devices in his laboratory at Cambridge University [23, 24]. Same year, Harry K. Ihrig used alkaline fuel cells to drive agricultural tractors, where 1008 cells powered up a 15 kW 75 V DC electrical engine [25]. The tractor can be seen on Figure 1.2 to the left, with the front part, conventionally occupied by a combustion engine, fitted with the fuel cell stacks. In 1971 Karl V. Kordesch from Union Carbide Corporation demonstrated a hybrid fuel cell/lead acid battery car [26]. It was a

remodelled Austin A-40 with 120 alkaline fuel cells providing 6 kW as a primary power source and 7 lead acid batteries, which served during start-up and peak times. The batteries and the engine were placed under the hood, while the fuel cell system occupied most of the back of the car. That left little space for the fuel, therefore the hydrogen tanks were placed on the top of the car, as can be seen on Figure 1.2 to the right.

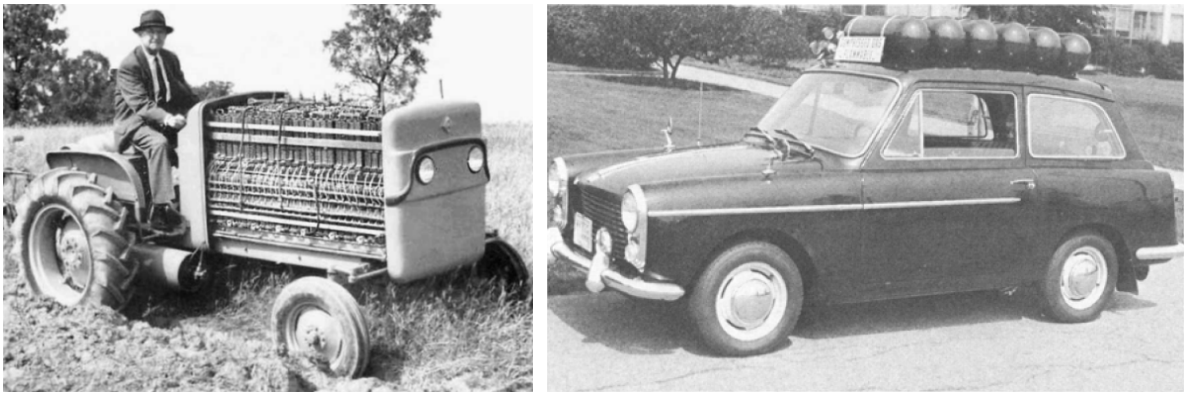

Figure 1.2: Left - Dr. Harry K. Ihrig driving the Allis-Chalmers alkaline fuel cell powered tractor [27]. Right – hybrid alkaline fuel cell/lead acid battery car by Karl V. Kordesch [26].

A General Electric Company (GE) chemist Willard T. Grubb invented the PEM fuel cell in 1959 in its current form [28, 29], with a polystyrene sulfonate membrane used as the electrolyte, on which platinum catalyst was deposited using a method developed by Grubb's colleague Leonard Niedrach a year earlier [23]. These cells had a power output of ca. 50 mW/cm² and were used for the Gemini flights. The first ion exchange membranes were not stable at higher temperatures, resulting in short lifetimes. A lot of effort went into mitigating the degradation until joint efforts of DuPont and GE led to invention of Nafion in mid-1960s [30]. Cells based on the new material had also higher power densities. A 350 W module with ca. 100 mW/cm² cell power density, almost double of the early Gemini missions, powered the Biosatellite spacecraft in 1969 [22]. The PEM fuel cell has been developed further during 70s and 80s, achieving performances of 5.4 A/cm² at 0.5 V and lifetime greater than 2000 h at 0.54 A/cm² by 1990 [24]. In 1993 Daimler-Benz used PEM stacks from the Canadian company Ballard for demonstration purposes, driving a car with the only exhaust being pure drinking water. Ballard also entered an agreement with the Government of British Columbia to develop zero-emission bus. The task was completed in 1992, where the installed PEM FC-based engine provided the same power as the diesel engine it was replacing, with pure water as the only exhaust. That came with a price of 25 % of the bus being occupied by the system [31]. This was solved in the next generation, where the PEM FC system was providing 200 kW without reducing the space available for passengers [32]. The project ended with Ballard providing two small bus fleets for Vancouver and Chicago. Besides being zero emission, they also proved to be 20 dB quieter than corresponding diesel busses [33].

PEM systems have won a great appreciation as power sources for the transportation sector, with a big number of actors trying to develop products that are efficient, clean and most importantly cost competitive to the current state of the art internal combustion engines (ICE) [34]. In general different types of fuel cells are used worldwide for many applications, like combined heat and power units (CHP), providing homes with heating and electricity, or as backup power in hospitals, schools, offices or hotels. Fuel cells are widely used to power telecommunication systems in areas where grid electricity is not available, providing a reliable and uninterrupted power supply. Many indoor storage facilities use forklifts run on fuel cells avoiding emissions from ICE engines. Moreover they have an advantage over battery power, as fuel cell refuelling time is a matter of minutes, compared to several hours for a battery. A big market for small portable fuel cells is in the world for telecommunication, where they can be used instead of batteries powering laptops, mobile phones and other gadgets. For these applications a Direct Methanol Fuel Cell (DMFC) would be the ideal choice due to the high volumetric energy density of the fuel [35].

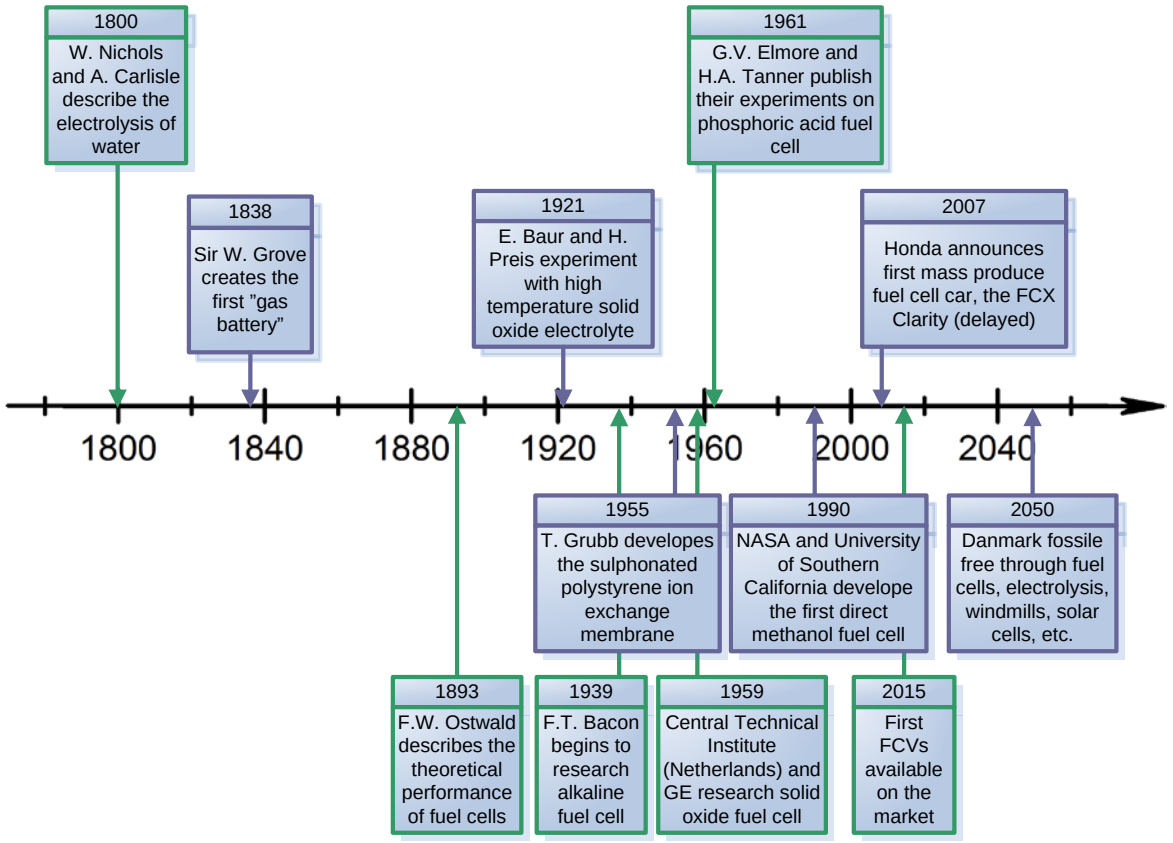

Figure 1.3: Fuel cell development milestone chart. Data adapted from [23].

Some of the key milestones in fuel cell development history are summarized in Figure 1.3. The two most important ones are probably the theoretical description of the processes in the fuel cell done by F.W. Ostwald in 1893 and the subsequent practical implementation of the principles by F.T. bacon in 1939. It is interesting to note that

the development of fuel cells has been on-going in the century dominated by the cheap and easily accessible oil and when environmental pollution wasn't an issue, so the was no apparent reason to develop alternatives to combustion engines. However the effort has paid off, now, when it is evident that the fossil fuel supply will run out in a foreseeable future and the atmosphere is heating up due to human activities.

1.3 Fuel Cell Types

The many different approaches to develop fuel cells since their discovery had led to a number of different technology tracks within the field. This gave rise to several types of fuel cells, which can be grouped in 2 categories, low temperature and high temperature. The low temperature includes PEM fuel cells, alkaline fuel cells, direct methanol fuel cells, which is a variety of PEM FC and phosphoric acid fuel cells (PAFC). The molten carbonate fuel cells (MCFC) and solid oxide fuel cells (SOFC) belong to the family of high temperature fuel cells. Common for the last three types is that they require auxiliary equipment to be operational, and should thus never be regarded simply as fuel cells. They are always a part of a complete heat and power generation and fuel processing system. With the exception of DMFC, the fuel cells are named accordingly to the electrolyte, which is considered a key component of a fuel cell. An overview of different types of fuel cells and their respective characteristics are given in Table 1.1.

Table 1.1 Fuel cell types and characteristics [36, 37]. Fuel cell efficiency is for chemical to electrical energy conversion.

Fuel cell type	Operating temperature	Mobile ion	Fuel efficiency	Catalyst	Applications
AFC	50 - 200 °C	OH^-	40 – 60 %	Ni, Ag, Pt	Space vehicles, transportation
PEM FC	30 - 200 °C	H^+	45 – 60 %	Pt	Transportation, space vehicles, small CHP, UPS
DMFC	30 - 200 °C	H^+	34 %	Pt, Pt/Ru	Low power and long use, e.g. portable electronics
PAFC	160 - 220 °C	H^+	55 %	Pt	CHP
MCFC	550 - 700 °C	CO_3^{2-}	60 – 65 %	Ni, Co	Stationary power and CHP
SOFC	500 - 1000 °C	O^{2-}	55 – 65 %	Pervoskites, Ni	Stationary power, CHP, APU

1.3.1 Alkaline Fuel Cells

F.T. Bacon invented the alkaline fuels cell in 1939 when he employed potassium hydroxide as electrolyte instead of acids used since W. Groves "gas battery". The KOH electrolyte conducts hydroxide ions from cathode to anode and is typically continuously circulated between the electrodes. Alkaline fuel cells can be operated at a broad range of pressures and temperatures, thus there is no standard type of electrodes, however very often Raney nickel is used on the anode and silver on the cathode [38, 39]. The activity within the alkaline fuel cell field is rather low. This is mainly due to the CO_2 reacting with the electrolyte, forming carbonate. The effects

are numerous – the hydroxide concentration is lowered, decreasing conductivity and reducing the rate of oxidation at the anode, the viscosity is increased, resulting in mass transportation losses and reduced oxygen solubility, which in turn increases activation losses at the cathode [20]. Thus the AFCs are extremely intolerant towards CO_2 and CO to some extent. The liquid electrolyte is also difficult to handle, which is another disadvantage. Among the advantages are the good kinetics on the cathode (air) side, low cost due to inexpensive and non-exotic materials, fast start and high efficiency, simple operation and low weight and volume.

1.3.2 Phosphoric Acid Fuel Cells

Phosphoric acid fuel cells, as the name implies, rely on phosphoric acid as electrolyte. G.V. Elmore and H.A. Tanner constructed a PAFC in 1961, using app. 65 % silica powder to form a paste electrolyte [40]. In a modern PAFC the acid is typically soaked up in a matrix of silicon carbide and PTFE, where it is contained by capillary forces. The matrix must be thin to minimize the ohmic loss, but have enough mechanical strength and thickness to prevent gas crossover from one electrode to another. The cells utilize gas diffusion electrodes with carbon supported platinum on both electrodes. Unlike alkaline fuel cells PAFC can tolerate up to 30 % CO_2 and can thus be operated on atmospheric air as oxidant. Due to the elevated temperature the waste heat can be utilized for cogeneration. The drawbacks of the cells are connected to the electrolyte – phosphoric acid is corrosive, causing safety and handling problems. Also, 100 % H_3PO_4 has a freezing point of 42 °C; therefore PAFC stacks are usually kept at elevated temperature after commissioning to avoid stress development due to freezing and thawing of the acid. Even though the vapour pressure of the H_3PO_4 is low, acid is lost over time, reducing conductivity.

The PAFC technology is believed to be mature enough for the developers to focus their aim on commercial production, with cell components being produced in right scale and appropriate quantities. A big number of intermediate power plants and several plants in hundred kilowatt-scale have been installed around the world, with United Technologies Corp. being one of the largest suppliers with more than 300 units installed worldwide [21]. The interest in the technology, however, has waned, mostly due to the high cost, but also due to the technical progress in the PEM FC field [20, 23].

1.3.3 Solid Oxide Fuel Cells

Tracing its origins back to Nernst lamps [12], the modern solid oxide fuel cells rely on an electrolyte made of yttria-stabilised zirconia (YSZ), which is able to conduct O^{2-} ions when heated above 800 °C. Other materials have been tried, e.g. lanthanum oxide, which was tested beside zirconium and yttrium oxides by the inventors of SOFC, E. Baur and H. Preis in late 1930ies [18, 19], or more recently ceria, Bi_2O_3 and the more exotic LaSrGaMgO (LSGM) [41-43]. Due to the high temperature, non-noble metals can act as catalysts for the SOFC, reducing the cost of the cells. Typically metallic nickel on YSZ skeleton is used on the anode and strontium-doped lanthanum manganite, a *p*-type semiconductor, on the cathode, although many other *p*-type

conducting perovskites have been tried [44]. Unlike most other fuel cell types, CO is not a poison to the SOFC. In fact, it is a fuel alongside hydrogen. The high temperature of the cells allow for spontaneous internal reforming of the fuel. The cells can be used to oxidize any combustible gas and can thus run on e.g. natural gas from the gas grid, provided there is less than 50 ppm sulphur contamination.

The SOFC systems are bulky and voluminous; therefore they are suitable for stationary applications, like CHP or APU. The efficiency of the cells is high, in the 50 – 60 % range. Used in combination with gas turbines, co-generation or hybrid systems the fuel efficiency can be even higher [21, 23, 45]. The commercialization of the technology is hindered by technical issues connected with materials required to withstand the high temperature of operation, chemical compatibility with other parts of the cell, conductivity and stability.

1.3.4 Molten Carbonate Fuel Cells

A binary mixture of lithium and potassium or lithium and sodium carbonates, heated to 600 – 700 °C, comprises the electrolyte of a molten carbonate fuel cell. At those temperatures the carbonates form a molten salt with high CO_3^{2-} conductivity. Absorbed in a ceramic matrix of $LiAlO_2$ it makes the backbone of the cell. Like with SOFC, due to high temperature noble metals are not required to promote the electrode reactions. Nickel on the anode and nickel oxide on the cathode are adequate to catalyse the electrochemical reactions. Another similarity with the SOFC is that molten carbonate fuel cells can internally reform hydrocarbons and use CO as a fuel. Unlike any other fuel cell types, there is a net transfer of CO_2 from cathode to anode, which makes addition of CO_2 to the cathode necessary for operation. This is usually achieved by supplying CO_2 containing anode exhaust to the cathode.

Using a hot liquid electrolyte gives rise to several problems; one of them is losses in the junctions between the electrodes and electrolytes. In PAFC, which also uses a matrix to immobilize the electrolyte, PTFE serves both as a binder and a wet-proofing agent and provides a stable interface between the gas and the electrolyte. There are no stable materials in the operation temperature range of MCFC that are able to provide the same properties as PTFE. Pore size distribution in the $LiAlO_2$ matrix and the electrodes is thus a very important factor, as the cell relies on a balance in capillary pressures to maintain the interfacial boundaries of the triple phase region [46]. Another problem is obvious – corrosion stability of the materials, both the manifolding, but also electrodes, as the nickel oxide on the cathode can be dissolved in the electrolyte. Handling of the hot electrolyte is also an issue. Although the MCFC power plants has demonstrated several thousand hours of operation [47] and a number of kW and MW-scale power plants deployed, the many degradation sources and handling difficulties prevented the technology from a major breakthrough [20, 23, 48].

1.3.5 Proton Exchange Membrane Fuel Cells

As mentioned earlier, PEM fuel cells were invented in 1959 by General Electric for NASA to be used on the first manned space flights [28, 29]. Later on, in mid 1960ies, DuPont developed a new polymer, Nafion, in the search for a more stable membrane material. It has soon become a standard for the PEM FC and is still in use today. The so-called membrane electrode assembly (MEA) is comprised of the membrane, which is proton conducting, and two gas diffusion electrodes with platinum catalyst on both sides, like in PAFC. The operating temperature is 60 – 80 °C, so the cells have a fast start-up time, however little waste heat, which makes them unsuitable for small scale CHP applications. The cells are compact and robust with simple mechanical design and have a fast response time, which makes them excellent candidates as replacement for internal combustion engines (ICE) in the transportation sector. In their study from 2001, B.D. McNicol et al. conclude that a fuel cell vehicle (FCV) performance will exceed that of an ICE vehicle on all parameters except the initial cost [49].

The main disadvantage of the PEM FC is their intolerance to CO, which limits the type of fuel to very pure hydrogen. Another disadvantage is the water management, since Nafion relies on liquid water for proton conductivity.

The PEM fuel cells have been extensively developed since their discovery, both on MEA and system level, improving performance, reducing the catalyst loading, mapping the influence of cell and stack components and reducing the cost. As an example – the 1 kW Gemini 1962 fuel cell system was running at 37 mA/cm² and 0.78 V with a platinum loading of 35 mg/cm² [50]. Many PEM FC units today utilize around or less than 0.3 mg_{Pt}/cm^2 [51], reducing the catalyst loading requirement by a factor of 100. The technology is ready for commercialization, but is being held back by the high cost and durability issues [23].

A direct methanol fuel cell (DMFC) is essentially a regular PEM FC, where the fuel is methanol instead of hydrogen. This gives a great advantage, since the fuel is liquid and contains much more energy per volume unit. The change of fuel is not without drawbacks, as there are 3 major issues connected with it. One is the more complicated mechanism of oxidation, which slows the reaction, effectively reducing the performance of the cell. As a consequence, large amounts of catalysts are required to overcome the large activation overpotentials. The third problem is the electrolyte. Since methanol is fully miscible with water, it readily diffuses from the anode to the cathode through the Nafion, reducing the fuel efficiency of the cell and also poisoning the cathode catalyst [52, 53]. This effect is called fuel crossover, and can be minimized using a thicker membrane or using a dilute solution of methanol [54]. Due to the lower performance DMFCs are primarily targeted at portable electronics equipment, replacing batteries, where high energy density and fast recharging are more important than high efficiency.

To minimize the catalyst activity limitations there was a desire to operate at a higher temperature than Nafion-based PEM fuel cells allowed. Another polymer material, polybenzimidazole (PBI), has been identified as a possible substitute for Nafion. Impregnated with H_3PO_4 it becomes a proton conductor, which besides being stable at temperatures up to 200 °C, thus improving the kinetics of the electrode reactions, also offered another advantage – the fuel crossover current of methanol was between 10 and 1000 times less than for Nafion-based cells [55-57]. The number was based on an un-doped membrane, so in praxis it would be much lower, however still superior to Nafion. Subsequently, the PBI PEM FC was used for the regular H_2/O_2 operation, which worked well at 150 °C [58]. The high temperature also allowed the cells to be run on reformate, since they are much more tolerant to impurities of CO (2% compared to a few ppm for Nafion-based fuel cells) and SO_2 (10 ppm) [59, 60]. Furthermore, since PBI/H_3PO_4 fuel cells do not rely on liquid water for proton conductivity, the water management is much easier, simplifying the system. At last, the cells produce usable waste heat, making it a much more suitable option for a CHP.

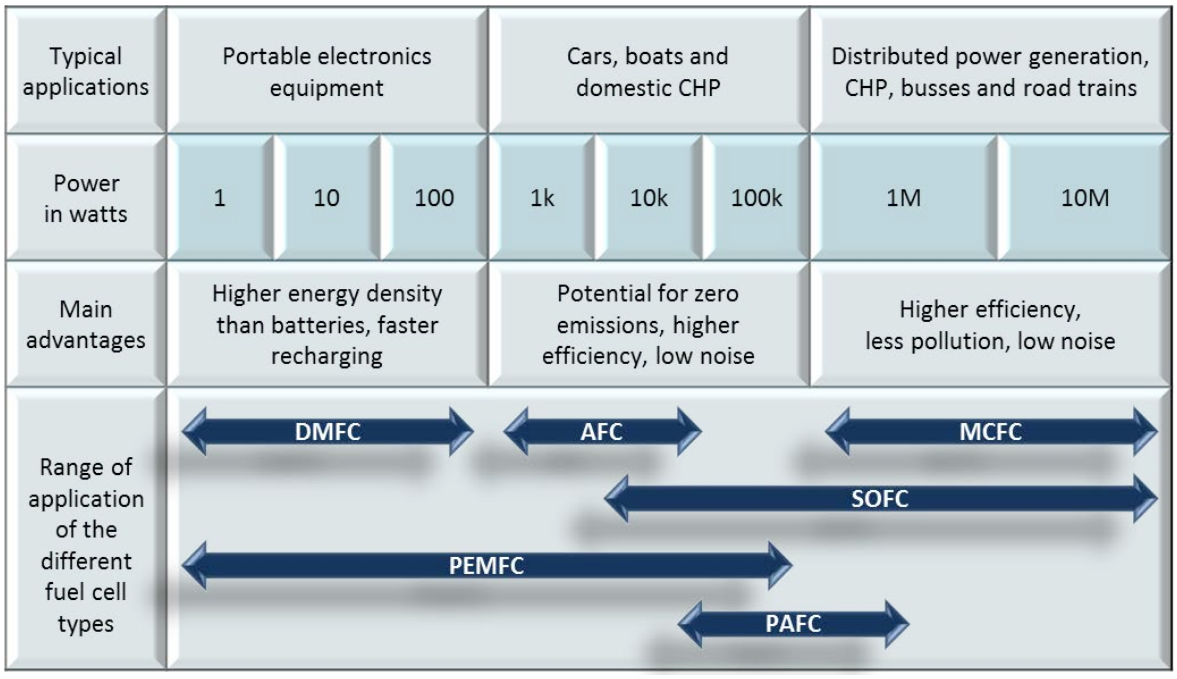

Figure 1.4: Fuel cell types, operation ranges and applications. Data adapted from [20].

Other types of direct PEM FCs are known, which are named according to the fuel they utilize – direct ethanol fuel cells (DEFC), direct formic acid fuel cells (DFAFC) and direct dimethyl ether fuel cells (DDMEFC), the latter being to focal point of the presented work. Their working principles are similar to DMFCs.

The different fuel cell types, their power and application ranges are summarized in Figure 1.4. It is evident that the different fuel cell types cover most of the applications needing powering, so it is indeed possible to break the dependency on fossil fuel and rely on fuel cells for clean power generation.

1.4 Fuels

In order to introduce new types of fuels there are certain criteria that must be met: availability, easy handling, economics, low environmental impact, versatility and high energy density. It is remarkable to note that a single barrel of oil has the energy equivalent of 12 people working all year, corresponding to 25000 man hours [61]. This, together with the cost, easy handling and a developed infrastructure poses a difficult task in order to find an acceptable alternative.

1.4.1 Hydrogen

Hydrogen, an inexhaustible and non-polluting element, is considered to become the energy currency of the future in the already mentioned hydrogen economy. Hydrogen is already being used on a large scale in petroleum and chemical industries, with upgrading of fossil fuels and production of ammonia being the largest applications. Processes such as hydrocracking, hydrodealkylation and hydrodesulphurisation are the key consumers in fuel processing. It is also widely used as a coolant in generators in power stations due to its favourable physical properties. As fuel it is rarely used with exception of propelling rockets and space shuttles, although it becomes more and more common for powering utility vehicles, such as forklifts.

Hydrogen is typically produced on site where it is needed from natural gas and coal, and is thus still linked to the non-renewable fuels. This is done in order to ensure safe supply and avoid difficulties with transportation, the latter being one of the main obstacles on the road to the hydrogen economy. The annual production is around 50 million tons of hydrogen, which is equivalent to ~140 Mtoe, marginally above 1% of the total annual energy demand shown in Figure 1.1. To fully cover the energy demand by hydrogen would require enormous investments not only in production facilities, but also in infrastructure, as storage and distribution of hydrogen is not a simple task. Being the lightest element hydrogen forms very small H_2 molecules that have the intrinsic property to diffuse through most materials. Furthermore it makes many steels brittle, especially at high pressure and/or temperature. It has the highest gravimetric energy density of all fuels, but, as described by Avogadro's law, 1 g of H_2 occupies 12.3 litres at ambient conditions. This results in a very low volumetric energy density, which has a consequence for practical applications. To store sufficient amounts of hydrogen needed for e.g. a vehicle it needs to be compressed to a very high pressure or cooled to below 20.39 K. Liquefying hydrogen is incredibly energy demanding, requiring a staggering 33 % of lower heating value (LHV). Furthermore, hydrogen-air mixtures are explosive in a very wide range, 4-75 vol% at ambient temperature [62].

At present state the 4 out of 6 criteria mentioned in the beginning of this section are not met by introducing hydrogen as a new fuel type. The low energy density makes it impractical to use in many applications. A comparison of energy densities of various fuels is given in Figure 1.5. Hydrogen, as mentioned before, has the highest gravimetric energy density, but even compressed to 700 bars it gives the lowest value,

only 4.6 MJ/L. The traditional gasoline and diesel top the scale. Those are relatively safe and easy to handle, transport and distribute, mainly because of the already developed infrastructure. As a consequence, the alternative fuels should be compatible with the existing infrastructure and uses. Such fuels could be methanol and dimethyl ether (DME), which are already proposed as excellent substitutes for gasoline and diesel respectively [21, 63-65].

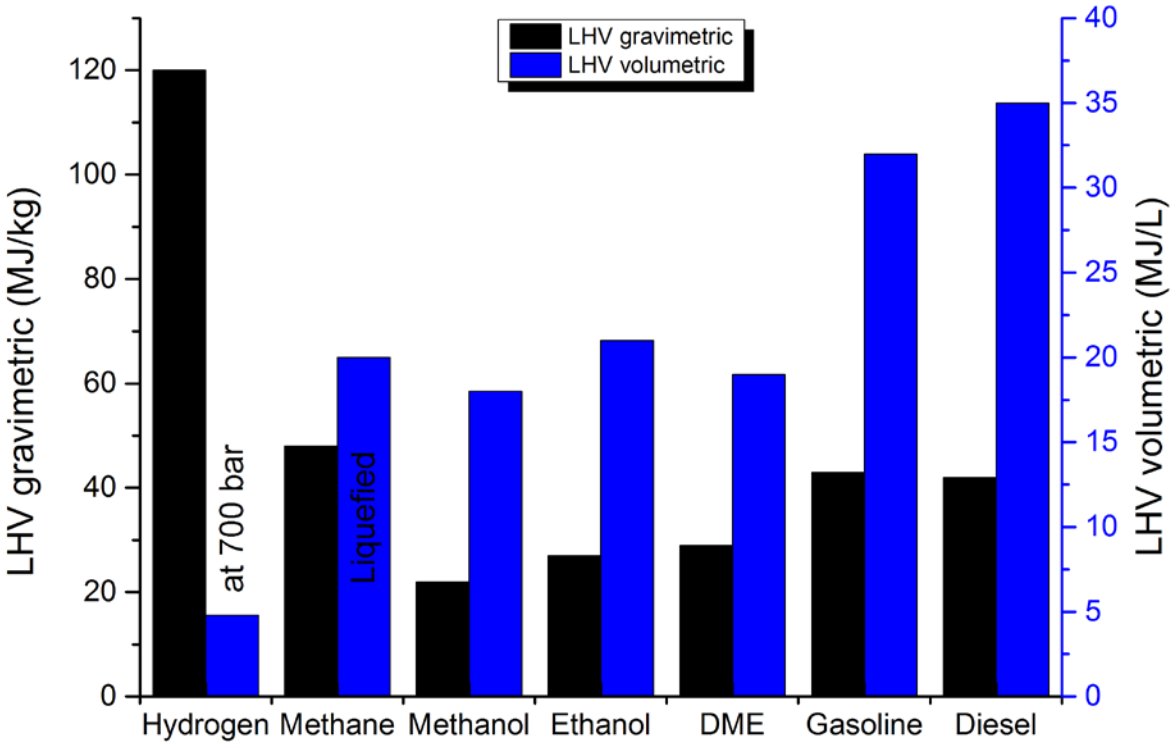

Figure 1.5: Gravimetric and volumetric energy densities of chosen fuels based on lower heating values (LHV). Data from [21, 63, 66].

1.4.2 Dimethyl ether and methanol

A concept called "methanol economy" has been introduced as an alternative to the hydrogen economy by the Nobel Prize laureate in chemistry George A. Olah [67]. It describes an approach to produce methanol and DME by hydrogenative recycling of CO_2 and storing and transporting them in an easy and safe way as liquids. The fuels are to be used both for combustion engines and fuel cells either through reforming or directly in the new generation of fuel cells (DMFC and DDMEFC). Besides their use as fuel, both methanol and DME serve as starting materials for basic chemicals and ethylene and propylene – the basis of synthetic hydrocarbons. The approach thus offers a way to break the dependency on fossil fuels without losing the benefit of their attractive properties and uses [21].

Methanol can be made from any resource that can be converted into synthesis gas. The conventional route is to catalytically crack natural gas with addition of steam

into a mixture of CO, CO_2 and H_2. The second step is to convert the mixture to methanol. The total reactions for the processes are given in eq. 1.1 and 1.2 [68].

$$2\ CH_4 + 3\ H_2O \rightleftharpoons CO + CO_2 + 7\ H_2 \text{ (synthesis gas)} \quad 1.1$$

$$CO + CO_2 + 5\ H_2 \rightleftharpoons 2\ CH_3OH + H_2O \quad 1.2$$

Today methanol is almost exclusively produced from natural gas, but it can be produced by gasification of biomass, or as proposed in methanol economy by capture of industrial or atmospheric CO_2 and H_2 from renewable sources. This would liberate mankind from the dependence on fossil fuels, simultaneously mitigating global warming caused by emissions of CO_2 through chemical recycling [69].

The global methanol demand in 2013 is expected to be 65 million metric tons, while the total production capacity is estimated at 100 million. Up to 70 % of annual production is used in chemical synthesis to produce various methylated compounds to be used in our everyday life, ranging from construction materials, plastics, antifreezing agents and gasoline additives to clothing, food preservatives and pharmaceuticals [70, 71]. The use of methanol directly as a fuel is estimated to 25 % and is gaining more and more attention. Although containing a little more than half the energy per volume than gasoline, it has a higher octane rating of 100, making the internal combustion engines (ICE) more efficient. As diesel fuel, methanol is not suitable, as it has a cetane number of 3 and will thus not ignite reliably [68].

The main concern about introducing methanol as an alternative fuel is that it is toxic. Being a colourless liquid with a mild alcohol scent it can be mistaken for water or ethanol. Ingestion of 25 – 90 mL is lethal without timely treatment, compared to 120 – 300 mL gasoline. Methanol is metabolised to formic acid, causing blurring or loss of vision and acidification of the blood, which can lead to death. In terms of fire hazard, methanol is much safer than gasoline. Although methanol vapour at 6 - 36 vol% is flammable [66], it takes long time to achieve the minimum concentration due to low vapour pressure. In case of ignition, it burns 4 times slower and radiates heat at one-eight rate of gasoline, reducing the risk of fire spreading. The U.S. Environmental Protection Agency has estimated that the fuel related deaths and injuries would decrease by 95 % and fires would decrease by 90 % if methanol is used instead of gasoline [72]. As for environmental safety aspects, methanol is degraded in both aerobic and anaerobic conditions and is a plant growth promoter. It has low toxicity to aquatic and terrestrial organisms. Only major spills present a potential hazard, as methanol can penetrate to and contaminate ground water [21, 68, 69, 71, 72].

Dimethyl ether is another small organic compound, which has been proposed as substitution for fossil fuels and alternative to hydrogen. It is the simplest ether, with a chemical formula CH_3OCH_3. At ambient conditions it is a gas, but it is easily liquefied by cooling to -24.9 °C or compressing above 5.1 bar [73]. The vapour pressure is that between propane and butane, allowing DME storage and handling by the already existing infrastructure for liquefied petroleum gasses (LPG).

Today DME is produced almost exclusively by dehydration of methanol, given by reaction 1.3. It is a simple process and a preferred method for small scale production due to the low cost of plant. The major feedstock is natural gas, mainly due to economics, but it is not limited to one resource and can be produced from anything that can be converted into syngas and/or methanol.

$$2\ CH_3OH \rightleftharpoons\ CH_3OCH_3 + H_2O \qquad 1.3$$

$$2\ CH_4 + O_2 \rightleftharpoons CH_3OCH_3 + H_2O \qquad 1.4$$

In recent years a lot of effort has been put to produce DME in one step from syngas via autothermal reactors and directly from natural gas in liquid phase slurry reactors [74-77], the latter given by reaction 1.4. Those routes are preferable for large scale operation, resulting in better yields and significantly decreasing the cost of the plant and the consumption of natural gas per unit of DME produced. Like methanol, dimethyl ether can also be produced by direct catalytic hydrogenation of CO_2 [21].

The global annual demand for DME was around 150,000 metric tons until 2004, but since then it has been increasing rapidly, mostly due to its growing use as fuel. The DME market is growing fast, especially in Asia, where DME is replacing residential gas. In China alone, the domestic production has risen from 50,000 tons in 2002 to 400,000 in 2006, 3 million tons in 2008 and 10 million in 2011, continuing to grow [78], although not so rapidly due to temporary saturation of the market. The primary use of dimethyl ether until 2000 has been as propellant in aerosol industry, with the remainder being used to produce dimethyl sulfate, a powerful methylation agent [79]. DME is also used as a refrigerant, precursor for agricultural chemicals and cosmetics and even as a treatment for warts [80].

DME has been promoted as a diesel substitute since mid 1990ies [21, 63, 64, 73]. Having a cetane number of 55 – 60 (regular diesel 40 - 55), DME ignites well on compression in diesel engines. There are several benefits using neat DME as a fuel in a CIDI (Compression Ignition Direct Injection) diesel engine. Lacking carbon - carbon bonds, it produces no soot upon combustion, which is one of the major pollutants from diesel engines. Due to the higher cetane number the amount of unburnt fuel is lower, reducing CO and hydrocarbons emissions. Emissions of NO_x are considerably less than that of a diesel fuel. The hydrocarbons emissions are almost non-existent. Some unused DME is emitted, which is environmentally harmless, and can easily be removed together with CO by an oxidation catalyst. The noise from the engine is also lower, becoming comparable to a gasoline engine. Finally, due to low boiling point DME instantly vaporizes upon injection to the combustion chamber, allowing for use of a very low injection pressures <300 atm vs. 2000 atm [64]. There is a small number of drawbacks, which are related to the physical properties of DME, the most challenging being the low viscosity, less than for diesel by a factor of 20 and the ability to dissolve or swell up many kinds of rubbers and plastics. This leads to premature wear of sealings, pumps and fuel injectors. Another issue is low lubricity of

DME, which can be solved to some extent by additives, which are also used for diesel fuels. The sealing issues can be solved using other materials, of which Teflon®, Kalrez® or non-sparkling metal to metal sealings are the most promising. The fundamental research on solving those issues is still ongoing [73]. The last consideration is the energy density of DME. As can be seen from Figure 1.5, the volumetric energy density of DME is roughly half that of diesel, requiring a tank twice the size to reach similar driving range. This is not a big issue, especially for trucks, as the additional space required for a larger tank is much less than the space occupied by the exhaust clean up system required to remove diesel particulate [81].

Dimethyl ether has been handled for many years and has a good safety record. Due to its similarity with LPGs the same safety procedures and regulations apply. It has a distinctive sweet ether-like odor and thus does not require an odorant. The flammability range is less than that of methanol, 3.4 – 27 vol% [66], but still higher than those of gasoline and diesel, 1 – 7.6 and 0.6 - 5.5 respectively [82]. Unlike other ethers, DME does not form peroxides. DME is non-toxic, unlike methanol, non-carcinogenic and non-mutagenic. A toxicology study on rats have shown that DME concentration in air of up to 20 000 ppm over exposure period of 8 months did not lead to any deaths [79]. With regard to the environment, DME has been found to have very little impact. The lifetime in the atmosphere is only 5.1 days and yields very small global warming potential (GWP), decreasing from 1.2 in a time horizon of 20 years to 0.3 and 0.1 for 100 and 500 years, respectively [83]. For comparison, methane has GWP of 56, 21 and 6.5 for the same time horizon. CO_2 is the reference with GWP 1 in all cases. The well-to-wheel (WTW) greenhouse gas emissions of DME are the lowest when compared to Fischer-Tropsch diesel, biodiesel, ethanol, methanol and methane. With exception of natural gas, dimethyl ether has also been found to have highest WTW efficiencies for all non-petroleum based fuels [63]. With the above in mind it can be said that DME is a safe and environmentally benign fuel alternative.

Although the discovery of the DME use as a fuel had been accidental, it is obvious that it has a great potential to replace diesel, allowing for a more environmentally friendly transportation with a possibility to become fossil free through DME production from biomass and eventually CO_2 recycling.

2 PEM Fuel Cell Fundamentals

Fuel cells have several advantages over power generating technologies conventionally used today. They are simpler, with few moving parts, which can lead to highly reliable and long-lasting systems. The fuel cell technology is a silent one, even the types with extra fuel processing equipment. They have the potential to be near zero-emission, but most important is their efficiency. Unlike combustion engines, fuel cells are not limited by the Carnot cycle, since they convert chemical energy directly to electricity. The Carnot efficiency is the maximum efficiency a heat engine burning fuel can have. In practice, the efficiencies are much lower due to irreversibilities. The Carnot cycle efficiency is given by a ratio between the maximum absolute temperature of the engine, T_h, and the temperature of the gas leaving the engine, T_c, see equation 2.1 [84].

$$\xi_{HE} = 1 - \frac{T_c}{T_h} \qquad 2.1$$

The maximum fuel cell efficiency is the same as thermodynamic efficiency of energy conversion, which is a ratio between the Gibbs free energy, ΔG, a measure of the available work of a system or a reaction, and the energy content of the fuel, given by the enthalpy, ΔH. The thermodynamic efficiency ξ_{th} is given in equation 2.2 [84].

$$\xi_{th} = \frac{\Delta G}{\Delta H} = 1 - \frac{T\Delta S}{\Delta H} \qquad 2.2$$

Since Gibbs free energy is a function of temperature, the thermodynamic efficiency is decreasing with increasing temperature. It would suggest that low temperature is favourable, but this is countered by the fact that the voltage losses at higher temperatures are almost always lower. The thermodynamic efficiencies of the Carnot cycles with different T_c are compared to the theoretical efficiencies of H_2/O_2 fuel cell in Figure 2.1. The jump in the curve is due to the water forming below 100 °C is in liquid form, the energy available from the fuel is lost due to lower entropy state of the product. This is reflected in the molar enthalpies for the formation of water, which is -285.83 kJ/mol for liquid product and -241.83 kJ/mol for steam product at 298.15 K and 1 bar [66, 85]. These values are usually referred to as the higher heating value (HHV) and lower heating value (LHV) of hydrogen, respectively. A more accurate efficiency limit would be based on the LHV for the entire temperature range, but when comparing to the Carnot cycle, where the efficiency is given by the temperature of the exhaust, it would be more proper to take the physical states of water into account.

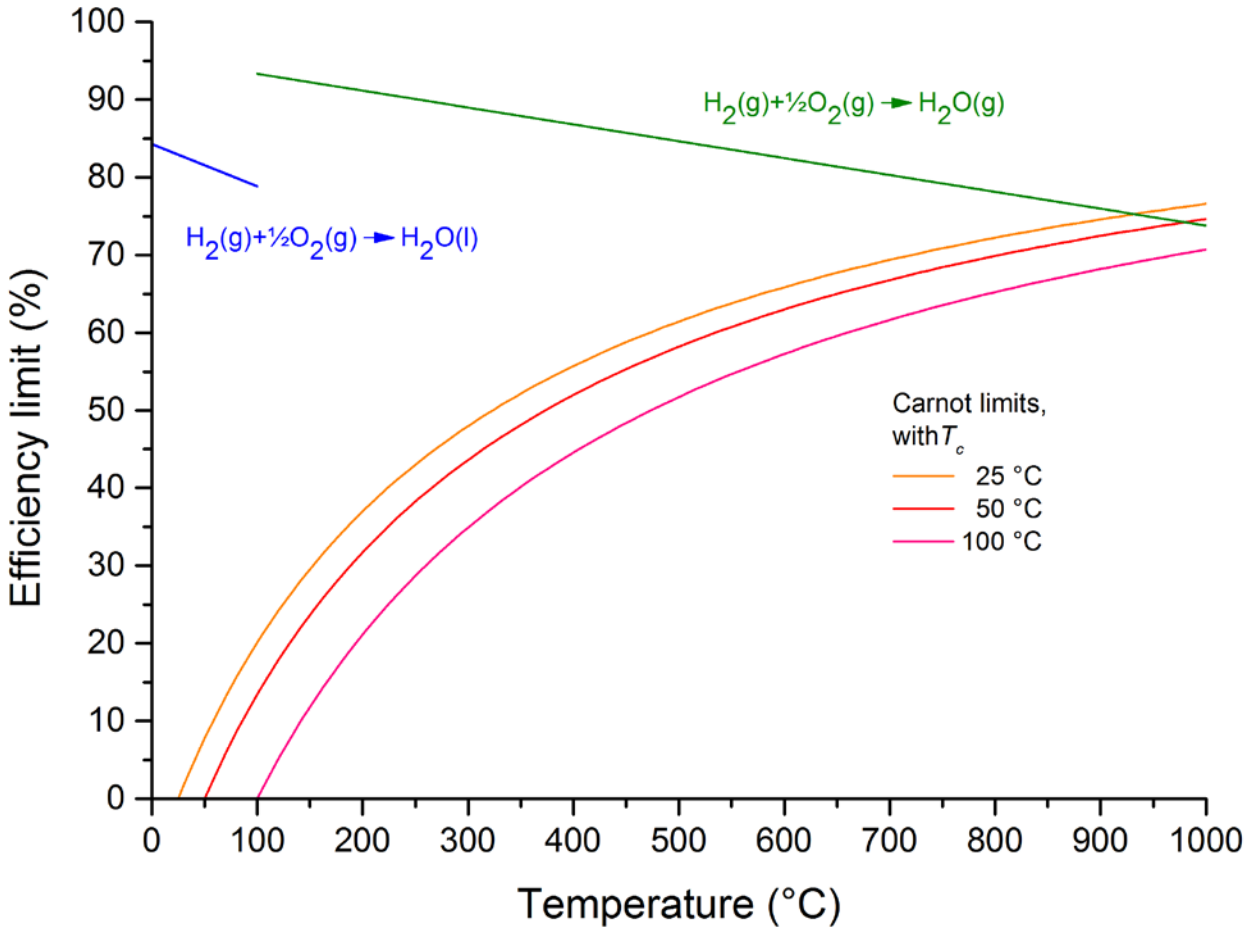

Figure 2.1: Comparison between thermodynamic efficiency limits for Carnot process with different T_c values and H_2/O_2 fuel cell at standard pressure. Thermodynamic fuel cell efficiency is calculated based on $\Delta_f H°$ and $\Delta_r G°$ values from [66, 85].

2.1 Electrochemical theory

The maximum energy available from a reaction, given by ΔG, and the electric work obtained, given by the electromotive force (emf) E, are related by equation 2.3. n is the number of electrons participating in the reaction and F is the Faraday's constant, their product giving the charge generated by the reaction. The negative sign is due to the convention of electric work obtained being positive number, but the work done by the system on the surroundings being negative by definition [22].

$$\Delta G = -nFE \qquad 2.3$$

The Gibbs free energy of the reaction is related to the composition of the reaction mixture Q, which is a ratio between the activities of products and reactants [84]:

$$\Delta G_r = \Delta G_r^\circ + RT ln Q \qquad 2.4$$

R is the gas constant, T is the absolute temperature and ΔG_r° is the value at standard conditions.

By substituting equation 2.4 into 2.3 and rearranging the Nernst equation is obtained:

$$E = E^{\circ} - \frac{RT}{nF} lnQ \quad 2.5$$

Nernst equation describes the dependence of the electromotive force on the activities of the reactants and products and temperature. E° is the standard emf of the reaction. It is also clear from the equation, that the potential of a cell is the difference between the individual electrode potentials [86]:

$$E_{cell} = E_{cathode} - E_{anode} \quad 2.6$$

2.1.1 Kinetics

The Nernst equation gives the electromotive force of the cell, which is merely Gibbs free energy in disguise, giving the theoretical maximum of electrical work available. In practical sense, a real fuel cell almost never reaches the theoretical emf value, and when current starts flowing through the cell, different components show characteristic current-voltage behaviours, resulting in negative contributions to the overall cell voltage.

Some of the most significant losses occur at the electrodes, where the kinetics of electrochemical reactions impede the performance of the cell. The deviation of the potential from equilibrium value can be derived from rate constants of electrode reactions and is called overpotential, η. The current at $\eta = 0$ is defined as the exchange current i_0, when the rate of the forward reaction is equal to the rate of the backward reaction. i_0 is an important kinetic parameter of electron transfer process. The total current can be expressed as a function of the overpotential and exchange current and is known as the Butler-Volmer equation [87]:

$$i = i_0 \left(e^{\frac{\alpha nF}{RT}\eta} - e^{\frac{(1-\alpha)nF}{RT}\eta} \right) \quad 2.7$$

where α is the charge transfer coefficient and is a measure of the symmetry of the activation barrier. The Butler-Volmer equation is derived from the Arrhenius equations for the rates of forward and backward reactions.

For small values of η the exponential can be approximated by the first term of the Taylor expansion to give a simple expression for the current:

$$i = -i_0 \frac{F}{RT} \eta \quad 2.8$$

The expression shows that the total current is a linear function of the overpotential when the latter is close to the equilibrium potential E. In this range, the ratio of the overpotential to current can be expressed as the charge transfer resistance R_{ct}, given in equation 2.9.

$$R_{ct} = -\frac{\eta}{i} = \frac{RT}{Fi_0} \quad (2.9)$$

At large η one of the exponents in the Butler-Volmer equation become negligible, since the reaction is totally irreversible, and equation 2.7 can be simplified to:

$$i = i_0 e^{-\alpha \frac{F}{RT}\eta} \quad (2.10)$$

In logarithmic form it is known as the Tafel equation [87]. If the overpotential is plotted against $\log i$, systems with sluggish electrode kinetics will show a good linear correlation. This is called Tafel behaviour and is an indicator of a totally irreversible process as the system is not allowing any significant current flow except at high overpotentials. The Tafel plot is a very simple way of determining the exchange current density and charge transfer resistance from the intercept with the ordinate and the slope of the line. The Tafel equation is given in 2.11 and the intercept and the slope in 2.12.

$$\eta = a + b \ln i \quad (2.11)$$

$$a = \frac{RT}{\alpha F} \ln i_0 \qquad b = -\frac{RT}{\alpha F} \quad (2.12)$$

2.2 The i-V relationship

The activation losses are not the only when it comes to the performance of a running cell. Whenever current flows through the system, Ohms law applies, equation 2.13, with the resistance of the cell decreasing the voltage with increasing current. In the fuel cell the resistance is caused mainly by the electrolyte, and is minimised by using a more conducting membrane or simply by decreasing the thickness.

$$V = iR \quad (2.13)$$

The electrolyte is also responsible for the internal current and fuel crossover losses. Even though the electrolyte is chosen due to its ion conductivity, there is still some minor electronic conduction, the electrons are not running through external circuit and their energy not put into electrical work. This loss is, however, minimal. More important is the fuel crossover, where a fraction of the fuel diffuses through the electrolyte to the cathode, producing no current. In case with DMFC the fuel is also poisoning the catalyst, aggravating the effect. Those losses can be minimised by using a thicker membrane, but at the expense of higher ohmic resistance. The easiest way to observe the effect on fuel cell performance is when no current is drawn. The cell voltage at zero current deviates from the theoretical emf by a sum of internal current, crossover and activation losses.

The last contribution is due to the mass transport losses, which are associated with transport of species in the electrolytic phase and of gas phase reactants and products.

If a reactant is consumed faster than it can be supplied, there is a change in pressure. From the Nernst equation (1.2) it follows that the voltage of the cell will decrease. If i_l is the current at which the fuel is consumed at the speed equal to the supply, then the Nernst equation can be rearranged to express the voltage loss [88]:

$$V = -\frac{RT}{nF} ln\left(1 - \frac{i}{i_l}\right) \quad \textbf{2.14}$$

The equation predicts a very rapid drop in voltage when the current approaches limiting value. This approach is purely theoretical and assumes uniform current distribution over the electrodes. This is not the case and some parts of the electrode can have reached limiting value while others are still working fine [89]. The production and removal of species is also not expressed. When air is used instead of pure oxygen, there can be a build-up of nitrogen, especially in passive cathodes where the air supply is not circulated, which is not accounted for by the equation. In practical fuel cells the limiting current is almost never reached, but the drop in voltage at high currents is still observed. To describe this phenomenon an empirical approach has been proposed by Kim et al. [90]:

$$V = me^{ni} \quad \textbf{2.15}$$

The constants m and n are purely empirical and depend on the conditions inside a particular fuel cell. Therefore they have to be determined experimentally for each cell. Nonetheless they are good descriptive markers when comparing individual cells to each other. The authors attribute the parameter m to the voltage loss due to mass transport limitations at intermediate currents and the parameter n to the steep voltage drop at high currents.

Combining all the losses yields the voltage of the cell as a function of current. This function is known as the fuel cell polarisation curve and is represented in equation 2.16 in its full form [20, 89]:

$$E_{cell} = E - \frac{RT}{\alpha_a F}\ln\left(\frac{i + i_{n,a}}{i_{0,a}}\right) - \frac{RT}{\alpha_c F}\ln\left(\frac{i + i_{n,c}}{i_{0,c}}\right) - iR - \frac{RT}{nF}\ln\left(1 - \frac{i}{i_{l,a}}\right) - \frac{RT}{nF}\ln\left(1 - \frac{i}{i_{l,c}}\right) \quad \textbf{2.16}$$

with E being the Nernst potential of the cell at given temperature and pressure and i_n giving the magnitude of the internal current and fuel crossover on the anode and cathode sides.

The equation can be approximated to yield eq. 2.17, assuming negligible crossover and very small anode losses, which is the case with H_2 fuelled cells. E_{OCV} is the open circuit voltage (OCV) of the cell at zero current, given by equation 2.18.

$$E_{cell} = E_{OCV} - b\ln i - iR - me^{ni} \quad \textbf{2.17}$$

$$E_{OCV} = E + b\ln i_0 \quad \textbf{2.18}$$

Equation 2.17 has been shown to give very good fits to experimentally obtained polarisation curves and is thus a powerful and simple tool to extract data and compare individual cells to each other [90, 91]. A modelled polarisation curve for a good performing HT-PEM FC at 160 °C is depicted on Figure 2.2. The dotted line gives the emf at actual temperature and pressure. The theoretical potential of 1.23 V is given by the dashed line. The difference between the E° and E_{cell} gives an indication of the fuel cell efficiency. On the same figure the product of potential and current is depicted, showing the maximum power the cell can achieve.

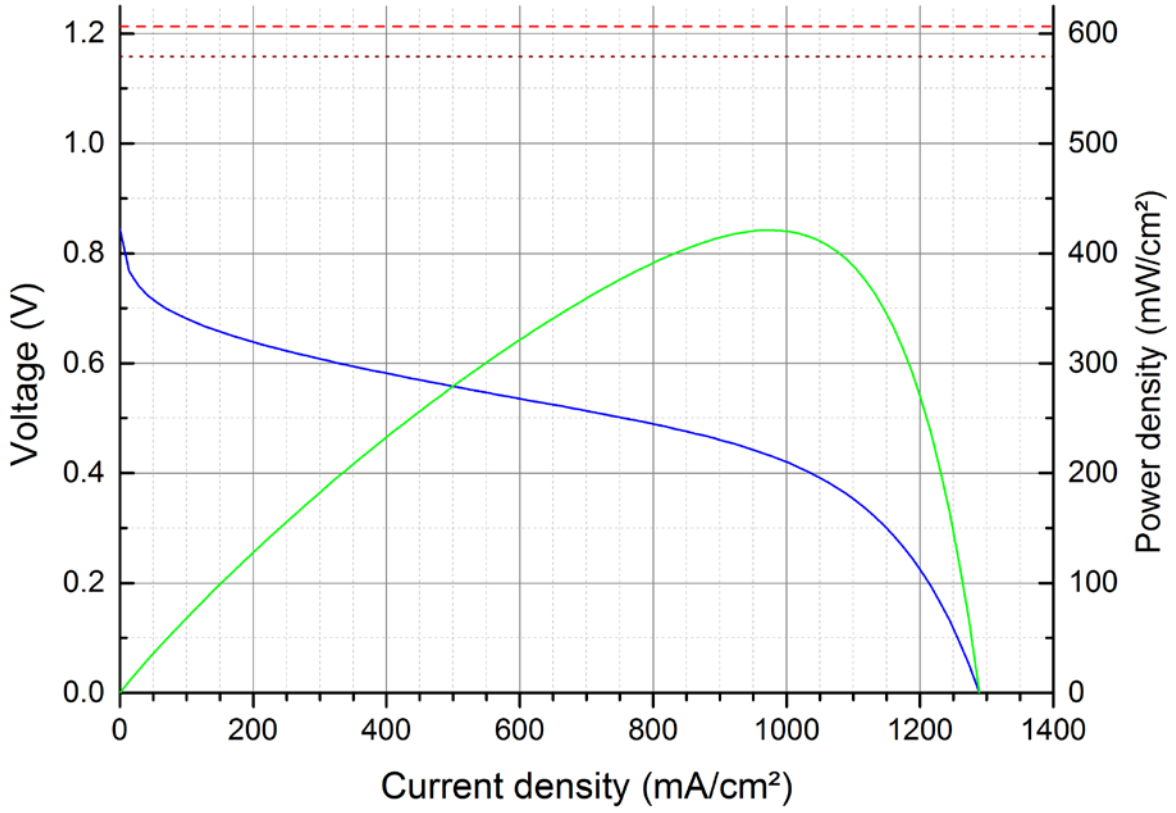

Figure 2.2: HT-PEM FC polarisation curve at 160 °C and 1 bar with H_2 and air on the anode and cathode respectively (blue) together with the resulting power curve (green). The dashed line (red) denotes the standard emf of the reaction, E°. The dotted line (dark red) indicates the emf of the reaction at operating temperature and pressure.

2.3 Practical fuel cell efficiency

The polarisation curve is a good tool for evaluating cells and comparing them to each other, but from application point of view a relationship between power and efficiency is more interesting. From Figure 2.3 it can be seen that the cell with the characteristics given in Figure 2.2 reaches maximum power density with efficiency of only 35%, even without taking into account fuel utilisation. This is much less than the theoretical efficiency of ca. 93% (LHV, from Figure 2.1 at 160 °C). For this reason fuel cells are almost never operated at their maximum power, but are sized with the particular application in mind. For stationary applications a high efficiency is

desirable, while space is typically not very important, therefore the cells are made large and operate at high nominal voltage. For applications where size is important, a lower nominal voltage is chosen, on expense of efficiency [89].

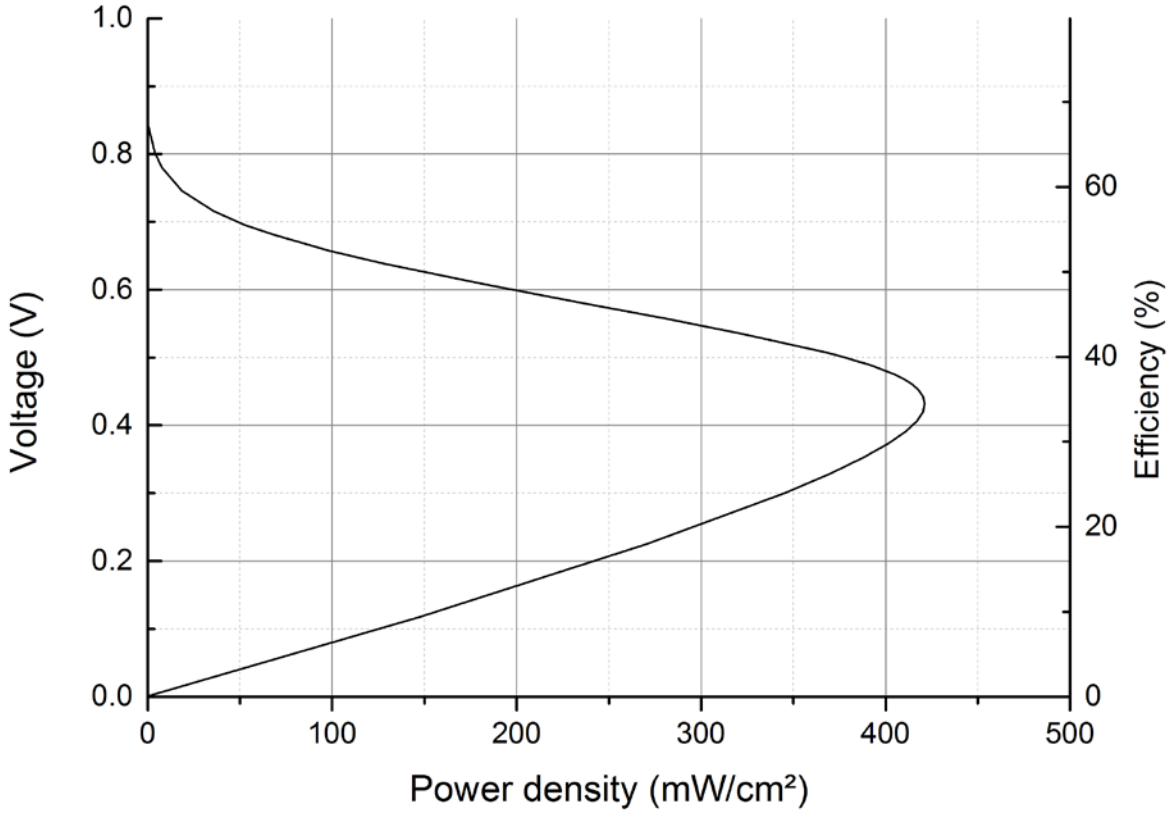

Figure 2.3: Cell voltage and efficiency as function of power density (LHV).

The efficiency of a practical cell is a product of the voltage efficiency, which is a ratio between the cell voltage E_{cell} and the energy content of the fuel given by E°, and fuel utilisation, sometimes also called current efficiency. The latter is calculated based on the ratio between the fuel reacted in the cell, which is proportional to the current drawn, I_{cell}, and the current theoretically available from the flow rate of the reactant fuel, I_{flow}.

$$\xi = \frac{E_{cell}}{E^{\circ}} \frac{I_{cell}}{I_{flow}} \qquad 2.19$$

$$I_{flow} = \frac{Fn}{Fuel\ flow} \frac{p}{RT} \qquad 2.20$$

where n is the number of electrons and p is the pressure of the fuel.

2.4 The working principle

The idea behind a fuel cell is electrochemical conversion of chemical energy of reactants into electrical energy. Water is the primary product of the reaction together

with CO_2 in case organic fuels are used. Heat is produced due to irreversibilities, described in section 2.1.1, according to the first law of thermodynamics. The oxidation of the fuel happens on the anode, while the reduction of the oxidant happens at the cathode. The oxidation of the fuel produces electrons, which flow from the anode to the cathode, where they reduce the oxidant. The current flows in the opposite direction. The flow of electrons must happen in an external circuit in order to harvest electricity from the cell; therefore an electronically insulating and gas tight electrolyte is employed to separate the anode and the cathode. Combining the anode and the cathode with the electrolyte in a sandwich structure gives the heart of a fuel cell, the membrane electrode assembly (MEA).

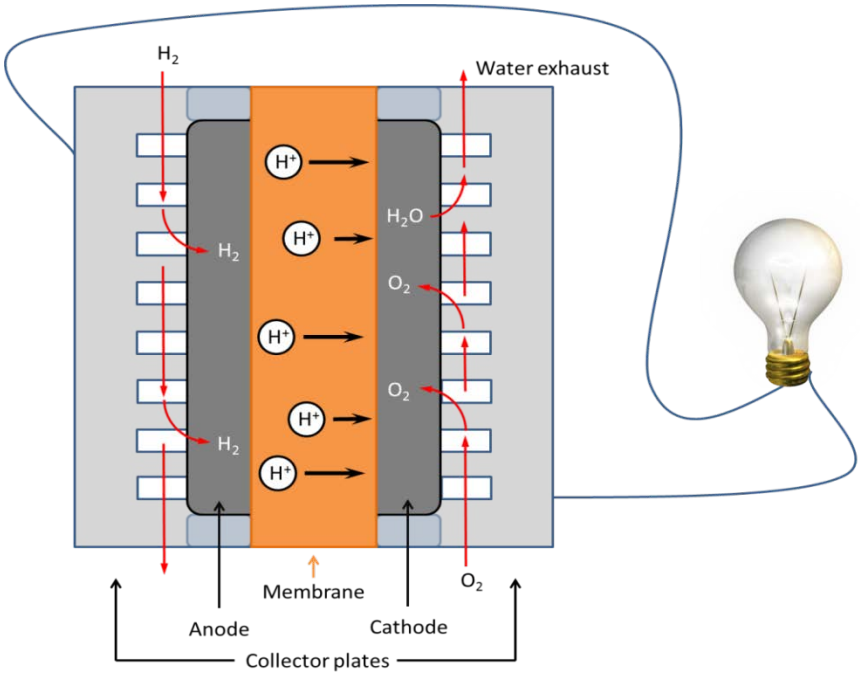

Figure 2.4: Main PEM fuel cell components (not to scale) and the working principle.

In a high temperature proton exchange membrane fuel cell (HT-PEM FC) a polymer poly-(2,2´-m-(phenylene)-5,5´-bibenzimidazole (also called polybenzimidazole and abbreviated PBI) impregnated with phosphoric acid is used as an electrolyte. The electrodes are porous to allow the reactant gasses to access the reactive sites on the catalyst and remove the product gasses. They are also electronically conducting to allow electron flow. On the anode side the fuel is deprotonated, and the protons flow through the electrolyte to the cathode, where they recombine with the oxidant, typically oxygen from the air, to form water. The MEA is put in between collector-separator plates in which there are channels for the gasses. The plates are called bipolar plates, because they physically and electrically connect the anode of one cell to cathode of the other in a stack, providing a pathway for the electrons, but also ensuring no mixture of the anode and cathode gasses is happening. The requirements for the bipolar plates are quite demanding – they must be electrically and thermally conductive, impermeable to gasses, conformable and strong and lightweight, as they

provide structural support. Not many materials are suitable; therefore a big part of the total cost of a fuel cell stack is due to bipolar plates. Since one cell can only give a maximum of app. 1 V, for practical applications they are typically stacked, with the above mentioned bipolar plates in between. The working principle of a fuel cell is represented on Figure 2.4.

With hydrogen as fuel and oxygen from the air as oxidant, the half-cell reactions on the electrodes and the total cell reaction can be expressed in equations 2.21 to 2.23:

Anode	$H_2 \rightarrow 2\,H^+ + 2\,e^-$	$E^\circ = 0\,V$	2.21
Cathode	$\frac{1}{2}\,O_2 + 2\,H^+ + 2\,e^- \rightarrow H_2O$	$E^\circ = 1.23\,V$	2.22
Overall	$H_2 + \frac{1}{2}\,O_2 \rightarrow H_2O$	$E^\circ = 1.23\,V$	2.23

The difference between the standard potentials of the oxygen reduction reaction (ORR) and the hydrogen oxidation reaction (HOR) gives the voltage of the cell, according to equation 2.6.

2.4.1 Membrane electrolyte

As mentioned in section 1.3.5, the traditional low temperature PEM fuel cells suffer from high CO intolerance. Since the major part of hydrogen produced today is made by reforming, it inevitably contains trace amounts of CO, which is poisonous for the cell. If other organic fuels are used, like methanol and dimethyl ether, the oxidation process goes via CO intermediates, as will be shown later. Improving the tolerance of the PEM fuel cells towards CO has been one of the main topics in early 2000ies. One way to solve the issue is to increase the operating temperature, so the catalyst is not poisoned by CO as easily. The traditional PEM fuel cells use perfluorosulfonic acid (PFSA) polymers, e.g. Nafion®, as electrolytes [51, 92]. The problem is that Nafion® relies on liquid water for proton conductivity. The cell must be supplied with humidified gasses and cannot be operated at temperatures very close to or above 100 °C without pressurisation. There is another problem connected with use of PFSA polymers when operating on methanol as a fuel. Due to the solubility of methanol in water, the methanol crossover is in the order of 10^{-6} mol/(cm²s), corresponding to a current density loss of 50 – 100 mA/cm², depending on the concentration, compared to 10^{-10} mol/(cm²s) for hydrogen, attributing to a loss of 1 – 10 mA/cm² [93, 94]. The crossover of methanol not only wastes fuel, but also results in a mixed potential on the cathode side, further reducing the performance of the fuel cell. In order to overcome the problems, different types of polymers and their blends have been investigated.

Polybenzimidazole was proposed for PEM FC with operation at temperatures approaching 200 °C by R.F. Savinells group in 1995 [55]. PBI was already then a commercially available polymer. Being oxidatively and thermally stable up to app. 435 °C, PBI fibers have been used in clothing for firefighters. Films made of the polymer were also used as vapour barriers. Impregnated with amphoteric acids, such

as sulphuric or phosphoric acid, PBI showed increasing proton conductivity with increasing acid concentration. This, together with the stability of the polymer allowed it to be used as a proton exchange membrane for direct methanol fuel cell, minimising the fuel crossover, allowing for operation above 100 °C, which enhances the electrode kinetics for methanol electrooxidation and depresses the CO and other intermediates poisoning effect on the catalyst. Further benefit is the obviation of complicated water management, required when using PFSA membranes. The last benefit is the relatively low cost of PBI, compared to Nafion®. The chemical structure of PBI is given in Figure 2.5. The proton conductivity in a matrix of PBI impregnated with phosphoric acid is achieved through the Grotthuss mechanism, where protons are transported through rapid reorganisation of hydrogen bonds [95, 96]. The mechanism does not involve net transport of molecules, in contrast to vehicle mechanism, which is proposed to be governing the proton conductivity in PFSA-based cells [97, 98].

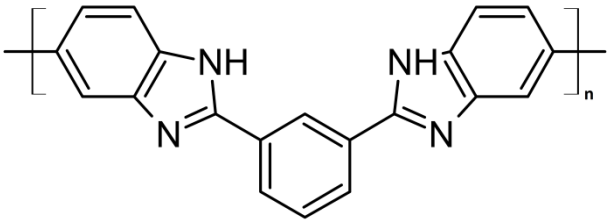

Figure 2.5: Chemical structure of m-PBI.

The operating temperature of a HT-PEM FC is 160 – 200 °C. Even though PBI has a higher glass transition temperature, the presence of phosphoric acid sets the limitation. Although thermogravimetric analysis of PBI loaded with fuel cell grade platinum and impregnated with H_3PO_4 showed no significant decomposition below 600 °C [57], the phosphoric acid is believed to dehydrate and polymerise rapidly at temperatures above 200 °C, losing proton conductivity. Another difficulty is faced during start-stop cycles, where temperature decrease below 100 °C involves phase transition of water condensation, which leads to acid leaching out of the membrane. While the dehydration and polymerisation of the acid is partly reversible, the leached acid is lost, irreversibly lowering the conductivity of the membrane with following decrease in cell performance [99].

Originally devised for DMFC operation due to low fuel crossover and higher operation temperatures, the PBI/H_3PO_4 system has subsequently been used for the regular H_2/O_2 operation [55, 58, 100]. This opened a possibility to make simple and compact integrated reformer and fuel cell systems, without the need of a complicated clean-up system of the reformed hydrogen, as PBI-based cells have shown tolerance of up to 3% CO in the hydrogen fuel feed at temperatures between 175 – 200 °C with minimal losses in performance. The efficient and compact systems are especially important in the transportation sector, where HT-PEM FC allows for combining the high energy density of liquid fuels with the good performance of hydrogen fuelled cell. The integration of the reformer and a fuel cell without elaborate fuel processing systems also benefits from the excess heat from the fuel cell to the reforming process.

2.4.2 Electrode materials

The electrodes facilitate the half-cell reactions and are comprised of several layers, each with its own functionality. Closest to the membrane is the catalyst layer, consisting of a mixture of the electrolyte, catalyst and support material. In order for the reactions to happen, three conditions must be met – protons must be able to travel to and from the reaction sites, therefore the presence of the liquid electrolyte. Electrons flow through solid catalyst and the support material. The reactant and product gasses are transported through the void, therefore the electrode is porous. Where all three conditions are fulfilled, the so-called triple phase boundary is formed. Maximising the triple phase boundary area has a tremendous positive effect on the performance of the cell.

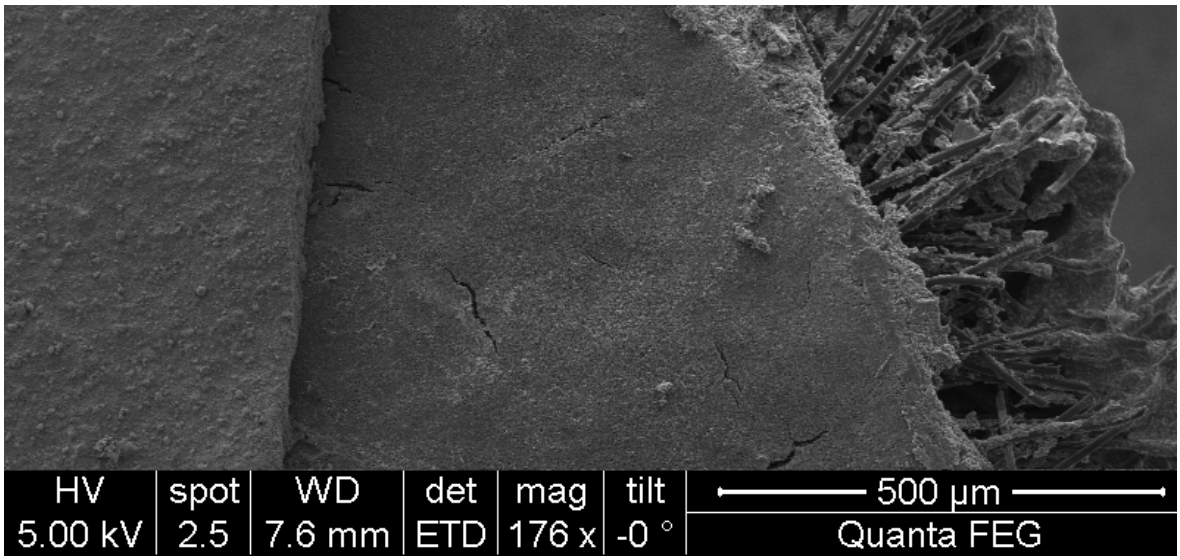

Figure 2.6: SEM image of an electrode edge. Carbon fibres comprising the GDL are seen on the right, the smooth microporous layer in the middle region and the catalyst layer on the left. The electrode is made of 5 mg_{metal}/cm^2 60 % Pt-Ru on 40 % C catalyst deposited on a PTFE treated non-woven carbon cloth.

On the outside of the electrode there is the gas diffusion layer (GDL). It consists of carbon cloth or paper, made up of carbon fibres, and is usually coated with polytetrafluoroethylene (PTFE, Teflon®). The coating facilitates water removal from the catalyst layer. As the name implies, the GDL is responsible for the diffusion of the gasses to the catalyst layer, but it also serves as electron conductor and provides physical support, as it is the most rigid part of the MEA. On the side towards the membrane the GDL is coated with a mixture of PTFE and carbon black, which ensures a smooth homogeneous surface, on which catalyst layer is applied. This is called the microporous layer, as it forms a plane surface, which is still highly porous to allow gas diffusion to and from the catalyst layer. The carbon black component ensures electronic conductivity between the catalyst and gas diffusion layers. The three different layers making up the electrodes of a HT-PEM FC can be seen on Figure 2.6. The GDL is made of a PTFE treated non-woven carbon cloth with a microporous layer consisting of a mixture of carbon black and PTFE, and the catalyst is a 60% Pt-Ru alloy on 40% carbon black. The loading of the precious metal is very

high for this particular electrode, 5 mg/cm², compared to regular electrodes for hydrogen fuelled HT-PEM FC (app. 0.3 and 1.0 mg/cm² metal on anode and cathode respectively), which is why the catalyst layer appears thick on the picture.

In the acidic HT-PEM FC the most active catalyst for both the HOR and ORR is platinum, although other catalysts, such as ruthenium or palladium, can be used with reduced performance. In the accordance with the Sabatier principle, the catalyst should strongly bind the substrate, but the strength of the bond must not be too great, so the substrate can subsequently leave the surface. There is a direct relationship between the metal-substrate bond and the exchange current density (reaction rate). A plot of exchange current densities for HER on different metals as a function of metal-hydrogen bond strength gives the typical volcano curve, as shown in Figure 2.7 to the left [101]. A similar plot can be derived for the ORR, with the oxygen reduction activity as a function of oxygen binding energy [102]. For both reactions platinum is on top, representing the optimum catalyst for both electrodes of a HT-PEM FC.

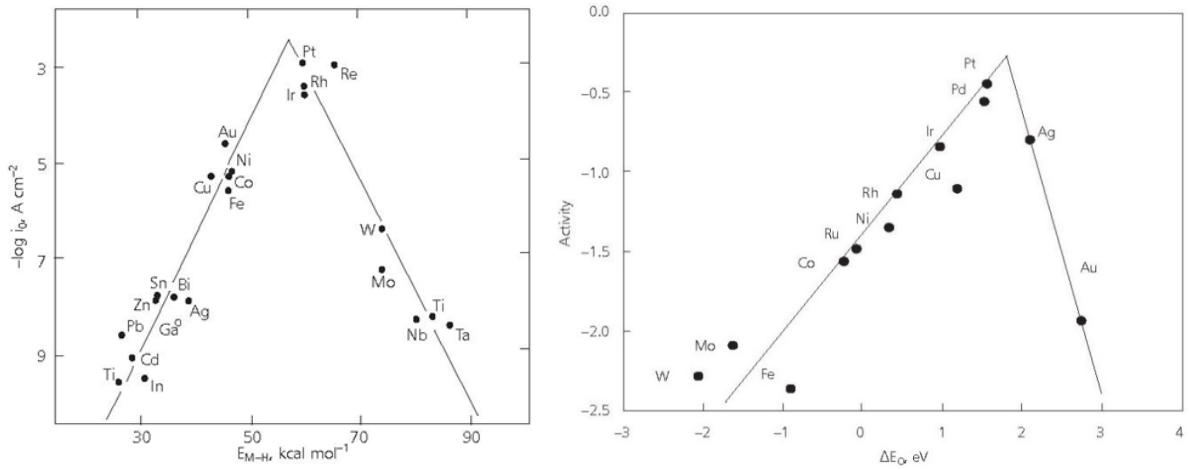

Figure 2.7: Volcano-plots showing the dependency of reaction rate on the bonding energies between the substrate and the metal. On the left – the logarithm of exchange current density for the HER as a function of the strength of metal-hydrogen bond [101]. On the right – the activity of the metal vs. the strength of oxygen-binding energy [102].

In the earlier days the amount of platinum loading on the electrodes was huge compared to the achievements today, up to 28 mg/cm² compared to 0.3 - 0.4 mg/cm² used today in conventional PFSA-based fuel cells [89]. This has been possible due to use of support, which allows platinum catalyst to be used as nanoparticles, compared to platinum mesh or platinum black powder, as it is the surface area of the catalyst that matters, not the weight. An optimum size of app. 4 nm platinum nanoparticles evenly distributed on a carbon black support with high mesoporous area, such as Vulcan XC72R from Cabot Corporation have been shown to give the best results [103]. Usually, with higher platinum loading in the catalyst layer the overall cell performance is increasing, but if calculated per area of platinum surface, the difference in voltage becomes negligible, as the intrinsic property of platinum activity towards HOR, given by Tafel slope, 70 mV/decade, is constant regardless of loading.

Thus, as the key to improve the performance of a fuel cell, platinum utilization rather than the loading should be increased.

The overpotential due to activation on the anode side is small, as the HOR is a relatively simple reaction, consisting only of 2 steps. Therefore the amount of catalyst required to facilitate HOR can be reduced [104, 105]. On the cathode side, however, the activation overpotential is large, as the ORR is complex, consisting of several elementary steps. In a phosphoric acid based HT-PEM the situation is aggravated further by the strong affinity of phosphate to platinum. It binds strongly to the catalyst particles, competing with oxygen for the reaction sites, impeding the performance of a cell. Capacitance measurements on platinum electrodes in H_3PO_4 solutions have shown that the $H_2PO_4^-$ ion is irreversibly adsorbed on platinum in the region of oxygen adsorption due to stabilisation resulting from a favourable electric field and oxygen adsorbed on neighbouring sites [106]. To overcome this, the catalyst loading on the cathode side is therefore typically higher than on the anode, 1 mg/cm² compared to 0.3 mg/cm². Based on density function theory (DFT) calculations, platinum has been found to bind oxygen 0.2 eV too strong [107]. The major part of the research on fuel cell catalysts is thus devoted to finding better alternatives by such techniques as alloying with other metals, core-shell structures or by growing nanotubes of the metal [108-112]. The initial activities of Pt-based binary alloys and core-shell structures are higher, but they suffer greatly from dealloying and leaching in stability tests [112-116].

2.4.3 Electrode reactions

The hydrogen oxidation reaction on the anode side, as mentioned above, is a relatively simple heterogeneous reaction. In short terms, the diatomic hydrogen molecule binds to the reaction site on the platinum catalyst, forming metal-hydrogen bonds, while the hydrogen-hydrogen bond is being broken, involving transfer of 2 electrons per hydrogen molecule. The hydrogen atoms then react with water to form oxonium ions, freeing the reaction site for the next molecule. It is generally agreed that the HOR in acidic media follows the Tafel-Heyrovsky-Volmer mechanism [117], given in equations 2.24 - 2.26:

Tafel (dissociative adsorption) $$H_2 \rightleftharpoons 2\,H_{ads}$$ 2.24

Heyrovsky (oxidative adsorption) $$H_2 \rightleftharpoons H_{ads} + H^+ + e^-$$ 2.25

Volmer (oxidative desorption) $$H_{ads} \rightleftharpoons + H^+ + e^-$$ 2.26

Depending on the nature of the active site on the platinum catalyst, the reaction proceeds either via the Tafel-Volmer reaction, involving dissociative adsorption of hydrogen molecule without electron transfer, or the Heyrovsky-Volmer mechanism, where both steps include electron transfer [118], and is thus dependant on experimental conditions, such as the type and composition of the electrolyte or the crystal orientation of the catalyst [104].

The oxygen reduction reaction, as mentioned previously, is a much more complicated process, as the oxygen molecule must be split in two and then protonated twice to form water, compared to the relatively simple splitting of hydrogen. It is generally agreed that the reduction of oxygen proceeds via two pathways, the direct 4-electron pathway, where oxygen molecule receives 4 protons and 4 electrons, forming 2 water molecules, and the peroxide pathway, where it forms peroxide with subsequent decomposition to water and molecular oxygen or further protonation to yield 2 water molecules. The preferential pathway depends on the nature of the catalytic cite, analogous to the HOR. The pathways in acidic media are summarised in equations 2.27 to 2.30 [119, 120]:

Direct 4-electron pathway $O_2 + 4\ H^+ + 4\ e^- \rightarrow 2\ H_2O$ **2.27**

Peroxide pathway $O_2 + 2\ H^+ + 2\ e^- \rightarrow H_2O_2$ **2.28**

followed by either

$2\ H_2O_2 \rightarrow 2\ H_2O + O_2$ **2.29**

or

$H_2O_2 + 2\ H^+ + 2\ e^- \rightarrow 2\ H_2O$ **2.30**

It has been shown by rotating disk electrode technique (RDE) on platinum in 0.55 M H_2SO_4, that 97 % of O_2 are reduced to water via the direct 4-electron pathway [121]. This can be explained by the nature of the oxygen molecule binding to the platinum surface. The peroxide route is followed when the oxygen molecule is adsorbed end-on, leaving the bond between the oxygen atoms almost unaffected. This leads to protonation of both oxygen atoms, forming peroxide. This can afterwards split in two and form two water molecules, or it can detach from the surface and dissolve in the bulk, leading to a voltage loss due to incomplete reduction. To follow the direct route both of the oxygen atoms must be bound to the metal. This can happen in two ways, a bridge bonding where the oxygen atoms are connected to two different platinum sites, and formation of two bonds to the same platinum site. Both of the possibilities put significant stress on the O-O bond, which is why it is easilier broken when both of the oxygen atoms become protonated, leading to the complete reduction to yield water. A schematic diagram of the ORR process can be seen on Figure 2.8.

It has been suggested that the rate determining step, responsible for the Tafel slope of -120 mV/decade, is the first charge tranfer step [119, 120]. Among other factors influencing the rate and the nature of the ORR pathway, pH has been found to have a strong influence, although the presence of adsorbed anions on the catalyst surface, such as oxides, also have a notable effect.

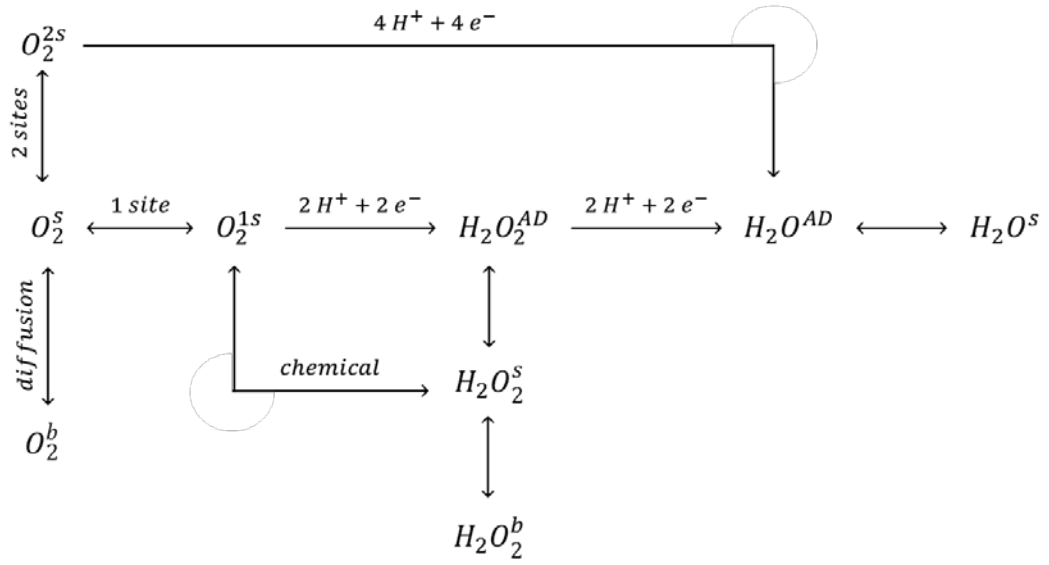

Figure 2.8: Model for the adsorption of molecular oxygen on platinum in acidic media with following reduction via different pathways. Note that the 2 sites bonding (top) can happen in 2 ways – with two oxygen atoms binding to the same or two different platinum sites, both including stretching of the O-O bond [120-122]. *b* –bulk, *s* –surface, *AD* – adsorbed.

3 HT-PEM FC and organic fuels

As discussed in section 1.4, it would be beneficial to use liquid fuels like methanol or dimethyl ether instead of hydrogen due to higher volumetric energy density. Those can be reformed to yield hydrogen and used in a HT-PEM FC due to increased tolerance to impurities from the reforming process, but it would be more advantageous to skip the fuel processing system altogether and use the liquid fuels directly. Unfortunately the oxidation mechanism of the liquid fuels is complicated, causing large overpotential losses, not unlike the ORR.

3.1 Direct methanol fuel cells

The direct methanol fuel cell is a long known technology and the mechanism of the methanol electrooxidation has been studied extensively over the years [54, 123, 124]. The overall anode reaction is given in equation 3.1:

$$CH_3OH + H_2O \rightleftharpoons CO_2 + 6\ H^+ + 6\ e^- \qquad 3.1$$

The emf of the total cell reaction at standard conditions is very close to that of hydrogen, 1.21 V vs. 1.23 V [117]. From the anode reaction it can be seen that for the complete oxidation of methanol to CO_2 there is a need of an extra oxygen atom, which is provided by a water molecule. The electrooxidation is thus much more complex than for HOR or ORR, requiring 2 molecules to react, involving 6 charge transfer steps and many intermediate species in between. There is also a risk of incomplete oxidation to CO and also formation of bi-products, such as formaldehyde and formic acid [125]. The complexity of the reaction is the reason for the MOR being slower than HOR by several orders of magnitude. It is generally agreed that the oxidation of methanol follows a parallel pathway with either a direct oxidation to CO_2 or indirect, with the formation of poisoning intermediates [126, 127], as depicted on Figure 3.1.

Both of the routes require a catalyst that is able to scissor C-H bonds, but also to assist the reaction between the resulting intermediates and water. Platinum catalyst is the best known for dissociating the C-H bonds, but in order for the reaction to occur, methanol must first be adsorbed on the catalyst surface. This does not happen at potentials below 0.2 V, as methanol is not able to displace the adsorbed hydrogen atoms. The activation of water on pure platinum occurs only above 0.4 V. Operating below this voltage on the anode would thus favour the incomplete reaction forming CH_2O and HCOOH [128]. It has been shown for smooth Pt electrodes that once the formaldehyde or formic acid are formed, especially at low potentials, the further oxidation is almost impossible, as the intermediates are dissolved and rapidly transported away from the electrode [127, 129]. Those factors explain the steep fall in voltage in the activation region. It should be kept in mind that both H_2CO [130] and HCOOH [131-134] are also oxidised on Pt catalyst, following different mechanisms,

again depending on the type of catalyst and reaction conditions. In fact, the formic acid has been proposed as a less toxic and more active alternative to methanol fuel [131, 135].

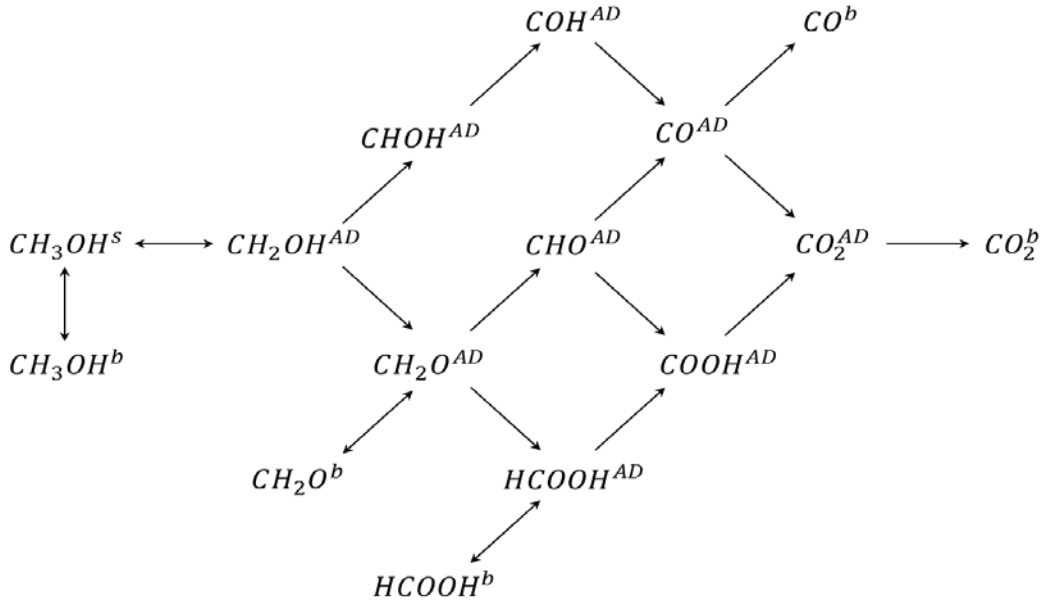

Figure 3.1: The mechanism for the electrooxidation of methanol. *b* –bulk, *s* –surface, *AD* –adsorbed. Adopted from [126, 127].

Crucial for the electrooxidation of adsorbed CO species, which are the most common intermediates in the reactions methanol and other organic fuels, is the presence of water, which acts as an oxygen source. In order to react with the CO, it needs to be activated. At high potentials platinum would be the most effective catalyst, but in the practical voltage ranges of a working fuel cell it is not viable, as mentioned above. Binary and ternary catalysts with metals forming oxygenated surfaces, like Sn, Re, Ru, Ge or Mo have been proposed, of witch platinum-ruthenium binary mixture is the most active towards methanol oxidation. Ru sites are known for nucleating water at potentials down to 0.3 V lower than the platinum surface [134]. It has been found that the oxidation step to yield CO_2 occurs only between the adsorbed CO on Pt site and OH adsorbed on Ru site via a bi-functional electrocatalysis [136, 137]. The oxidation mechanism for the MOR to CO_2 can thus be summarised to equations 3.2 to 3.4:

$$Pt + CH_3OH \rightarrow Pt\text{-}CO_{ads} + 4\,H^+ + 4\,e^- \quad (3.2)$$

$$Ru + H_2O \rightarrow Ru\text{-}OH_{ads} + H^+ + e^- \quad (3.3)$$

$$Pt\text{-}CO_{ads} + Ru\text{-}OH_{ads} \rightarrow Pt + Ru + CO_2 + H^+ + e^- \quad (3.4)$$

Another binary catalyst, Pt-Sn has been found to give comparable results to Pt-Ru system [138-140]. The mechanism of MOR on Pt-Sn is quite paradoxical. It appears that Sn is not active towards methanol oxidation, but it is very active towards the oxidation of dissolved CO, which is explained by CO_{ads} on the surface formed at high

concentration of CO in the bulk through direct adsorption rather than the C-H bond scissoring of methanol. The latter requires multiple Pt sites, which are blocked by CO_{ads} at low coverage, thus resulting in a lower total rate of methanol oxidation. One can say that the rate determining step is shifted from equation 3.4 to 3.2 [141]. Ternary system with Pt-Ru-Sn has also been tried, with Pt-Ru being primarily responsible for the MOR and Sn decreasing the particle size of the catalyst, thus increasing the activity for the oxidation [142].

Oxygen from the air is used as oxidant on the cathode side, like for the traditional PEM FC running on hydrogen as a fuel. The mechanism of the ORR on the cathode is therefore the same, as described in section 2.4.3. As mentioned before, the methanol crossover in PFSA-based membranes is high, corresponding up to 100 mA/cm² just in fuel loss. There is another problem once methanol reaches the cathode. As the cathode catalyst is platinum, methanol is readily adsorbed and oxidised on the surface. The ORR and MOR occur simultaneously on the platinum electrode. Studies have shown that while the presence of oxygen does not influence the rate of methanol oxidation, even low concentrations of methanol (0.25 M) have a significant effect on the ORR current, although the mechanism of the ORR is unchanged [143, 144]. It is proposed that the CO covers the flat surfaces of the Pt catalyst, forming inactive islands, which is dependent on the concentration and independent of the voltage, unlike the MOR.

One way to improve the performance of the DMFC cathode is to develop alternative catalysts capable of supressing the methanol oxidation and promoting the oxygen reduction. Metalloporphyrins, iron tetraphenylporphyrins (FeTPP) in particular, are known to favour 4-electron reduction of oxygen to water and are additionally insensitive towards methanol poisoning [145]. A binary carbon-supported Ru-Se have shown even better results in DMFC operation [146], with the enhanced activity attributed to Se being a promoter for electron transfer [147].

Alternative catalysts for the ORR have the drawback of being less active than Pt, therefore completely avoiding the methanol crossover would be an optimal solution. Since the amount of permeated methanol is a function of separator thickness, increasing the width of the membrane would be the obvious choice. It has its limits however, as the major part of the ohmic resistance the cells originates in the membrane. As mentioned previously – the thicker the membrane, the larger is the ohmic drop. Here the PBI-based HT-PEM FC is more advantageous than the PFSA-based LT-PEM FC. Besides the better catalytic activity at elevated temperature, as discussed before, the methanol crossover is reduced by a factor of 10 to 1000 than that of Nafion® at operating conditions, corresponding to a loss of only 10 mA/cm² in comparison to 100 mA/cm² [53, 55, 56, 93, 148]. The permeability increases with increasing temperature and methanol concentration, but never reaches the same range as that of Nafion. This gives a possibility to use a much thinner membrane. The most commonly used PFSA membranes are Nafion 115 and 117, which are 150 and 170 µm thick in dry state, and up to 200 µm when fully hydrated. The corresponding PBI membranes are 100 µm thick or less. Unfortunately, the strong affinity of Pt to

phosphoric acid requires higher catalyst loadings on both electrodes. Nevertheless, the performances of the HT DMFC are in the same range as the conventional PFSA-based LT DMFC [149, 150], and are usually higher when simple systems are used with air as oxidant and no pressurisation.

Both the LT and the HT DMFC system are theoretically very attractive to be used for propulsion, as the systems are in principle simple, but this is hindered by the practical performance being inferior for the use. Reforming to hydrogen with subsequent use in H_2/air cells is therefore preferable. Despite this DMFC has been employed in prototypes, such as Daimler DMFC go-cart, JuMOVe forklift from the German Research Center Jülich or the Yamaha FC06, which is a motorcycle fitted with 500 W DMFC [21]. For portable applications the DMFC technology offers compact systems featuring high energy density, fast and simple recharging and longer life span than the Li-ion batteries commonly used in modern portable equipment [151, 152]. Among others Toshiba dedicated a lot of effort in DMFC development for powering electronics for PDAs (obsolete), laptops, mobile phones and off-grid battery chargers [153]. The ease of using methanol in fuel cells also excels for powering very small devices. Very recently a micro DMFC as an alternative to Zn-air batteries has been used to power a hearing aid [154, 155]. It is clear that there are niches where DMFC is the most preferable technology, and with the predicted increased availability of methanol as an environmentally friendly fuel it is here to stay.

3.2 Direct dimethyl ether fuel cells

With the anticipated widespread of dimethyl ether as a common fuel it would be convenient to use it for something else than combustion. Direct conversion in a fuel cell, like the one seen for DMFC, would be a great possibility for a clean electricity production. The physical properties of DME give several advantages in comparison to hydrogen and methanol as fuels, many of them already mentioned in section 1.4. The liquefied storage enables a pumpless delivery system, like the one used in the common butane lighter. Compared to other C2 compounds, DME does not contain C-C bonds, which in principle makes the complete oxidation to CO_2 possible with minimal kinetic losses. The dipole moment of DME molecule is lower than that of methanol, 1.3 D vs. 1.7 D, which leads to lower fuel crossover in a fuel cell. Apparently there are no big obstacles to use DME as a fuel in fuel cells. The possibility has been investigated since late 1990ies, with Tsutsumi and his co-workers reporting the first feasibility study of direct dimethyl ether fuel cell on XII International Symposium on Alcohol Fuels in 1998 [156]. Following there has been a number of reports investigating the mechanism of DME electrooxidation, but the total amount of publications on direct DME fuel cells is scarce. Some of the results have been summarised in a review from 2009 by A. Serov and C. Kwak [157], while a more detailed and updated description will be given in the following pages.

3.2.1 DME electrooxidation mechanism

The anode reaction is given in equation 3.5. The emf of the direct DMEFC is 1.18 V. The complete electrooxidation requires 3 molecules of water to react with one molecule of DME, involving transfer of 12 electrons. The mechanism is therefore very complex and can have several pathways, but it is expected to resemble the MOR due to similarity in molecular structure and the fact that DME is known to be hydrolysed to methanol in acidic environment. Since the discovery of dimethyl ether use in a fuel cell, there have been some controversy with regard to the mechanism. The following section will give a chronologic review of the mechanism investigations, trying to shed some light on the topic.

$$CH_3OCH_3 + 3\ H_2O \rightleftharpoons 2\ CO_2 + 12\ H^+ + 12\ e^- \qquad 3.5$$

Müller et al. were the first to report the possible mechanism of the dimethyl ether oxidation in 2000. It was based on half-cell voltammetry measurements and gas chromatography (GC) analysis of the exhaust from a Nafion 117 based fuel cell [158]. Cyclic voltammetry measurements on Pt disk in sulphuric acid showed that the adsorption of DME occurs in potential region 0.3 - 0.8 V and can therefore not compete with hydrogen or intermediate oxygenated species. This is somewhat different to MeOH behaviour, which readily adsorbs at lower potentials, 0.2 V, and has a wider potential adsorption range. The authors attribute the difference to the structure of dimethyl ether, with the second methyl group being less reactive for C-H bond scissoring due to steric hindrance. The exhaust of the direct DME FC at open circuit voltage didn't show any trace of methanol or CO_2 in a GC, therefore the authors concluded that DME is not hydrolysed to methanol, contradicting the fact that the hydrolysis is catalysed by acidic conditions. Furthermore, the GC measurements showed that there was a significant fuel crossover, amounting up to 100 mA/cm². Unlike methanol, the concentration of DME in cathode outlet stream didn't change with increasing current, indicating that DME is not oxidised at the cathode. An interesting find was traces of CO_2 detected in the cathode exhaust, which could only originate from intermediates of DME electrooxidation diffusing from the anode. The results were further elaborated and confirmed in a patent [159]. The authors proposed a reaction mechanism based on their findings, where DME is adsorbed, forming a bond between one of the carbons and platinum catalyst with subsequent dehydrogenation. The resulting adsorbed C2 species is attacked by water forming COH_{ads} and a methanol molecule. The remainder of the mechanism is the same as for DMFC, already discussed in previous section, see Figure 3.1. A slightly different mechanism was proposed by Tsutsumi et al. [160], who detected formic acid in the outlet stream of a direct DME FC, which increased with increasing current, but no methanol or formaldehyde This lead to the conclusion that both of the methyl groups are oxidised simultaneously. By addition of up to 4 % of DME in the oxygen inlet stream the authors did not observe any significant performance decrease, confirming that dimethyl ether is not oxidised at the cathode at operating conditions [161].

In 2006 there was a number of reports by different groups employing various kinds of spectroscopy and electrochemical techniques [162-164]. A comprehensive study combining surface enhanced infrared reflection absorption spectroscopy with attenuated total reflection (ATR-SEIRAS) and Fourier transformed infrared spectroscopy (FT-IR), both coupled with cyclic voltammetry were used in situ to study DME electrooxidation [163]. In dilute solutions, 0.1 M and 0.025 M DME, the authors observed large suppression of hydrogen adsorption peaks, indicating that DME is adsorbed in low potential region, contradicting Müller et al. However, for a saturated DME solution the voltammogram was featureless in that region due to Pt surface being blocked by CO_{ads} and other intermediate species. Based on their results, the authors proposed that DME is dissociatively adsorbed at low potentials with following cleavage of C-O bond, yielding adsorbed formate or CO and methyl residues. Formate and CO then proceeds to CO_2 analogous to MOR reaction. The fate of the adsorbed methyl group is not discussed by the authors and remains unclear. For very dilute solutions, however, the results were different. The IR showed linear bonded DME residues, forming acetate and methyl carbonate, which were concluded to be the oxidation products in potential regions 0.3 - 0.95 V vs. Ag/AgCl electrode.

Mizutani et al. [164] combined GC with half-cell and direct DME FC to investigate the influence of DME on cathode performance and the mechanism of the oxidation. Half-cell measurements in 1 M H_2SO_4 at 30 °C with and without the addition of DME and methanol showed no effect of DME on the rate of ORR in the practical voltage range of fuel cell operation, while the effect of MeOH was pronounced, confirming the results of Müller et al. GC measurements of the fuel cell cathode exhaust showed that substantial amounts of DME were diffusing through the membrane at OCV at 30°C, but fell rapidly with increasing load and temperature. This is contrary to the methanol behaviour, which tends to increase with increasing temperature. From the anode exhaust it was found that the main products from direct DME operation were CO_2, methanol and methyl formate, in that order. There was no correlation between the amounts of methanol and methyl formate produced, therefore it was proposed that the processes of formation of the two species are independent. The rate of methanol formation was independent of the load and increased with temperature. The authors suggested that methanol is formed by hydrolysis of DME, which could explain the temperature dependence, but it contradicts the results reported by previous publications given above. The opposite was observed for methyl formate, where the rate of formation decreased with temperature and increased almost linearly with the load. This confirms the reaction pathway for dilute DME solutions proposed by Shao et al. [163], as discussed in previous paragraph. It also suggests that the complete electrooxidation to CO_2 is favoured by high temperature, which is expected.

In situ IR spectroscopy and cyclic voltammetry on bulk platinum electrode was used to study the DME electrooxidation by Kéranguéven et al. [162]. The voltamograms were in relatively good agreement with that reported in [163], showing supressed hydrogen adsorption peaks at low potentials, which confirms that DME is

dissociatively adsorbed on platinum surface. The slight shift of the voltammograms in the positive direction in the 0.3 – 0.65 V potential range and a steep oxidation peak starting at app. 0.65 V showed that DME molecule is partially oxidised in the medium potential range, with further reaction with the oxygenated species at high potentials to yield CO_2. The DME adsorption peak at low potentials was decreasing with increasing scan rate, and the oxidation region between 0.55 and 0.9 V was increasing and shifting in the negative direction, implying that DME adsorption is the limiting reaction step. Furthermore, with the decreasing sweep scan rate the peak at high potential grew and separated in two distinct peaks at app. 0.65 and 0.75 V, implying that either different platinum sites are involved in the oxidation, or that the oxidation proceeds via different pathways. The presence of the two peaks led the authors to reject the reaction mechanism proposed by Müller et al. [158]. DME stripping experiments coupled with IR spectroscopy suggested that the adsorption requires three adjacent Pt sites, while the intermediates resulting from the dehydrogenation required two sites, which led to the conclusion that bridge bonded CO was formed at the surface during the DME oxidation reaction. Fuel cell testing with direct DME operation expressed relatively high open circuit voltages. This, together with in situ IR measurements showing adsorbed CO species, led the authors to conclude that DME oxidation indeed takes place at low potentials. It was also postulated that DME is hydrolysed in the acid environment of the Nafion® based fuel cell to methanol, which could explain the somewhat high maximum power density of 30 mW/cm² at 90 °C, half that of methanol, despite the fact that the reactivity of DME at room temperature was very low. To summarise, the IR spectroscopy showed presence of various adsorbed species, such as methanol, formic acid and formate residues together with linear- and bridge-bonded CO.

$$CH_3OCH_3 + H_2O \rightarrow CH_2OH_{ads} + CH_3OH + H^+ + e^- \quad (3.6)$$

and/or

$$CH_3OCH_3 + H_2O \rightarrow 2\,CH_2OH_{ads} + 2\,H^+ + 2\,e^- \quad (3.7)$$

$$CH_2OH_{ads} \rightarrow CHO_{ads} + 2\,H^+ + 2\,e^- \quad (3.8)$$

$$CHO_{ads} + H_2O \rightarrow CO_2 + 3\,H^+ + 3\,e^- \quad (3.9)$$

and/or

$$CHO_{ads} + H_2O \rightarrow HCOOH + H^+ + e^- \quad (3.10)$$

and/or

$$CHO_{ads} \rightarrow CO_{ads} + H^+ + e^- \quad (3.11)$$

$$H_2O \rightarrow OH_{ads} + H^+ + e^- \quad (3.12)$$

$$CHO_{ads} + OH_{ads} \rightarrow CO_2 + 2\,H^+ + 2\,e^- \quad (3.13)$$

$$CO_{ads} + OH_{ads} \rightarrow CO_2 + H^+ + e^- \quad (3.14)$$

Based on their results, the authors proposed a reaction mechanism explaining the observed behaviour on cyclic voltammogram and intermediates from in situ IR, given in equations 3.6 - 3.14, with reactions 3.13 and 3.14 explaining the two peaks at 0.65 and 0.75 V [162].

The proposed reaction mechanism was confirmed by Zhang et al. [165] with the addition of a possible bridge-bonded dissociative adsorption of DME molecule as the first step. The voltammograms from cyclic voltammetry experiments with platinum black powder microelectrodes in sulphuric acid showed similar results to those obtained by Kéranguéven et al. The hydrogen peaks in the adsorption region were severely depressed, further disproving the early results reported by Müller et al. In the high potential region the two oxidation peaks were also observed, although slightly shifted in the positive direction. Contrary to the work described in the previous paragraph, the peaks grew and shifted in the positive direction with increasing scan rate, which was attributed to an irreversible charge transfer processes. There was no relationship between the current increases of the two peaks, therefore the processes are deemed independent and ascribed to equations 3.13 and 3.14. From the experiments on Pt-Ru black powder microelectrode it was not possible to distinguish the two oxidation peaks, which was attributed to the bi-functional mechanism enriching the catalyst surface with adsorbed OH species required for the oxidation and desorption of carbonaceous intermediates. Based on DME and CO stripping experiments and cyclic voltammetry at different temperatures it was argued that there is a possibility of two kinds of DME adsorption on the catalyst surface, with one or both methyl groups reacting with the catalyst, forming linear and bridge-bonded intermediates. The presence of the latter requires more active sites. As ruthenium is considered inactive towards DME oxidation, the diminishing difference in peak currents on Pt and Pt-Ru as function of temperature and disappearance of the two distinct oxidation peaks were consistent with the expectation. At last, direct DME FC operation coupled with gas chromatography of the exhaust revealed presence of methanol in the anode stream, confirming its formation as one of the intermediate oxidation steps or by hydrolysis of the fuel in acidic conditions of the Nafion® based cell.

Electrochemical and ATR-FTIR studies on DME electrooxidation by Liu et al. [166, 167] were consistent with the results reported in previous two paragraphs. CVs from Pt/C and sputtered Pt electrodes in sulphuric acid electrolyte showed depression of hydrogen desorption and adsorption peaks and presence of two oxidation current peaks at 0.75 and 0.8 V vs. RHE. The IR study confirmed presence of linear and bridge-bonded CO together with formate, formic acid and methanol residues on Pt electrode, with CO_L being the dominant species. It was found that the adsorption of linear-bonded CO was affecting the kinetics of the DME electrooxidation at low potential, with the coverage of the adsorption species being app. 90 % in the 0.1 to 0.45 V region. An interesting observation was made at voltages above 1 V. Contrary to MeOH, there was no oxidation current for DME. This shows that DME

electrooxidation is hindered by the presence of oxide species present on platinum at those voltages. The phenomenon can explain why the DME crossover does not influence the ORR on the cathode, opposite to methanol.

The idea of structure dependent DME electrooxidation was pursued by Lu et al. [168-175]. As described above, there is a degree of inconsistency in the reports regarding DME electrooxidation, which the authors attribute to the different surface structures of the used electrodes, which is a well-known factor for affecting the electrooxidation of C_1 molecules. The first paper [170] reported very different cyclic voltammogramms on Pt(111) and Pt(100) surfaces, with the latter having 10 times higher oxidation currents. Chronoamperometric profiles on different facets showed small currents for Pt(111) and Pt(110) and larger for the polycrystalline, Pt(310), Pt(910) and Pt(100), in increasing order, with a very small current drop for the latter. The electrooxidation mechanism of DME was compared to MOR, proposing two possible pathways for initial adsorption of DME molecule, involving scissoring of either C-H bond, like in methanol electrooxidation, or cleavage of C-O bond. It was known that C-H cleavage in methanol requires 3 adjacent Pt sites, provided by Pt(111) with and further oxidation taking place on the Pt(111) surface [176]. This was found by using cyanide modified platinum electrode. While the adsorption region remained unaffected, the oxidation peak disappeared completely. The results for that crystal orientation in DME solution were somewhat different. The current in the DME adsorption region was depressed, confirming the similarity to MOR, while no direct oxidation of DME took place on the Pt(111) surface, as the voltammogram in DME saturated solution for the cyanide modified Pt(111) electrode was almost identical to the one without DME in the electrolyte. For the Pt(100) surface it was found that it selectively scissors C-O bond, playing a crucial role in DME oxidation. From the IR spectroscopy studies it was found that no formate was formed and the hydrolysis of DME did not occur on a significant scale.

The discrepancy in the reported intermediates was in the following paper suggested to be caused by different methods used during the in situ IR spectroscopy experiments [171]. It is argued that diffusion processes can be responsible for methanol or formic acid contributions not being observed. The authors constructed a flow cell, where the formed soluble products would be rapidly transported away from the catalyst surface, enabling study of the intermediate species directly on the electrode. The CVs were in general agreement with the previously reported, although much higher currents were observed in the adsorption region, compared to the work done by Shao et al. [163]. This was attributed to the latter using a cell with much smaller volume, where accumulated intermediates and products would have a higher influence, blocking the surface for DME adsorption. The CVs at different scan rates were in agreement with those reported by Kéranguéven et al. [162], with the peaks in the adsorption region decreasing in magnitude and the oxidation peaks increasing with decreasing scan rate, confirming that DME oxidation is a kinetically controlled and irreversible process. In situ IR studies showed formation of $(CH_3OCH_2\text{-})_{ads}$, confirming the

dissociative adsorption step with subsequent formation of linear-bonded CO, which was also the main intermediate species observed.

A more thorough investigation on DME electrooxidation on Pt(111) was reported in [168], expanding on the preliminary results described previously. CVs at different scan rates showed a decrease in peak currents with increasing scan rate in both low and high potential regions, although the decay of the oxidation peak was much more pronounced, implying that DME adsorption is a slow process on Pt(111) surface. Kinetic studies showed that the reaction rate of dissociative adsorption of DME have a maximum at 0.35 V, which is near the potential of zero charge (PZC) on Pt(111) electrode in the experimental conditions used. This is expected, because at PZC the electrode has the maximum available reaction sites as the surface is relatively free of strongly adsorbed species. Therefore it is concluded that DME forms a very week interaction with the Pt(111) surface, hence the low activity. From a comparative study with methanol it was yet again confirmed that the first DME adsorption and dissociation step has a similar mechanism to that of MOR. It was also found that the C-O scissoring, which is an important step towards complete oxidation of the molecule is inactive on Pt(111). For the Pt(100) surface it was found that the hydrogen adsorption peaks are strongly suppressed by addition of DME, contrary to Pt(111) surface, showing that the dissociative adsorption proceeds at a much higher rate [169]. Based on the cyclic voltammetry and in situ IR spectroscopy studies on Pt(100), the authors proposed two possible reaction mechanisms, given in eq. 3.15 to 3.20, that are somewhat different from the one reported by Kéranguéven et al. [162]. It is argued that one of the paths is similar to the MOR, with complete dehydrogenation of one of the C atoms in the DME molecule with following oxidation, happening at potentials lower than 0.5 V. The other involves immediate cleavage of the C-O bond with formation of methoxy intermediate and methanol and following direct oxidation to CO_2 at potentials above 0.6 V.

$$CH_3OCH_3 \rightarrow CH_3OCH_{2,ads} + H^+ + e^- \quad \textbf{3.15}$$

$$CH_3OCH_{2,ads} \rightarrow CH_3OC_{ads} + 2\,H^+ + 2\,e^- \quad \textbf{3.16}$$

$$CH_3OC_{ads} + H_2O \rightarrow CO_{ads} + CH_3OH + H^+ + e^- \quad \textbf{3.17}$$

$$CO_{ads} + OH_{ads} \rightarrow CO_2 + H^+ + e^- \quad \textbf{3.18}$$

or

$$CH_3OCH_3 + H_2O \rightarrow CH_3O_{ads} + CH_3OH + H^+ + e^- \quad \textbf{3.19}$$

$$CH_3O_{ads} + H_2O \rightarrow CO_2 + 5\,H^+ + 5\,e^- \quad \textbf{3.20}$$

The first pathway is also proposed in a quantitative kinetic analysis by in situ IR spectroscopy study by the same authors on polycrystalline platinum electrodes [173], however no reaction intermediates with exception of $CH_3OCH_{2,ads}$ and CO_{ads} were observed. This is explained by the possible fast reaction rates, rendering the

equipment unable to detect it. From the studies it is evident that development of Pt based catalyst for direct DME fuel cells should focus on maximising the amount of (100) terraces, which would be much more CO-tolerant and active towards DME electrooxidation.

With the proven activity of Pt(100) terraces and the proposed mechanism in mind, together with the known activity of a binary platinum-ruthenium catalysts towards electrooxidation of organic molecules and CO, Lu and co-workers published a paper investigating the ruthenium modified platinum electrodes for DME electrooxidation [172]. The electrodes were obtained by spontaneous deposition of Ru on Pt(hkl) surfaces. Cyclic voltammograms in saturated DME solution showed enhanced oxidation activity for the Pt(100) surface. Although the adsorption peaks were decreasing in magnitude, the oxidation peak shifted from 0.72 V on clean surface to 0.60 V on Ru-modified surface and increased in magnitude by 28 times. The decrease of adsorption peaks fits well with the theory that 3 adjacent Pt-sites are required for dehydrogenative adsorption, with their amounts decreasing with increasing Ru coverage of platinum surface. The results on ruthenium modified Pt(110) and Pt(111) surfaces showed and inhibitive effect with decreased currents due to diminishing of neighbouring Pt sites, thus rendering the electrodes of the practical importance for direct DME fuel cells. The optimum coverage of Ru for Pt(100) surface was found to be 1 : 4, before the dilution of available adjacent Pt sites expressed negative effects on performance.

An in situ FTIR spectroscopy study of DME electrooxidation on platinum electrode at different pH values by Pan et al. [177] confirmed the mechanism proposed in eq. 3.6 to 3.14 with one addition. It was found that DME is not oxidized in alkaline media, which is in sharp contrast to other organic molecules. E.g. methanol has been found to have considerable oxidation activity in both strong alkaline, up to 6 M KOH and acidic solutions [124]. The cyclic voltammograms in buffer solutions showed a decrease in oxidation peaks for the forward scans and a complete disappearance of the peaks in the backwards scan when the pH exceeded 7, suggesting the inhibition of dissociative adsorption and blocking of direct oxidation with increasing pH. The possible effect of different DME solubility in acidic and alkaline media was ruled out by FTIR spectroscopy, with the spectra in 0.1 M H_2SO_4 and 0.1 M NaOH being almost identical. The difference in the reactivity was thus attributed to the concentration of H^+ ions. In 0.1 M H_2SO_4 solution on Pt electrode in-situ FTIR spectroscopic studies showed presence of DME decomposition species, linear-bonded CO, CO_2 and formic acid, confirming the results obtained by other authors. Pan et al. argue that protonation of the oxygen in the C-O-C bond is essential for the DME electrooxidation, hence the dependency of the mechanism on pH.

The preferential adsorption of DME in protonated form is backed by Votchenko et al. [178]. It is known that DME, unlike esters, are not hydrolysed in either alkaline or dilute acidic media, while in medium and strong acids it is protonated to form an oxonium salt. The voltammetric studies performed by the authors on platinised Pt

electrodes were not enough to propose a reaction mechanism, but they are in agreement with [162] and [165-167]. Furthermore it was shown yet again that DME is not oxidised at high potentials where oxygen species cover the electrode surface, which is different from oxidation of other organic molecules, like methanol, and explains why DME crossover has a negligible effect on cathode performance.

Very recently an explanation for the preferential oxidation of DME on Pt(100) surfaces have been proposed by Li et al. [179], who conducted elaborate electrochemical studies coupled with online Electrochemical Mass Spectrometry (OLEMS) and online high performance liquid chromatography (HPLC) measurements together with density functional theory (DFT) calculations on Pt(100) and Pt(510) and Pt(10 1 0) surfaces. Cyclic voltammetry in dilute $HClO_4$ showed a peak at 0.3 – 0.35 V on all surfaces, indicating weak DME dissociative adsorption, competing with the hydrogen adsorbate on the catalyst surface, in agreement with [168]. A single oxidation peak was observed with the onset at ca. 0.72 V, with highest currents on Pt(100). To confirm that the C-O bond breaking is affected by the structure of the platinum surface stripping experiments were performed by keeping the electrode potential at 0.5 V and following increase to 0.85 V with and without holding the potential at 0 V prior to the stripping. In the voltammogram for the latter experiment there was an extra oxidation peak at 0.76 V, which was attributed to existence of reducible fragments $CH_{x,ads}$. The total amount of adsorbed species was decreasing with increasing step density, and the amount of reducible fragments was increasing with the step density. This proved that Pt(100) provides the active sites for the scissoring of C-O bond, while steps prohibit the oxidation of $CH_{x,\,ads}$. This was backed up by the DFT calculations, which showed that the $CHOC_{ads}$ species, the most likely precursor for the bond breaking step, is the most stable at intermediate potentials on all surfaces, but it does not adsorb strongly on step sites and the step edges on Pt(100) terraces do not contribute to the adsorption energies. It should be noted that the C-O scissoring is a purely chemical step and is therefore not directly influenced by electrode potential or pH of the electrolyte, contradicting the findings of Pan et al. [177].

$$CH_3OCH_3 \rightarrow CH_3OC_{ads} + 3\,H^+ + 3\,e^- \qquad 3.21$$

$$CH_3OC_{ads} \rightarrow CHOC_{ads} + 2\,H^+ + 2\,e^- \qquad 3.22$$

$$CHOC_{ads} \rightarrow CO_{ads} + CH_{ads} \qquad 3.23$$

$$CH_{ads} + H_2O \rightarrow CO_{ads} + 3\,H^+ + 3\,e^- \qquad 3.24$$

$$CO_{ads} + H_2O \rightarrow CO_2 + 2\,H^+ + 2\,e^- \qquad 3.25$$

The findings, together with the OLEMS and HPLC detecting only CO_2 at high oxidation potentials with no methanol, formaldehyde, formic acid or methane, in contrast to other authors described above, lead to the proposition of a reaction mechanism where the DME molecule is sequentially dehydrogenatively adsorbed first

on one and then another C-atom with following cleavage of C-O bond and subsequent oxidation of the $CH_{x,\,ads}$ and CO_{ads} fragments to CO_2, as depicted in eq. 3.21 to 3.25. The activity of Pt(100) was found to arise from a square arrangement of 4 surface atoms, which form the active site able to provide geometric and electronic symmetry for charge donation, binding the CH and CO parts of the $CHOC_{ads}$ on different surface atoms, stabilising the intermediates and facilitating bond breaking and making [179].

It is evident from this section that the electrooxidation of DME is a complex mechanism, which is influenced by many factors, such as the type of electrolyte or kind and structure of the electrodes. Although there is a degree of disagreement in the available literature, most of the data suggests that the direct oxidation of DME on a PEM FC anode would more or less proceed via the mechanism proposed by Kéranguéven et al. [162], given in eq. 3.6 to 3.14.

3.2.2 Direct DME PEM FC performance, parameters and optimisation

The knowledge about the mechanism of DME electrooxidation is the first step on the path to improve the activity of direct DME duel cells. This can be achieved through a combination of finding an optimal catalyst for the oxidation, improvement of MEA components and manufacturing techniques and choosing the right operating conditions.

As CO is one of the main intermediate products in DME electrooxidation process, an improvement of the commonly used platinum electrodes is needed, because platinum materials are poisoned by adsorbed CO species. This can be achieved through addition of metals known for their activity towards CO oxidation. The intermediates of DME electrooxidation must be addressed as well. Alloying Pt with metals that facilitate oxidation of those intermediates will lead to higher activity on the anode. As in the case with methanol, a binary mixture of Pt and Ru has been shown to yield enhanced performance, and is thus a most common catalyst used for direct DME FC anodes. Two explanations for the improved performance exists – the bi-functional theory [137, 180-182], where Ru facilitates activation of water molecules, providing the oxygen species necessary for the oxidation, and the ligand effect [183-185], where Pt structure is modified by addition of e.g. Ru, reducing the Pt-CO bond strength, facilitating rapid oxidation.

An extensive catalytic activity study of carbon supported Pt alloyed with different metals was performed by Liu et al. [166]. The alloying metals were Ru, Sn, Mo, Cr, Ni, Co and W. The electrooxidation of DME was performed in a half-cell in 1 M H_2SO_4 at 50 °C and compared to MeOH electrooxidation. The activity of PtRu/C was the best among tested, followed by Pt_3Sn/C, with currents 12 and 4.4 times higher than on pure Pt/C at 0.4 V. The activities of Pt_3Mo/C, Pt_2Cr/C, PtNi/C, PtCo/C and PtW/C were from 3.4 to 1.3 times higher than on Pt/C, in decreasing order. At higher potentials, >0.6V however, Pt/C performs better than even PtRu/C, which is in accordance with other studies [165, 186], as the poisonous species are easier oxidised at high potentials and there is no dilution of the active Pt sites by secondary metals.

This has no practical application in terms of fuel cell performance, as the anode of a working cell is never expected to reach such potentials. The Tafel slopes of the DME oxidation reactions at 50 °C were 65, 100 and 120 mV/dec on Pt/C, Pt_3Sn/C and PtRu/C respectively. The apparent activation energies decreased in the same order, showing the enhancement of poisoning toleration of Pt by addition of secondary metals. Compared to methanol, the activation energies of DME oxidation were larger for the 3 chosen catalysts, e.g. 57 kJ/mol vs. 35 kJ/mol for the PtRu/C, indicating higher temperature dependence.

Kéranguéven et al. [186] performed a series of voltammetric measurements in 0.1 M H_2SO_4 at 20 °C and DDMEFC experiments with Nafion® 117 as the electrolyte membrane and Pt/C, PtRu/C and PtSn/C as catalyst materials. The performance trend was the same as observed by Liu et al. [166]. A peculiar thing was observed for $Pt_{0.5}Ru_{0.5}$/C compared to $Pt_{0.8}Ru_{0.2}$/C, the former showing high initial performance, but the voltage was unstable at fuel cell operating conditions. It was argued that the lack of stability during operation with increased ruthenium content was caused by Ru diluting the amount of Pt adsorption sites, in accordance with the conclusions of [165] and [166]. The DME adsorption capacity of the anode is thus lowered with large potential drop at lower current densities as a consequence. However, for low Ru content, the performance of the fuel cell was increased compared to a fuel cell with pure Pt/C anode. Also, the experiments showed that addition of Ru or Sn did not influence the OCV of the cell and, in contrast to methanol and ethanol direct fuel cells, those metals did not show any ligand effect for DME adsorption. As for $Pt_{0.9}Sn_{0.1}$/C the voltage of the direct DME FC was highest at current densities below 10 mA/cm², but fell rapidly below the level with Pt/C anode. The OCVs for all the catalysts were 0.8 V, app. 0.1 V higher than that of DMFC operation performance on the same cells. Influence of such parameters as temperature and pressure were also investigated. With Pt/C as anode catalyst and 90 °C and pure oxygen at 2 bar on the cathode side, the power density increased from 16 to 19 to 30 mW/cm² at 1, 2 and 3 bar on the anode side respectively. The same cell with pressures of 3 and 2 bar of 1.65 M DME and oxygen on anode and cathode respectively showed an increase in performance from 30 to 50 mW/cm² at temperatures from 90 to 110 °C. The increasing temperature was attributed responsible for activation of the oxidation while increased pressure promoted the adsorption of DME on platinum catalyst. It should be noted that 110 °C is the absolute temperature limit for PFSA-based cells, and needs to be pressurised to keep the water in liquid state for proton conductivity. The highest power density was 60 mW/cm² with a $Pt_{0.8}Ru_{0.2}$/C anode catalyst at 110 °C and 3 and 2 bar on the anode and cathode respectively. The same cell running on methanol had twice the performance, 120 mW/cm².

Yu et al. [187, 188] have performed experiments with non-supported Pt-Ru, Pt and Pt/Pd catalysts in a Nafion 115 based cell at 80 °C. Pd has been reported as a good catalyst for electrooxidation of formic acid [189], therefore it was expected to enhance the performance of the cell, as formic acid is believed to be one of the intermediates in

the oxidation of DME, see eq. 3.11. As maximum power density of the Pt/Pd catalyst was the lowest, only 7 mW/cm², it was concluded that no formic acid or only trace amounts are produced. Pt-Ru anode proved to have the best performance with 0.86 V at OCV and peak performance of 40 mW/cm². Temperature influence has shown an increase from 8 mW/cm² at 50 °C to 40 mW/cm² at 80°C. The apparent activation energy was thus 50 kJ/mol on Pt-Ru black, comparable to those obtained by Liu et al. [166]. This confirms the higher temperature dependency compared to DMFC cells.

Additionally, the authors investigated the influence of the flow field geometry on the performance. Since DME solubility in water is low, 7.6 % at 20 °C, decreasing with temperature, phase separation has been attributed responsible for the low performance of PFSA-based direct DME fuel cells. An interdigitated flow field showed an increase to 40 mW/cm² from 18 mW/cm² with a serpentine flow field at 80 °C. The interdigitated flow field forced the DME-water mixture into the catalyst layer, promoting the adsorption of DME on the catalyst surface with subsequent oxidation. This showed that mixing of liquid water and gaseous DME is an issue that needs to be addressed if PFSA-based membranes are to be used.

Recently a ternary catalyst $Pt_{0.6}Ru_{0.15}Pd_{0.25}/C$, more active than the conventionally used $Pt_{0.5}Ru_{0.5}$ alloy, has been proposed [190]. Even though a binary Pt/Pd catalyst has shown inferior performance, the ternary catalyst was found to have both slightly higher OCV and better performance in the kinetic region in direct DME fuel cell. Linear sweep voltammetry and DME stripping experiments showed better adsorption and larger oxidation currents, shifted to lower potentials, for the ternary catalyst. The enhancement was attributed to a positive effect Pd has on C-O bond scissoring when introduced into the PtRu catalyst.

The effect of anode gas humidifier temperature and a comparison between pure Pt and alloyed Pt-Ru as catalysts supported on carbon on a gas fed Nafion® 117 based cell at 95 °C was reported by Ueda et al. [191]. The preliminary cyclic voltammetry of the two catalysts were in general agreement with the results described in section 3.2.1. The subsequent FC measurements showed smaller activation losses for the Pt-Ru catalyst, however the performance decayed faster and expressed mass-transport limitations already after 100 mA/cm², while the cell with Pt catalyst was still in its linear region. The slope of the polarisation curve in the linear region was also significantly steeper for the cell with Pt-Ru catalyst. The authors attribute it to inefficient steam supply, as the performance increase was relatively large when the temperature of the anode gas humidifier was increased, from 17 to 27 mW/cm² at 80 and 95 °C. This doesn't explain the difference though, as the performance of the cell with Pt/C on the anode increased from 13 to 30 mW/cm² in the same temperature range. While the increase in performance for both electrodes seems indeed to be because of the higher water content, facilitating faster oxidation rate, as also shown by decreasing resistance from EIS measurements, the difference of the two electrodes must have been due to higher total catalyst loading. While 1 mg/cm² Pt was used in both cases, the Pt-Ru catalyst layer contained 50 % more mass due to Ru content,

which is a very probable cause for the slightly increased ohmic resistance, but most certainly the mass transport limitation issue.

The same trend was reported by Haraguchi et al. [192], who also investigated the influence of operating temperature and humidification. At atmospheric pressure and 80 °C the performance of the cell with a Pt-Ru/C catalyst had the highest OCV, 0.8 V, but dropped to 0 V almost immediately when current was drawn. The came MEA expressed the best performance when using methanol as fuel. It was concluded that Ru is inhibiting the performance. However, at 4.5 bar and 130 °C with additional humidification the Pt-Ru catalyst was clearly better than Pt catalyst. In general, it was shown that when operating above 100 °C the performance of the alloyed catalyst was superior to pure Pt. Additionally, severe mass transport limitation effects have been shown below 100 °C, which could be an indication of phase separation in the fuel stream. The authors also investigated effect of conditioning on the performance. A cell running at 4.5 bar, 80 °C and fixed 100 % relative humidity showed significantly improved performance after being heated up to 130 °C and cooled down again, with no mass transport limitations on the polarization curve. No explanation of the effect was given, but it might be caused by initial flooding of the electrode at low temperature.

The catalyst support material is also known to influence the performance of fuel cells. Cai et al. [174] made a comparison between the commonly used Vulcan XC72R carbon black powder support and multiwall carbon nanotubes (MWNT). The MWNTs have beneficial structural and electric properties, which help on better distribution and utilization of the catalyst metal, and also enhance the activity. The prepared Pt/Vulcan XC72R had a slightly narrower platinum particles size distribution and mean particle size, obtained from TEM images and XRD data, but PT/MWNTs had better platinum utilization. Cyclic voltammetry showed higher current densities for DME adsorption and oxidation over the potential range from 0 to 1 V. Peak power densities from solution fed direct DME FC operation at 80 °C were 38 and 32 mW/cm² for PT/MWNTs and Pt/Vulcan XC72R respectively. The stability test over 56 hours at 100 mA/cm² showed peak power decay decreases of 14 and 32 % for the cells with the corresponding catalysts. It was clear that use of MWNTs as support material is beneficial in terms the performance and durability.

It has previously been shown that the surface structure of the catalyst has an influence on activity of DME electrooxidation [168, 169, 172, 175]. A slightly different approach was reported by Si et al. [193], who synthesized platinum nanowires supported on Vulcan XC72R and compared them to the conventionally used platinum nanoparticles on the same support. The XRD data showed that both of the catalysts crystallized similar to bulk Pt, however the nanowire Pt had a higher electrochemically active surface area. From voltammetry measurements it was found that larger consecutive surfaces have a positive effect on CO tolerance and adsorption capacity of DME. The electron transfer coefficient α was more than 2.5 times larger for Pt nanowire than for Pt nanoparticles, indicating higher activity for the DME

electrooxidation. The observations are in agreement with the findings in [179], where it was found that DME electrooxidation is disfavored by kinks and step sites.

A different approach on improving performance has been reported by Ferrel et al. [194, 195]. Instead of optimizing the electrodes by alloying platinum with other metals, the authors incorporated 3 different heteropolyacids, phosphomolybdic acid (HPMo), $H_3PMo_{12}O_{40}$, phosphotungstic acid (HPW), $H_3PW_{12}O_{40}$ and silicotungstic acid (HSiW), $H_4SiW_{12}O_{40}$, in the Pt/C electrodes. It is known that heteropolyacids with the lightest heteroatom elements that naturally tend to tetrahedral environments are the most stable. HSiW is known to be more acidic and HPMo is known for good facilitation of redox reactions. The authors have previously shown enhancement of the oxidation of both CO and methanol. Together with their strong affinity to ethers, heteropolyacids are expected to enhance the performance of the direct DME fuel cells. The results from polarisation measurements showed 8, 10 ,12 and 19 mW/cm² at 0.1 V for Pt control, Pt-HPMo, Pt-HSiW and Pt-HPW respectively at 100 °C with oxygen on the cathode side. The improvement was attributed to a combination of improved interfacial resistance in the MEA, proven by electrochemical impedance spectroscopy (EIS) and the enhanced electrocatalysis of the DME oxidation. Unfortunately no explanation was given for the latter. Among other effects, influence of excess humidification, pressure and membrane thickness were also investigated. The stoichiometric ratio of water to DME is 3, but it wasn't feasible to provide such low flow. Ratios of 7.5, 14.9 and 22.4 were used, with the highest performance achieved at 14.9, showing that excess is required for enhanced oxidation. Increasing the DME flow keeping the ratios constant led to a decrease in performance, showing that an optimisation of gas diffusion layer (GDL) is needed. The rate of crossover was shown to be dependent on membrane thickness, as the OCV of a cell utilising a Nafion® 112 membrane was lower by 140 mV than that of Nafion® 117 based cell, which is in agreement with the results obtained by other authors [164, 196, 197], who saw a significant decrease in performance when changing to a thinner membrane due to fuel crossover.

An investigation of GDLs reducing mass transfer effects was reported by Cai et al. [198]. They compared gas diffusion layers at the anode with hydrophobic, 30 wt% PTFE, hydrophilic, 5 wt% Nafion, and mixed coating, with 50 % of the surface coated by Nafion and the other 50 % by PTFE. Scanning Electron Microscope (SEM) images of the gas diffusion layers showed presence of both regions in the latter. The idea was that the hydrophilic layer promotes water transport, while the hydrophobic benefits gas diffusion. Cell tests at 50 °C with saturated DME solution as fuel and oxygen on cathode side, Pt/C on both electrodes, showed no difference at low currents, but a noticeable improvement from 26 mW/cm² to 31 mW/cm² was seen at above 100 mA/cm². The authors attributed the enhancement to decreased mass transfer losses, which could be clearly seen from polarisation curves. It is also tried explained from EIS Nyquist plots obtained at 400 mV, however no equivalent circuit was proposed. It is seen that the total impedance is less for the cell with optimised GDL, which can be

due to larger area of triple phase boundary. This can in turn be indirectly attributed to enhanced mass transport. To clearly see the effect of mass transport limitations additional set of EIS spectra should have been obtained in the mass transport region of the polarisation curve at larger currents and lower potentials, i.e. at 150 mV, or by reducing the fuel flow. In a later paper the authors propose an improved anode flow field [199], which mitigates the performance drop caused by phase separation of the fuel. The same set of measurements was performed now at 70 °C, increasing the peak power of the novel flow field by 10 % over the conventional serpentine flow field to yield 67 mW/cm² at ambient pressure with pure oxygen on the cathode.

A detailed investigation of the effect of pressure and the fuel delivery was performed by Im et al. [200]. The MEAs were made with Nafion® 117 membrane, 4 mg/cm² Pt/Ru black on anode side and Pt black on the cathode. The cell was operated at 80 °C with pure oxygen on the cathode. The polarisation curves obtained with gas and solution fed fuel showed poor performance of the first, only 7 mW/cm² in peak power, compared to 40 mW/cm² for the latter. The poor performance of the gas fed cell was due to insufficient water supply. At the chosen conditions of atmospheric pressure, the gas ratio of steam to DME was 2.2, when stoichiometric amounts should be 3. This decreased the kinetics of the DME electrooxidation, severely limiting the performance of the cell. The DME-water solution had a ratio of 4.5, so sufficient water was available to drive the reaction. However the authors argued that significant amounts of DME would separate from the liquid phase as soon as the fuel stream depressurized from the container kept at 5 bar to atmospheric pressure of the cell. Therefore an experiment with pressurisation of the solution fed cell was performed to keep as much DME in the solution as possible, showing significant improvements in performance to 65 mW/cm² at 2 bar and following small increases to 70 and 75 mW/cm² when pressurising the cell to 3 and 4 bar respectively. The large difference between gas and solution fed cell has also been shown in [201], where power densities of 38 and 56 mW/cm² respectively were obtained at 80 °C, atmospheric pressure and Nafion® 115 membrane as electrolyte.

Li et al. [202] has also seen the trend in the performance increase due to pressure. Their results from a Nafion® 117 based cells with 6 mg/cm² unsupported Pt-Ru black on the anode and 4 mg/cm² Pt black on the cathode at 80 °C with air as oxidant showed an increase from 50 mW/cm² at 1.7 bar to 70 and 85 mW/cm² at 2.4 and 3 bar respectively. Increasing the flow rate of the fuel instead of pressure didn't have much impact on performance however. The authors also studied the effect of ruthenium content in the catalyst on direct DME FC performance. It was found that increasing Ru content up to 50 atom% had a positive effect on the OCV and the performance in the low potential region, but at the expense of peak power density. The highest performance of 100 mW/cm² was obtained using a $Pt_{0.8}Ru_{0.2}$ catalyst at 3 bar with air at 2.4 bar as oxidant. The results were in accordance with the work of Liu et al. [166], who found that addition of ruthenium increases the apparent activation energy for DME electrooxidation. An investigation of DME crossover was also carried out and

compared to that of methanol. The oxidation current on the cathode side fed with nitrogen was much lower for DME than for methanol, increasing to 35 mA/cm² at 0.55 V and falling back to 0 at higher potentials. The methanol oxidation current had a steep increase to 65 mA/cm² at 0.4V and was constant at increasing potentials. This indicated that DME crossover is lower than that of methanol and that the Pt catalyst on the cathode is inactive to DME oxidation, which is in accordance with other studies [161, 164, 178].

A detailed study on optimisation of MEA components composition was made by K.-D. Cai and G.-P. Yin [197], who varied the amounts of Nafion® and PTFE in the catalyst layers of both the anode and cathode, but also the metal loading in the anode catalyst layer and carbon black content on the anode gas diffusion layer together with the thickness of the membrane. It was found that there was an optimum for all the parameters, with the highest performance obtained at 20 wt% Nafion and 30 % PTFE in both electrodes, with 3.6 mg/cm² Pt catalyst loading and 1 mg/cm² carbon black in the diffusion layer. With the chosen parameters and a Nafion® 115 membrane the solution fed cell with oxygen on the cathode side the performance was 46 mW/cm² at 80 °C.

An elaborate degradation study was performed by Xing et al. [203] on a solution fed Nafion® 115 based cell with Pt/C catalyst on both electrodes at 60 °C with pure oxygen on the cathode. The durability testing consisted of a 70.5 hours operation at 30 mA/cm² interrupted every 5 hours to replenish the fuel solution by replacing the reservoir. At 40.5 h of operation cyclic voltammetry was performed on both electrodes to study the degradation mechanisms. The voltage decay rate was progressively increasing throughout the experiment, starting at 11 mV/h and accelerating to 28 mV/h after 65 hours of operation. The cell voltage was partly recovered after each subsequent interruption, which was attributed to the replenishment of the fuel and removal of water on the cathode. After the voltammetry measurements at 40.5 h of operation the cell voltage recovered to initial levels, but the degradation rate accelerated. The obtained cyclic voltammograms of the anode showed a large DME oxidation peak, which decreased and almost completely disappeared after 28 cycles between 0.05 and 1.2 V vs. dynamic hydrogen electrode (DHE). Simultaneously the peaks for hydrogen adsorption increased in size, showing that the catalyst is poisoned by DME during continuous operation. Cyclic voltammograms of the initial and aged anodes revealed halving of electrocatalytic activity towards DME oxidation and decreasing the area of the triple phase boundary. XRD patterns and TEM images of the anodic catalyst revealed growth of the Pt nanoparticles from 3.0 nm to 5.5 nm, which was responsible for the decreased activity. The possibility of platinum detaching from the catalyst layer and migrating into the membrane, thereby becoming inactive, was excluded by energy dispersive analysis of X-ray (EDAX), which showed same platinum content in pristine and aged anode. Using EIS and equivalent circuit fitting the authors were able to de-convolute anodic and cathodic contributions, revealing that the performance drop could be attributed mainly to

anode degradation. The effect on the peak power was indeed tremendous. From the initial power density of 40 mW/cm² only 12 mW/cm² could be harvested from the cell after 70.5 hours of operation.

This section summarises more or less the available literature on direct DME low temperature PEM fuel cells to date. An overview of the highest power densities obtained and the testing conditions for the direct DME fuel cells is given in Table 3.1. From this section it is evident that the performance is highly influenced by all the operating parameters and compositions of the membrane electrode assembly. An interesting note is that unlike with direct methanol fuel cells, the performance of a certain catalyst is also dependant on the potential of the cell, so a catalyst showing high performance in the activation region might not be the one yielding the highest peak power densities, making the search for the optimal catalyst only more complicated. One reoccurring problem was the phase separation of the fuel, which was attempted solved by increasing the pressure or feeding the DME as humidified gas. The latter has the drawback in that a fully humidified gas at 90 °C contains only 2.2 molecules of water per DME molecule [200], and even the stoichiometric ratio of 3 was proven not to give the best performance. The problem is worsened by the fact that PFSA-based membranes require water for proton conductivity. Insufficient humidification would result in membrane dryout and performance failure. With the DME solution the problem is turned upside down – the DME solubility in water at 20 °C is only 7.6 wt%, while the required ratio of 3 corresponds to a 46 wt%, thereby containing too much water in the solution and the excess of the DME separating into gas phase.

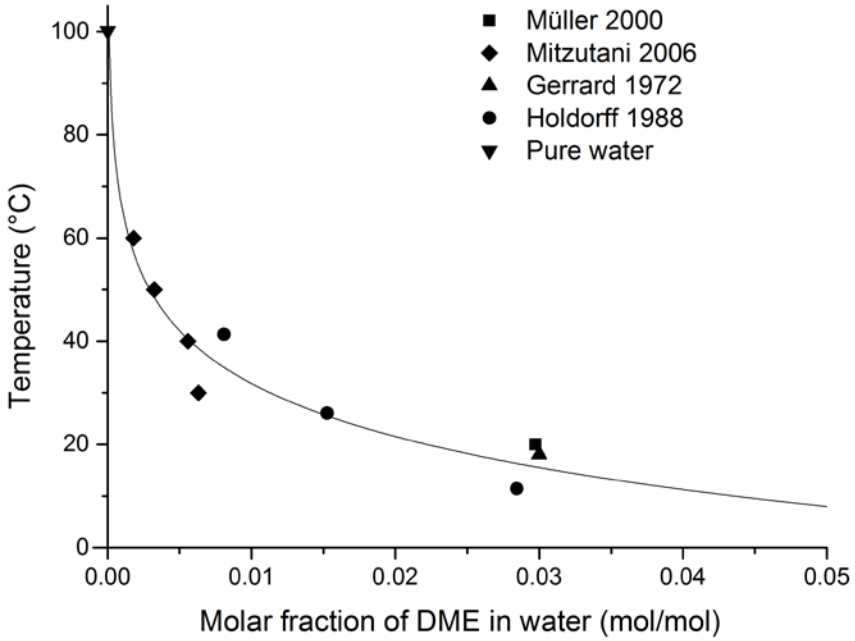

Figure 3.2: Equilibrium molar fractions of DME in water at different temperatures. Data from [158, 164, 204-206].

At the operating temperature of a PFSA-based fuel cell of ca. 80 °C the solubility is much lower, as can be seen from the boiling point curve for DME-water solution at atmospheric pressure depicted on Figure 3.2. The logarithmic line with $T = \ln(x) - 36.41$ was arbitrarily chosen based on the available DME solubility data from [158, 164, 204-206]. It is evident that obtaining a DME molar fraction of 0.25, which is equivalent to the stoichiometric theoretical water –DME ratio of 3 is not possible without pressurisation

For a direct methanol fuel cell there is a benefit for using dilute solutions, typically ca. 1 M, corresponding to 3 wt%, to reduce the fuel crossover. DME is much less hydrophilic than methanol, as indicated by the lower solubility in water and the lower dipole moment, therefore the dilution have probably only a very limited effect on DME crossover.

3.2.2.1 High temperature direct DME PEM fuel cells

A way to completely mitigate the phase separation problem and simultaneously harvest the benefit of increased performance due to higher temperature would be to use a PBI-based PEM fuel cell system. Since all gasses are fully miscible with each other, no separation of the fuel occurs and DME to water stoichiometry can be controlled by simply supplying more of either the components to the cell without the need for sophisticated humidification equipment. This method has been proposed very recently and only 4 papers and a patent are available on the topic to date, with 3 of the 5 mentioned being from the authors group [207-211]. The papers show improved peak power densities over PFSA-based direct DME fuel cells, with the same trends observed, such as improvement of performance with increasing temperature and pressure. With the little information available a significant amount of research is needed in order to find the optimum parameters of MEA composition, operation conditions and methods together with the understanding of the mechanisms involved during operation of a direct DME high temperature PEM fuel cell. Those topics constitute the scope of the presented work.

Table 3.1: Direct DME FC characteristics, operating conditions and peak power densities in chronologic order.*RT – room temperature.

Reference	Year	Membrane	Temp. (°C)	Pressure (bar abs.)	Fuel	Oxidant	Anode catalyst	Cathode catalyst	Power (mW/cm^2)
Müller [158]	2000	Nafion® 117	130	5	1.5 M DME aqueous solution	air	4 mg/cm² Pt/Ru black	4 mg/cm² Pt black	120
Tsutsumi [160]	2002	Nafion® 112	80	1	humidified gas at 80 °C	humidified oxygen at 80 °C	1 mg/cm² 50 wt% Pt/C	1 mg/cm² 50 wt% Pt/C	50
Mench [196]	2004	Nafion® 117	95	3	humidified gas at 95 °C	humidified air at 95 °C	4 mg/cm² Pt/Ru black	1 mg/cm ² Pt black	45
Yu [187, 188]	2005	Nafion® 115	80	5	1.65 M DME saturated solution	air	4 mg/cm² Pt/Ru black	1 mg/cm² 50 wt% Pt/C	40
Haraguchi [192]	2005	Nafion® 117	130	4.5	fully humidified gas	humidified oxygen	1.5 mg/cm² 40 wt% $Pt_{50}Ru_{50}$/C	1 mg/cm² 50 wt% Pt/C	125
Ueda [191]	2006	Nafion® 117	95	1	humidified gas at 95 °C	humidified oxygen at 80 °C	1.5 mg/cm² 40 wt% $Pt_{50}Ru_{50}$/C	1 mg/cm² 50 wt% Pt/C	30
Mizutani [164]	2006	Nafion® 112	80	1	fully humidified gas	humidified oxygen	3 mg/cm² 50 wt% Pt/C	3 mg/cm² 50 wt% Pt/C	50
Kerangueven [162, 186]	2006	Nafion® 117	110	3	1.65 M DME saturated solution	oxygen	2 mg/cm² 40 wt% Pt/C	2 mg/cm² 40 wt% Pt/C	50
Im [200]	2008	Nafion® 117	80	4	humidified gas at 90 °C	unknown	4 mg/cm² Pt/Ru black	4 mg/cm² Pt black	75

Reference	Year	Membrane	Temp. (°C)	Pressure (bar abs.)	Fuel	Oxidant	Anode catalyst	Cathode catalyst	Power (mW/cm^2)
Zhang [165]	2008	Nafion® 117	107	3.5	1.65 M DME saturated solution	oxygen	2.3 mg/cm² Pt/Ru black	1.2 mg/cm² Pt black	45
Cai [197, 198, 201]	2010	Nafion® 117	80	1	DME saturated solution (at RT*)	oxygen	5 mg/cm² 40 wt% Pt/C	3.6 mg/cm² 40 wt% Pt/C	45
Ferrell [195]	2010	Nafion® 117	100	3	steam/DME	humidified oxygen at 80 °C	0.3 mg/cm² 20 wt% Pt/C	0.5 mg/cm² 20 wt% Pt/C	25
Li [202]	2011	Nafion® 117	80	3	humidified gas at 85 °C	humidified air at 90 °C	6 mg/cm² $Pt_{80}Ru_{20}$ black	4 mg/cm² Pt black	100
Xing [203]	2012	Nafion® 115	60	1	1.5 M DME aqueous solution	oxygen	3.2 mg/cm² 40 wt% Pt/C	2.5 mg/cm² 40 wt% Pt/C	40
Cai [199]	2012	Nafion® 115	70	1	DME saturated solution (at RT*)	oxygen	3.5 mg/cm² 60 wt% Pt/C	1.5 mg/cm² 60 wt% Pt/C	70
Neutzler [209]	2012	PBI	210	3	steam/DME	air	4 mg/cm² Pt/Ru black	1 mg/cm² Pt/C	130
This work [211]	2012	PBI	200	1	steam/DME	air	4 mg/cm² 60 wt% $Pt_{50}Ru_{50}$/C	1 mg/cm² 60 wt% Pt/C	80
Li [212]	2014	Nafion® 212	80	3	fully humidified gas	Air	6 mg/cm² Pt/Ru black	4 mg/cm² Pt black	120

4 Experimental methods and equipment

4.1 X-ray powder diffraction

One of the most common techniques for characterisation of catalysts for fuel cells and in solid state inorganic chemistry in general is powder X-ray diffraction [213]. It can be used to identify the atomic structure and chemical composition of the specimen, based on an extensive available database of diffraction patterns, but also for detecting the degree of crystallinity, different crystalline phases, lattice parameters and particle size. The technique is based on the ability of crystalline powder samples to reflect an incident beam of X-rays in a specific manner, where constructive interference results in a diffraction pattern unique to the nature of the specimen. A Cu $K_{\alpha 1}$ radiation is typically used as a source of monochromatic X-ray waves. Fine ground crystalline powders have a large number of randomly oriented crystallites, which when placed in a monochromatic X-ray beam will diffract it from planes oriented in the correct angle to the incident beam to give a diffractogram in accordance to the Bragg's law. The sample is typically rotated to obtain a truly random orientation, as large and non-random crystallites lead to peak intensity variation.

$$n\lambda = 2d_{hkl}\sin\theta \qquad 4.1$$

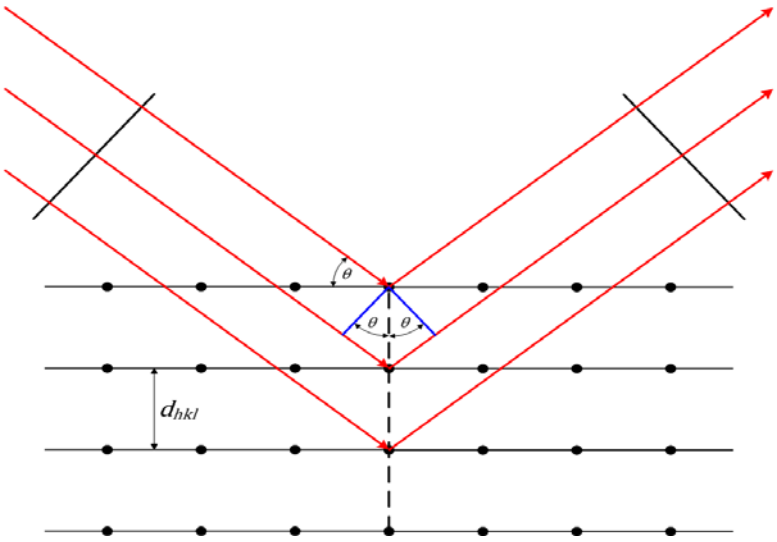

Figure 4.1: Schematic representation of Bragg reflection from a set of crystal planes with spacing d_{hkl}.

The Bragg's law is given in equation 4.1 and is illustrated in Figure 4.1. The interplanar distance between the crystal planes, d_{hkl}, can be found from the knowledge about the incident beam wavelength λ (0.15418 nm for Cu K_α radiation) and the incident angle θ based on simple trigonometry. n is an integer, and can in principle be omitted, as second order reflections from a *hkl* plane are indistinguishable from first order reflections from *2h 2k 2l*.

It is also possible to calculate the mean crystallite particle size, as with the decreasing particle size the width of diffraction peak increases due to smaller particles having fewer planes to produce complete destructive interference, responsible for the sharp peaks. From the peak widths it is thus possible to determine the thickness of a crystallite using the Debye-Scherrer equation:

$$T = \frac{C\lambda}{B\cos\theta} \tag{4.2}$$

where T is the crystalline thickness, C is the shape factor, usually taken as 0.9, and B is the full width of the peak at half its maximum (FWHM).

The diffractometer used for characterisation of synthesised electrocatalysts was a Huber G670 operated in transmission mode and a Rigaku Miniflex 600 operated in reflection mode. In the former case the catalysts were ground and transferred to a sample holder on a strip of tape. The diffractograms were obtained during 10 minutes of exposure time with rotation of the sample. In the latter case the catalyst powders were applied directly on the clean glass slate sample holder and the diffractograms were obtained from 3 to 90 ° at 3 °/min acquisition rate with continuous tilting of the sample.

4.2 Thermogravimetric analysis

Thermogravimetric analysis (TGA) is commonly used to study mass changes in a material due to temperature increase. By a combination of TGA with differential thermal analysis (DTA) changes due to decomposition, oxidation or evaporation can be identified in a sample material. This technique relies on recording the mass changes of a sample during a controlled uniform thermal treatment and relating it to an inert reference. The qualitative enthalpy changes can then be estimated, determining whether a process involved in the mass change was exo- or endothermal.

In the present work a Nietzsch STA 409 PC TGA-DTA instrument was used to determine the carbon content of the synthesised electrocatalysts. The temperature profile was heating from room temperature to 1000 °C at 5 °C/min with a synthetic air flow of 20 mL/min. Mass and differential thermal data were recorded throughout the measurement.

4.3 Scanning electron microscopy

Detailed information about the morphology, structure, size and topography of virtually any solid sample can be obtained using scanning electron microscopy (SEM) [214]. The technology is based on electron interactions of the source and the sample, improving the resolution down to a few nm compared to app. 0.2 µm for optic microscopes. A schematic overview of a SEM is represented on Figure 4.2 to the left. A tungsten filament or a field emission gun (FEG) is used as the source of electrons, which are accelerated to 1 to 30 keV and focused to a spot between 2 and 10 nm in

diameter when the beam hits the surface, interacting with the surface in a number of different ways, as depicted on Figure 4.2 to the right. Depending on the type of the detector, information can be obtained on the structure or composition of the sample. Secondary electrons have low energy and therefore the smallest sampling volume, giving the best spatial resolution for topographic images of the specimen. Backscattered electrons have higher energies and are used for imaging as well, but also for diffraction and crude chemical analysis, as atoms with high atomic number produce more backscattered electrons and thus appear brighter on the image.

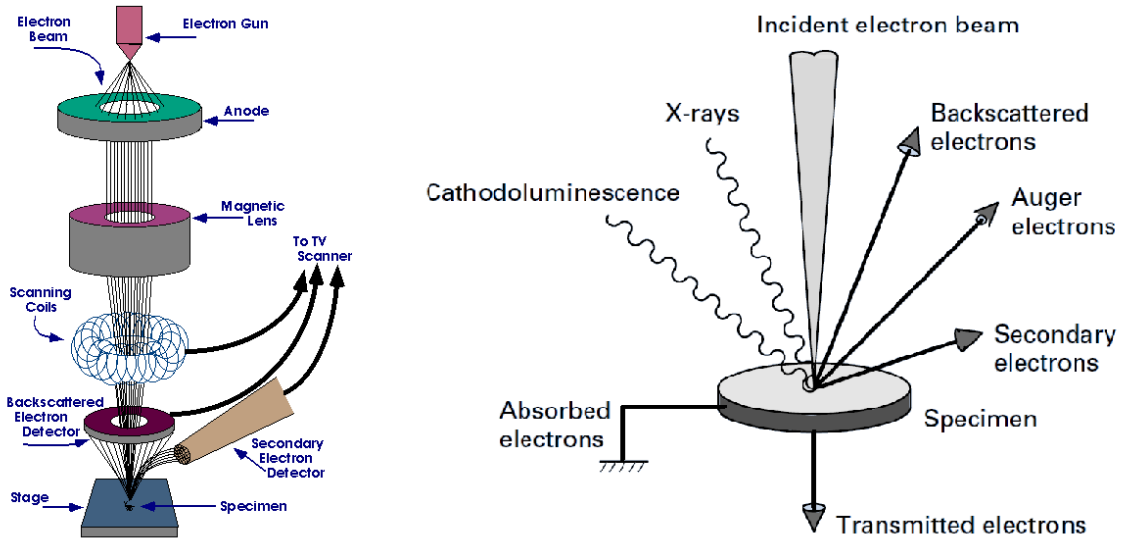

Figure 4.2: Left – schematic overview of a scanning electron microscope, adopted from [215]. Right – representation of emission of electrons and electromagnetic waves from a specimen, adopted from [216].

The SEMs used for electrode characterisation were a FEI Quanta 200 ESEM FEG and a Carl Zeiss EVO MA 10. The electrode samples were cut into appropriate sizes or used as a whole and mounted on aluminium sample holder by carbon tape. Since the samples were made of conductive material, no coating was required to avoid charging. For the FEI Quanta 200 ESEM FEG the sample was additionally glued to the sample holder on the edges of the electrode with silver paint.

4.3.1 Energy dispersive X-ray spectroscopy

When a SEM is equipped with energy dispersive X-ray spectrometer (EDX) it is possible to perform elemental analysis, since interaction of the electron beam with the sample also produces X-rays, as indicated on Figure 4.2. The technique enables for a qualitative and quantitative determination of the sample composition, together with spatial distribution of an element in the sample. There are also a couple of limitations to consider which are connected mostly with the quantitative analysis. First, it is not possible to detect elements lighter than boron. Second, the resolution of the detector is relatively poor, as the X-ray lines are not detected as sharp lines, but rather broader peaks, making it very difficult to resolve closely spaced lines, like e.g. $P_{K\alpha 1}$ and $Pt_{M\alpha 1}$, with the energies and associated wavelengths being 2.01 keV and 0.61 nm and 2.05 keV and 0.60 nm respectively. Those two elements are of particular interest when

analysing a fuel cell electrode or MEA cross-section, as a proper distribution of the platinum catalyst and the phosphoric acid in the catalyst layer determines the performance of a fuel cell. The sample volume is also to be considered, as the depth from which X-rays are produced increases with the increasing accelerating voltage and is also dependent on the nature of the specimen in terms of the wavelength and energy of the X-ray studied and the atomic weight.

The electrodes in the present study were examined by a Carl Zeiss EVO MA 10 scanning electron microscope fitted with an X-MAX 80 mm² EDX detector from Oxford Instruments Analytical. The sample preparation procedure was analogous to the SEM procedure, described in previous section.

4.4 Gas chromatography

As a direct HT-PEM fuel cell uses an organic fuel, the products from the anode exhaust can give information about mechanisms involved in electrooxidation of the fuel, together with the fuel utilisation and fuel efficiency. One of the methods used for analysing gas compositions is gas chromatography (GC). This technique relies on different adsorption strength of molecules on a substrate. When a sample is injected in the column with appropriately chosen packing material, it is adsorbed on the walls with every different type of molecules having its own progression rate. This effectively separates the gasses, which are detected by the order they emerge from the column. Two of the most commonly used detectors are the non-destructive thermal conductivity detector (TCD) and the flame ionization detector (FID). TCD is a very universal detector, distinguishing the analyte gasses from the carrier gas based on the different thermal conductivities. FID is more sensitive to hydrocarbons, but cannot detect water. The combination of those two are suitable for analysing the gas composition of the anode outlet stream of a direct DME or methanol fuel cell, as it can contain a variety of small organic molecules, see section 3.2.1.

The gas chromatography results present in this work were done externally by one of the project partners, Danish Technological Institute, using a combination of TCD and FID detectors. The samples were collected by connecting the fuel cell anode outlet to 1 L gasbags from Supelco Analytical, model 30213-U, that were filled with nitrogen and subsequently evacuated 3 times prior to exhaust gas sampling to avoid contamination.

4.5 Electrochemical Impedance Spectroscopy

Besides the polarisation curve, which is the main tool to evaluate the electrochemical performance of an MEA, as described in section 2.2, there are not many techniques available to characterise a running MEA under operating conditions. The classical voltammetry experiments are not possible due to the lack of reference electrode, which is very difficult to place into a working cell. This has been tried with both an in-house made and a commercial reference electrode from balticFuelCells with limited success, but the reference values were not reliable and were prone to drift

significantly during the experiment. There is a number of reports on reference electrode integration into a working MEA in the literature [217-223], but it usually involves custom built flow field plates and cell housing and such considerations as placement of the reference electrode and current distribution profiles must be taken into account, making the method much less trivial as in the regular 3-electrode cells or half-cells usually employed for voltammetric measurements.

To separate contributions from different components of an MEA, but also to study the processes and kinetic mechanisms involved in the electrochemical conversion of a fuel and oxidant electrochemical impedance spectroscopy (EIS) can be employed, also known as alternating current (AC) impedance or simply impedance spectroscopy [223-225]. In this technique a small AC perturbation with changing frequency is added to a constant DC signal in either galvanostatic or potentiostatic mode, depending on whether the instrument is in current or potential control mode, respectively. By scanning the frequency, changes in impedance due to different components responding differently to the perturbation can be obtained. The treatment of the data is based on a modified version of Ohm's law, where the resistance is substituted for impedance, which is a complex number relating current and potential. If we consider a HT-PEM FC running on hydrogen and air at very low currents, mass transfer limitations are negligible. The impedance of the fuel cell will then be mainly dependent on the resistance of the electrolyte membrane and the charge transfer resistances and double layer capacitances of the anode and cathode plus some inductance mostly due to wiring. Resistance is an obvious term, representing a barrier, on which some energy (voltage) is spent on overcoming the barrier, showing a loss in the system. The capacitor represents energy-storing capacity, delaying changes in the voltage with the passing current, very well representing the charge build-up of a double layer. The inductor delays changes in current, which describes well the current-voltage relationship in e.g. coils and wires. The mathematical descriptions of the modified Ohm's law and the resistance R, capacitance C and inductance L in terms of impedance $Z(\omega)$ are given in equations 4.3 to 4.6:

$$V(t) = I(t)Z(\omega) \tag{4.3}$$

$$Z_R(\omega) = \frac{V(t)}{I(t)} = R \tag{4.4}$$

$$Z_C(\omega) = \frac{V(t)}{I(t)} = \frac{1}{i\omega C} \tag{4.5}$$

$$Z_L(\omega) = \frac{V(t)}{I(t)} = i\omega L \tag{4.6}$$

Impedance spectra are usually plotted in the so called Nyquist-plot with the real resistance as the abscissa and the imaginary part of the resistance as the ordinate. If

we take the considered hydrogen/air operated cell, the so-called equivalent circuit for the system can be defined as the charge transfer resistances and double layer capacitances of each electrode connected in parallel with each other for the anode and cathode respectively. The resulting 2 circuits are then connected with the electrolyte resistance, electronics inductance and each other in series, forming the complete equivalent circuit for the cell. Quantification of the contributions from each element in the proposed equivalent circuit is only possible if the measured system was in steady state, meaning that the changes in impedance were only due to enforced perturbation. The AC impedance technique is thus very sensitive to any kind of disturbances and all possible care must be taken to avoid external influences, such as electrical noise, fuel and oxidant flow fluctuations and fluctuations of temperature and pressure.

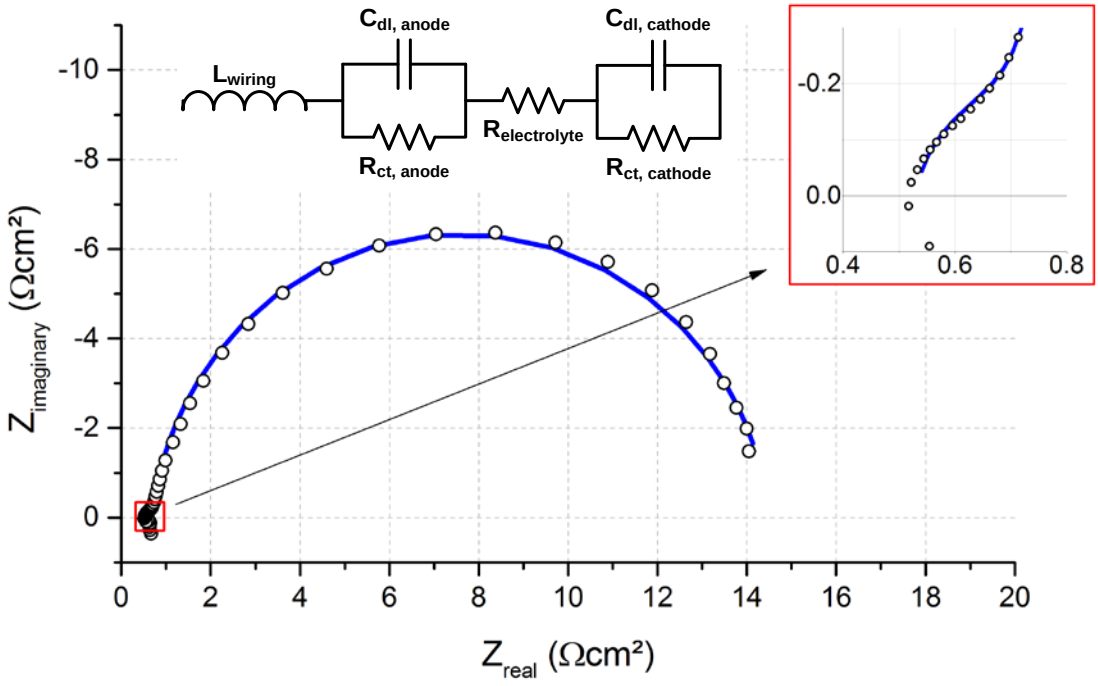

Figure 4.3: Impedance spectrum and the equivalent circuit of a hydrogen/air HT-PEM FC at 200 °C at 0.8V and 10 mA/cm². The points represent the measurement data and the blue line is the fitting based on the proposed equivalent circuit with prior removal of inductance contribution. R_{el} = 0.53 Ω/cm², $C_{dl,anode}$ = 0.0046 Fcm², $R_{ct,anode}$ = 0.17 Ω/cm², $C_{dl,cathode}$ = 0.0094 Fcm², $R_{ct,cathode}$ = 13.79 Ω/cm².

A Nyquist plot of impedance measurement data on a hydrogen/air HT-PEM FC at 200 °C and 0.8 V at 10 mA/cm² is given in Figure 4.3. The quantification of the contributions from different elements require some knowledge about the studied system, as it is always possible to obtain a satisfying fit if enough elements are used in the equivalent circuit. With the knowledge about the response of different components to AC perturbations it is possible to identify the elements and propose a fitting equivalent circuit. The inductance in the wires is identified by a straight vertical line below the abscissa at high frequencies. The resistance of the membrane electrolyte is identified at high frequencies as the displacement of the curve from the ordinate. On the Nyquist plot a resistor and capacitor in parallel result in a semicircle. The kinetics on the anode in case of a hydrogen fuelled cell are much faster

than those on the cathode, resulting in a lower charge transfer resistance. A small semicircle is therefore expected from the anode contribution and a larger from the cathode.

As can be seen from the inset on Figure 4.3 at higher frequencies (low Z_{real}), there is a shoulder in the measurement points, indicating the presence of a semicircle. Based on the obtained information an equivalent circuit can be proposed and quantification can be carried out, usually by a non-linear least squares fitting (NLLS) algorithm. The blue line on Figure 4.3 represents the fitting of the data with prior removal of inductance contribution information, as it represents intrinsic electrical property of the wiring and is thus of no value for the quantification of the processes occurring in the MEA itself. In principle it should be corrected for, rather than simply omitted, as it can have some limited influence on the remainder of the spectrum. It should also be noted that with the increasing complexity of the processes occurring at the electrodes of a direct dimethyl ether or methanol fuel cells the impedance spectra would be changing, reflecting the slower kinetics and a more complicated oxidation mechanism and effect of fuel crossover. Additional elements would therefore be required to obtain a satisfying fit, where care should be taken not to over parameterise the equivalent circuit by adding elements which are not meaningful for the studied cell. This will be discussed in further detail in section 5.2.3.

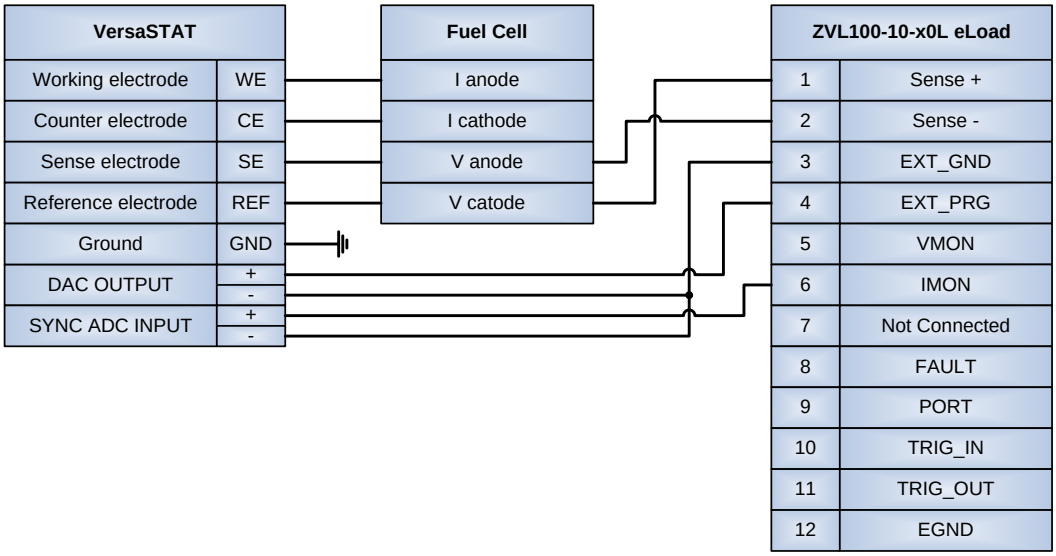

Figure 4.4: Wiring diagram between the potentiostat, fuel cell and the load terminal.

The electrochemical impedance spectroscopy measurements presented in this work were made using an AMREL ZVL100-10-40L eLOAD as the current sink in constant current mode and a PAR VersaStat 4 for the impedance measurements. The spectra were acquired in potentiostatic mode from 10 kHz to 0.1 Hz with 10 points per decade in different parts on the polarisation curve to investigate the processes occurring during MEA operation. To improve the quality of the data 5 full cycles of a spectrum were collected and averaged. The wiring between the potentiostat, the load terminal and the fuel cell is depicted in Figure 4.4.

4.6 Equipment and procedures

4.6.1 Electrode spraying

The manufacture of the electrodes involved preparation of the catalyst containing ink and deposition on the supporting gas diffusion layer (GDL). The latter was a PTFE treated non-woven carbon cloth with a microporous layer consisting of a mixture of carbon black and PTFE, an H2315 C2 from Freudenberg FCCT. The catalyst ink was made by adding a certain amount of polybenzimidazole (100 mesh polymer powder, Celanese) dissolved in concentrated formic acid (≥ 98%, Sigma-Aldrich) to the catalyst added a certain amount of phosphoric acid (≥ 85%, Sigma-Aldrich) in a Schott bottle. The amounts were specific to the experiments and will be given in the respective sections later. The components were then shaken vigorously and placed in an ultrasonic bath overnight for dispersion. The bottle was taken out of the bath several times and shaken to disperse any possible sediment on the bottom. If the catalyst was not well dispersed after the sonication, seen by visual inspection as particle agglomerates, the ink was subjected to high shear mixing at 13500 rpm for 5 intervals of 1 min mixing followed by 1 min rest.

The spraying of the electrodes was done using hand spraying with an air brush and later automatically by a spraying robot. The hand spraying was done by fixating a strip of the non-woven carbon cloth GDL on a heating plate with tape and warming up to 90 °C. The ink, sonicated for at least 30 min prior to spraying, was filled in a 50 mL Schott bottle and the air brush with an ascension pipe screwed on top. The air pressure was adjusted to 2 bar to provide an optimal spray velocity. The ink was then sprayed on the GDL in an overlapping serpentine spray pattern with rest periods to allow the solvent (formic acid) to evaporate. The finished electrode was then cut into 5 x 5 cm² pieces and weighted to determine the catalyst loading using average weight of the pristine GDL as base. The hand spraying equipment and the electrodes at different stages of the process can be seen on Figure 4.5.

Evident from the picture is the significant amount of catalyst sprayed outside of the GDL area. During spraying formation of ink pools on the GDL surface was observed if the applied pressure on the air feed button was just a little bit too high, leading to a suspected non-uniform distribution of the catalyst. It was also difficult to accurately control the catalyst loading and with the amount of expected waste a whole 100 % more ink than the theoretical 0% was used. To overcome the challenges, reducing waste and ensuring reproducible electrodes with an even distribution of the catalyst a spray robot, Exacta-Coat from SONO-TEK Corporation was acquired for the manufacture of the electrodes. The programmable 3-axis system with an Accumist ultrasonic nozzle allowed for deposition of the ink at very low flow rates, reducing overspray and ensuring precise control of the catalyst loading. The latter could be determined directly from the weight of the pristine 5 x 5 cm² GDL and after spraying for each individual electrode, as the carbon cloth could now be cut prior to spraying. The GDL pieces were placed in a mask and the ink was sprayed at 0.150 mL/min flow rate with the nozzle tip 5 cm above the substrate in an alternating serpentine pattern

with switching of the axes. The ultrasonic generator was operated at an effect of 2 W to obtain proper atomisation of the ink. The catalyst loading could then be controlled by the number of spray cycles. The spray robot and the Accumist ultrasonic nozzle operating principle can be seen on Figure 4.6.

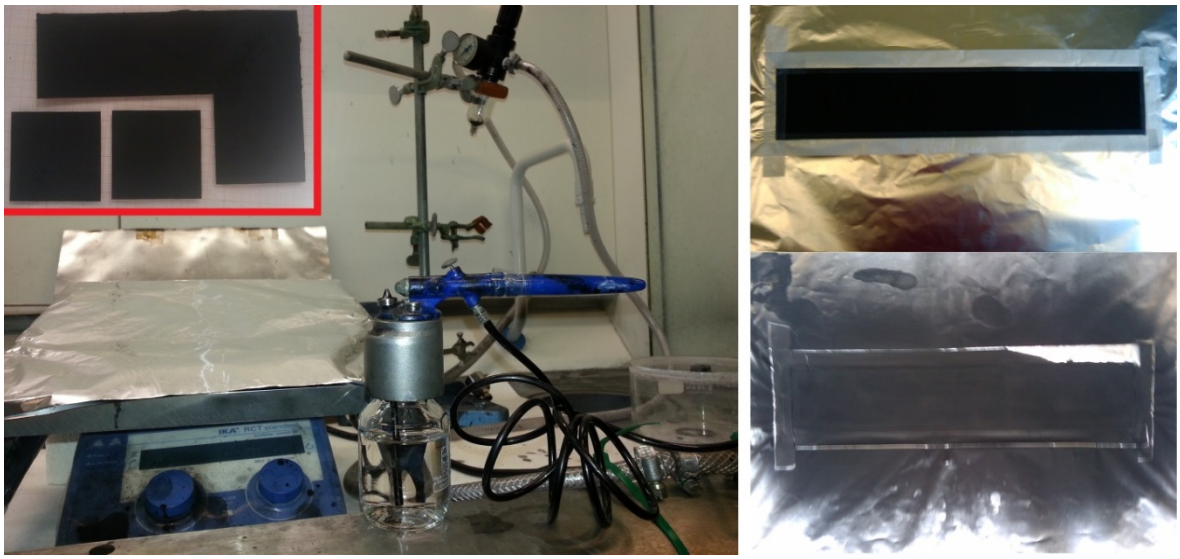

Figure 4.5: Hand spraying of the electrodes. Left – air brush, heating plate and air pressure regulator. Right above – pristine GDL, right below – GDL after spraying. Left upper corner – finished electrodes.

Figure 4.6: Left – spray robot. Right – Accumist ultrasonic nozzle operating principle, adopted from [226].

While being very simple in operation, the preparation of the ink and the spray robot had to follow a very specific procedure to obtain reproducible electrodes. First of all the catalyst ink should be free of dispersed air bubbles, so the ink was always subjected to sonication for at least 30 minutes prior to spraying to prevent segregation during spraying, as the ink was fed to the robot using a syringe pump. Second it was

made sure that the ink didn't contain agglomerate particles, as those would block the nozzle partly or completely, resulting in a non-controlled ink deposition on the electrodes or in worst cases completely ruined electrodes. The tubing should also be clean and flushed or better filled with the solvent, formic acid, prior to the introduction of the ink, as the PBI would precipitate instantaneously upon contact with e.g. water or ethanol. Care should also be taken not to spill the ink, as concentrated formic acid is very dangerous on contact with e.g. skin, and the ink is extremely flammable. In fact, a wipe or a piece of paper towel would spontaneously combust if dipped in the catalyst ink.

The catalyst loading was confirmed by low energy X-ray analysis, performed on InnospeXion® X-ray measurement system. Image software *Isee!* from BAM was used to analyse the results. The longer X-ray wavelengths used allow for identification of very small thickness- and density variations. The excitation voltages below 25 keV result in images with a very high grey scale value contrast, which was used to determine the catalyst loading. Additionally a spatial analysis and identification of irregularities could be performed. A series of electrodes with increasing PtRu/C catalyst loading was made in connection with the experiments described in section 5.1.2. Those were subjected to the low energy X-ray analysis. As can be seen from the graph on Figure 4.7, the catalyst loading determined experimentally from the weight of the electrodes corresponds very well with the grey scale values obtained by the analysis. The reason for the trend line not going through origin is the additional PBI and H_3PO_4 in the electrode structure, not present in the pristine gas diffusion layer.

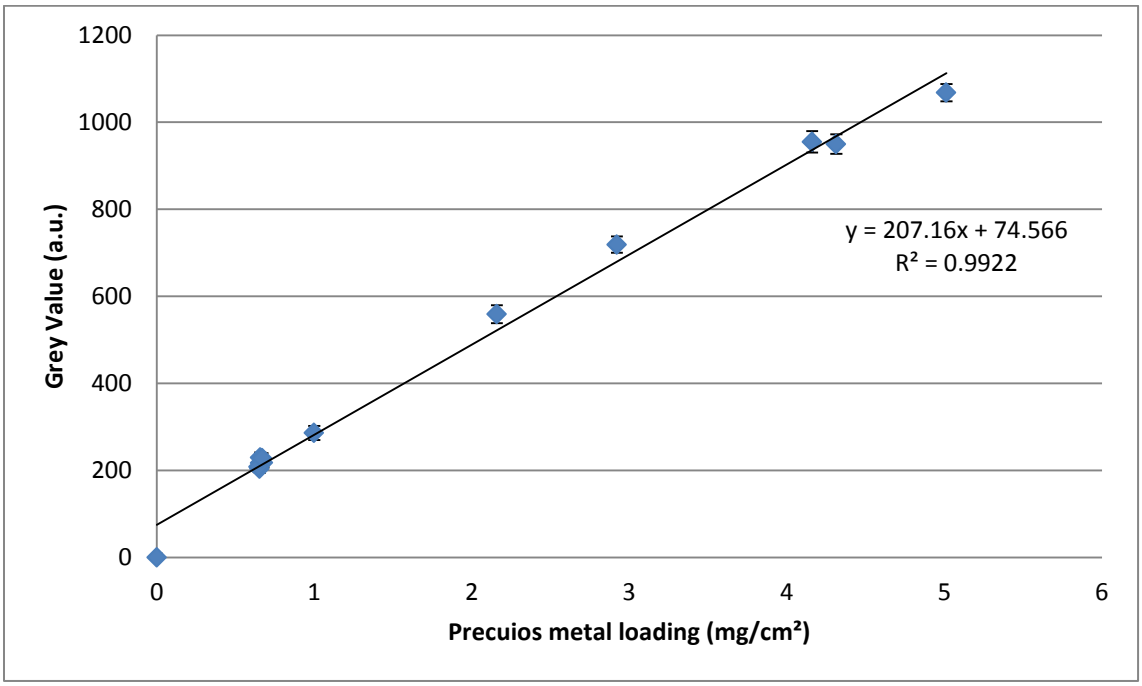

Figure 4.7: Grey scale value readings as function of anode catalyst metal loading experimentally determined by weight of pristine GDL and final electrode with the base taken as the grey value of the untreated GDL.

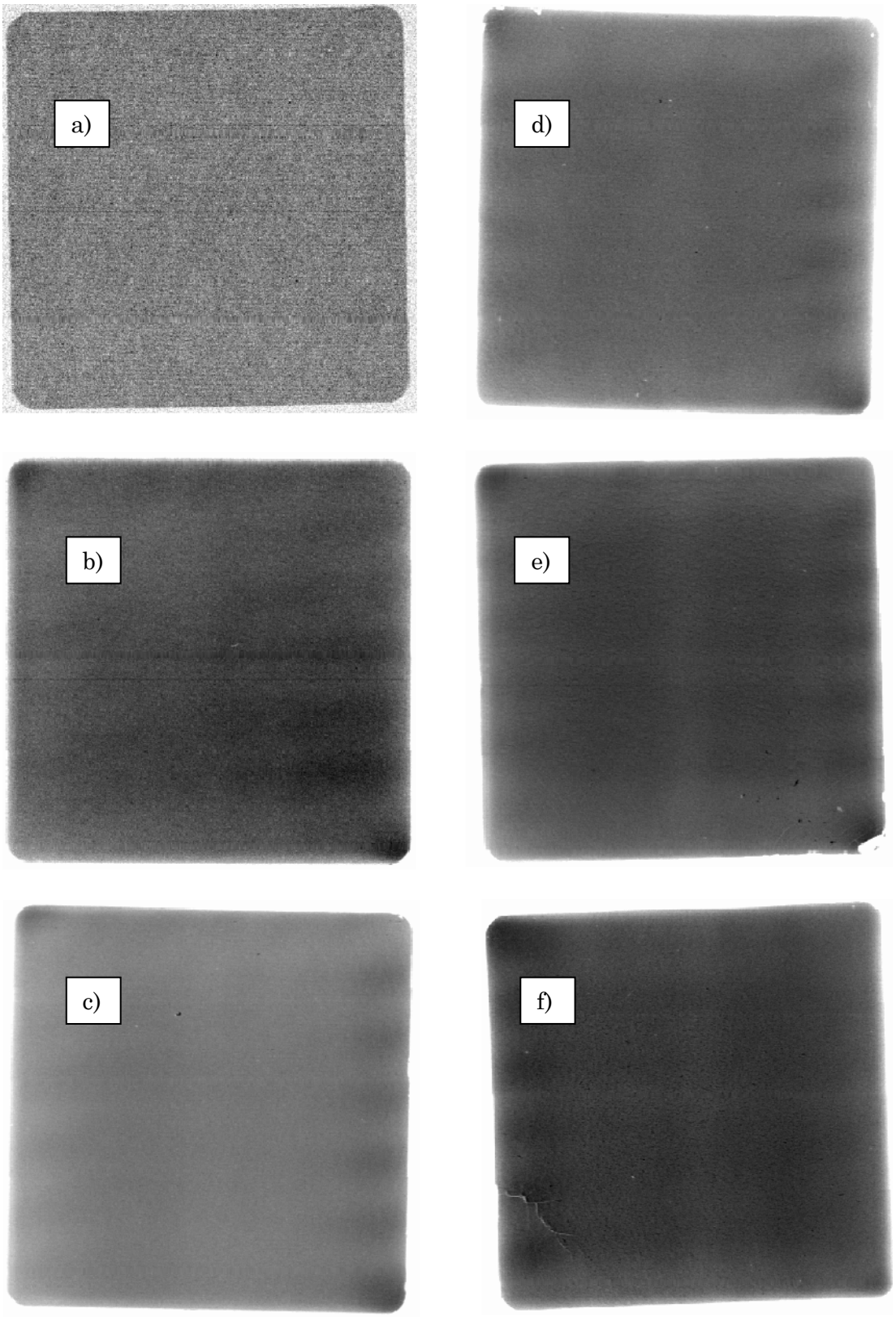

Figure 4.8: Low energy X-ray analysis of the electrodes. The grey scale contrast is individual for every electrode picture to emphasize spray patterns and features. a) – pristine carbon cloth, b) – 0.999 mg/cm°, c) – 2.159 mg/cm², d) – 2.920 mg/cm², e) – 4.313 mg/cm², f) – 5.012 mg/cm².

Figure 4.8 shows the low energy X-ray analysis pictures of the pristine GDL and the electrodes with varying catalyst loading from app. 1 to 5 mg/cm². The grey scale contrast is different from picture to picture to emphasize the features and spray patterns on the electrodes, as the contrast optimised for showing e.g. the electrode with 2 mg/cm² catalyst loading would result in completely black squares for the electrodes with 4 and 5 mg/cm² loading and the electrode with 1 mg/cm² and the pristine carbon cloth would not be visible at all. It can be seen from the pictures that the catalyst is relatively well distributed over the electrode surface, although some features originating from the spraying pattern do exist with more catalyst deposited on the turns of the serpentine curve. The dark diagonally opposite corners of the electrodes were probably due to the pieces of carbon cloth lying not completely flat in the mask. The crack in the catalyst layer on f) was also visible with the naked eye.

4.6.2 MEA preparation

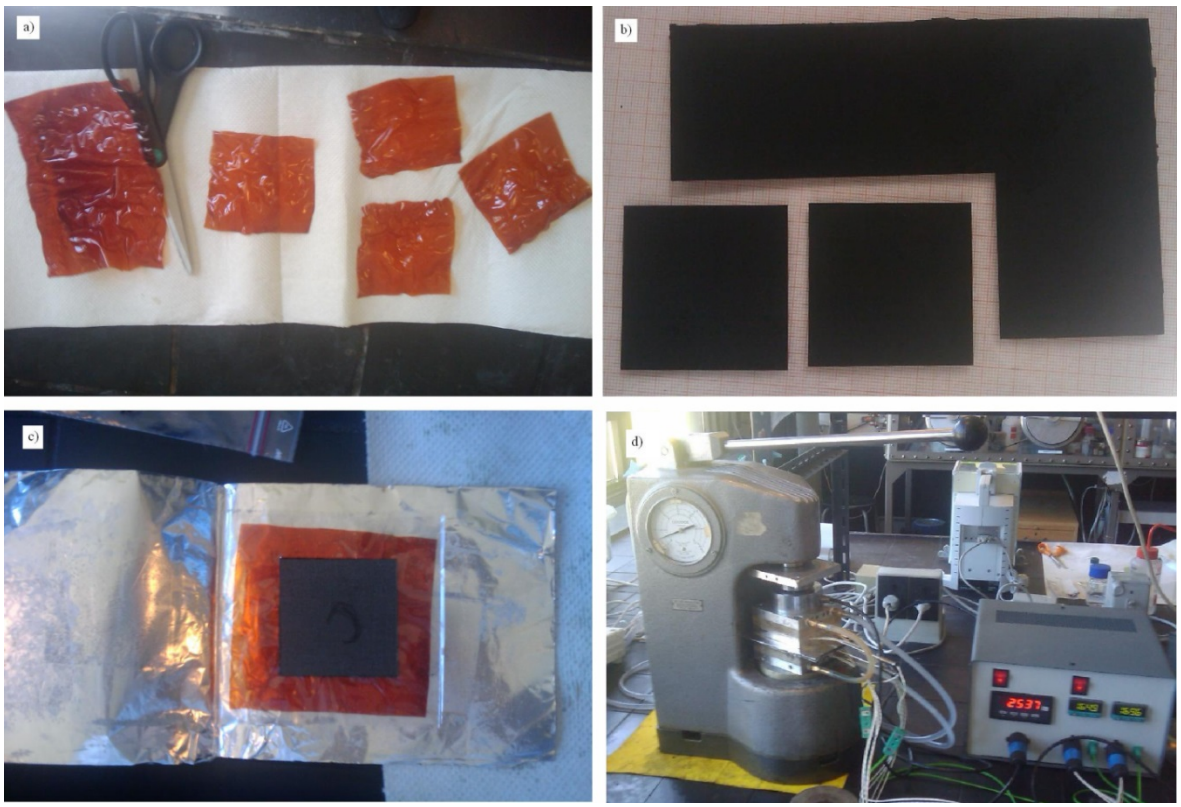

Figure 4.9: MEA preparation. a) – PBI membrane cutting, b) – electrode cutting, c) – MEA assembly and d) – hot press in action.

The prepared electrodes were used to make membrane electrode assemblies. This was done by first taking a phosphoric acid doped PBI membrane out of the 85 % phosphoric acid bath and wiping it clean with lint free wipes. The membrane was then cut into 8 x 8 cm² pieces and the approximate thickness measured. Two 8 x 8 cm² protective sub gaskets were cut out of a roll of polysulfon film with 4.8 x 4.8 cm² holes in the middle to accommodate the electrodes. The electrodes were then put on and aligned to cover those holes. The obtained sandwich structure was then wrapped in aluminium foil and placed in a hot press at 150 °C and 2500 kg force (100 kg/cm² of

the active area) for 7 minutes. The resulting MEA was taken out of the press and aluminium wrapping and was then ready for testing. It must be noted that the assembly of the components must happen as quick as possible, as the phosphoric acid contained in the PBI membrane is very hygroscopic and immediately starts absorbing moisture from the air with "sweat" droplets forming on the surface of the membrane. For that reason sizzling noises were heard and steam coming out of the aluminium wrapping was seen upon contact with the hot plates of the press. All the steps in MEA preparation are depicted on Figure 4.9.

MEAs provided by Danish Power Systems were assembled in the same manner, but instead of hot pressing them wrapped in aluminium foil, special metal tools were used for better aligning of the membrane and the electrodes during assembly and hot pressing itself. A more even pressure distribution across the active electrode area was also achieved. The hot pressing parameters were 200 °C and 1 ton total force, 40 kg/cm² for 3 minutes.

4.6.3 Purpose built equipment

4.6.3.1 Single cell test station

A big part of the work done was spent on design, construction, programming and maintenance of the setups used to test the manufactured MEAs. The single cell test station was constructed during previous work, but heavily modified to provide for more stable and reliable measurements. The functioning of the setup was fairly simple, but achieving it was quite demanding. All the tubing in the setup was made of ø 6 mm 316 stainless steel tubes and all the fittings were 316 Swagelok® fittings. The setup consisted of in-house made fuel cell housing with two 220 W cartridge heaters and a thermocouple inserted into the anode end plate. The gasses were supplied to the cell by 5800 S series mass flow controllers (MFCs) from Brooks Instruments. The internal sealings for the DME mass flow controller had to be changed from the standard Buna rubber to PTFE, as the former was found incompatible with the gas and would result in operation failure. The oxidant (air or oxygen) was supplied straight to the cell without prior heating. The fuel stream was passed through an evaporator, where it was mixed with water vapour when applicable, and sent further to the anode inlet via a heated gas line. The water or methanol-water mixture was supplied by means of a peristaltic pump, a Cole Parmer Masterflex Console Drive (model no. 77521-47). The evaporator was in-house made from a 250 mm long ø 19 mm 316 steel pipe wrapped in 250 W heating coil with a thermocouple taped to the outer surface of the pipe. The gas and water inlets were engineered to provide a more homogeneous flow of steam without bursts and oscillations and ensure good mixing of fuel and steam. Prior to evaporator inlet a drilled out Swagelok® union tee fitting with a stainless steel capillary tube for the water stream running through it was connected to the fuel feed tube. The resulting assembly was then attached to the evaporator pipe with the capillary tube protruding ca. 80 mm or 1/3 into the evaporator. The latter was filled with stainless steel balls to increase the thermal mass.

A very simple evaporator usually employed, consisting of a heated steel pipe with the capillary attached to the inlet, has the drawback of large flow oscillations, as the water droplet formed at the end of the capillary would hit the hot surface of the pipe and evaporate instantaneously, causing large volume expansion and thereby a burst and oscillations in the gas flow rate. With the proposed improved design the idea was that the water at the outlet of the capillary is heated to the boiling point or is already in vapour phase, so the bursts would not occur. The fuel gas is supplied at the evaporator inlet and the stainless steel balls have the extra function of providing better mixing of the gas with the formed water vapour. The functionality of the improved design over the regular was shown in an electrolysis study [227], where a constant homogeneous flow of steam without bursts and oscillations is much more important, as it is the sole reactant. The voltage response at fixed current contained almost no oscillations or spikes, proving the concept. A cross section of the novel evaporator design can be seen on Figure 4.10. The stainless steel balls are probably much more randomly distributed in reality.

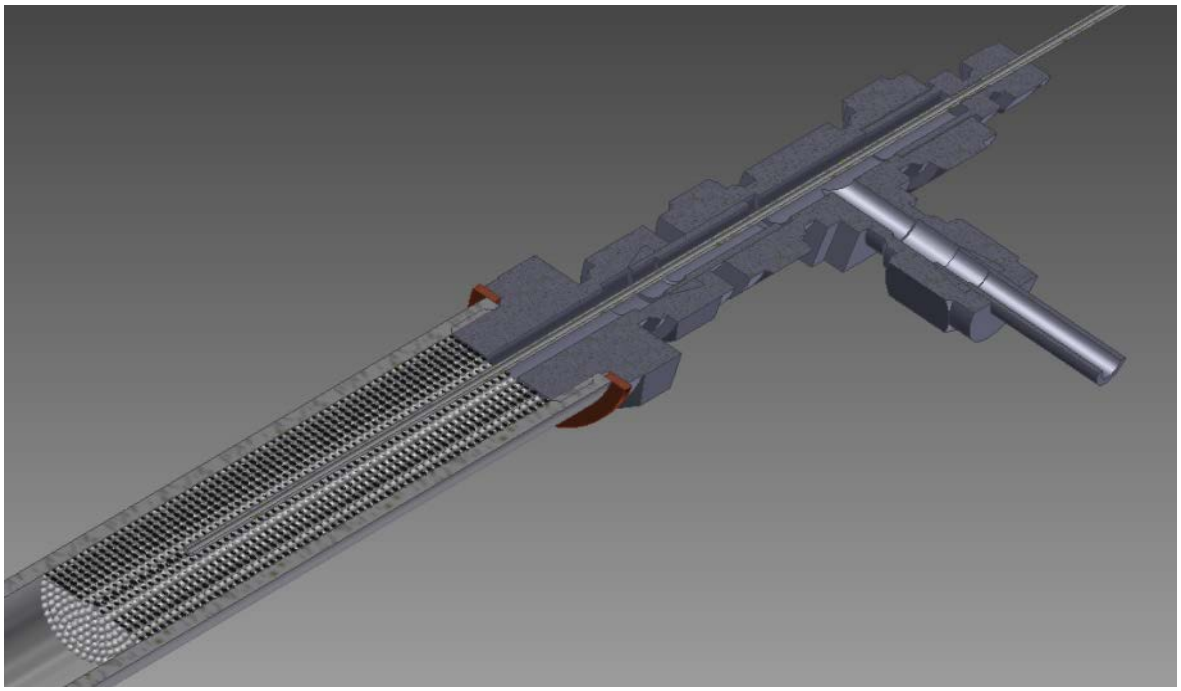

Figure 4.10: Cross section view of the novel evaporator design. A capillary tube is protruding through a union tee and 80 mm into a steel balls filled ø 19 mm steel pipe.

The heating control of the evaporator, the gas line and the cell was achieved using CAL 3200 and 3300 PID controllers with type K thermocouples. The latter were chosen due to their good linearity in the expected operation temperature range. The thermocouples were also connected to an ICP-CON i-7018 analog input module to log the temperature. The mass flow meters were controlled and the resulting fuel flow monitored by ICP-CON i-7024 analog output and ICP-CON i-7017 analog input modules respectively. The i-7017 module was additionally used for monitoring cell voltage. The communication between the modules and the PC was achieved by means

of an ICP-CON i-7520 RS-232 to RS-485 converter, as the modules communicate through RS-485 protocol and the PC serial port supports RS-232 protocol. The mass flow controllers and the ICP-CON modules were powered by a 24 V 2 A DC power supply from RS components (model no. DR-4524). The data acquisition, cell voltage and current control and gas flow control were done using in-house developed software on LabView platform from National Instruments. The ICP-CON i-7017 and i-7024 had to be calibrated and the inputs and outputs trimmed to ensure correct readings.

The load for MEA evaluation was initially a Laboratory Power Supply (model no. EA-PS 3016-20 B) from Elektro-Automatik GmbH&Co. It wasn't optimal for the fuel cell measurements as the resolution in the low current range was poor and OCV measurements had to be done by unplugging the current leads. Additionally it was only able to draw a maximum of 20 A total, which was not always sufficient when testing cells 5 x 5 cm² with hydrogen as fuel. Furthermore it was not possible to programmatically automate it to obtain polarisation curves. Therefore it was subsequently exchanged for a dedicated 40 A load from Amrel, a ZVL100-10-40L eLoad. Besides being more accurate in the low current region, providing for more reliable measurements around OCV, it came with dedicated LabView drivers, making it much easier to acquire i-V data from the MEAs and adding the possibility to control the setup remotely.

Even though the novel design of the evaporator unit has been proven to dampen the bursts in the fuel and steam flow, oscillations and sudden drop offs in voltage were observed, indicating obstacles in the reactant flow. To eliminate any possible oscillations caused by the peristaltic pump, which was operated in the lowest flow range due to very low liquid flows required, it was replaced by a high precision HPLC pump from Shimadzu, LC-20AD, with parallel-type double plunger able to provide pulse-free delivery. This has brought the oscillations to the minimum, but the sudden voltage drop offs still occurred, which was thought to be caused by recondensation of water in the gas line. The possible cold bridges were identified and either better insulated or additional heating solutions were applied, which seemed to resolve the issue.

The in-house made fuel cell housing consisted of two 20 mm thick 100 x 100 mm² aluminium end plates with holes to accommodate the heating cartridges and the thermocouple together with holes for 8 bolts and gas channels machined. The current collectors were made of 2 mm Cu plates electroplated with a thin layer of silver and then gold for corrosion resistance. The gas flow field was made of a 6 mm thick graphite plate with parallel gas channels. The electronic conduction and gas tightness between the gas flow field plate and the current collector was facilitated by a 1 mm thick piece of soft graphite (PapyEx). The MEA was put between the two halves of the cell housing with PTFE gaskets of suitable thickness (the difference between the thickness of the MEA structure and the membrane alone) and the bolts were tightened by 2 Nm. The individual components and the assembled fuel cell can be seen on Figure 4.11.

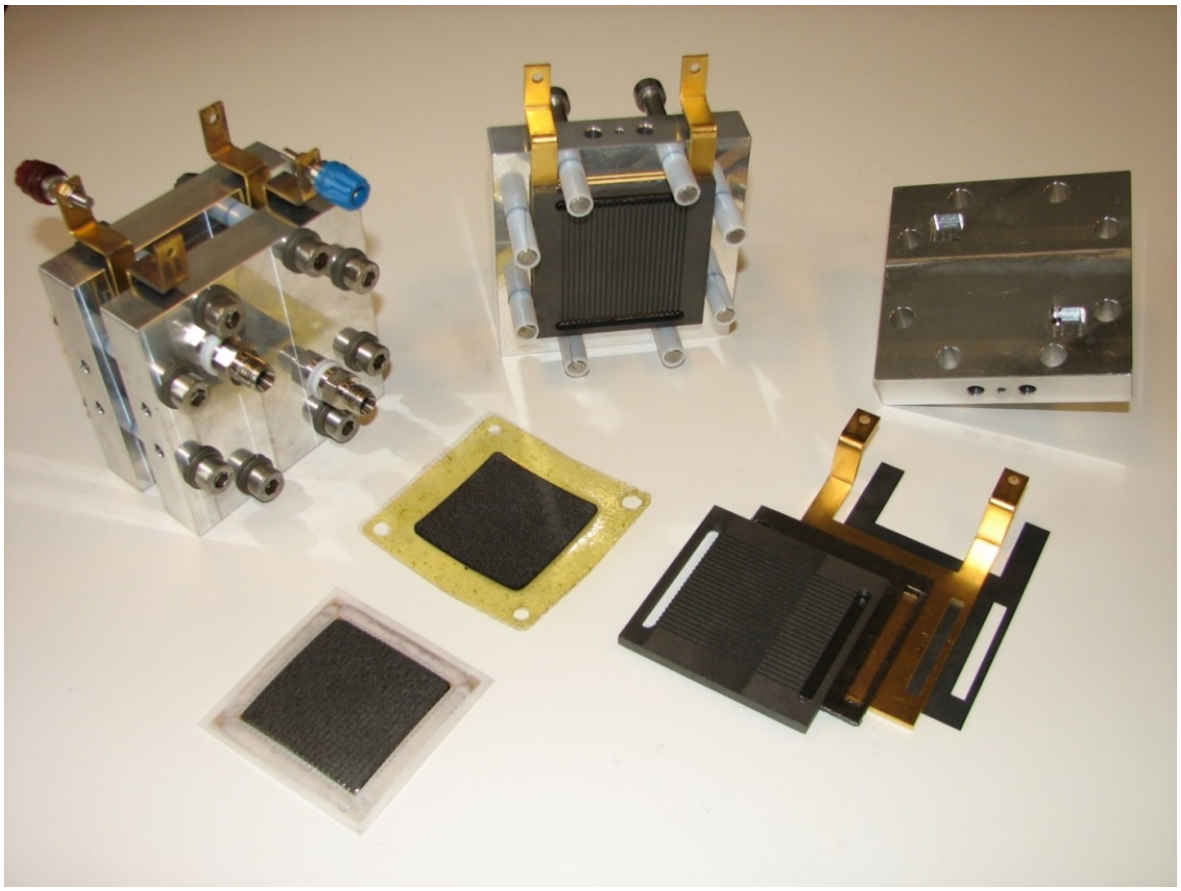

Figure 4.11: MEA and in-house made fuel cell housing. Center – unused MEA, bottom left – used MEA with PTFE gaskets attached, bottom right – graphite flow field plate, soft graphite (PapyEx) sealing, gilded current collector and Viton gasket, top right – aluminium end plate, top left – assembled cell.

The in-house made design was replaced in the middle of the project due to insufficient gas tightness and handling inconvenience, causing uneven and non-reproducible pressure distribution on the electrode area during assembly. It was replaced by commercial fuel cell housing from balticFuelCells GmbH, featuring a moving piston providing for adjustable contact pressure and a special sealing concept ensuring no gas leakage. The temperature of the cell was also more homogeneous due to the larger heating area. Furthermore it allowed for tool free and fast assembly without the need for reattachment of the gas tubes and electronics wiring. The hardware consisted of two parts, a quickCONNECTfixture Type FC25/100 and a cellFixture cF25/100 HT. An overview and cross section of the fixture is given on Figure 4.12.

The power and heating management of the commercial cell fixture required an additional control box to be made with its own temperature control. As the built-in temperature sensor was placed in the heating plate on the moving piston, the actual cell temperature was expected to be lower, therefore the cF25/100 HT was drilled out to accommodate a thermocouple close to the MEA. For that reason the control box contained a programmable PID control from Eurotherm, model 3216, with an RS-232 communication terminal to control and monitor the temperature of the cell and an alarm, Eurotherm 3216, to ensure that the piston did not overheat. The

communication module made it possible to alter the cell temperature remotely after a fitting accommodation of the LabView program was performed.

The described equipment together with a DME bottle were fitted into a stainless steel rack divided in sections, where the upper part was encased in transparent acrylic plates with a suction hole cut in the top to prevent exposure to potential intermediate dimethyl ether or methanol oxidation products and build-up of hydrogen due to possible leaks. The anode and cathode exhaust streams were also led straight to the ventilation shaft for the same reason. The bottom part contained the DME bottle, water and methanol bottles, PC and the load. The shelves in the middle accommodated the mass flow controllers, the pump and the temperature control for the cell housing together with the manual controls for the MFCs and evaporator, reformer and gas line temperatures. The upper part contained the cell housing, evaporator, reformer, gas and power outlets and any additional equipment when applicable. A picture of the setup is given in Figure 4.13.

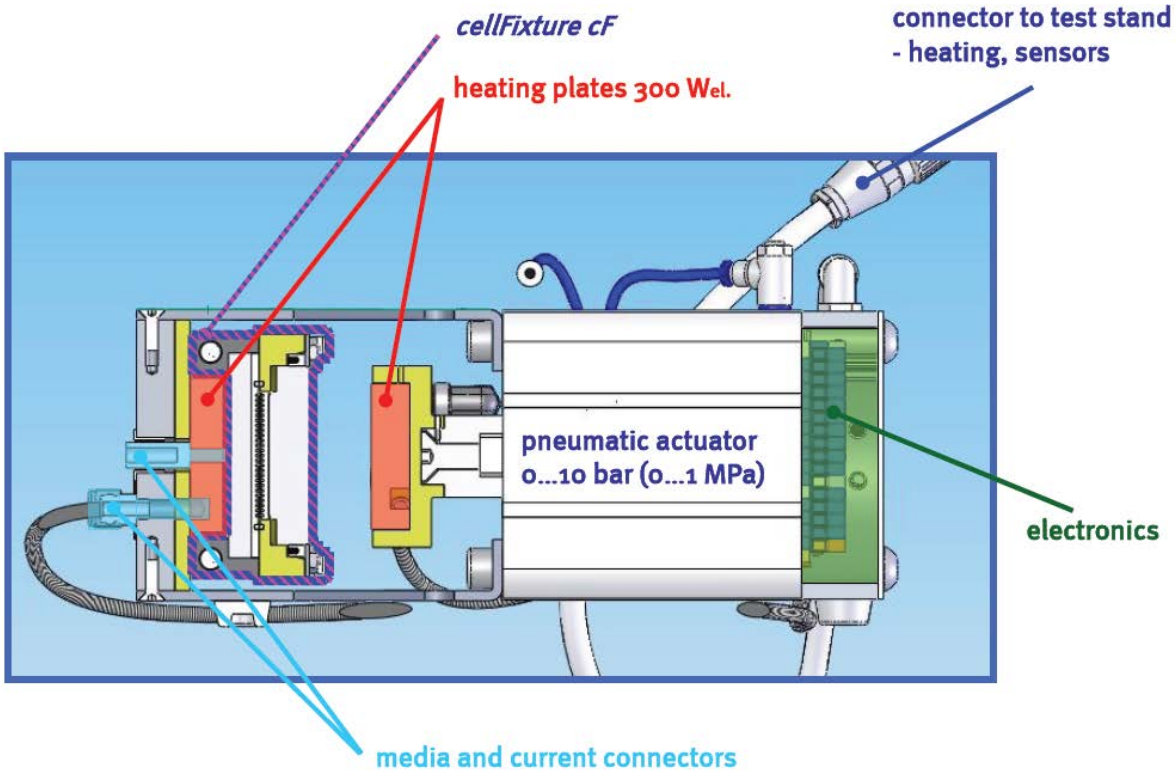

Figure 4.12: Overview and cross section of balticFuelCells quickCONNECT fixture. Adopted from [228].

Figure 4.13: Single cell test setup. a) – DME bottle, b) – load, c) – pump, d) – evaporator, e) – reformer, f) – cell housing, g) – temperature control of the cell, h) – data acquisition and control box.

4.6.3.2 Durability setup

For the purpose of testing the MEAs in terms of durability for direct DME operation a very flexible setup was planned, designed and constructed. The idea was to make a setup for simultaneous testing of 6 cells, where the testing conditions could be changed independently for every cell. The lessons learned from the operation with the single cell test setup regarding securing a steady burst-free steam delivery was incorporated in the design with complete elimination of the heated gas line prior to the cell inlet. The design accommodated an independent changing of the anode and cathode gas compositions with mixtures of up to 3 different gasses on either side, making it possible to simulate e.g. reformate on site without the need of purchasing pre-blended gas mixtures, if needed. The mounting of the mass flow controllers was made to allow for a simple and quick exchange if e.g. range and type of gas on a particular line had to be altered. To simplify the construction process the setup design was first visualised using computer-aided design (CAD) in Autodesk Inventor 2013 software. It allowed for an easy positioning of the desired pieces of equipment and also routing and dimensioning of the tubing. Bosch Rexroth 40 x 40 mm aluminium strut profiles modular system was chosen to make up the skeleton of the setup for its excellent mechanical strength, flexibility and versatility. The lower parts of the setup were designated to accommodate the loads, the pumps, water bottles, control box and the major part of the gas handling system. The upper part of the setup was split into the front piece containing two shelves for the integrated evaporator-fuel cell assemblies and the front panels for the electronic connections and temperature control of each individual channel, 3 of each on one shelf. The back side contained the gas distribution system, complete with the 4 mass flow controllers for each channel and all the auxiliary electronics needed for the heating system. The in-house fuel cell housing design was changed slightly compared to the one described in previous section. The size of the end plates were enlarged to 140 x 140 mm² and additional 30 mm ø 6 mm PTFE steering rods were introduced for a correct alignment of the gaskets, current collectors, flow field plates and the MEA, instead of the tightening bolts as in previous design. The distance between the gas channel in the current collectors and the outside border was also enlarged to minimise leakage. The flow field plates were now commercial 5 mm thick 80 x 80 mm² graphite plates with a 5-channeled serpentine flow pattern from balticFuelCells. The gas sealing around the MEA was now achieved by Viton O-rings placed opposite of each other on the anode and cathode instead of the flat PTFE gaskets used in previous version. The temperature control was analogous to the one on the single cell setup, with 2 CAL 3300 PID controllers for each channel, one for the cell heating and one for the evaporator. Additionally, 30 A 600 V AC solid state relays, GNR30DCZ from Crouzet, were used to extend the lifetime of the PID controllers, bypassing the internal relays.

The evaporator design was altered slightly, so it could be connected directly into the cell housing, making a single integrated system. The internal structure of the evaporator was still the same as previously described. The fittings were now custom made out of solid blocks of 316 steel, ø 25.4 mm (1 inch), and 2 aluminium half-shells

were made to cover the ø 19 mm evaporator pipe, enlarging the diameter to ø 25.4 mm, allowing for heating to be achieved using 4 120 W nozzle heaters with ø 1 inch internal diameter, one on each of the fittings and two on the tube itself. The heating of the fuel cell was done using 2 150 W cartridge heaters, one in each end plate. The pumps were the same as in the single cell setup, Shimadzu LC-20AD. The mass flow controllers were GF040CXX Multiflo Mass Flow Controllers from Brooks Instruments with Kalrez® sealings in the fuel MFCs due to the requirement for DME tolerance. The sealings in the remainder of the MFCs were made of Viton. The control of the gas flow rates in case of changed gas types were done programmatically multiplying the N_2-calibrated gas flow rate with a gas conversion factor available from Brooks Instruments website [229]. The physical changing in the gas type was achieved by a discontinuation of the gas inlet to the setup and gas inlet to the MFCs, were 7 outlets with on-off ball valves (42 in total) from Swagelok®, one for each gas, could be connected to any of the 4 inlets to the mass flow controllers on each channel.

The loads used were initially ZVL-100-xx loads from Amrel due to long delay in delivery time of the in-house made 80 A 4 channel loads, which were subsequently implemented in the setup upon delivery. The communication module of the control program had to be re-written to accommodate the control of the changed hardware. The control program was made on LabView platform from National Instruments and had a modular structure, with the communication module sending and receiving voltage signal values and the channel control panel module transposing those signals into real flow, temperature and cell current and voltage values. It was made such that the setup of each individual channel could be altered independently of others, reflecting the hardware flexibility of the testing setup.

The control box facilitating communication between the channels and the PC contained 18 ICP-CON modules - 9 i-7024 analog output modules for control of the MFCs and possible backpressure valves, 6 i-7017 analog input modules for monitoring the actual flow rates, 2 i-7018 analog input modules for recording the temperatures and 1 i-7561 USB-to-RS232/485 converter linking the communication between the PC and the rest of the modules. A lot of effort was spent on keeping track of the connections between the modules and mass flow controllers, as each MFC needed 6 connections going to designated i-7017 and i-7024. The complexity was also reflected in the control program.

The CAD drawings of the durability setup can be seen on Figure 4.14 and the front view photo of the finished setup on Figure 4.15. An exploded view of the custom made evaporator and fittings can be found in Appendix 9.1. A diagram of the MFC wiring to the control box ICP-CON modules and addresses is given in Appendix 9.2.

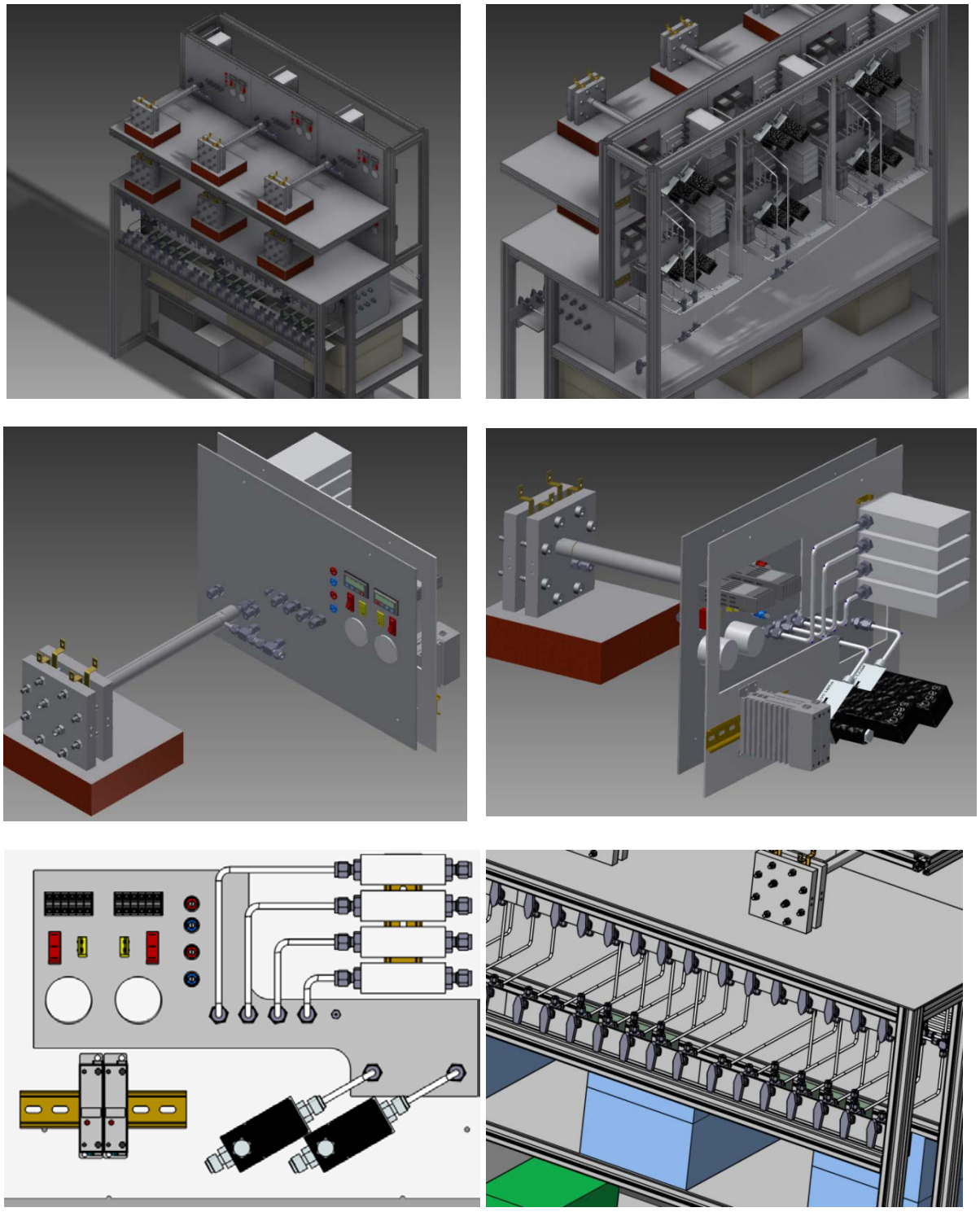

Figure 4.14: CAD drawings of the 6 channel durability setup. Top – front and back views of the complete setup, middle – front and back views of single cell slot instrumentation, bottom left – single cell slot instruimentation, bottom right – valve panel for gas changing.

Figure 4.15: Front view photograph of the 6 channel durability setup.

5 Fuel Cell Performance

5.1 MEA components optimisation

The triple phase boundary (TPB) is of essential importance when optimisation of the fuel cell performance is considered. As already mentioned in Section 0, a large and well-functioning TPB requires high ionic and electronic conductivities of the catalyst layer and a good access for the reactant gasses and facilitation of products removal. All the components comprising the catalyst layer have a specific task and by altering their amounts various effects on the final fuel cell performance can be obtained.

5.1.1 Effect of PBI amount in cathode catalyst layer

One of the important components in the catalyst layer is PBI, acting as a binder and ensuring structural integrity, so the catalyst particles stick to the surface and are not brushed away during handling of the electrodes. It also acts as a matrix for the phosphoric acid, providing a pathway for the protons. While PBI is necessary in small amounts, adding too much may cover the catalyst particles completely, rendering them inactive and reducing the triple phase boundary as a consequence.

To investigate this effect, electrodes with different amounts of PBI in the catalyst layer were prepared and their physical structure and composition studied by low energy X-ray imaging, SEM and EDX. The electrochemical performance was evaluated using the prepared electrodes as cathodes in a single cell under hydrogen/air operation. The ink series were prepared by weighing 0.157 g 57.4 % Pt/C HiSPEC 9100 catalyst from Johnson Matthey (lot 214291001) and then adding 0.6 wt% PBI in >98% formic acid solution in a 7 mL vial. At last extra formic acid was added to fulfil the criterion of 0.012 carbon to solvent ratio (g/g). No phosphoric acid in the catalyst ink was used in this investigation, as the desired catalyst layer was aimed to contain app. 0.65 mg_{Pt}/cm^2 and thus would be much thinner than the ones for the direct DME operation because of the requirement for a high catalyst loading, as will be evident from section 5.1.2 later. The phosphoric acid contained in the PBI membrane was supposed to impregnate the cathode catalyst layer, thereby achieving proton conductivity. An overview of the prepared inks and their composition is given in Table 5.1.

For the inks with the highest carbon to PBI ratio (low PBI content) of 30 and 40, it was not possible to achieve dispersion, as the catalyst particles would not go into suspension even after an overnight treatment in the ultrasonic bath. Apparently with the chosen composition of the ink with formic acid as the solvent there needs to be a minimum amount of dissolved PBI to stabilise the catalyst, to prevent it from agglomeration and to keep it suspended. In general for the whole ink series it was noted that a very homogeneous dispersion could not be achieved for any of the formulations shown in Table 5.1, with clearly visible agglomerates present in all the

inks. Due to the small volume of the batches it wasn't possible to use high shear mixing. Another thing to note was the many sparks during addition of the formic acid solution to the catalyst powder and during spraying originating from the catalyst particles spontaneously igniting when leaving the nozzle. The absence of phosphoric acid, which acts as a flame retardant in the case of catalyst ink preparation and spraying, is the most probable explanation for the observed effect. Another effect was observed during spraying. Due to the non-homogeneous ink composition a proper atomisation was hard to achieve with irregularities in the spraying as a consequence.

Table 5.1: Overview for ink compositions and resulting electrode platinum loadings for the PBI content investigation.

Ink ID	C:PBI ratio	C:solvent ratio	PBI wt%	Pt loading mg/cm²
015	40	0.012	0.029	NA
014	30	0.012	0.039	NA
013	20	0.012	0.058	NA
012	15	0.012	0.078	0.67
006	13.5	0.012	0.086	0.65
007	9	0.012	0.130	NA
008	6	0.012	0.194	0.61
009	4.5	0.012	0.259	0.64
010	3	0.012	0.388	0.67
011	2	0.012	0.580	0.65

Additional features were revealed by SEM imaging of the obtained electrodes. As can be seen from Figure 5.1 the amount of PBI has a big effect on the structure of the catalyst layer. The upper row shows images obtained using secondary and backscatter electron detectors for the electrode with C:PBI 6, which are representative for the electrodes with C:PBI ratio between 15 – 4.5. It can be seen that it is a rather dense layer comprised of many ink droplets deposited on top of one another with bigger agglomerates scattered over the entire surface. This also applies for the electrodes with C:PBI ratio of 3 and 2, but additional features appear on the latter. It can be seen that with increasing amount of PBI the electrode surface becomes less and less coherent with a network of holes and cracks spanning the entire area. There can be two explanations for this – first, it seems that the wetting properties of the ink changes with increasing amount of PBI, with increasing contact angle and subsequently added layers responsible for the formation of the holes. The cracks are due to the PBI contracting upon drying with the effect becoming more and more pronounced once the minimum threshold is passed. The electrode with C:PBI ratio of 3 shown in the middle row of Figure 5.1 shows one large ring on the secondary electron detected image with an additional one in close proximity obtained by backscatter detector. The rings originated from a temporary short blockage of the spray nozzle with subsequent release of accumulated material forming a large droplet of the ink. Upon hitting the surface of the electrode it dried depositing more material along the circumference of the contact. From the presence of the second ring seen by backscatter detector, this must have happened a number of times during spraying, as the ring is buried below additional layers of the catalyst ink deposition. It is easier to

see by backscatter detector as the sampling volume lies deeper below the surface compared to the secondary electrons, as described in section 4.3.

The SEM imaging results are in accordance with of the ones reported by J. Lobato et al. [230], who found that the electrode structure was finer and more homogeneous with decreasing PBI content. The authors used inks with N,N-dimethylacetamide

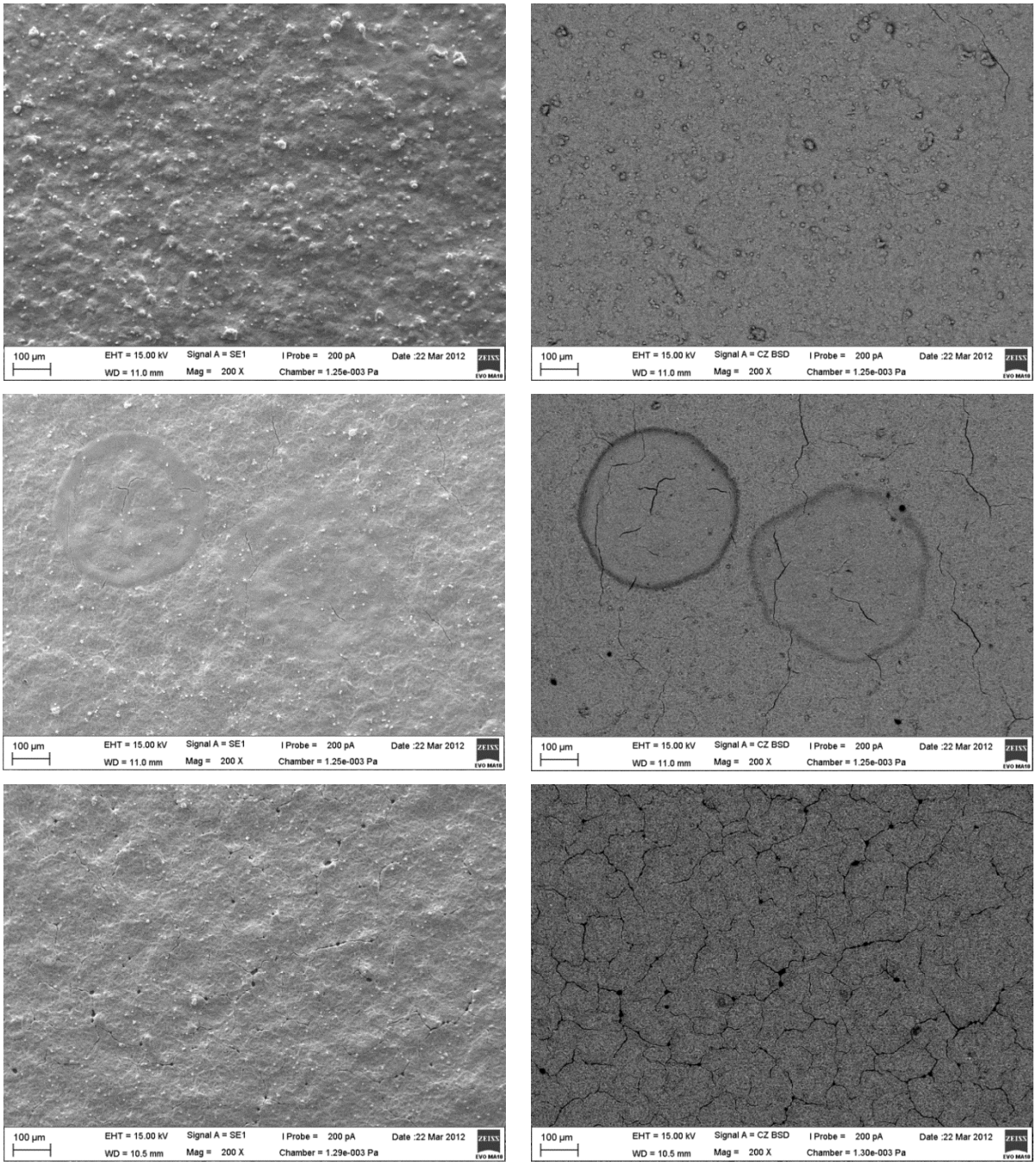

Figure 5.1: SEM images of electrodes with varying PBI content. To the left images acquired using secondary electron detector, to the right images acquired using backscatter detector. Upper row – C:PBI ratio 13.5, representative for electrodes with ratios 15 – 4.5. Middle row – C:PBI ratio 3. Bottom row – C:PBI ratio 2.

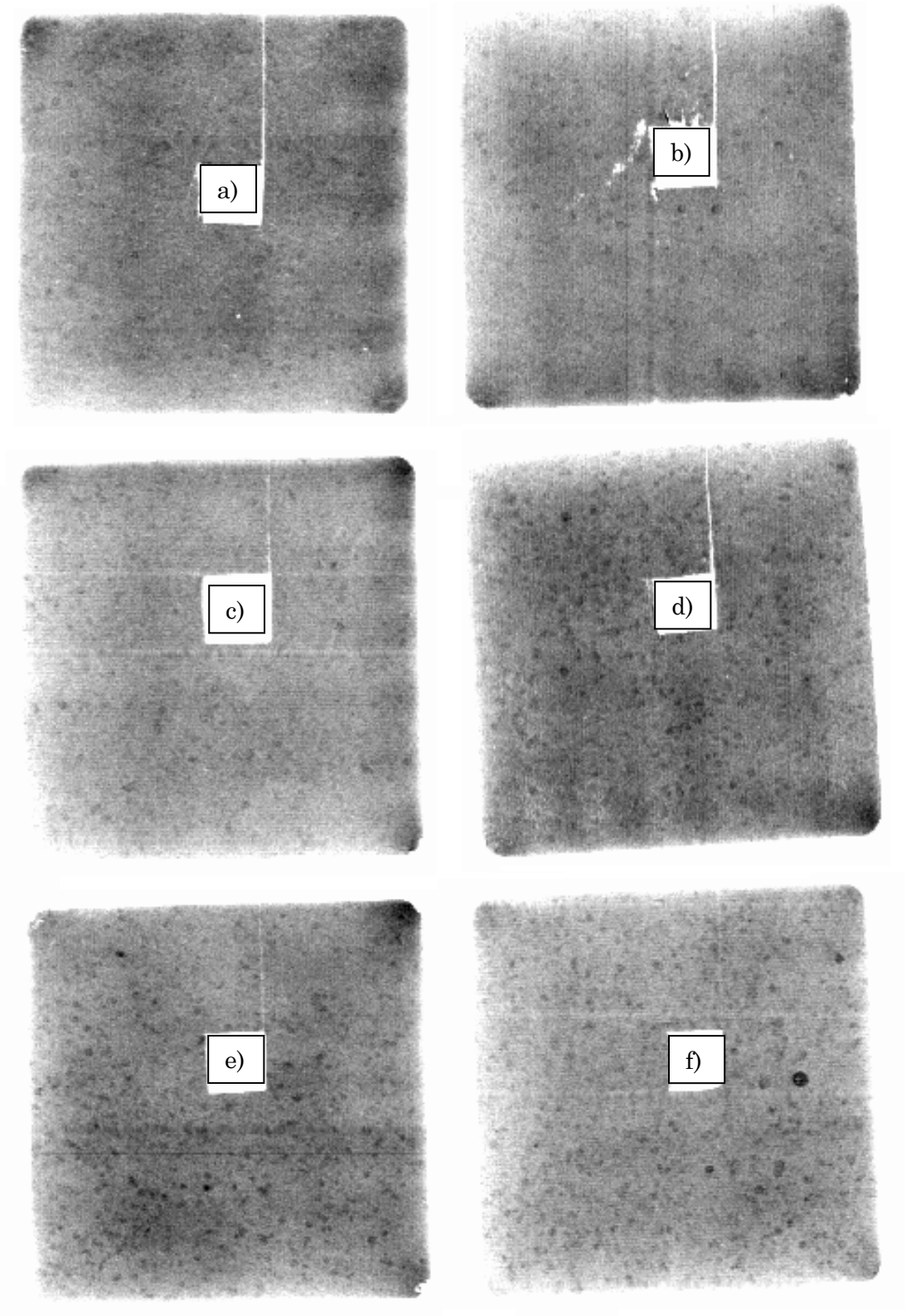

Figure 5.2: Low energy X-ray imaging of the electrodes with different amount of PBI in the catalyst layer. C:PBI ratios a) - 15, b) – 13.5, c) – 6, d) – 4.5, e) – 3, f) – 2. The holes in the middle of the electrodes are samples cut for SEM imaging. The grey scale contrast is the same for all the electrodes, chosen to emphasise the sputter features.

(DMAc) as solvent and were thus able to obtain C:PBI ratios ranging from 4 to 40 and the deposition of catalyst ink was done by spraying. In another paper J.-H. Kim et al. [231] found the same trend with tape cast electrodes.

Low energy X-ray analysis, shown in Figure 5.2 shows presence of the ink sputtering during spraying, with the darker dots originating from the larger droplets of catalyst ink, making the surface non-uniform in terms of catalyst loading and thickness profile. Whether it is an effect of absence of the phosphoric acid in the ink or simply a batch scaling issue remains unsolved, but it is evident that proper ink preparation is crucial in order to obtain a uniform electrode. It seems though that the PBI amount has an influence, as the number of dots is clearly larger for the C:PBI ratios between 4.5 – 2.

The prepared cathodes were subsequently used together with anodes from Danish Power Systems (lot E-12-008) with 0.33 mg/cm² platinum loading of a 60% Pt/C catalyst from Johnson Matthey with a Danish Power Systems PBI membrane (lot M-11-727 and M-11-728, 40 µm undoped) with phosphoric acid doping of 8 molecules per PBI repeating unit. The cells were hot pressed for 1 min at 125 °C with 1.5 ton total force, 60 kg/cm² pressure.

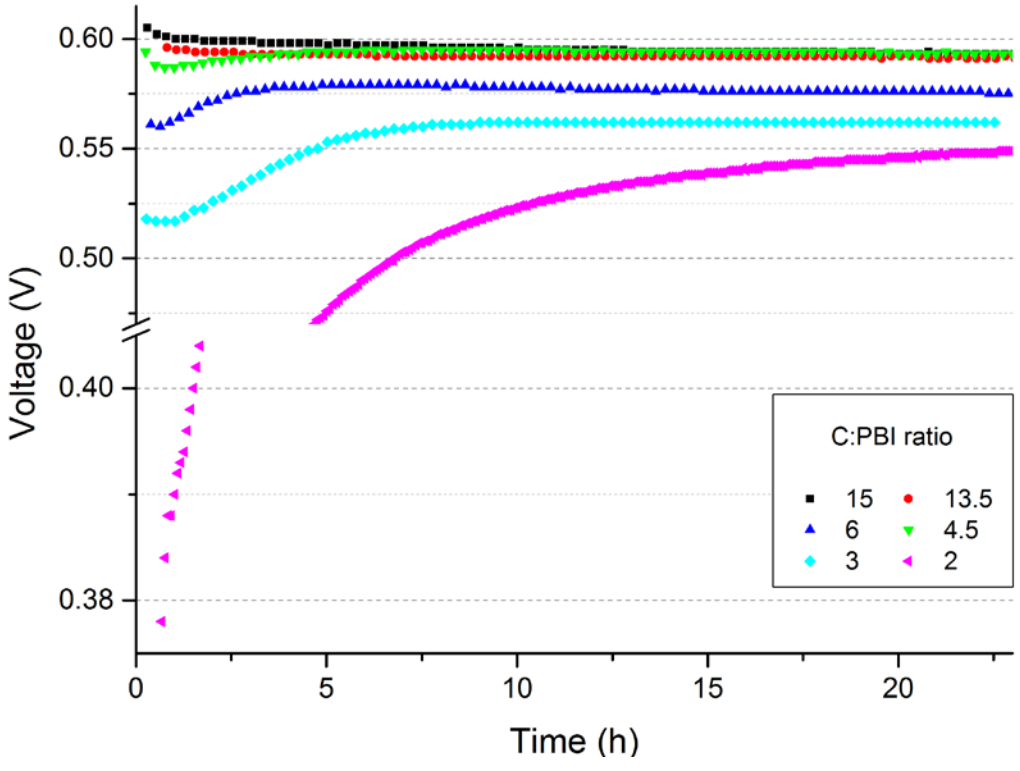

Figure 5.3: 24 hours run-in period for MEAs with different C:PBI ratios in the cathode catalyst layer. The cells were kept at 200 mA/cm² with exception of the MEA with C:PBI ratio of 2, which was kept at 50 mA/cm² due to low voltage.

The electrochemical testing was done at 160 °C with hydrogen and air flows fixed at 190 and 905 mL/min respectively, corresponding to a stoichiometry of $\lambda = 1$ and $\lambda = 2$ at 1 A/cm² in the in-house made cell housing. λ is a measure of how much current can

be theoretically drawn based on the magnitude of the reactant supply. The cells were run in for 24 h at 200 mA/cm² and changes in cell potentials recorded. Polarisation curves were recorded after 24 and 48 hours of operation at 200 mA/cm². The run-in period can be seen on Figure 5.3 and gives an indication of the distribution rate of phosphoric acid, which increases the proton conductivity and the area of triple phase boundary in the catalyst layer, thereby promoting the performance of the cell. For the cells with high amount of PBI in the cathode catalyst layer it takes longer time, with the amplitude decreasing with decreasing amount of PBI. In cases of very low PBI content it seems that there is a surplus of phosphoric acid in the electrodes from the start and the excess is removed during operation, indicated by immediate drop in voltage, decreasing in magnitude with increasing PBI content. PBI helps retaining the phosphoric acid and the optimum is thus around 9 PBI repeating units per carbon in the catalyst layer.

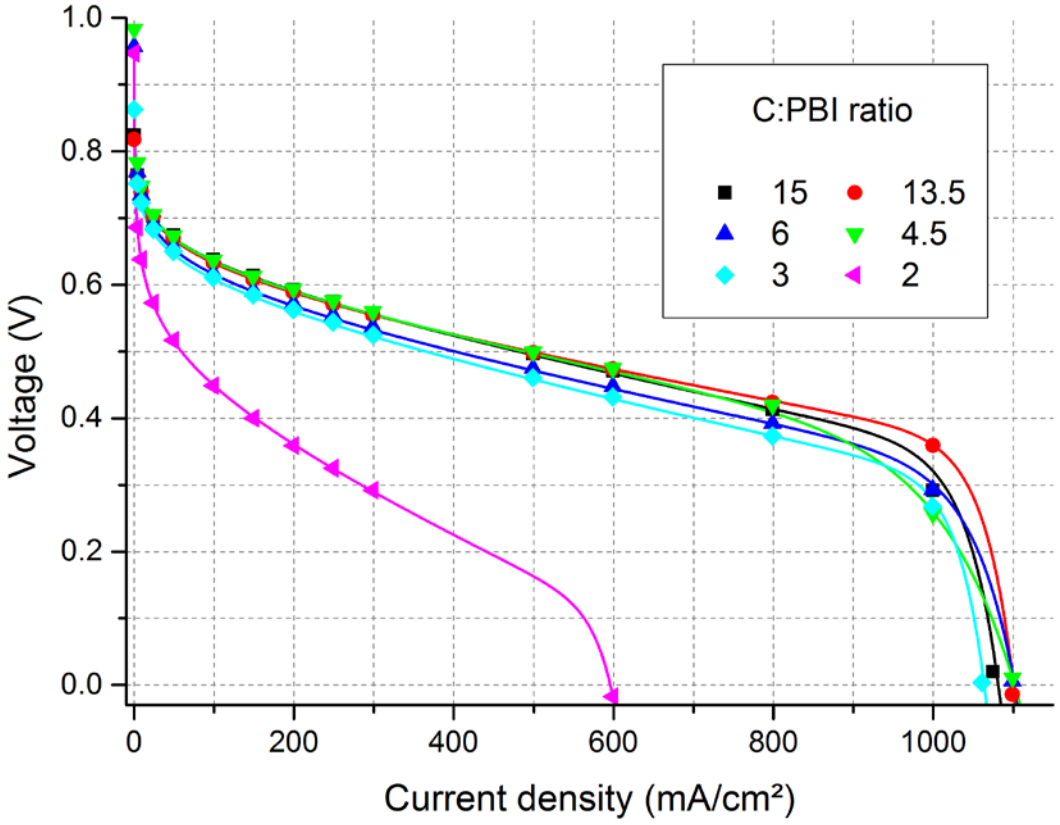

Figure 5.4: Polarisation curves for MEAs with different C:PBI ratios in the cathode catalyst layer after 24 h run-in period. The points represent the actual measurements and the lines are based on a curve fitting, given in eq. 5.2. Hydrogen and air flows correspond to λ = 1 and λ = 2 at 1 A/cm² at ambient pressure.

The polarisation curves obtained after 24 hours of run-in time are shown in Figure 5.4. It can be seen that there is no distinctive difference in the performance of the MEAs utilising 15 to 3 C:PBI ratios in the cathode, but there are clear limitations when too much PBI is added to the catalyst layer, as it is the case with C:PBI ratio of 2. In order to extract more information from the data curve fitting was performed based on the model described in section 2.2. The treatment was performed in

OriginPro 9.0 with a custom defined non-linear curve fit based on equation 2.18, repeated in eq. 5.1 for convenience. To obtain better fitting an overall estimation of the parameters was first performed over the whole data range. The values for open circuit voltage, Tafel slope and ohmic resistance were refined by fitting a simpler equation, given in equation 5.2 below, over 10 – 600 mA/cm² (10-300 for C:PBI = 2) range, where the cell voltage response is governed mainly by the exponential Tafel behaviour and the linear ohmic relationship. The obtained values were then fed as initial values to eq. 5.2 to obtain fittings with R-square values above 0.9999, suggesting good validity of the derived parameters. The standard errors were also usually smaller than their respective parameter values by at least one order of magnitude.

$$E_{cell} = E_{OCV} - b\log i - iR - me^{ni} \quad 5.1$$

$$E_{cell} = E_{OCV} - b\log i - iR \quad 5.2$$

The parameters extracted from polarisation curve fittings are given in Figure 5.5. It can be seen that there is no apparent trend and coherence between the fitted and measured OCVs. There can be a number of reasons for the observed effect. The fitted values do not correspond to the measured because of deficient description of the current-voltage relationship in the region below 10 mA/cm², where the Tafel behaviour is not yet valid. The measured values should in principle be equal, but are not so most probably due to deviations during the assembly of the cells, resulting in different amounts of gas leakage. Another reason could be imperfections in the membrane electrolyte, causing small changes in gas crossover, affecting the apparent open circuit voltage.

Since the kinetics of the hydrogen fed anode with platinum catalyst are very fast, the oxygen reduction reaction (ORR) mechanism and kinetics are the major contributors to the derived Tafel slope and cell voltage at 25 mA/cm², the latter being an indirect indication of the area of the triple phase boundary. The Tafel slope is increasing slightly with increasing PBI content, again until too much PBI is present in the catalyst layer. The values ranging between 76 to 93 mV/decade shows that the presence of H_3PO_4-PBI in the electrode structure positively affects the cathode side reaction, where the Tafel slope generally reported for ORR is 120 mV/decade, as described in section 2.4.3. For C:PBI ratio of 2 the Tafel slope is actually higher, 139 mV/decade. The opposite trend is observed for the cell voltages at 25 mA/cm², which tends to be increasing with decreasing amount of PBI. Obviously, too much PBI in the catalyst layer results in a lower exchange current density and a higher Tafel slope, showing that PBI impedes the cathode reaction.

The resistance obtained by polarisation curve fitting suggests that there might be a minimum in the region between 6 and 13 C:PBI ratios. Having too much PBI in the catalyst layer obviously leads to increased resistance due to increased thickness of the catalyst layer and also due to higher coverage of catalyst particles. However it is

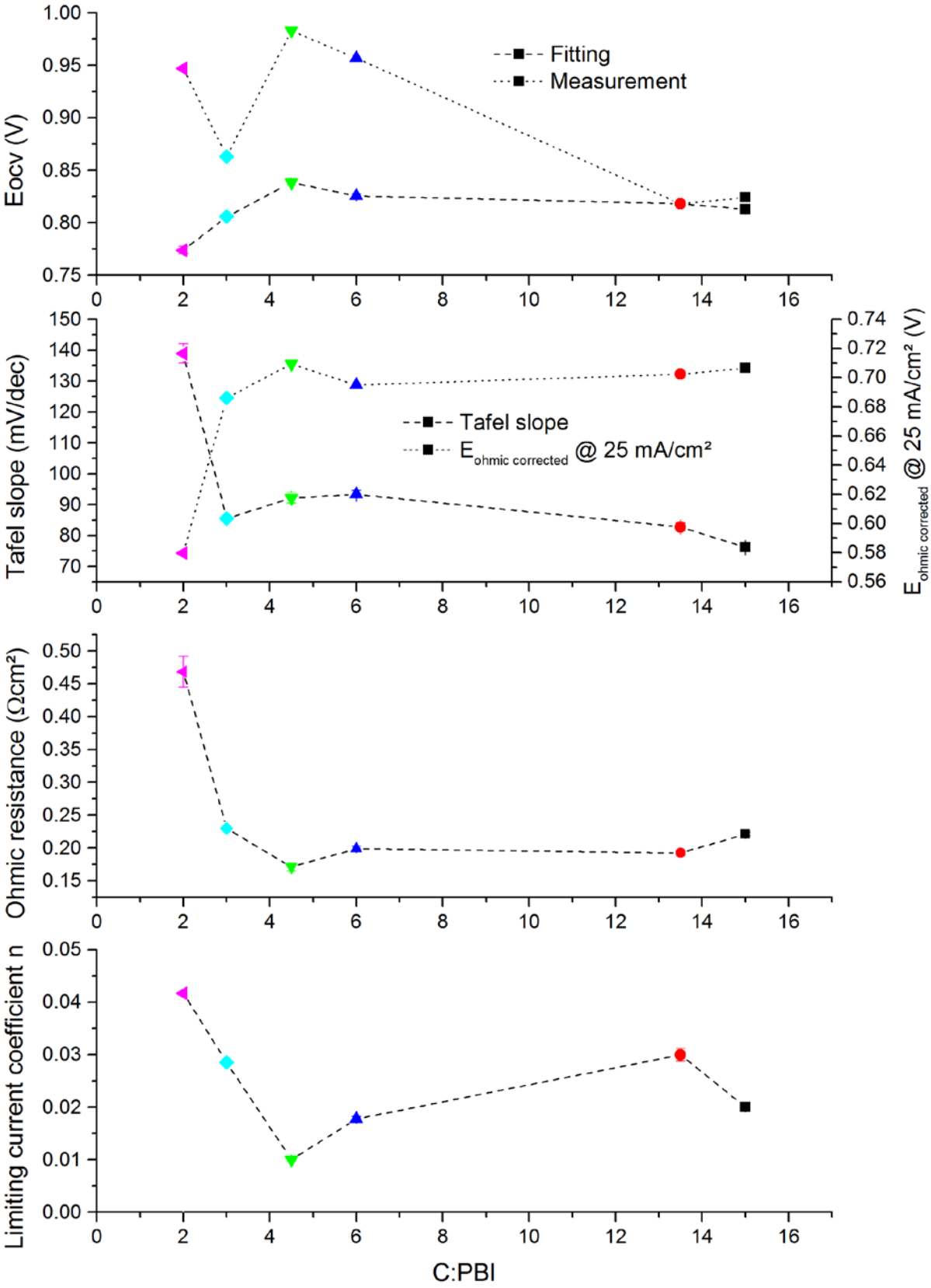

Figure 5.5: Parameters extracted from the i-V curves by fitting model according to eq. 5.2 as functions of C:PBI ratio.

interesting to see that with very low PBI loadings the resistance is increasing, which can be ascribed to deficient linking of the platinum sites with the electrolyte. It is known that the electrolyte resistance is not a constant, but changes slightly with increasing current due to the cell producing water, which tends to increase conductivity of non-humidified cells. A more proper estimation of the resistance could therefore be more advantageously determined by the electrochemical impedance spectroscopy (EIS), where the resistance is measured directly at each particular point of the polarisation curve, but the technique was unfortunately unavailable at the time of the experiments.

The mass transport limitations in these experiments was mostly due to fuel starvation, as the fuel flow rate was fixed at 1000 mA/cm² with $\lambda = 1$. The curve fitting took the limitations into account nonetheless. The parameter m is an empirical parameter describing the voltage deviation from the ohmic governed region of the polarisation curve at higher current densities range, when limiting current is not yet reached. Not enough measurement points were taken in that region to properly estimate this parameter and the obtained fitted values were very small, having little effect on the fitted curves. The values represent little informational value and are therefore omitted from the discussion. More interesting is the parameter n, which is connected with the limiting current. Even though the limiting current is dictated by the anode for most of the investigated MEAs, from the bottom graph on Figure 5.5 it can be seen that too much PBI is harmful for the electrode structure, as the limiting current coefficient for the MEA with C:PBI ratio of 2 is clearly much higher than the rest. From the polarisation curves on Figure 5.4 the voltage drop of the latter around 600 mA/cm² is clearly due to the insufficient mass transport on the cathode side, as the anodes are the same in all MEAs. The open porous electrode structure collapses and no longer facilitates sufficient transport of reactants and products to and from the reaction sites. This is in the agreement with the observed electrode structure by SEM seen in Figure 5.1.

The obtained results are in general agreement with the ones reported by J. Lobato et al. [230], J.-H. Kim et al. [231] and A. Su et al. [232]. The two first papers described structural and electrochemical evaluation of MEAs with varying C:PBI ratios and the latter presented a model simulation of oxygen concentration and current distribution and confirmed the data by electrochemical evaluation and impedance measurements. All three papers concluded that with large amount of PBI the electrochemical active surface area decreases due to electronic blockage of the catalyst particles together with the increase in the mass transport limitations due to reduced porosity of the electrodes. In the other end, with too little PBI it was found that there is an insufficient ionic conduction, leading to a slightly reduced performance, but the electrochemically active surface area and mass transport properties were scarcely affected. The optimum ratio of C:PBI the authors found to be 20, 11.5 and 11.5 respectively. This is slightly higher than in the present study, showing an optimum

around 9, which confirms that the method of catalyst ink preparation and composition plays a tremendous role for the final performance.

Another interesting observation was made when the cells were left at 200 mA/cm² for 48 hours. Most of the MEAs didn't show much difference between 24 and 48 hours with only slight drops in voltage for cells with C:PBI ratios 15 – 6 and slight increase in voltage for cells with ratios 3 and 4.5. The one with C:PBI ratio of 2 however showed a very significant improvement and was left for 190 h total. There was a steep growth of the potential in the first 20 hours, after that the curve flattened out, but continued the increase, as can be seen from Figure 5.6 on the left. Polarisation curves were taken at 24, 48 and 190 hours of operation. The region between 10 and 300 mA/cm² was used for extracting the Tafel slope and the ohmic resistance at different times. From Figure 5.6 on the right it can be seen that both parameters decrease with time, indicating that the structure of the cathode is changing for the better, allowing higher conductivity, as reflected in the ohmic resistance decrease from 0.47 Ωcm² to 0.35 and 0.34 Ωcm² at 24, 48 and 190 h respectively. Tafel slope is likewise decreasing from 139 mV/decade to 131 and 115 mV/decade for the same times respectively, and the cell voltage at 25 mA/cm² was increasing from 0.579 V to 0.591 V and 0.618 V, indicating increased triple phase boundary. The effects are probably due to increased degree of phosphoric acid doping of the polymer in the catalyst layer. A suitable break-in period is thus also of an issue when reporting the data for this kind of fuel cells, as the restructuring and reorganisation of the components in the electrodes of high temperature PEM fuel cells is time dependent.

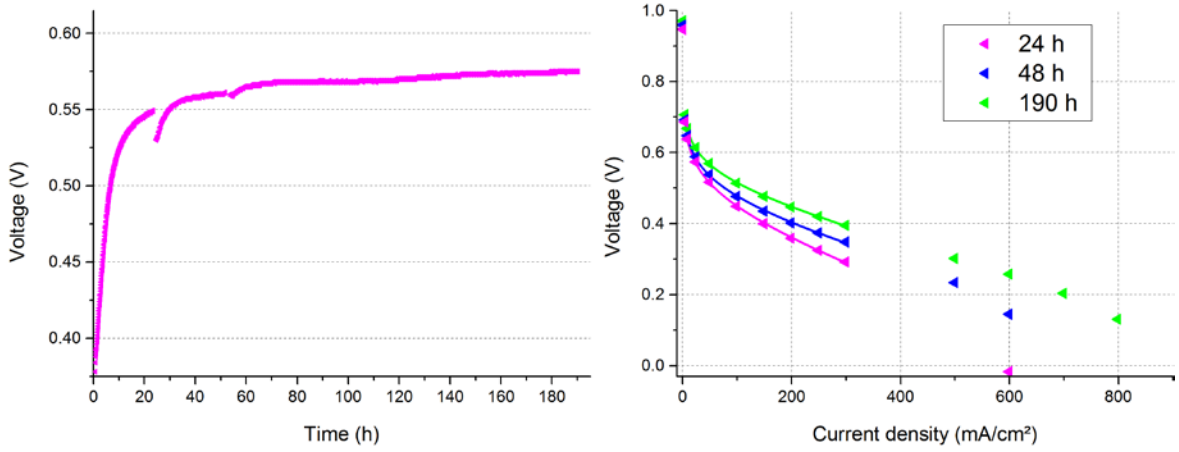

Figure 5.6: Potential development over time at 200 mA/cm² and polarisation curves at different times for the MEA with C:PBI ratio of 2. The lines on the right graph indicate the fitting from 10 to 300 mA/cm² using eq. 5.2.

5.1.2 Effect of catalyst loading on the anode

The catalyst is responsible for the electrocatalytic activity of the electrodes. It is therefore important to optimise the catalyst loading to get the highest activity, as too little will result in insufficient fuel turnover frequency and too much will result in a very thick catalyst layer with only a fraction of it being truly active and the rest simply contributing to a higher ohmic resistance and possibly mass transport limitations. At the same time the catalyst is one of the most expensive components of

a PEM fuel cell, as it contains precious metals. As already mentioned in section 1.3.5, many commercial LT-PEM units utilise less than a total of 0.3 mg_{Pt}/cm^2 with the amount decreasing constantly due to significant amount of research in the field. The loading of the precious metal in HT-PEM FCs is usually higher, in the range between 1 - 2 mg_{Pt}/cm^2, which is done to overcome the limitation of strong adsorbance of phosphate on platinum sites. When the cells are fed with reformate hydrogen, the fuel stream typically contains additional water vapour, CO and CO_2 and additional catalyst is required to overcome the limitations arising from the impurities. Therefore the platinum loading on the electrodes is usually between 0.5 – 1 mg/cm^2 on the anode and 1 – 2 mg/cm^2 on the cathode. In case with direct HT-PEM FCs fed with e.g. methanol, ethanol or dimethyl ether even higher amounts of catalyst are required to overcome the limitations set by the decreased kinetics of the anode reaction. Additionally the fuel crossover to the cathode enforces the use of higher catalyst loadings to minimise the crossover currents. Therefore it is not unusual to see catalyst loadings as high as 6 $mg_{Pt\text{-}Ru}/cm^2$ and 4 mg_{Pt}/cm^2 on the anode and cathode sides respectively for direct methanol fuel cells, although mostly for research and demonstration purposes [54, 123]. At the moment of the study, no detailed investigation of the effect of anode catalyst loading on direct DME HT-PEM FC performance was reported in literature. The optimum amount was expected to be around the same as for DMFCs, therefore series of anodes with varying catalyst loadings in range between 1 – 5 mg/cm^2 were made and incorporated into MEAs with cathodes made in-house or from Danish Power Systems with a platinum loading of 0.7 - 1 mg/cm^2. The cathode loading was relatively low compared to the ones reported in literature for direct methanol fuels cells, but it was chosen based on the reported findings of DME not being oxidised at the cathode in case of fuel crossover, as described in section 3.2.

In general, the direct DME HT-PEM FC experiments suffered from poor reproducibility, which applies for the following chapters as well. There can be many reasons for this, as the manufacturing of the MEAs is a process involving many steps with each one having a more or less pronounced influence on the final performance. Moreover, the fixture of an MEA into cell housing can have a tremendous effect, if the gas tightness is insufficient, making diffusion of air to the anode possible, as the cells were tested without backpressure. It could also affect fuel crossover, which would flow into the cathode compartment around the electrode area if the sealing between the membrane and fuel cell housing is not gas tight. Additionally misalignment could cause increased ohmic drops, due to the electron conducting components of the fuel cell being poorly connected. More pressure on the clamping bolts of the in-house made cell fixture or additional pressure on the actuator of the commercial cell fixture would help on resolving the issue, but at the expense of too much compression of the MEA, in which case the open and porous electrode structure might collapse, leading to loss of triple phase boundary and increased mass transport losses. Moreover, there might also be a risk of damaging the membrane and formation of pinholes, causing the MEA to fail.

The catalyst ink was made by first dissolving 0.1020 g polybenzimidazole (100 mesh polymer powder, Celanese) in 114.8 g concentrated formic acid (≥98%, Sigma-Aldrich) in a 150 mL beaker under magnetic stirring for an hour. The solution was added to a mixture of 3.417 g 40.07 wt% Pt and 18.72 wt% Ru on carbon catalyst from Johnson Matthey (lot 140496001) and 0.992 g phosphoric acid (≥85%, Sigma-Aldrich) in a 100 mL flask. The final ratios between the ink components were 13.5, 8.27 and 0.012 for C:PBI, PA:PBI and C/solvent respectively. The ink preparation was done according to description in section 4.6.1. The resulting ink was very well dispersed, thus the high shear mixing was not required. The electrodes were then made by the spray robot with the ink kept in the ultrasonic bath between the refilling of the ink feed syringe to avoid agglomeration of catalyst particles.

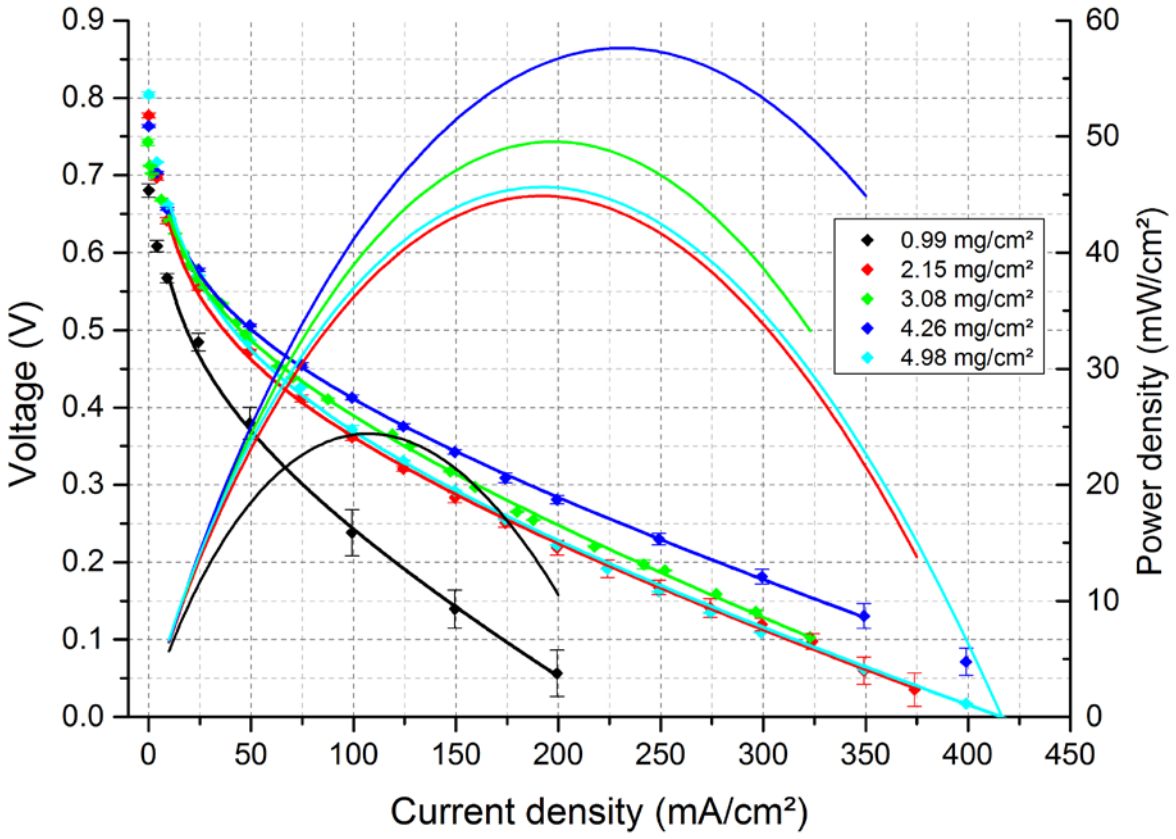

Figure 5.7: Effect of anode catalyst loading on direct DME HT-PEM FC performance at 200 °C. Anode - 32 mL/min DME and 0.07 mL/min H_2O, cathode - 905 mL/min air, corresponding to λ = 1 at 1 A/cm² and DME/water ratio of 3 on the anode side and λ = 2 on the cathode. Points are representing the mean voltage value with the respective error bars indicated. The lines are corresponding curve fittings performed over the indicated current range.

The resulting electrodes were analysed using low energy X-ray spectroscopy, with the results given in section 4.6.1 and used as anodes together with cathodes from Danish Power Systems with 1.07 mg_{Pt}/cm^2 loading (lot Ka-11-019) and phosphoric acid doped membrane, also from Danish Power Systems (lot M-11-785) with the doping level of 7.5 phosphoric acid molecules per PBI repeating unit. The MEAs were hot pressed for 3 minutes at 200 °C using pressing tools for correct alignment. The testing was done in the commercial fuel cell fixture at 200 °C with 32 mL/min DME and 0.07 mL/min

H_2O flows on the anode side and 905 mL/min air on the cathode side, corresponding to $\lambda = 1$ at 1 A/cm² and DME/water ratio of 3 on the anode side and $\lambda = 2$ on the cathode. The results are given in Figure 5.7 with the points representing the mean of voltage response measurement, taking every 15 seconds over a period of 2 minutes. The large deviations from the mean values on e.g. MEA with 0.99 mg/cm² anode catalyst loading, indicated by the error bars, were most probably due to a malfunctioning DME mass flow controller, with the flow oscillating with up to 1 mL/min in that particular measurement. The water to DME ratio was thus not stable, which explains the growth of the voltage oscillations with increasing current. Another reason for the oscillations could be the observed water condensation in the outlet tube temporarily blocking the flow of the gas until it is blown out of the tube, thus introducing pressure changes, which has been shown to have tremendous effect on the performance of direct DME fuel cells.

As evident from the figure, there is a trend with increasing anode catalyst loading leading to improved performance until saturation is reached at 4.26 mg/cm² for this particular series of measurements and a decrease when the catalyst loading is increased further. To quantify the causes for the trend curve fittings were performed based on equation 5.2. The obtained values together with the measured open circuit voltages are given in Figure 5.8. There is a good correlation between the observed values and the fitted OCVs of the different cells compared to the ones presented in previous section. This is because the cell housing used this time was the commercial, so alignment of different cell housing components was the same every time and the gas leakage around the MEAs was minimized if not eliminated. There is still a discrepancy between the observed and fitted values, which is due to the simplicity of the fitting model not being able to describe the phenomena governing the voltage response of the cells at currents below 10 mA/cm² with the Tafel behavior not yet valid.

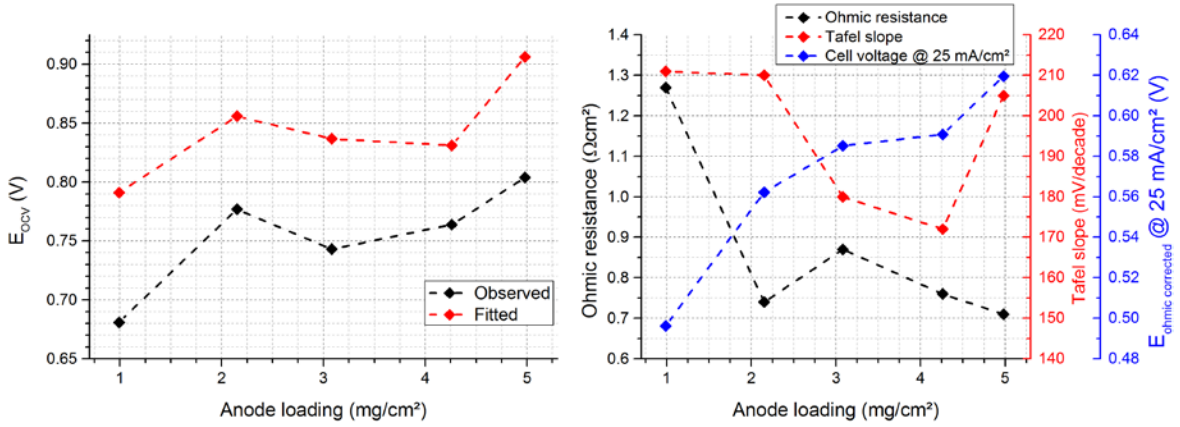

Figure 5.8: Parameters of the polarisation curves for direct DME HT-PEM FC performances with different anode catalyst loadings.

The ohmic resistance seems to be falling with increasing catalyst loading, which is surprising, as an increase in catalyst layer thickness should in principle lead to a slightly increased resistance. On the other hand the value of the resistance for the

MEA with 1 mg/cm² anode catalyst loading could be wrong due to the already mentioned oscillations in the fuel flow and could in principle be fitted to a 0.3 Ωcm² lower value, still being within the error of the measurement. In that case the curve for the ohmic resistance as function of anode catalyst loading would be relatively flat and possibly reflect the thickness variation of the membrane, which is the main source of the resistance. If the same curve fitting is performed on the hydrogen-fed experiments, there was indeed a very small increase in resistance, within 0.06 Ωcm² with the increasing loading, again with MEA utilising 1 mg/cm² catalyst loading deviating from the trend.

The Tafel slope shows no apparent correlation with anode catalyst loading. It should not be changing, as the catalyst was the same on the tested MEAs together with testing conditions and temperature. The mechanism should therefore not be changing considerably. Ohmic corrected cell voltage at 25 mA/cm² is increasing, indicating a larger triple phase boundary which is expected from increased amount of catalyst.

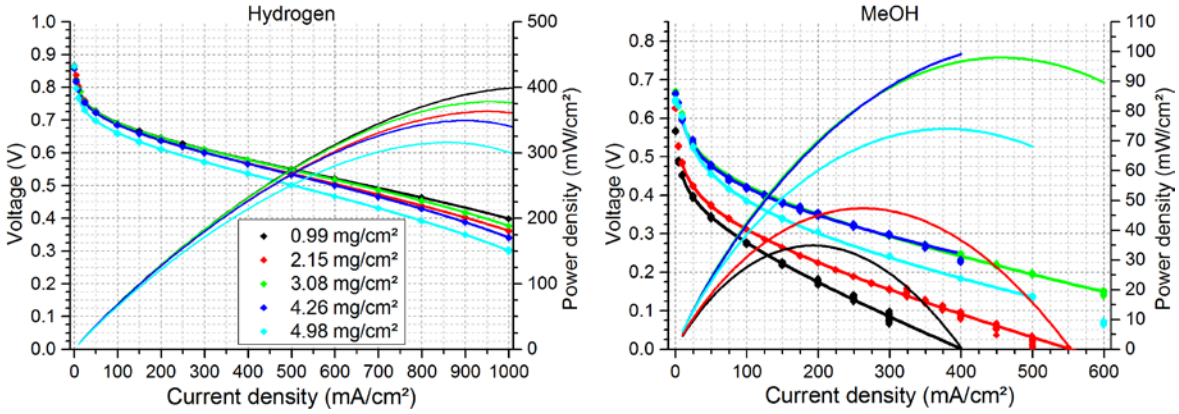

Figure 5.9: Effect of anode catalyst loading on fuel cell performance when operated with H_2 (left) and methanol (right) as fuel. The cells were operated at 200 °C with 905 mL/min air on the cathode side and 191 mL/min hydrogen or 0.31 mL/min 1:1 MeOH/water mixture, corresponding to λ = 1 at 1 A/cm² and DME/water ratio of 3 on the anode side and λ = 2 on the cathode.

It seems though that there is a general tendency for the OCV to increase with increasing catalyst loading. This can be explained by consideration of the term exchange current density i_0, see section 2.1.1. As it was the same catalyst used in the series of measurements, its activity towards DME electrooxidation should in principle be the same. The number of actives sites is however different, therefore the exchange current density must be different. The current at OCV is ideally zero, but it is never so in real conditions, as little fuel crossover or internal currents would be present even if the electrical circuit is open. From the Butler-Volmer equation (eq. 2.7) it can be seen that for constant current density a larger exchange current density gives smaller overpotential, yielding higher measured OCVs for MEAs with high anode catalyst loadings. To confirm this effect a comparison with MEA operation on hydrogen was made and is depicted on Figure 5.9 on the left. As the kinetics of hydrogen oxidation are very fast, there is more than enough catalyst present even at the lowest anode loading, so the voltage response of the MEAs at low currents is governed by the

cathode kinetics. As the cathodes are from the same batch with equal catalyst loadings, the OCVs should be the same for hydrogen operation regardless of the anode catalyst loading. This is indeed the case.

The series of measurements with different anode catalyst loadings were repeated 4 times with different procedures for MEA manufacture and different cell housings. The peak power densities for direct DME operation for the different series are given as function of anode catalyst loading on Figure 5.10 to the left. Series 1 utilised hand-sprayed electrodes on both sides and the MEA testing was performed using in-house made cell housing while Series 3 MEAs were made of robot sprayed anodes and commercial cathodes from Danish Power Systems and were tested in the commercial fuel cell housing from balticFuelCells. Series 1 utilised MEAs with very large variations of membrane thickness and unknown H_3PO_4 doping level. Series 2 and 3 utilised PBI membranes from Danish Power Systems with 51±1 µm un-doped thickness. As evident from Figure 5.10, there is a large spread in the measured values. A part of it could be explained by the different conditions used, but that should be mostly in between the different series. Series 3a and 3b should give the same results, as they were made in the same batch. Nonetheless, 2 MEAs of series 3a failed, with the rest giving non-identical results with series 3b, representing poor reproducibility observed throughout the whole study.

From the investigations represented on Figure 5.10 it seems that there is an optimum in anode catalyst loading between 3 and 4 mg/cm² where there are enough active sites to facilitate the oxidation of DME as rapid as possible before the effects of the increased thickness begin to play a role. From the right on Figure 5.10 the peak power densities are seen for methanol operation on the same MEAs. The same trend appears, although it seems to be shifted towards 3 mg/cm² rather than 4. This indirectly shows that the electrooxidation of MeOH on Pt-Ru catalyst is indeed faster than DME. The experiments were repeated at 150 °C and some also at 175 °C, showing similar trend in performance development.

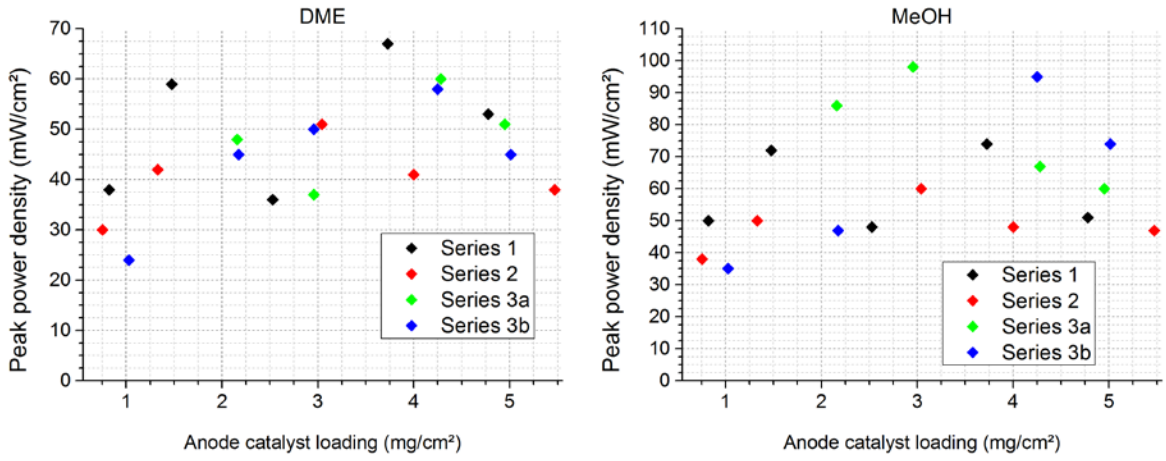

Figure 5.10: Direct DME and MeOH HT-PEM FC peak power densities of the series investigation with different anode catalyst loadings at 200 °C.

5.1.3 Effect of catalyst composition

There is a number of studies on DME electrooxidation on different catalysts, as already described in section 3.2. Most of them were done as half-cell tests and a few in low temperature PFSA-based cells, with their operating conditions pressed almost beyond the limit to allow for direct DME operation. While the findings agreed that additional Ru or Sn to the standard Pt/C catalyst was beneficial [166, 186, 190], no detailed studies on the ratios between the metals have been performed at the time. This section presents the results obtained from MEAs made with in-house made catalysts with varying metal ratios prepared by simple impregnation-reduction method. The synthesis of catalysts with controlled atomic ratios was performed by simultaneous reduction of different metal salts onto the carbon powder substrate with a powerful reducing agent [233-235].

For the experiments appropriate amounts of water solutions of hexachloroplatinic acid, orange coloured (nom. 37.8 wt% Pt, Metalor Technologies LTD, batch pmc2716), ruthenium trichloride, deep brown coloured (nom. 40.32 wt% Ru, Johnson Matthey, lot 76447) and tin tetrachloride, unclear, (98 %, BDH Chemicals LTD) were added to a beaker containing Vulcan XC72R carbon black powder dispersed in water. The solutions were heated up to 80 °C and stirred by a magnetic stirrer for app. 1 hour before 5 wt% $NaBH_4$ solution, made from sodium borohydride (≥96 wt% Sigma-Aldrich, lot STBC2667V) dissolved in water, was added over 2 hours in ca. 10 mL portions at a time and then were left overnight under stirring to complete the reduction. The obtained powders were then filtrated using PES membrane filter and the waste water was clear for all presented samples, showing complete reduction of metals. The catalysts were subsequently washed to remove any remaining chloride from the powder, as presence of even a small amount would poison catalyst in the final MEA with inferior performance as a consequence [236]. Tests with 12 wt% $AgNO_3$ solution did not produce any reaction with the last portions of waste water, indicating proper removal of chloride. The catalyst powders were then dried in a vacuum oven overnight at 70 °C and grinded in a coffee mill.

The obtained catalysts have been analysed by XRD, TGA-DTA, SEM and EDS. They were also attempted analysed by ICP, but the samples were not possible to prepare, as the catalyst metal would not dissolve in concentrated aqua regia added a few percent hydrogen peroxide agitated by high pressure microwave. The SEM imaging showed no apparent differences in the morphology and structure of the synthesised catalysts down to app. 50 nm. The EDS analysis results, shown in Table 5.2 show a good correlation between the nominal theoretical values of the ratios between the metals and the metal ratios obtained in the final catalysts.

Thermogravimetric analysis was performed on the catalysts to determine whether the desired metal loading in wt% was obtained during synthesis. The analysis was carried out with a heating rate of 5 K/min from room temperature to 1000 °C. As evident from Figure 5.11 there is a relatively good correlation between the nominal 60 wt% metal on 40 wt% C for Pt_xRu_y catalyst investigation and the obtained values (left) and the

nominal 80 wt% metal on 20 wt% C for $Pt_xRu_ySn_z$ catalyst investigation and the obtained results (right). It means the syntheses were successful with very little precious metals lost. The reason for the somewhat higher residual masses can be explained by oxidation of ruthenium to RuO_2, which was calculated to give an increase of up to 7 wt% in case of $Pt_{20}Ru_{80}$/C, corresponding very well with the residual mass obtained by TGA. The DTA peak at 400 °C fits very well with that assumption, as ruthenium has been reported to oxidize to dioxide at 400 °C and further to tri- and tetra-oxide in small quantities at higher temperatures [237]. The weight loss step starting after 300 °C is attributed to oxidation of carbon support to CO_2, which was found to occur at 580 °C in absence of metal. This is an indication of catalyst activity already prior to the electrochemical testing. The DTA peak at 480 °C shows an exothermal reaction occurring, increasing with platinum content, which is a further indication of the exothermic oxidation of carbon black to CO_2. Additionally it also shows that ruthenium is not active towards carbon oxidation, determined by electrochemical measurements, as discussed in section 3.2.1. There are other small, insignificant features on the obtained DTA spectra, which are most probably caused by instrumental response to the sample-containing crucibles or instrumental errors, e.g. the shift of all the spectra at 700 °C.

Figure 5.12 shows X-ray diffractograms of the different obtained catalysts. Platinum peaks dominate all of the diffractograms with the exception of $Pt_{20}Ru_{80}$/C and to some extent $Pt_{33}Ru_{66}$/C. The reason for this can be found from platinum-ruthenium phase diagram [238]. Up until ca. 0.6 at% Ru content the metal particles retain platinum fcc lattice structure, producing the dominant reflections from the respective planes. With higher Ru content the metals form a unit cell with lower symmetry, resulting in a change of the diffractogram with lower peak intensities. In general the dominant Pt peaks at ~40°, 46°, 68° and 82°, representing 111, 200, 220 and 311 planes respectively [234], grow in intensity with increasing Pt content, confirming the compositional analysis obtained by EDS. It can be seen that the peaks decrease in intensity and tend to broaden with increasing content of Ru, suggesting that the catalyst particles are decreasing in size, which is also reflected by the crystallite size obtained by Debye-Scherrer equation (4.2), given in Table 5.2. The very small nanocrystalline particles give rise to significant broadening of the peaks and also low intensity, making it difficult to determine the size precisely. The values are a therefore a crude estimation. Nonetheless, it shows that the synthesised catalyst crystallites are in the expected range of a few nm in diameter. Reference data from Johnson&Matthey for the HiSPEC 10000 catalyst suggests crystallite size being 2.66 nm, in agreement with the 3 nm measured. The synthesised catalysts have subsequently been utilised to make anodes and MEAs for fuel cell testing, accordingly to the method described in sections 4.6.1 and 4.6.2. The catalyst ink was made by first dissolving 0.2655 g polybenzimidazole (100 mesh polymer powder, Celanese) in 298.64 g concentrated formic acid (≥98%, Sigma-Aldrich) in a 500 mL beaker under magnetic stirring for an hour. 57.4 g of the solution was poured to a mixture of app. 1.7 g of the synthesised catalyst and 0.475 g phosphoric acid (≥85%, Sigma-Aldrich) in a 50 mL

Table 5.2: Elemental compositions of synthesised catalysts by EDS analysis on powders. The values are obtained based on relative intensities of metal peaks. The crystallite sizes based on Pt (111) peak at ~40 ° from XRD measurement, Figure 5.12.

	$Pt_{20}Ru_{80}/C$	$Pt_{33}Ru_{66}/C$	$Pt_{50}Ru_{50}/C$	$Pt_{66}Ru_{33}/C$	$Pt_{80}Ru_{20}/C$	HiSPEC 10000	$Pt_{60}Ru_{30}Sn_{10}/C$	$Pt_{60}Ru_{20}Sn_{20}/C$
Pt wt%	32	48	62	77	87	63	68	69
Pt at%	19	32	46	63	78	47	54	56
Ru wt%	68	52	38	23	13	37	23	15
Ru at%	81	68	54	37	22	53	35	23
Sn wt%							9	16
Sn at%							11	21
Crystallite size (nm)	1.4	1.7	3.4	4.5	5.5	3.0	3.0	5.0

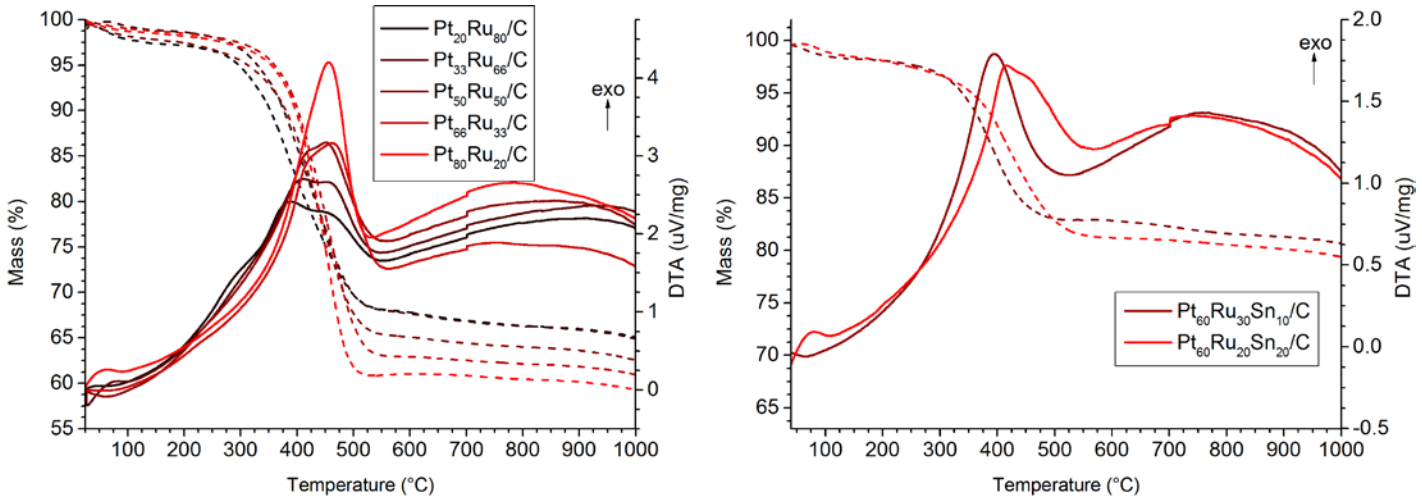

Figure 5.11: TGA and DTA analysis of the synthesised catalysts. Dotted lines represent TGA data and solid lines DTA.

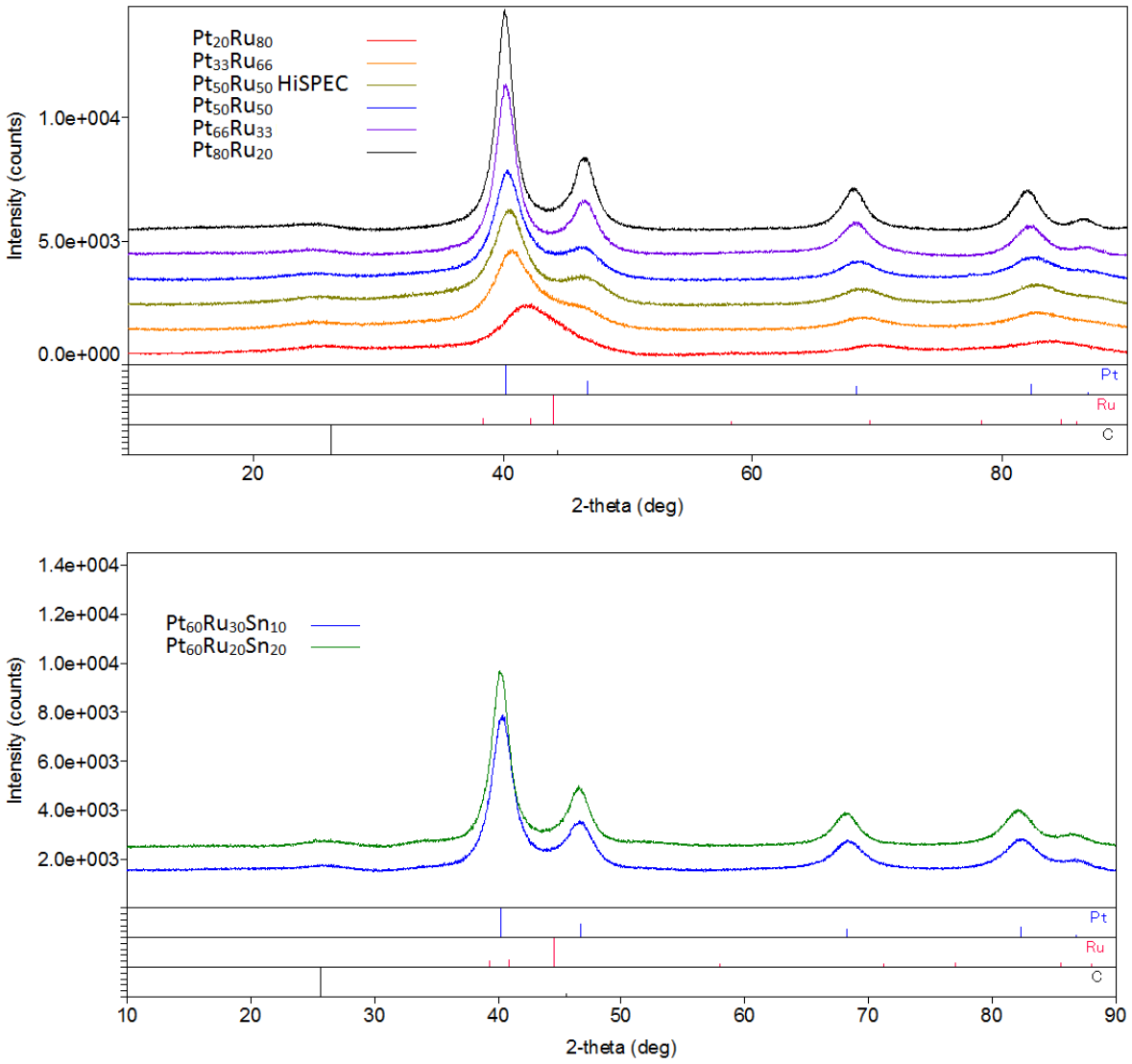

Figure 5.12: X-Ray diffractogramms of the synthesised catalysts. Top – 60 wt% Pt_xRu_y on 40 wt% C catalyst with J&M HiSPEC 10000 catalyst as a reference material. Bottom – 80 wt% $Pt_xRu_ySn_z$ on 20 wt% catalyst.

flask and sonicated for 5 hours. The final ratios between the ink components were 13.5, 8 and 0.012 for C:PBI, PA:PBI and C/solvent respectively. The resulting ink was not well dispersed, therefore high shear mixing was employed at 13500 rpm for 2 periods of 1 minute. After additional sonication to remove dissolved air the inks were used to make electrodes.

The resulting electrodes were used as anodes together with cathodes from Danish Power Systems with 1.02 mg_{Pt}/cm^2 loading (lot E-12-030) and phosphoric acid doped membrane, also from Danish Power Systems (lot M-11-9) with the doping level of 7.5 phosphoric acid molecules per PBI repeating unit and 39 µm undoped initial thickness. The MEAs were hot pressed for 3 minutes at 200 °C using pressing tools for correct alignment. The testing was done in the commercial fuel cell fixture with a run-in time of app. 24 h at 150°C and 200 mA/cm^2 with hydrogen as fuel. The cells were

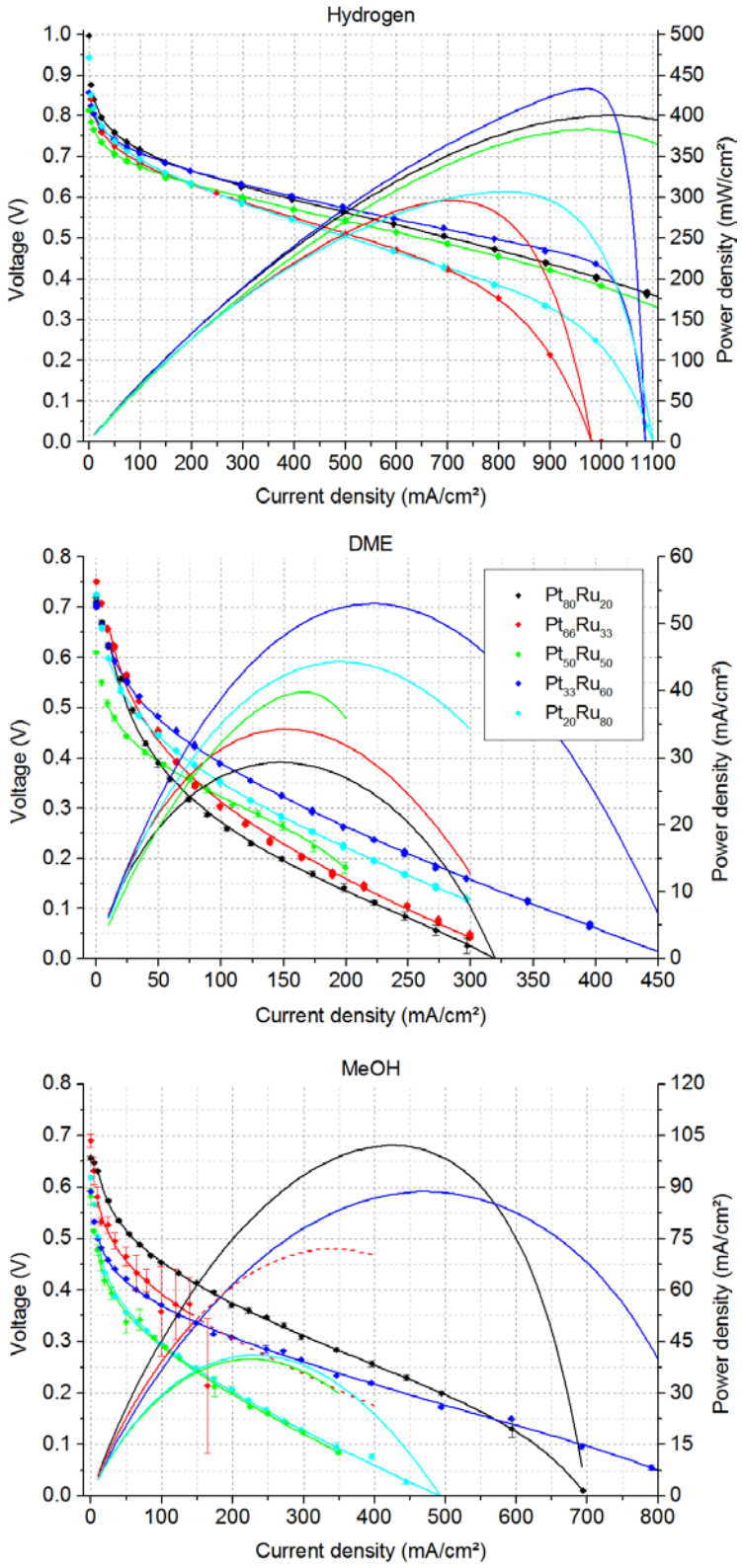

Figure 5.13: Effect of varying platinum ruthenium ratios in the anode catalyst on fuel cell performance with hydrogen, DME and MeOH as fuels. Points represent the measured values, points with error bars represent averaged voltage response at particular currents and the lines represent curve fittings. A 60 wt% metal on 40 wt% carbon black anode catalyst.

then heated to 200 °C and polarisation curves were obtained for 3 different fuels, first hydrogen for reference with λ_{fuel} = 1.3 on anode side and 905 mL/min air on the cathode side, then 32 mL/min DME and 0.07 mL/min H_2O flows on the anode side, corresponding to DME/water ratio of 3, and in the end 0.23 mL/min of 1:1 mixture of MeOH/water, corresponding to λ_{fuel} = 1 and λ_{air} = 2 at 1 A/cm² on the anode and cathode side respectively. The cells were left at 50 mA/cm² for 1 hour after the fuel changes to allow the system to purge with desired fuel and to allow the cell voltage to stabilise. The resulting polarisation curves and the curve fittings based on equation 5.2 can be seen on Figure 5.13.

From the hydrogen polarisation it is evident that apart from the different catalysts there are other effects affecting the voltage response of the cells. The linear parts of the polarisation curves are different, and since the membranes used are from the same batch variation should be minimal. This is not the case, and the variation could arise from non-optimal contact between the MEA components. Alternatively, as the MEAs were made in the same batch in one day, but the experiments were carried out over a course of app. 30 days the shelf life could have an effect. Even though the MEAs were kept in a sealed plastic bag, atmospheric air could still diffuse through and contribute with water vapour, altering the acid doping level of the PBI membrane and thereby the conductivity. The last possible explanation could be that a part of one or both electrodes were flooded with liquid to a certain degree, thereby adding to the thickness of the electrolyte, altering the ohmic resistance. At higher current densities there is evidence of mass transport limitation. Whether those arise from poor porosity of the catalyst particles below 50 nm scale, where the resolution of the SEM did not allow for a clearer picture, or non-optimal ink dispersion, is unknown. This was however of low importance, as the purpose of the study was the influence of the nature of the catalyst on oxidation of the fuel, which is mainly deduced at low current densities.

From the polarisation curves with dimethyl ether as fuel the MEA with $Pt_{50}Ru_{50}$/C deviated quite a lot from the others, with what resembles the shape of mass transportation losses already at 200 mA/cm². This might have been due to contamination with methanol-water mixture, present from the preceding MeOH measurement despite the usual purging time between the measurements. This would result in a performance similar to MeOH, until the residue was converted. A collapse of the catalyst layer structure can be excluded, as the cell showed adequate performance with the following hydrogen operation. When methanol was used as fuel, MEA with $Pt_{66}Ru_{33}$/C behaved erratically. The cell voltage was oscillating far more than usual and it was only possible to record the polarisation curve up to 175 mA/cm², where the voltage dropped off to 0 V. The reason for this was probably again faults in the fuel delivery. The recorded data were averaged and still used for curve fitting and extrapolation beyond 175 mA/cm². The curve fitting parameters are summarised on Figure 5.14.

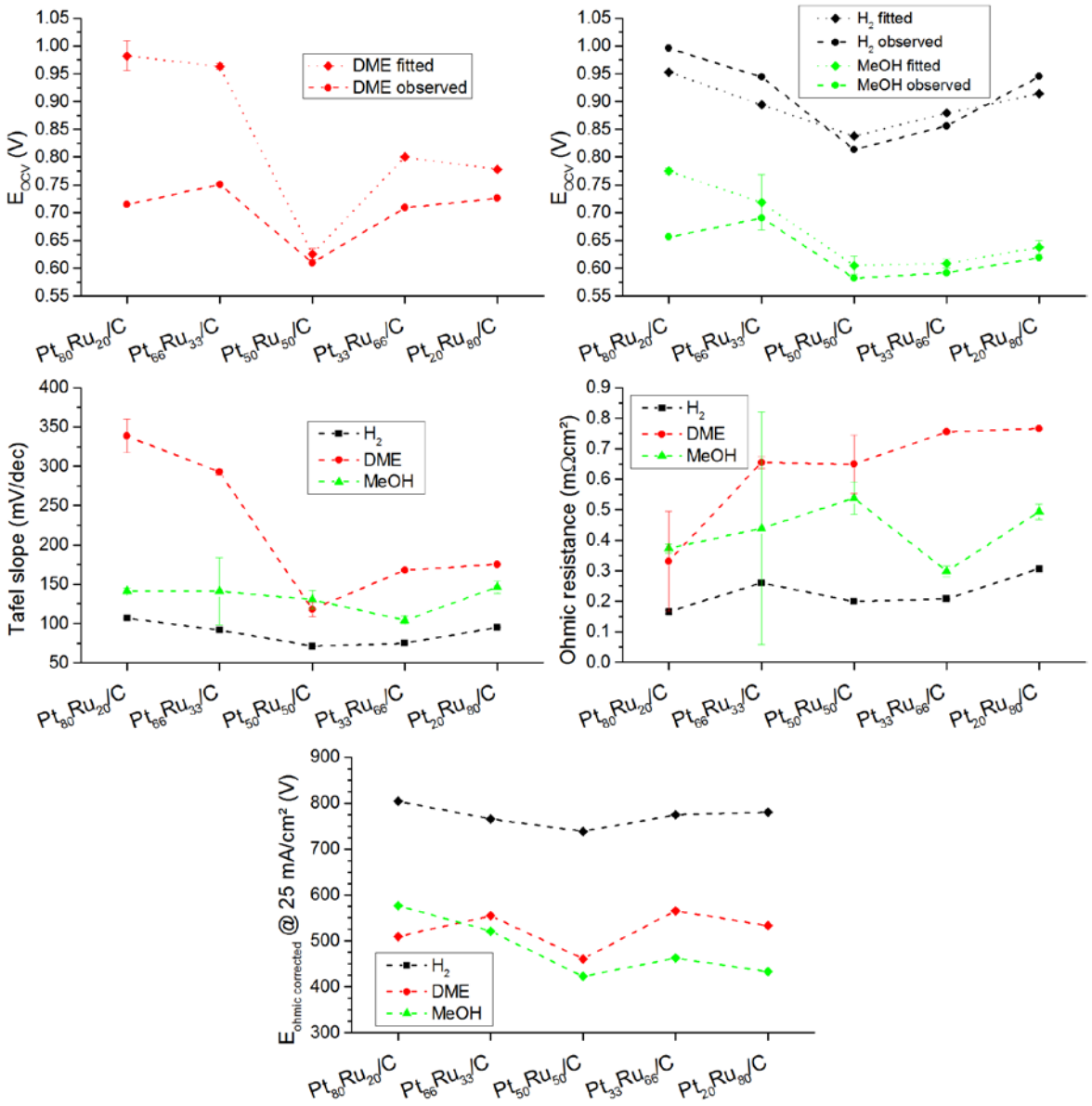

Figure 5.14: Parameters extracted from the i-V curves by fitting according to eq. 5.2 as functions of Pt:Ru ratio. A 60 wt% metal on 40 wt% carbon black anode catalyst.

There appears to be a trend in the open circuit voltages with a minimum at a 50-50 Pt-Ru ratio, independently of the type of fuel used. The trend has no scientific explanation, as the OCV is mainly dependent on fuel crossover or impurities present in the reactants. The nature of the electrolyte membrane governs the degree of fuel crossover and thus should in principle give a randomly distributed variation of OCVs with the same type of fuel. However, as the trend is the same for all 3 fuels experimented with indicates consistency between the fuel cell performance and the MEA used with respect to fuel crossover. There was a good agreement between the fitted parameters and the observed open circuit voltages for hydrogen and methanol as fuels, while there was a larger discrepancy when DME was employed as fuel. It could be partially explained by the fitting model not being very precise in the very low

current range and the fact that the fitting was performed on current density range from 10 mA/cm², but it could also imply that the fitted Tafel slope is too large and the OCV is fitted too high. When comparing the two parameters for $Pt_{80}Ru_{20}$/C and $Pt_{66}Ru_{33}$/C on Figure 5.14 it seems plausible that the latter is the case. The presented values are, however, those that gave the largest R^2 value for the overall fitting.

While there appears to be minima in Tafel slopes when operating with hydrogen and methanol as fuels, the values are quite close to each other, indicating that the metallic composition of the binary platinum-ruthenium catalyst does not play a crucial role in maximising the performance of the cell. It is surprising, that the lowest Tafel slope for hydrogen operated cells was recorded for $Pt_{50}Ru_{50}$/C. Since platinum is the best known metal to facilitate hydrogen oxidation one would expect the catalyst with the highest Pt-Ru ratio to give the lowest Tafel slope. This can again be a discrepancy in the fitting model, where the OCV and the Tafel slope are fitted too high in some cases. Another explanation can be crossover of the oxygen to the anode, where it is known to form peroxide on hydrogen-covered platinum catalyst in acidic systems at low potentials with subsequent reduction to water by reacting with OH groups [239, 240], whose formation is facilitated by Ru at low potentials.

A proper way to determine the activity of a given catalyst would be to make a Tafel plot and extract the exchange current density i_0, but in that case the i-V curves should be obtained by potentiostat, which has much higher resolution than the loads usually used for the general assessment of MEA performance. It was thus not possible to do so with the data available.

Ohmic resistance is not a very relevant parameter when comparing catalysts with the same metal loading, but it is interesting to see that it is dependent on the type of fuel used. The less complicated the oxidation of the fuel, the lower is the ohmic resistance. This is due to the oxidation reaction contributing the most to the energy generated closest to the electrolyte membrane in case of hydrogen. The resistance losses from the part of the layer closer to the GDL minimises the contribution of that part to the total current. As the oxidation mechanism of the fuel becomes more complicated, the outer parts of the catalyst layer contribute more to the total current, which is also the reason for increased catalyst loading in direct DME or methanol fuel cells compared to hydrogen fuel.

Figure 5.15 shows a compilation of polarisation curves and Figure 5.16 the extracted parameters for the investigation of 80 wt% metal on 20 wt% Vulcan XC72R carbon black catalyst with different platinum, ruthenium and tin ratios. It should be mentioned that the polarisation curves here were obtained with a laboratory power supply mentioned in section 4.6.3.1, which was imprecise in the low current region with OCV being measured by unplugging one of the current leads to the cell. Upon reconnection of the circuit the voltage would drop while the current reading would still be 0, which means some leak current was running, shifting the abscissa to the

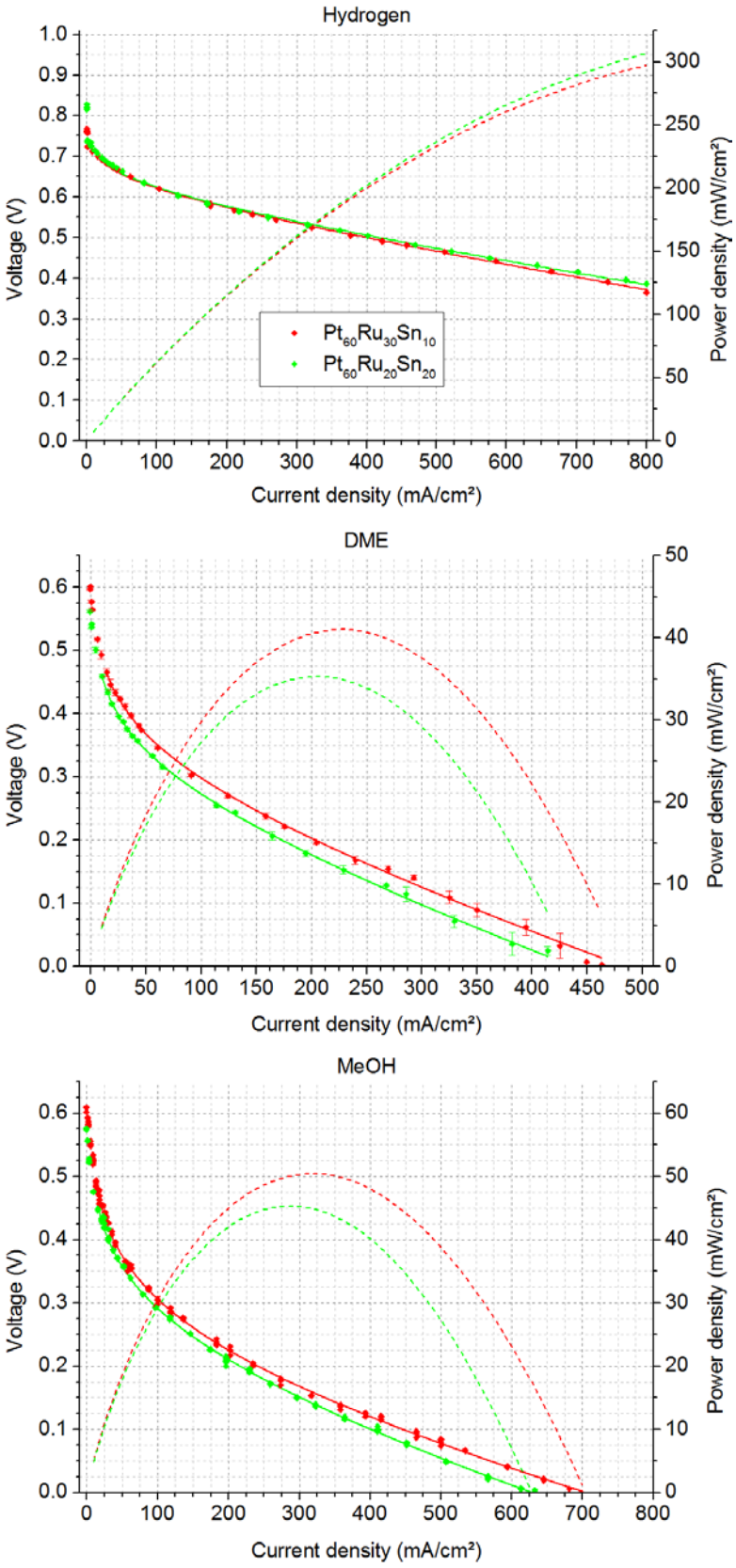

Figure 5.15: Effect of platinum, ruthenium and tin ratios in the anode catalyst on fuel cell performance with hydrogen, DME and MeOH as fuels. An 80 wt% metal on 20 wt% carbon black anode catalyst.

left. This has a more pronounced effect for hydrogen operation, as the degree of fuel crossover is less than for dimethyl ether and methanol operation, as can be seen from the low current density regions of the polarisation curves on Figure 5.15. In the experiments described previously in this section it was shown that addition of ruthenium has a positive effect on the performance of the cells. Likewise, addition of Ru and Sn to Pt catalyst increased cell voltages, but apparently Ru has a more pronounced effect, as the performance of the MEA with higher Sn and lower Ru contents was inferior. Because of the quality of the data caused by poor instrumentation available at the time of the experiments, the fitted Tafel slopes and the fitted open circuit voltages cannot be used to directly compare with the Pt_xRu_y investigation above, but should be looked at relatively to each other

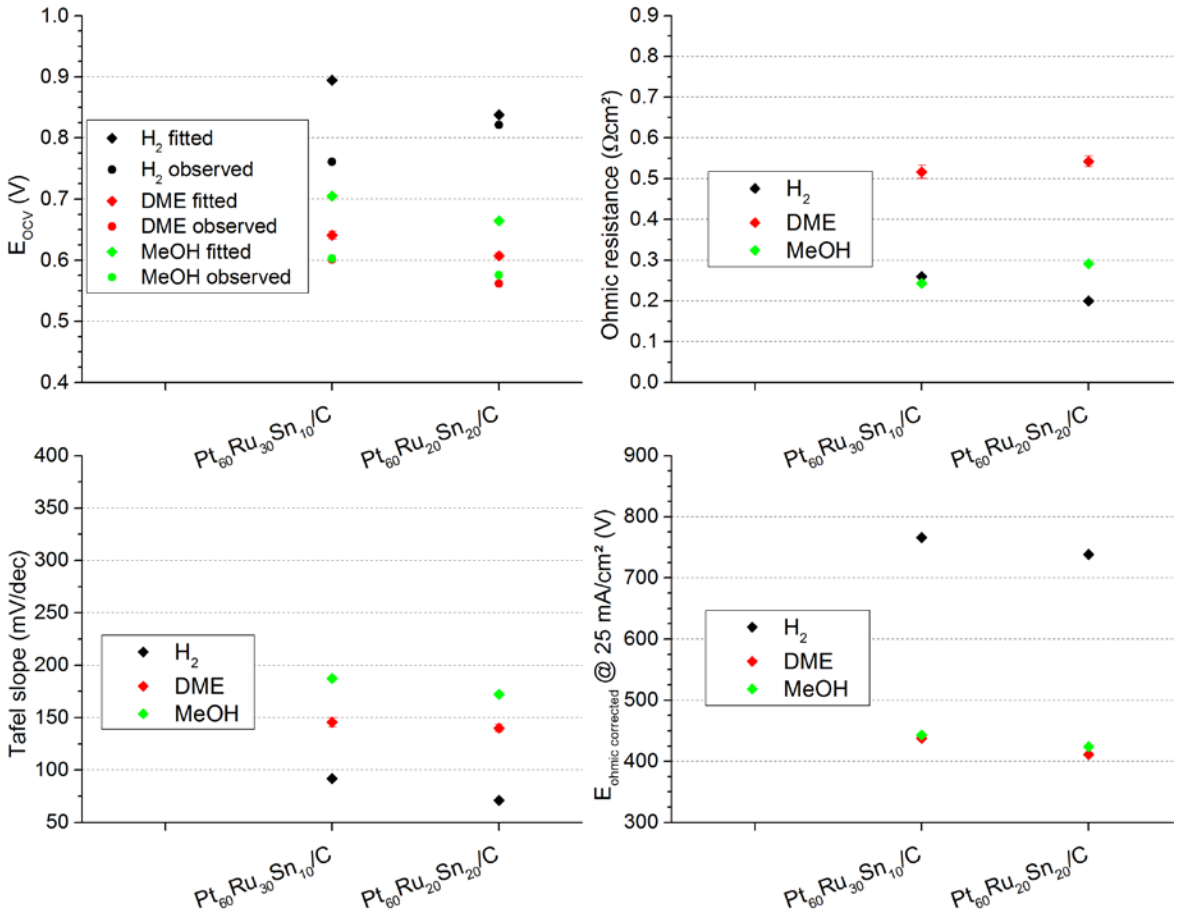

Figure 5.16: Parameters extracted from the i-V curves by fitting according to eq. 5.2 as functions of Pt:Ru:Sn ratios. An 80 wt% metal on 20 wt% carbon black anode catalyst.

5.2 Direct DME operation

The previous section dealt with how various components of an MEA affect the performance of direct dimethyl ether fuel cells. In this section the influence of such parameters as operating temperature or oxidant content will be presented, together with approaches on determining the mechanism of the DME oxidation by in- and ex-situ methods.

5.2.1 Temperature effect

An MEA was made by sandwiching the in-house made electrodes made by hand spraying with an in-house made PBI membrane doped in 85 wt% H_3PO_4 with a thickness of ~97 µm after doping. The electrodes had 4 mg/cm² 60 wt% $Pt_{50}Ru_{50}$ on 40 wt% carbon black from Johnson Matthey (lot 03-02082) catalyst on the anode and 0.7 mg/cm² of 60 wt% Pt on 40 wt% carbon black from Johnson Matthey catalyst on the cathode and ratios of 13.5, 8 and 0.012 for C:PBI, PA:PBI and C/solvent respectively on both electrodes. The MEA was hot pressed at 150 °C for 7 minutes at 100 kg per cm² electrode area pressure. The MEA was tested with only 1 hour of run-in time at 200 mA/cm² with hydrogen as fuel at desired temperature with fuel and air flows fixed to fulfil $\lambda = 1$ and $\lambda = 2$ at 1 A/cm² on anode and cathode sides respectively. The results are given on Figure 5.17. The testing was done using the laboratory power supply with low precision around OCV, which is why the abscissa is shifted to the left, which is most obvious for hydrogen operation, as there is a lesser degree of fuel crossover.

As evident from Figure 5.17, there is a considerable gain by increasing the temperature from 150 °C to 200 °C for all 3 fuels. Elevation of the temperature provides the molecules with additional energy to overcome the kinetic barrier, which is seen from the higher measured open circuit voltages and the higher cell potentials at low current density. The ohmic resistance was also found to decrease with temperature from 150 to 200 °C, as increasing the temperature increases conductivity. With the temperature limit of PBI-based cells at 200 °C measurements at 225 °C takes its toll with the cell degrading very fast, which can clearly be seen from the increased slope of the linear part of the curves. This is due to membrane dryout despite the additional waster supplied in case of direct DME and methanol operation and also polymerisation of phosphoric acid electrolyte, both of which decreases conductivity. Even though, the cell voltages in the low current density region are superior at higher temperature, which is expected.

5.2.2 Oxygen influence

An MEA was made by sandwiching the in-house made electrodes made with the spray robot with a PBI membrane (Danish Power Systems, M-11-263) doped in 85 wt% H_3PO_4 with initial thickness 43 µm and ~86 µm after doping. The electrodes had 4.02 mg/cm² 60 wt% $Pt_{50}Ru_{50}$ on 40 wt% carbon black from Johnson Matthey (lot 03-02082) catalyst on the anode and 0.7 mg/cm² of 60 wt% Pt on 40 wt% carbon black from Johnson Matthey on the cathode and ratios of 13.5, and 0.012 for C:PBI and C/solvent on both electrodes and PA:PBI ratio of 8 on the anode side. The MEA was hot pressed at 150 °C for 7 minutes at 100 kg per cm² electrode area pressure, 2.5 ton total force. The MEA was subjected to a run-in period at 200 mA/cm² with hydrogen as fuel and air as oxidant at 150 °C with $\lambda = 1$ and $\lambda = 2$ at 1 A/cm² on anode and cathode sides respectively. The fuel was then changed to DME and temperature increased to 200 °C. Polarisation curves with DME, MeOH and hydroen as fuels with air as oxidant were obtained in that order. Cathode gas supply was then changed to pure oxygen at the same flow rate, resulting in $\lambda = 10$ at 1 A/cm². Polarisation curves for the 3 fuels were

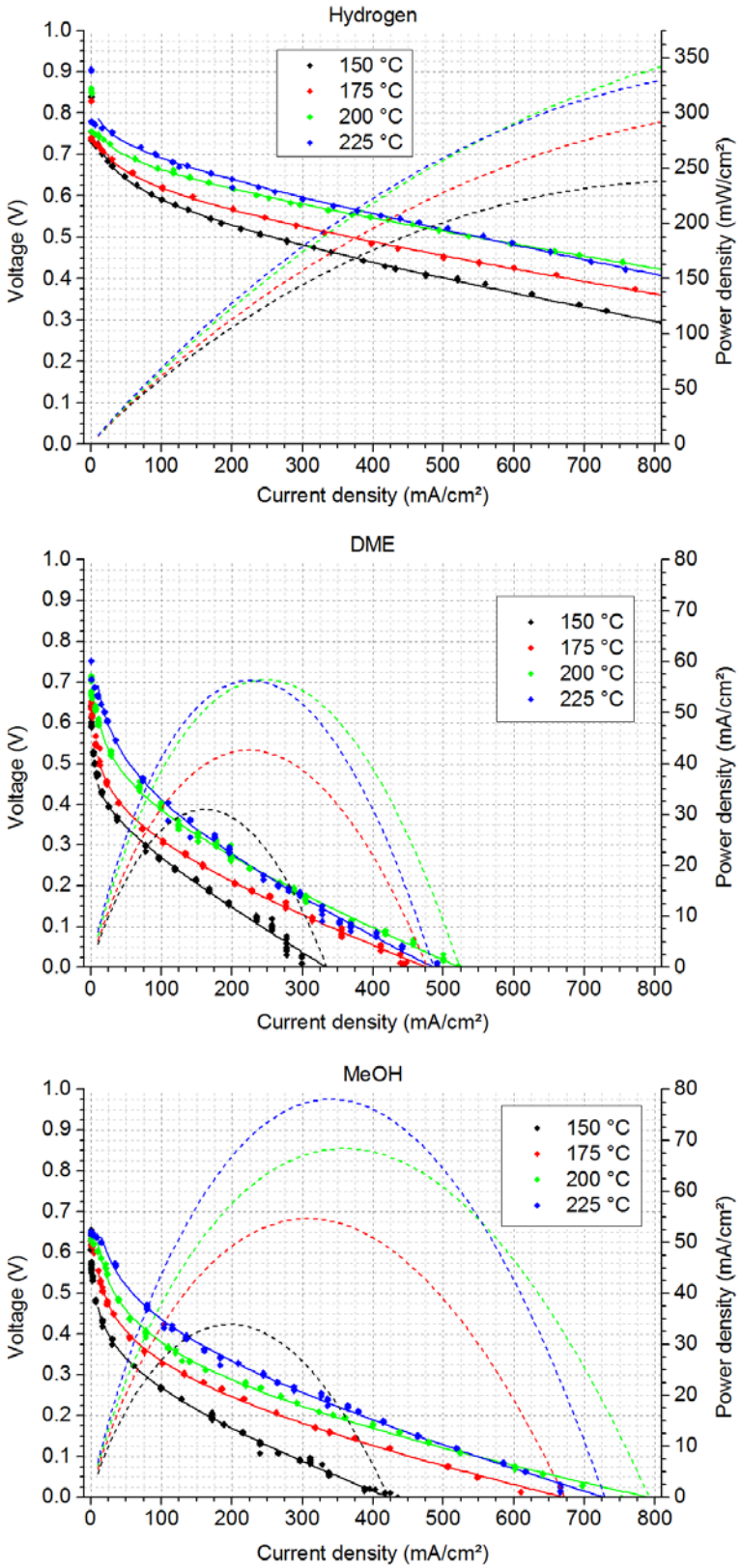

Figure 5.17: Effect of temperature on the performance of an MEA utilising 4 mg/cm² carbon supported $Pt_{50}Ru_{50}$ and 0.7 mg/cm² carbon supported Pt catalysts on anode and cathode sides respectively. Fuel and air flows fixed to λ = 1 and λ = 2 at 1 A/cm² on anode and cathode sides respectively. The axes are kept the same for DME and MeOH operation for comparing convenience.

obtained after an hour of stabilisation time. The results are given on Figure 5.18. The testing was done using the laboratory power supply with low precision in the ~0-35 mA/cm² current density range, with the OCV values obtained by disconnecting one of the current leads. The OCV value was thus the true voltage value, while the voltage response in the indicated current range was suppressed and distorted by the small leak current.

Polarisation curve fitting was performed based on equation 5.2 in the current density range indicated by the solid lines on Figure 5.18. The curve fitting parameters and chosen characteristic values are given in Table 5.3. The OCV increases as predicted by the Nernst equation, as the partial pressure of the reactant is increased. However the theoretical voltage increase predicted by Nernst equation at 200 °C would be only 16 mV, if the activity of the formed water is assumed to be 1. The observed OCV increased with 60 – 75 mV. Apart from the activity of water being different from 1, which would have dramatic effects on the voltage, another explanation could be proposed from consideration of increased exchange current density, decreased Tafel slope and fuel crossover. With the higher exchange current density due to increased partial pressure and the constant fuel crossover the difference between the reversible voltage and observed OCV would be higher for the hydrogen/air fed cell. The OCV increase for DME was higher than for MeOH, confirming the theory of methanol crossover having a larger effect on cathode potential. The Tafel slope for DME and MeOH as fuels was increasing with increased oxygen partial pressure, showing a change in mechanism. It can be that in this case the oxygen crossover to the anode side has a more pronounced effect than for hydrogen fuelled operation. The ohmic resistance was decreasing probably due to more catalyst particles being active because of reduced dilution effect of the oxidant. Another explanation could be the slightly increased proton conductivity due to the higher hydration of the membrane. With the increased oxygen partial pressure and the same total gas flow rate on the cathode, there was more water formed, but the rate of water removal stayed the same, thus increasing the hydration level of the membrane and thereby conductivity. As a consequence of the positive effect of oxygen as oxidant the peak power density was increased by 25 % for DME and 35 % for methanol, with the higher gain of the latter again confirming the larger degree of fuel crossover.

Table 5.3: Polarisation curve parameters from the investigation of effect of oxidant type on fuel cell performance. (*) R corrected.

Fuel	Oxidant	OCV observed	OCV fitted	Ohmic resistance	Tafel slope	E at 25 mA/cm²(*)	Peak power density
		V	V	Ωcm²	mV/dec	V	mW/cm²
Hydrogen	Air	0.870	0.894	0.31	99	0.756	288
	Oxygen	0.941	0.936	0.22	93	0.807	396
Dimethyl Ether	Air	0.770	0.889	0.46	214	0.596	66
	Oxygen	0.846	0.961	0.44	222	0.661	83
Methanol	Air	0.653	0.789	0.35	175	0.532	78
	Oxygen	0.719	0.876	0.26	199	0.593	105

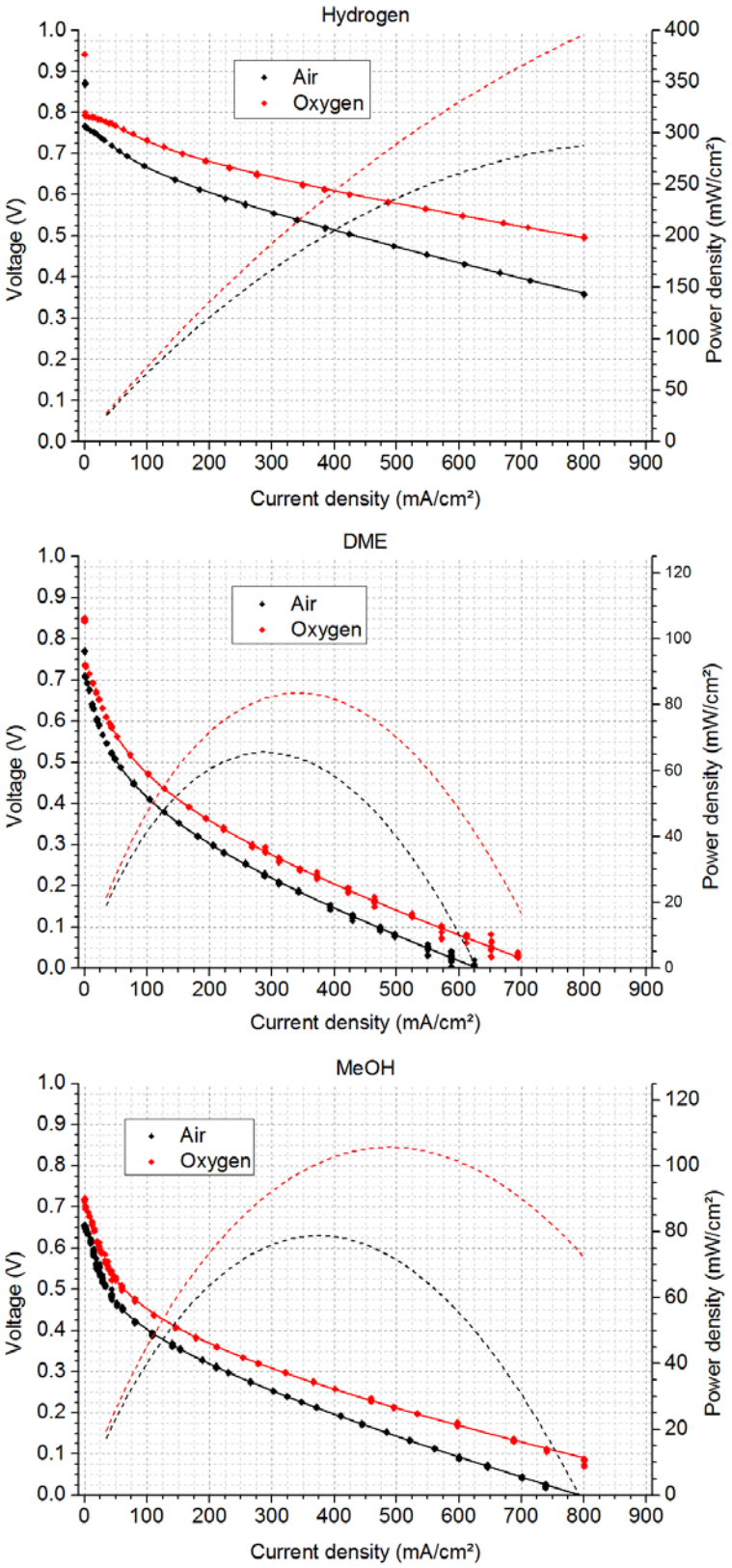

Figure 5.18: Effect of oxygen concentration on the performance of an MEA utilising 4 mg/cm² carbon supported $Pt_{50}Ru_{50}$ and 0.6 mg/cm² carbon supported Pt catalysts on anode and cathode sides respectively. Fuel and air flows fixed to λ = 1 and λ = 2 at 1 A/cm² on anode and cathode sides respectively. The axes are kept the same for DME and MeOH operation for comparing convenience.

5.2.3 Impedance spectroscopy

As already described in section 4.5, electrochemical impedance spectroscopy is a great tool to evaluate the performance of an MEA under operation, adding detailed information to that extracted from polarisation curves by separation of contributions from different MEA components without the need for a reference electrode. Although a great tool, the technique should be approached with great care, as any instability of the system would disturb the measurements. Additionally, some preliminary knowledge about the measured system is required in order to propose an equivalent circuit without adding too many elements, which may provide the best fitting of the obtained data, but have no physical meaning. In this section an EIS analysis performed on an arbitrarily chosen MEA with different fuels at 200 °C will be presented.

The MEA used was utilizing the in-house made 60 wt% $Pt_{66}Ru_{33}$ on 40 wt% Vulcan XC72R carbon catalyst. For the details regarding the catalyst and MEA preparation procedure and cell operation conditions refer to section 5.1.3. The impedance spectra at different current densities of 10, 40, 70, 100 and 200 mA/cm² were recorded immediately after the polarization curves presented in section 5.1.3. The changing of the fuels was done in the sequence H_2 (a) – DME (a) – MeOH – DME (b) – H_2 (b). The impedance spectra for DME (a) measurement were very similar to DME (b) at high and intermediate frequencies, but were influenced by fuel flow fluctuations at low frequencies and were therefore not used for further analysis. The spectra were obtained in 10 kHz – 0.1 Hz frequency range with 10 mV amplitude, 10 pts/dec sampling rate and data quality settings averaging 5 full cycles to yield the final values. Nyquist plots for the measurements can be seen on Figure 5.19.

Before fitting of the spectra to equivalent circuits, as described in section 4.5, the basic knowledge about impedance spectroscopy allows to evaluate the ohmic

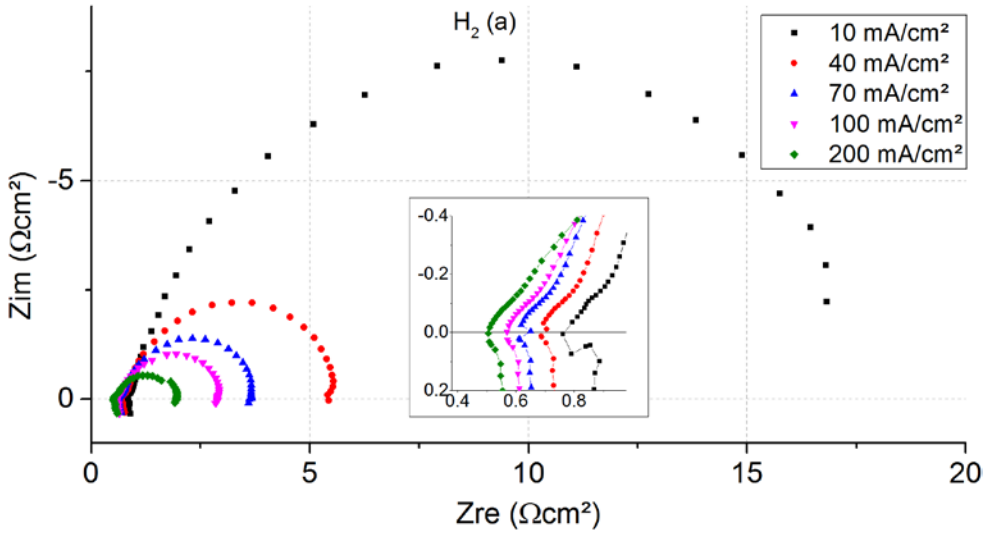

Figure 5.19 is continued on next page.

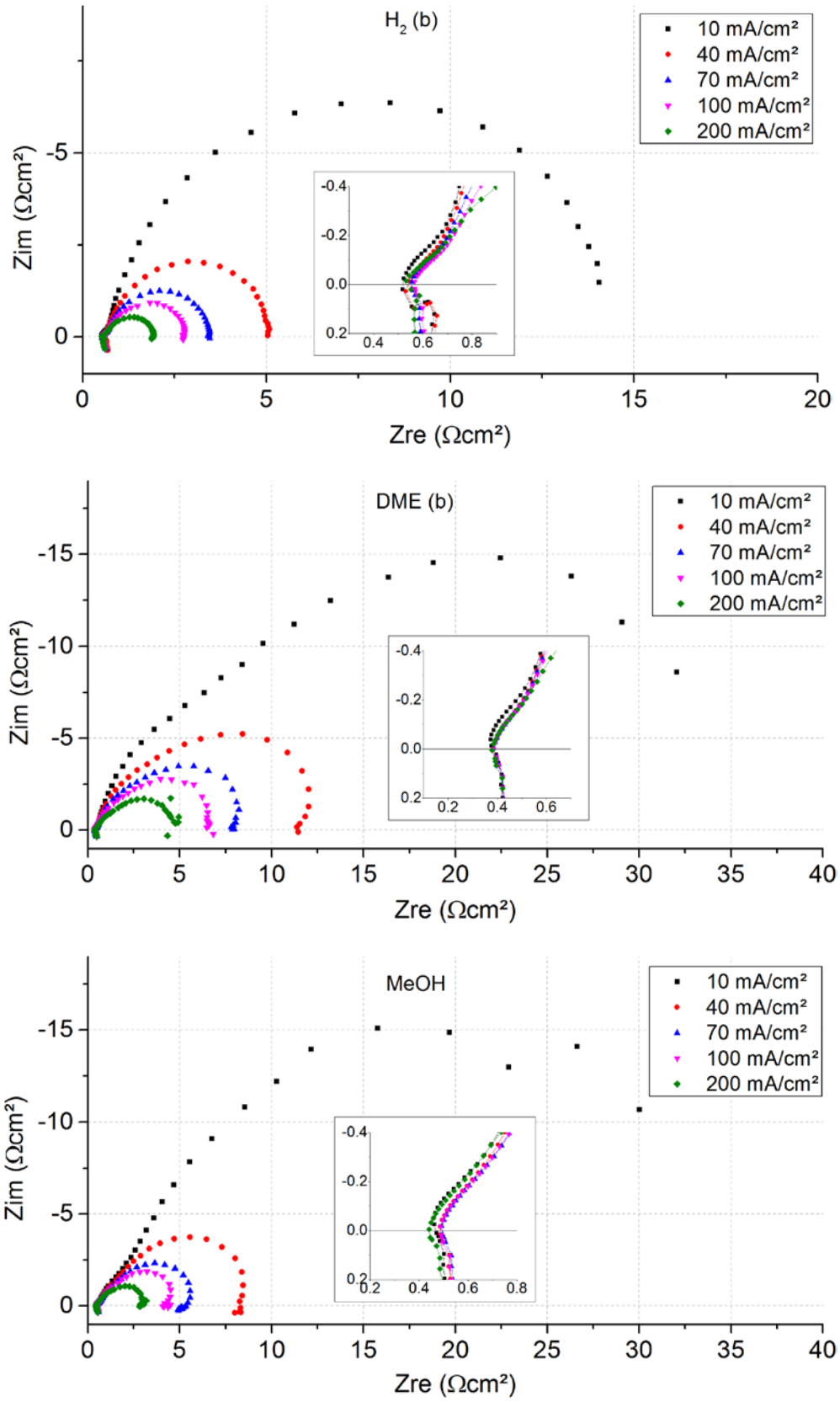

Figure 5.19: Nyquist plots with different fuels at different current densities and 200 °C operating temperature. Insets show magnification at high frequencies.

resistance of the electrolyte based on the spectra offset from the ordinate. Here an interesting observation was made when initially operating in hydrogen fuel mode. From the inset in the top left graph on Figure 5.19 it can be seen that the intersection with the abscissa is shifting from 0.79 to 0.50 Ωcm² with increasing current density from 10 to 200 mA/cm². This shows that the conductivity of the electrolyte is not a constant value, but is dependent on the hydration of the membrane, as more water is formed with increasing current. This information would not be available form a simple polarisation curve. Additionally it shows that one of the arguments about advantages of HT-PEM fuel cells regarding complete independency from the water management is not entirely correct, which has though no importance in practical applications. The phenomenon is not present in case with DME and MeOH fed operation, as sufficient amounts of water were present in the fuel stream to fully humidify the membrane. There was no significant shift in the final hydrogen fed operation mode (H_2 (b) on Figure 5.19), showing that the hydration effect is persistent over several hours.

The ohmic resistances obtained by the fitting of the polarisation curves and the ones obtained by impedance were somewhat close to each other, as can be seen from Table 5.4. It should be noted that the values obtained by impedance are without correction for the inductance, making them appear larger if the resistance is small, which can partially explain the discrepancy between the methods for hydrogen fuel operation. In case with DME the value obtained by polarisation curve was larger than the one recorded by impedance spectroscopy. This can be explained by the model failing to recognise that the exponential term at higher current densities can also be approximated to a linear function, thus taking part of the charge transfer resistance into the ohmic resistance term. To fully rely on the data obtained by impedance spectroscopy the spectra should be corrected for the inductance contribution, but this is made difficult by the instrumental error occurring systematically at the high frequencies, making the data between 10 and 1 kHz unreliable.

Table 5.4: Comparison of ohmic resistance values for an MEA operated with different fuels obtained by fitting of the polarisation curves and impedance measurements.

Fuel	Ohmic resistance from i-V curve	Ohmic resistance from impedance
	Ωcm²	Ωcm²
H_2 (b)	0.26	0.54
DME (b)	0.66	0.38
MeOH	0.44	0.47

To verify the impedance data Kramers-Kronig (K-K) transformation tests were made using a program “Kramers-Kronig test for Windows” by B.A. Boukamp. K-K relations prescribe that the real and imaginary part of the impedance are interdependent, provided that the measured response is only due to the applied perturbation, that the response is linear and the system is in steady state and does not change over time or oscillate beyond the termination of the perturbation signal. Additionally, a set of

adequate initial values is not required for data validation [241, 242]. Thus Kramers-Kronig relations are very effective in testing for data influenced by non-steady-state behaviour. A set of K-K test results from impedance spectra recorded on an MEA running with different fuels, H_2 (b), DME (b) and MeOH at 100 mA/cm² load and 0.709 V, 0.393 V and 0.390 V respectively is given in Figure 5.20.

H_2 (b) operation

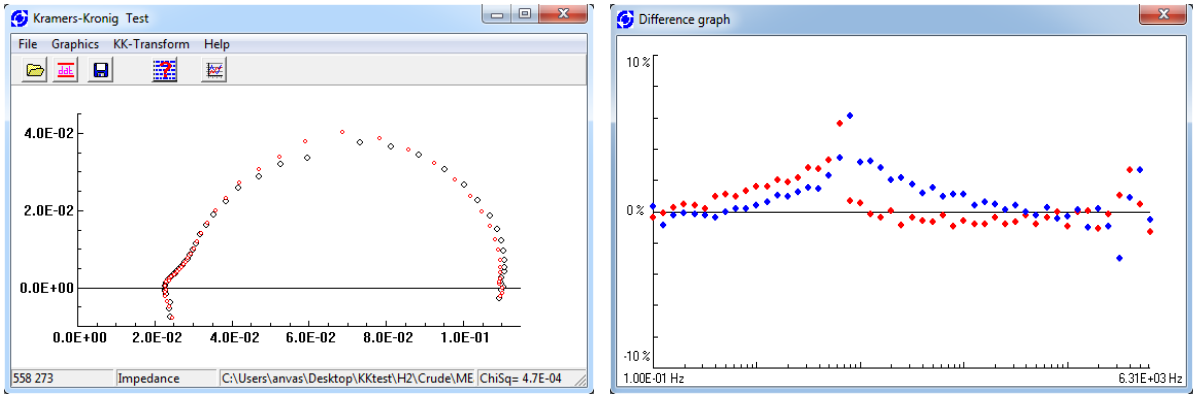

DME (b) operation

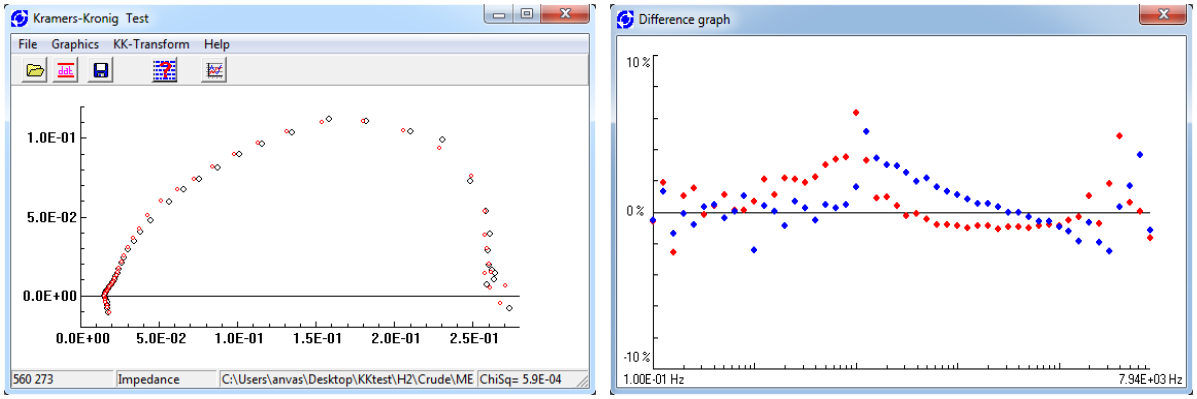

MeOH operation

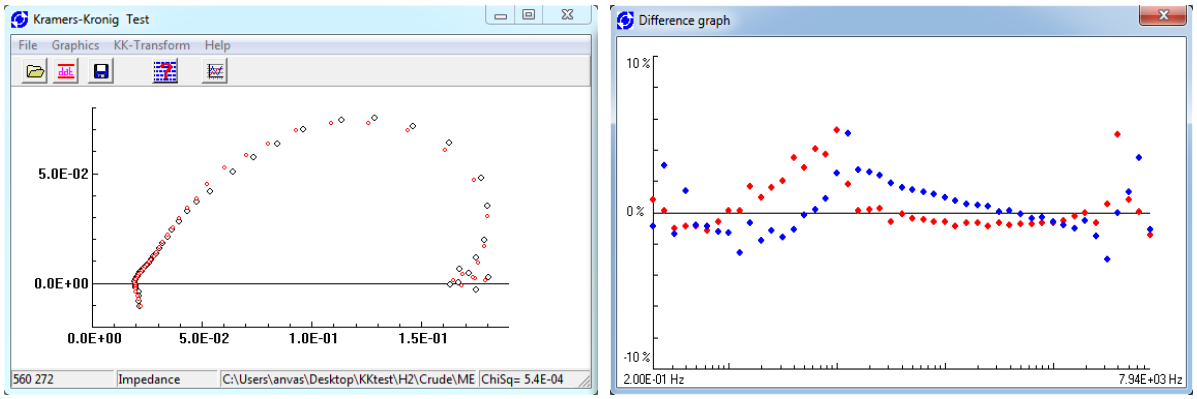

Figure 5.20: Screen shots of the Kramers-Kronig tests for an MEA operating with different fuels and air at ambient pressure at 100 mA/cm². Left spectra show the impedance values with the real and imaginary parts of the resistance in Ω on the abscissa and ordinate respectively. The measurement values are represented by the black circles and the K-K transformed by red dots. On the right the respective residual plots are given with the frequency in Hz on the abscissa and the relative error on the ordinate. The red dots represent the real part residuals and the blue dots the imaginary part differences.

As evident from Figure 5.20, the studied system deviated quite significantly from K-K behavior, especially at high frequencies, which has already been attributed to instrumental error, but also in 1 - 11 Hz region for all 3 fuels. This was also true for all recorded spectra (not shown). A deviation at 50 Hz would be expected if the studied system was not sufficiently well isolated from the main grid, but this is not the case. Whether the error was caused by the potentiostat, the load or any auxiliary equipment is unknown. The error due to any non-steady-state originating from the MEA performance can be excluded, as it was present with all 3 fuels and at different current densities.

Despite the relatively poor quality of the obtained data, as deemed by K-K test, an attempt on fitting the equivalent circuits was done nonetheless. The χ^2 values for the fittings should be in the range, but not less than the ones obtained by the K-K tests (given in the bottom right corner of the impedance plots on Figure 5.20, "ChiSq"). The equivalent circuit for the H_2/air cell has already been discussed in section 4.5. Because of the large error at high frequencies the data were trimmed to contain only negative values for the imaginary resistance in that frequency range, thereby also removing the need for the inductive term to fit the wiring contribution. The ideal capacitors used initially to fit the capacitance of the porous electrodes were replaced with constant phase elements, as they gave a better fit. The exponent factors were close to or in many cases also equal 1, thus showing only slight deviations from ideal capacitors. The resulting equivalent circuit used to fit the impedance spectra for H_2 operation can be seen on Figure 5.21 a.

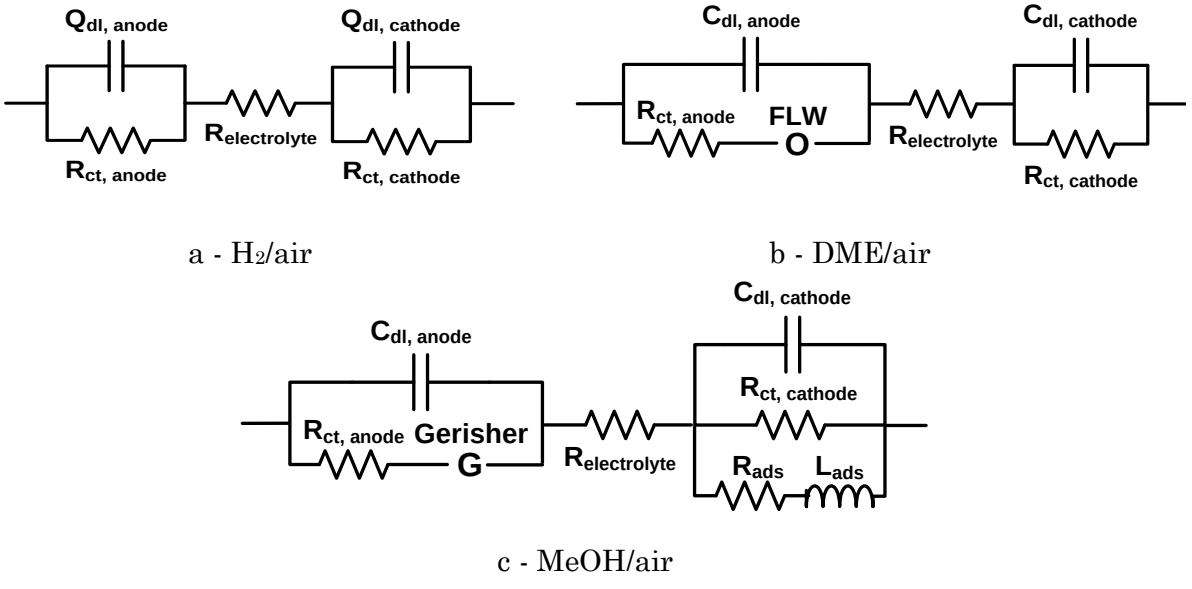

a - H_2/air

b - DME/air

c - MeOH/air

Figure 5.21: Equivalent circuits used to fit the impedance data.

Direct methanol fuel cells are relatively well studied, also by means of electrochemical impedance spectroscopy [224, 243, 244]. The loop observed at low frequencies on the impedance spectra is usually attributed to adsorption of methanol and/or CO on the platinum catalyst of the cathode, originating from the fuel crossover. To model this in

terms of equivalent circuits, a resistor and an inductor in series are added parallel to the cathode charge transfer resistance and capacitance. Another feature of the obtained spectra for direct methanol operation at medium frequencies, the beginning of the large semicircle appears to be somewhat linear, which usually indicates bonded diffusion. Taking into consideration the high temperature of operation, 200 °C, opening up the possibility of the fuel to reform internally in the cell, a Gerischer element was added to the equivalent circuit for the anode side, which is used to describe a diffusion process coupled with a chemical reaction [245, 246]. The Gerischer also gave the best fitting compared to other types of bonded diffusion elements. The resulting equivalent circuit for the MeOH/air cell is given on Figure 5.21 c.

As mentioned in section 3.2.2 the information on direct DME PEM FC impedance is very limited, mostly using EIS as a tool to qualitatively verify improvement of parameters affecting fuel delivery e.g. by alteration of GDL or flow field structure [191, 198, 199, 201], and only one paper gives an attempt on equivalent circuit fitting [195]. The authors of the latter observed an inductive loop at low frequencies, like the one for DMFCs. Some indication of the phenomenon was observed in the conducted measurements at 40 and 70 mA/cm², as evident from Figure 5.19, but it was chosen not to include the element into the equivalent circuit. Based on the quality of the data due to instability of the system at low frequencies the observed feature could indeed be inductive behaviour, but also possibly another semicircle or simply noise. With the curvature of the larger semicircle expressing a linear part, like for the DMFC operation, the Gerischer element was initially included to reflect the assumed internal reformation of the fuel, but it gave very poor fits. It can be that 200 °C was enough to initiate reforming of methanol, but not DME, which usually has a higher reforming temperature. Other types of bonded diffusion elements were tried to account for the deviation from the semicircle shape, where Finite Length Warburg (FLW) gave the best fit. The presented fittings were done with the equivalent circuit seen on Figure 5.21 b.

It should be noted that the performed analysis was based on very simple equivalent circuits proposed from the previous knowledge and assumptions on the cell processes and the shape of untreated Nyquist plots. It should therefore by no means be taken as an in-depth description, but rather as an indication. Further work is needed in order to fully map the electrode processes, with improvement of system stability to obtain more reliable data and an additional and more detailed treatment of the results by distribution of relaxation times (DRT) technique prior to proposition of equivalent circuits, as it would e.g. enable resolving two semicircles appearing as one due to close time constants. More detailed measurements with varying conditions like partial pressures of the reactant gasses or changing the cathode gas feed to hydrogen would also greatly help on resolving the anode and cathode contributions.

The equivalent circuit fittings were done using the software “ZSimpWin” from Princeton Applied Research with prior removal of the datasets containing positive

values of the imaginary parts of impedance at high frequencies because of the already described instrumental error. The values for resistance read from the Nyquist plots were fed as initial values for the fitting. The fitting values for the obtained impedance spectra are given in Table 5.5 - Table 5.7.

Table 5.5: Equivalent circuit fitting data for the H_2 (b)/air operated cell.

Obtained at		10 mA/cm² 0.808 V	40 mA/cm² 0.755 V	70 mA/cm² 0.728 V	100 mA/cm² 0.709V	200 mA/cm² 0.664 V
$R_{electrolyte}$	Ω cm²	0.54	0.56	0.57	0.58	0.55
$R_{ct,\ anode}$	Ω cm²	0.17	0.16	0.16	0.18	0.14
$C_{dl,\ anode}$	mF/cm²	4.61	5.45	4.91	4.64	3.80
$R_{ct,\ cathode}$	Ω cm²	13.79	4.32	2.70	1.99	1.21
$C_{dl,\ cathode}$	mF/cm²	9.40	12.27	12.34	12.96	12.14
χ^2		1.19E-3	8.68E-4	1.04E-3	1.05E-3	9.82E-4

From Table 5.5 it can be seen that the resistance of the electrolyte is not changing significantly with increasing current and also the charge transfer resistance and the capacitance for the anode do not vary much, showing that the hydrogen electrode is not polarised a lot with the increasing current. The double layer capacitance of the cathode is also more or less constant, but the resistance is decreasing with increasing current, as expected. From the expressions for the frequency and the charge transfer resistance the experimental Tafel slope b for the oxygen reduction reaction can be determined:

$$f = \frac{1}{2\pi R_{ct} C_{dl}} \tag{5.3}$$

$$R_{ct} = \frac{d\eta_{ct}}{di} = \frac{d}{di}\left(a + b\log(i)\right) = {}^{b}/_{i} \tag{5.4}$$

where f is the frequency, R_{ct} is the charge transfer resistance, C_{dl} is the capacitance of the double layer and η_{ct} is the electrode overpotential. As the capacitance was constant, by plotting the resistance as a function of the reciprocal current density, a

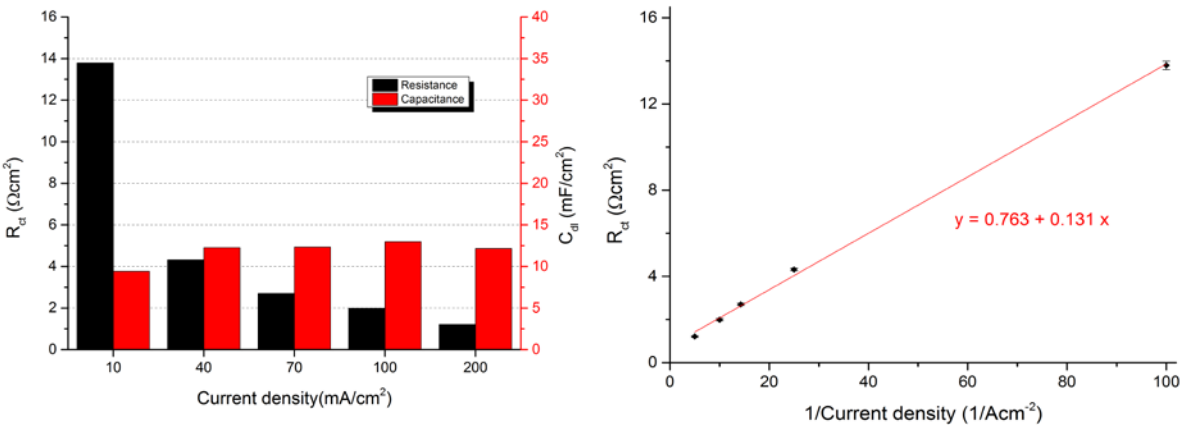

Figure 5.22: Left - fitted cathode impedance parameters of the H_2(b)/air operated cell. Right – Tafel slope determination.

linear relation can be observed with a slope that equals Tafel slope, which can be seem from Figure 5.22. The obtained value of 131 mV/dec is very close to the 120 mV/dec mentioned in section 2.4.3 regarding the ORR.

Table 5.6: Equivalent circuit fitting data for the DME (b)/air operated cell.

Obtained at		10 mA/cm² 0.614 V	40 mA/cm² 0.509 V	70 mA/cm² 0.447 V	100 mA/cm² 0.393 V	200 mA/cm² 0.264 V
$R_{electrolyte}$	Ω cm²	0.41	0.40	0.40	0.40	0.39
$R_{ct,\ anode}$	Ω cm²	0.002	0.031	0.09	0.11	0.16
$C_{dl,\ anode}$	mF/cm²	4.00	2.31	2.75	2.90	3.26
$O\text{-}Yo_{FLW,\ anode}$	$sek^{0.5}$/ Ω cm²	0.064	0.137	0.158	0.162	0.185
$O\text{-}B_{FLW,\ anode}$	$sek^{-0.5}$	0.37	0.24	0.20	0.19	0.15
$R_{ct,\ cathode}$	Ω cm²	27.68	9.80	6.39	5.01	3.24
$C_{dl,\ cathode}$	mF/cm²	23.78	14.7	14.94	16.67	24.53
χ^2		1.61E-3	3.98E-3	3.15E-3	2.19E-3	1.23E-3

Table 5.7: Equivalent circuit fitting data for the MeOH/air operated cell.

Obtained at		10 mA/cm² 0.533 V	40 mA/cm² 0.450 V	70 mA/cm² 0.410 V	100 mA/cm² 0.390 V	200 mA/cm² 0.330 V
$R_{electrolyte}$	Ω cm²	0.46	0.50	0.50	0.50	0.46
$R_{ct,\ anode}$	Ω cm²	0.05	0.11	0.16	0.17	0.17
$C_{dl,\ anode}$	mF/cm²	16.12	2.02	2.17	2.27	2.80
$G\text{-}Yo_{Gerischer}$	$sek^{0.5}$/ Ω cm²	0.092	0.118	0.141	0.153	0.201
$G\text{-}Ka_{Gerischer}$	sek^{-1}	13.28	28.25	38.57	43.03	78.14
$R_{ct,\ cathode}$	Ω cm²	29.55	6.93	4.17	3.30	2.10
$C_{dl,\ cathode}$	mF/cm²	25.35	19.41	17.73	16.97	16.38
$R_{ads,\ cathode}$	Ω cm²	NA	19.36	11.09	9.00	8.53
$L_{ads,\ cathode}$	Henri cm²	NA	19.85	4.73	1.75	0.77
χ^2		2.54E-3	1.51E-3	1.11E-3	1.30E-3	1.50E-3

The equivalent circuit fittings for the DME and MeOH operated cell resulted in quite large standard errors for the anode parameters, especially at 10 mA/cm² measurements, probably due to the magnitude of the cathode contributions making it very difficult to resolve the data at high frequencies. This is the reason why they deviate so much from the rest of the fitting series. Apart from that, the R_{ct} and C_{dl} for the anode were not changing significantly, and were quite similar to the values obtained for the hydrogen fed operation, showing either that the assignment is not correct and the parameters in reality describe other phenomena, or that the proposed internal reforming of the fuel indeed occurs and therefore reflects hydrogen oxidation on the anode. For the methanol operation the inductance due to fuel crossover on the cathode side was decreasing with increasing current, as expected. The R_{ct} for the cathode decreased somewhat, but was still much larger than for hydrogen or DME operation, showing that the fuel crossover still has a significant effect, or that there is a resistance of another process involved, which may be identified by DRT technique and thus properly resolved and estimated. For the DME operation the situation is different. While starting at the same magnitude as for MeOH, the resistance decreased rapidly to a level on par with H_2 operation, confirming the smaller fuel

crossover effect. The admittance of the Gerischer and FLW elements for MeOH and DME operations respectively were increasing, expressing a less restricted diffusion with increasing current density.

Again, it is stressed that the performed impedance measurements and the equivalent circuit fittings did not have the purpose to suggest a fulfilling description of the processes occurring in the fuel cell under operation at this point, but were rather performed to confirm the information extracted from the polarization curves, e.g. electrolyte resistance, and to illustrate that a reference electrode can be avoided. For the latter the MEA must be studied more carefully by varying one parameter at a time and analyzing the response, before an attempt to fit the data to equivalent circuits, which could be part of a future work.

5.2.4 Gas chromatography

As an attempt to map the processes happening on the anode side of the direct dimethyl ether and direct methanol fuel cells at elevated temperature the anode exhaust gas from the cells at different currents was collected and sent to analysis by gas chromatography using a thermal conductivity detector (TCD) for identification of lighter molecules, such as elementary gasses, CO and CO_2, and a flame ionisation detector (FID) for detection of molecules with carbon-hydrogen bonds, such as methane, methanol and dimethyl ether.

An electrode with 4 mg/cm² 60 wt% $Pt_{50}Ru_{50}$ on 40 wt% carbon black from Johnson Matthey (batch 140496001) catalyst and ratios of 13.5, 8 and 0.012 for C:PBI, PA:PBI and C/solvent respectively was made by spraying robot and used as an anode to make an MEA (MEA-12-B109 by Danish Power Systems). The MEA was run-in over night at 160 °C with hydrogen and air flows fixed to $\lambda = 1$ and $\lambda = 2$ at 1 A/cm² on anode and cathode sides respectively while 200 mA/cm² were drawn from the cell. The temperature was then increased to 200 °C and a series of polarisation curves were obtained using hydrogen, DME, MeOH, DME and hydrogen again as fuels. The flows of DME and MeOH were fixed to satisfy $\lambda = 1$ at 1 A/cm² with the water stoichiometry of 3 and 1 for the respective fuels. The air flow was fixed at $\lambda = 2$ at 200 mA/cm² for the low current densities from 0 – 200 mA/cm² and increased to sustain $\lambda = 2$ at higher currents.

After obtaining satisfactory cell responses with the 3 fuels, showing that the cell was functioning properly, as seen from polarisation curves on Figure 5.23 for H_2 a, DME a and MeOH, the anode exhaust was connected to gas bags dead-end and the cell left at 0, 200 and 600 mA/cm² with MeOH as fuel to collect the samples. Subsequently the gas was changed to DME and the gas bags filled at OCV and 200 mA/cm². The cell voltage was then decaying rapidly and the last sample was obtained at 400 mA/cm² instead of 600. To ensure that the voltage decay was due to sudden MEA degradation and not a temporarily blockage of the gas supply, as has been observed previously, polarisation curves for DME and hydrogen as fuels were recorded, seen as DME b and H_2 b on Figure 5.23. The performance loss was probably due to the pressure difference

between the anode and cathode resulting in a detachment of some catalyst from the membrane, as the gas collection resulted in a dead-end on the anode side. The collected samples were sent to GC analysis nonetheless (Technological Institute).

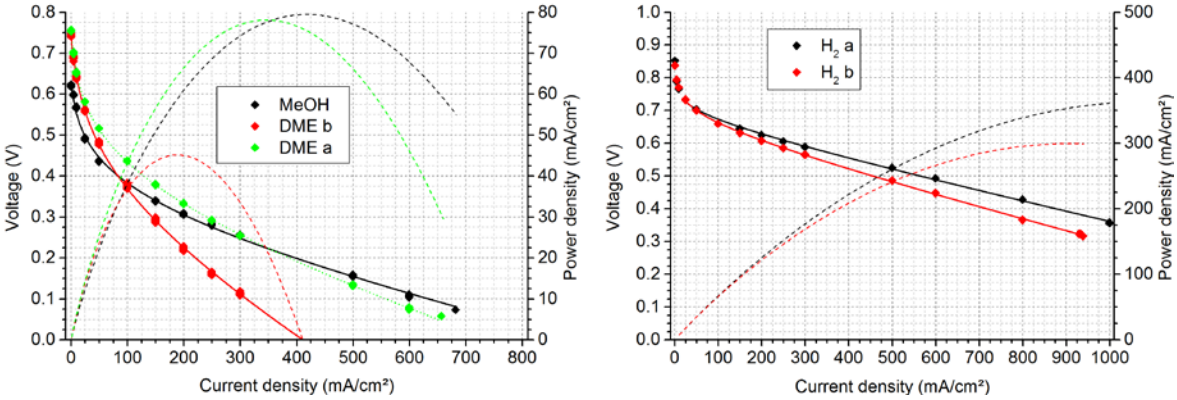

Figure 5.23: Polarisation curves for the MEA used to collect samples for gas chromatography analysis of anode exhaust gas. The MEA was tested with a gas changing sequence H_2 a – DME a – MeOH – DME b - H_2 b. The GC samples were collected after MeOH and DME b polarisation curves were obtained.

GC analysis results are given in Figure 5.24 below. It should be noted that there were large fractions of condensed liquid on the bottom of the sample bags, which were not analysed, wherefore the analysis does not provide a true composition of the anode exhaust gas, as the liquid contained water, but also probably methanol and maybe formic acid, which could be one of the intermediate products from both DME and MeOH oxidation reactions. It can though still be used as indication of the processes occurring in the running cell. On another occasion the gas bags were attempted heated slowly to evaporate the liquid with the unfortunate outcome that they melted, rendering analysis impossible.

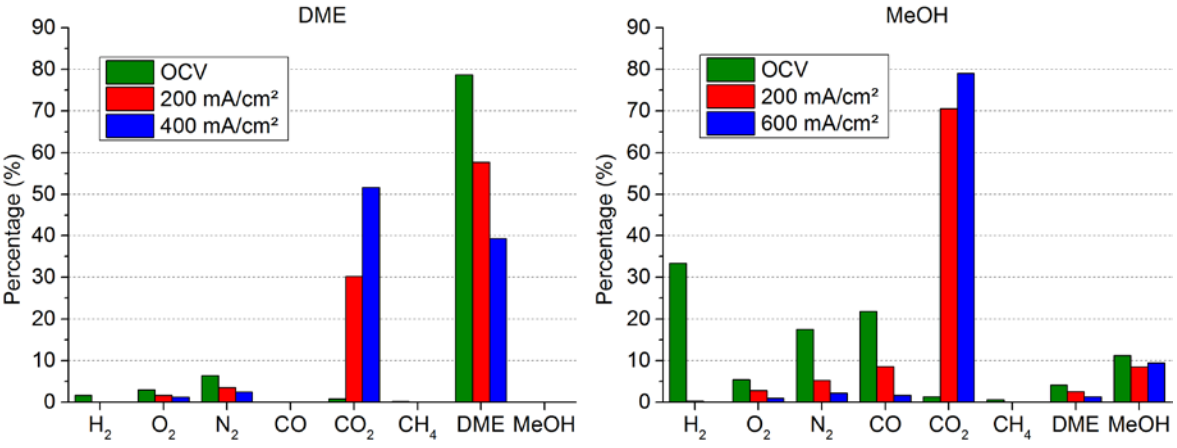

Figure 5.24: Composition of the anode exhaust gas from direct DME and direct methanol fuel cell operation at 200 °C.

From Figure 5.24 it can be seen that the amount of DME in the anode exhaust gas was decreasing and the amount of CO_2 was increasing with increasing current, as expected. No amounts of MeOH were detected, which could be due to the trace amounts formed being in the liquid phase. Trace amounts of hydrogen were detected at OCV for the first time for direct DME fuel cells, which could be an indication of

internal reforming process occurring, as the elevated temperature of the HT-PEM FC is closer to the reforming temperature of DME than for low temperature PEM FCs and investigations described in section 3.2. No CO was observed, but trace amounts of CO_2 and methane at OCV have been present in the sample. This could indicate that DME is internally reformed according to eq. 5.5 below:

$$CH_3OCH_3 + H_2O \rightarrow CO_2 + CH_4 + 2\,H_2 \qquad 5.5$$

The presence of oxygen and nitrogen in the samples is probably due to contamination from the air, as the analysis was performed on a different day than the collection. The permeability of the polymer the gas bag was made of towards atmospheric air did, however minor, have an effect.

The results from methanol operation were very different. Here, substantial amounts of hydrogen and CO, some DME and trace amounts of methane and carbon dioxide were detected at zero current. The large amounts are mostly due to the unspent fuel being mostly in the liquid phase. The gas composition however indicates a different process for the internal reforming towards syngas. Interesting to note is the presence of dimethyl ether, which is probably formed by dehydration of methanol, the amount decreasing with increasing current. This obviously occurs at 200 °C even in the presence of sufficient water. Almost no CO_2 was observed at OCV, but rose significantly with current, indicating increased rate of (complete) oxidation, as expected. The residual amount of methanol measured cannot be taken as an indicator for conversion, unlike the above experiments with DME, as the major part of the fuel would be present in the liquid phase.

6 DDMEFC Durability

The ultimate goal for direct dimethyl ether high temperature fuel cell technology is commercialisation. In order for the technology to be commercialised it is important not only to optimise the power output, but also to have a long lifetime. The high catalyst loading demand, as shown in section 5.1.2, requires the cells to last as long as possible. There are hardly any durability studies of DDMEFC available in literature, with the 56 h stability test at 100 mA/cm² by K.-D. Cai et al. [174] being the only reported work on the topic. For those reasons a thorough investigation of direct DME HT-PEM FC was performed using the optimum conditions found throughout the presented work.

6.1 Durability tests

The anodes were sprayed by the EXACTA-Coat spray robot, as described in section 4.6.1. The ink contained HiSPEC 10000 40 wt% Pt, 20 wt% Ru and 40 wt% C (nominal) catalyst from Johnson Matthey (lot 142947001), PBI, H_3PO_4 and CHOOH as solvent with following weight ratios – C : PBI 13.5, H_3PO_4 : PBI 2.9 and C : solvent 0.012. The ink was ultrasonically agitated between the refills of the feed syringe on the spray robot to avoid dispersion of air in the ink and prevent sedimentation. The target catalyst loading was 3.5 $mg_{Pt\text{-}Ru}/cm^2$. The anodes were combined with cathodes from Danish Power Systems (lot E-13-017) with 1.15 mg/cm² platinum loading and phosphoric acid doped PBI membranes also from Danish Power Systems (lot M-12-015 and M-12-018) with acid doping level 10.5 and 10.1 of phosphoric acid molecules per PBI repeating unit respectively. The MEAs were hot pressed using guiding tools at 200 °C for 3 minutes at a total pressure of 1 ton, resulting in MEAs with 21.16 cm² active area.

The MEAs were tested with the following conditions. The fresh MEAs were mounted in the cell housing with 5-channeled serpentine flow field plates and tightened at 1 Nm force applied to the 8 fastening bolts in a cross pattern to ensure even alignment and pressure distribution across the MEA. The cells were heated to 120 °C at OCV without gas flows on. At 120 °C the cells were supplied with 50 mL/min H_2 on the anode side and 228 mL/min air on the cathode side, corresponding to λ 1.2 and 2.5 at 200 mA/cm² respectively. At 160 °C the loads were turned on and the cells were left for 24 hours at 200 mA/cm² with hydrogen as fuel for break-in. After that i-V curves were obtained with the above mentioned λ values. The fuel was then changed to 32 mL/min dimethyl ether and 0.07 or 0.14 mL/min liquid water supplied to the cell via an evaporator at 150 °C. The cells were left for an hour at 25 mA/cm² to purge hydrogen from the system. The initial i-V curves with DME were then recorded at 160 °C, the temperature increased to desired set point and additional polarisation curves

were obtained. The cells were then left at 100 mA/cm² for durability testing with i-V curves recorded each 3 or 4 days.

The initial polarisation curves at 160 °C with hydrogen and DME as fuels can be seen on Figure 6.1. As evident from the curves the performance with hydrogen as fuel is not the same for the different MEAs despite all the components being from same batches which should therefore be equal. The striking difference was the ohmic resistance, which was higher for the MEA-13-363. Obviously the assembly of the cell housing has a significant effect on performance, where bad contact resulting from poor alignment of MEA components or uneven pressure distribution upon assembly has led to increased ohmic resistance. Despite the observed differences with hydrogen as fuel, the deviation in the performance of direct DME operated cells was not as pronounced. This can be explained by the fact that the current range for direct DME testing is much lower, so catalyst activity behaviour is dominating the performance, while ohmic resistance and eventual mass transfer limitations has less influence, as they typically govern the voltage response of the cells at higher currents.

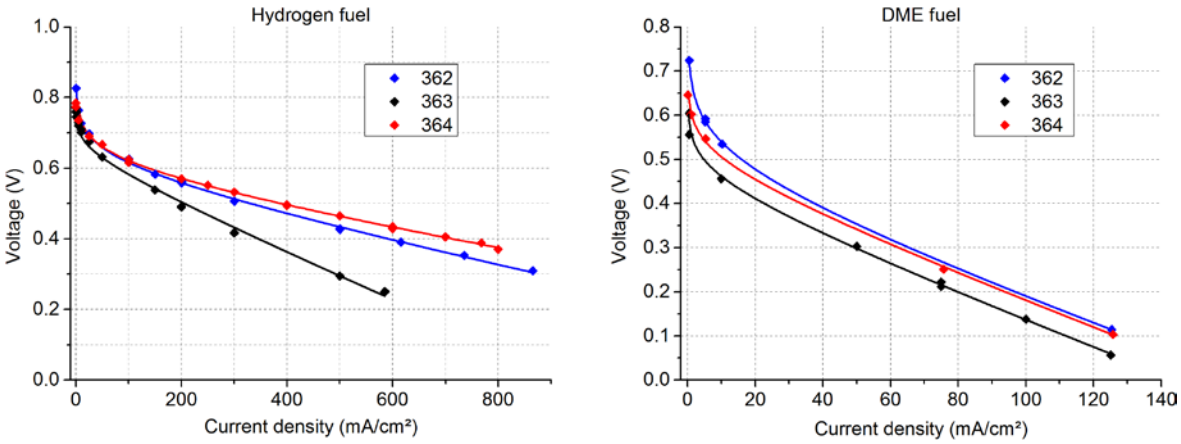

Figure 6.1: Initial polarisation curves at 160 °C with different fuels, hydrogen and dimethyl ether (H_2O/DME = 3). The points represent the instrumental readouts, while the lines are based on curve fitting according to equation 5.2.

The decay of the cell voltages running at 100 mA/cm² at different temperatures over time can be seen on Figure 6.2. The cell running at 200 °C shows highest performance from the beginning, due to higher activity of the catalyst at the increased temperature, but the degradation rate is also the highest, with ohmic resistance steadily rising over time. This may be attributed to growth of catalyst particles. The fitted and observed open circuit voltage values were generally dropping over time, which could indicate thinning of the membrane, thereby increasing the rate of fuel crossover and thus lowering the OCV. Both of the degradation mechanisms evolved with increasing voltage degradation rate as the result until the MEA was so damaged that the voltage rapidly dropped off, marking the end of life just short of 300 h operation time.

The cells running at 160 and 180 °C showed a different behaviour. There was an initial increase in voltage, which is usually attributed to removal of the impurities on

the catalyst, hydration of the membrane and redistribution of H_3PO_4 in the catalyst layer of the electrode [247-249]. The same processes are thought to happen in the MEA running at 200 °C as well, but the degradation rate was higher, therefore the improvement was not observed. After the initial improvement, the degradation mechanisms governed the voltage response of the MEAs with a usually increasing degradation rate until the end of life. The general trend was that the cell running at higher temperature had a higher performance, but lower life time. The MEA running at 180 °C showed an irregularity in the last 100 hours with reasons unknown. It might be connected to the refilling of the inlet water reservoir, where impurities or dissolved air can have unpredicted effects on the performance, most probably negative. Emptying (or failure to do so) the exhaust water reservoir could alter the humidity of the system, thereby increasing performance due to higher conductivity.

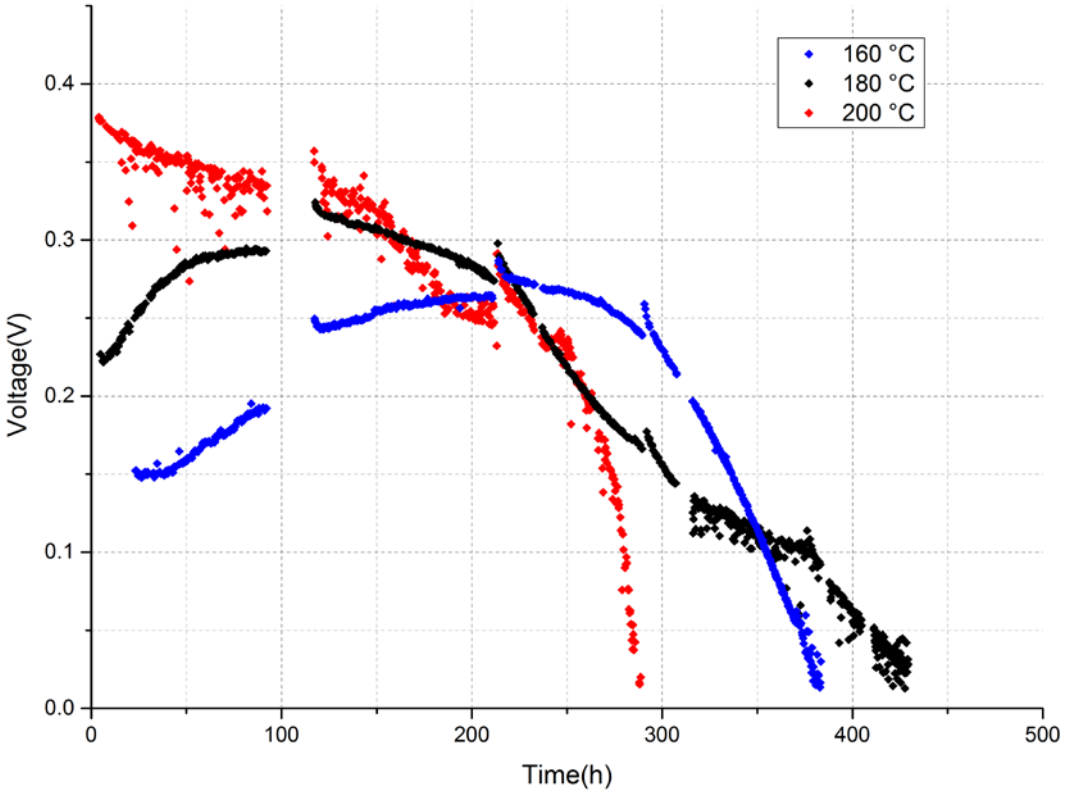

Figure 6.2: Cells running at 100 mA/cm² and different temperatures with water-to-DME ratio of 3 (single stoichiometry). The spikes in voltage are due to recording of polarisation curves.

Polarisation curves for all 3 cells were recorded each 3 or 4 days and could provide valuable information regarding degradation mechanisms by obtaining curve fitting parameters following eq. 5.2. The fitted parameters are summarized in Table 6.1 and the obtained data with the fitted curves are given in Figure 6.3. Due to the quality of the obtained data with only a few points recorded in the very low current density region, because of a flaw in the programming of the data logging for some polarization curves, different fitting parameters could be obtained depending on the input initial values to the algorithm. In those cases the solutions resembling the rest of the polarization curves for that particular MEA were chosen. Again, as already mentioned

in section 5.1.1, there was no coherence between the fitted OCV parameters of the different cells. The potentials at open circuit for one cell recorded over time could however be used to monitor the degradation of the membrane. In principle, if the membrane was to get thinner, the OCV should fall as the fuel crossover would increase due to lower barrier thickness. This appears not to be the case except for the polarisation curves obtained at the end of life. This can indicate that the degradation of the membrane is not an overall thinning, but rather formation of pinholes, which is also backed up by post-mortem analysis, as will be shown later. Another degradation mechanism connected with the membrane can be deduced from the development of the ohmic resistance. It generally follows the temperature trend observed from the durability plots on Figure 6.2, explaining the voltage gain the first 250 and 125 hours for the cells running at 160 and 180 °C respectively, with the hydration of the membrane probably being the main reason, but possibly also redistribution of electrolyte in the catalyst layer, thereby enlarging the triple phase boundary. At last, the clear development of the Tafel slope and cell voltage at 25 mA/cm² indicates degradation of catalyst in the form of catalyst particle growth, decreasing specific activity of the catalyst.

Remarkable for all 3 temperatures were their comparatively equal and short life times, when related to hydrogen fed cells with lifetimes exceeding several thousand hours, reported in [60, 250] and observed in unpublished work done by the authors group. There is definitely a temperature effect, as indicated by the experiments shown on Figure 6.2, but the main degradation mechanism must be due to the different fuel, DME, which is also a known organic solvent. Its effect on PBI polymer has not yet been demonstrated. Therefore it was decided to decrease the partial pressure of DME by increasing the amount of water supplied to the cell to double stoichiometry. The same initiation procedure was carried out as described earlier. The initial performances with hydrogen and DME as fuels at 160 °C can be seen on Figure 6.4 below. There was not a very big difference in initial hydrogen performance, but a slight deviation in direct DME performance. The deviation from the trend was due to a single point in MEA-13-368 at 100 mA/cm². As already observed previously, the DME performance is highly influenced by the stability of the system, with slightest deviations in fuel flow giving large voltage variations. It can be that the point was recorded at such an event and the true performance of the MEA-13-368 at 100 mA/cm² is on par with the two others. The difference between the initial direct DME performance with double water and single water stoichiometries was quite insignificant, so any difference in direct DME HT-PEM FC life time must be due to lower DME concentration and possible higher hydration of the membrane, and not enhanced catalyst activity.

The durability test data with double water stoichiometry for the three different temperatures are represented on Figure 6.5. There was an evident improvement in the lifetime of the cells with the cell running at 160 °C achieving the maximum of 60 % improvement. The general trend in performance with regard to voltage degradation

Table 6.1: Fitting parameters from the polarisation curves of direct DME cells at different temperature and operation time, H_2O/DME = 3. (*) – R corrected.

	MEA-13-362 at 160 °C				MEA-13-363 at 180 °C				MEA-13-364 at 200 °C			
Time (h)	OCV (mV)	R (Ωcm²)	Tafel slope (mV/dec)	Voltage(*) @ 25 mA/cm² (mV)	OCV (mV)	R (Ωcm²)	Tafel slope (mV/dec)	Voltage(*) @ 25 mA/cm² (mV)	OCV (mV)	R (Ωcm²)	Tafel slope (mV/dec)	Voltage(*) @ 25 mA/cm² (mV)
0	705	2.27	146	501	707	1.57	145	505	794	0.62	179	544
140	770	0.97	198	492	797	0.77	186	538	876	1.36	182	621
236	808	0.67	214	508	797	0.76	208	505	858	1.49	207	569
314	797	0.83	217	494	857	1.22	268	483	841	2.82	262	474
408	820	1.70	317	377	645	2.66	285	247				

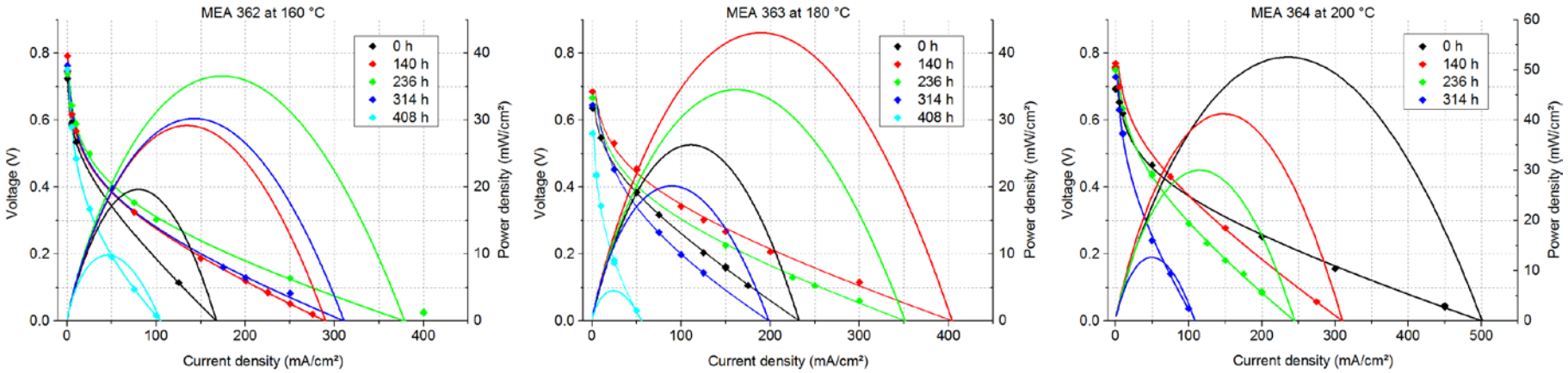

Figure 6.3: Polarisation curves for direct DME cells at different temperatures and operation times, H_2O/DME = 3. The points represent the instrumental readouts, while the lines are based on curve fittings according to equation 5.2.

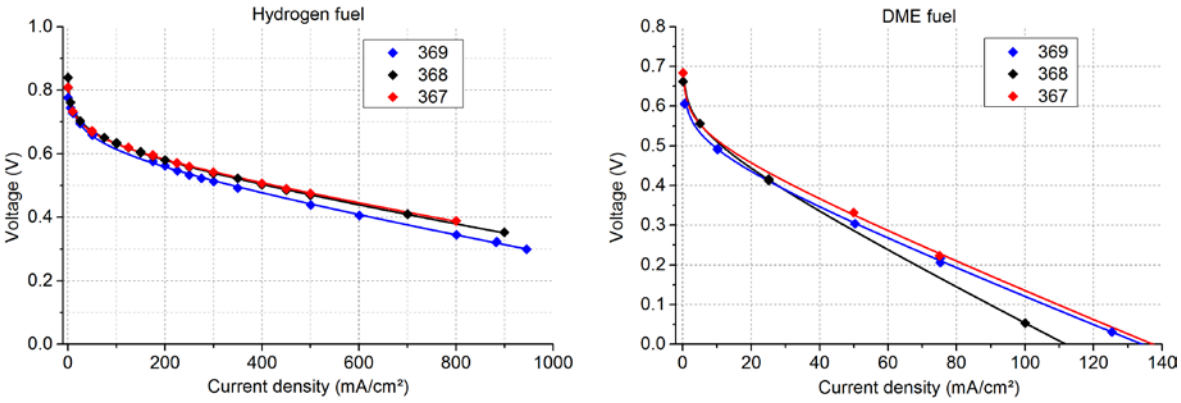

Figure 6.4: Initial polarisation curves at 160 °C with different fuels, hydrogen and dimethyl ether (H_2O/DME = 6). The points represent the instrumental readouts, while the lines are based on curve fitting according to equation 5.2.

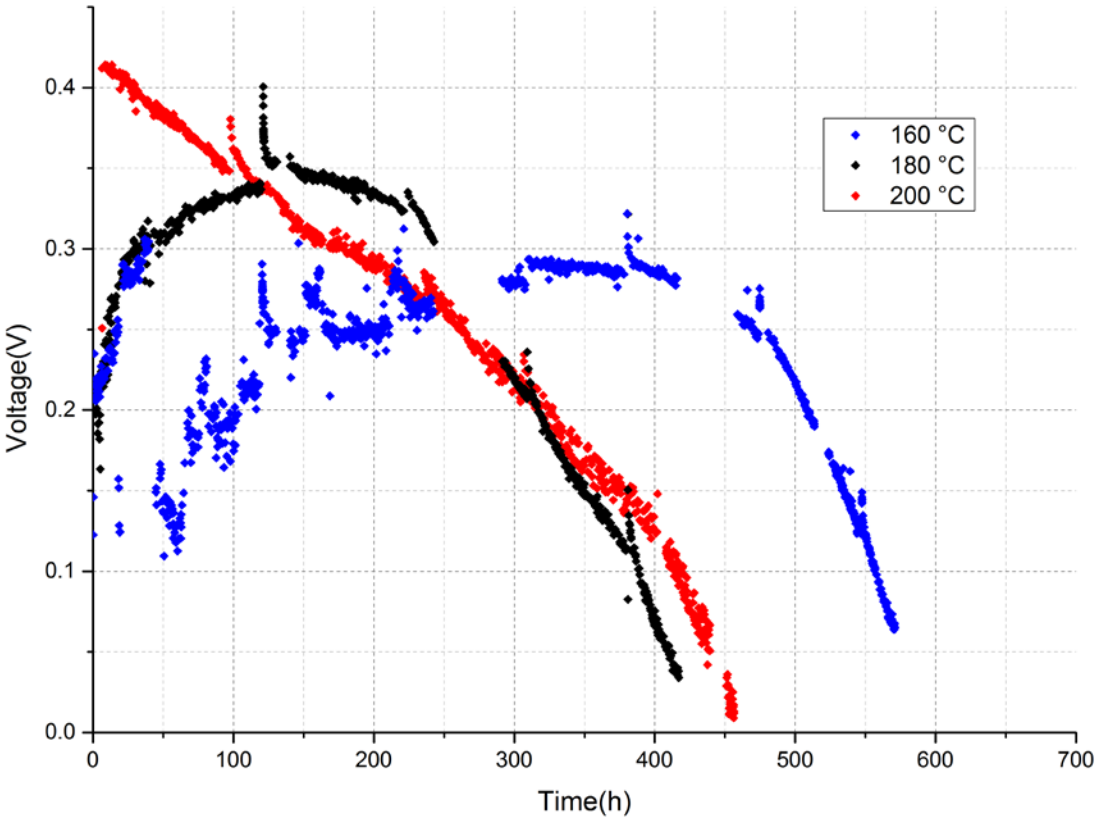

Figure 6.5: Cells running at 100 mA/cm² and different temperatures with water-to-DME ratio of 6 (double stoichiometry). The spikes in voltage are due to recording of polarisation curves. The cell running at 160 °C was operated at 50 mA/cm² the first 50 hours due to low initial voltage.

was the same as with single water stoichiometry, although the cell running at 180 °C showed deviating behaviour after app. 250 hours of operation with the increasing degradation rate, causing the end of life before the expected cell running at 200 °C.

Like for the cells running at single water to DME stoichiometry, polarisation curves were recorded with 3 or 4 days regularity to monitor the degradation mechanisms. The curve fitting parameters according to eq. 5.2 are given in Table 6.2 and the data
.

Table 6.2: Fitting parameters from the polarisation curves of direct DME cells at different temperatures and operation times, H_2O/DME = 6. (*) – R corrected.

	MEA-13-369 at 160 °C				MEA-13-368 at 180 °C					MEA-13-367 at 200 °C				
Time (h)	OCV (mV)	R (Ωcm²)	Tafel slope (mV/dec)	Voltage(*) @ 25 mA/cm² (mV)	OCV (mV)	R (Ωcm²)	Tafel slope (mV/dec)	Voltage(*) @ 25 mA/cm² (mV)		Time (h)	OCV (mV)	R (Ωcm²)	Tafel slope (mV/dec)	Voltage(*) @ 25 mA/cm² (mV)
0	607	3.22	82	492						0	719	1.98	78	610
147					835	0.79	186	575		100	844	0.77	177	597
248	735	1.47	142	536	844	0.72	211	549		190	931	0.67	246	587
336	769	0.96	180	517	843	1.56	217	540		327	860	1.39	206	572
408	810	0.62	219	504	831	2.04	237	500		400	853	1.59	221	544
502	766	1.27	181	513	892	2.39	360	389		494	874	2.29	251	523
575	741	1.76	206	453						551	821	2.59	264	452

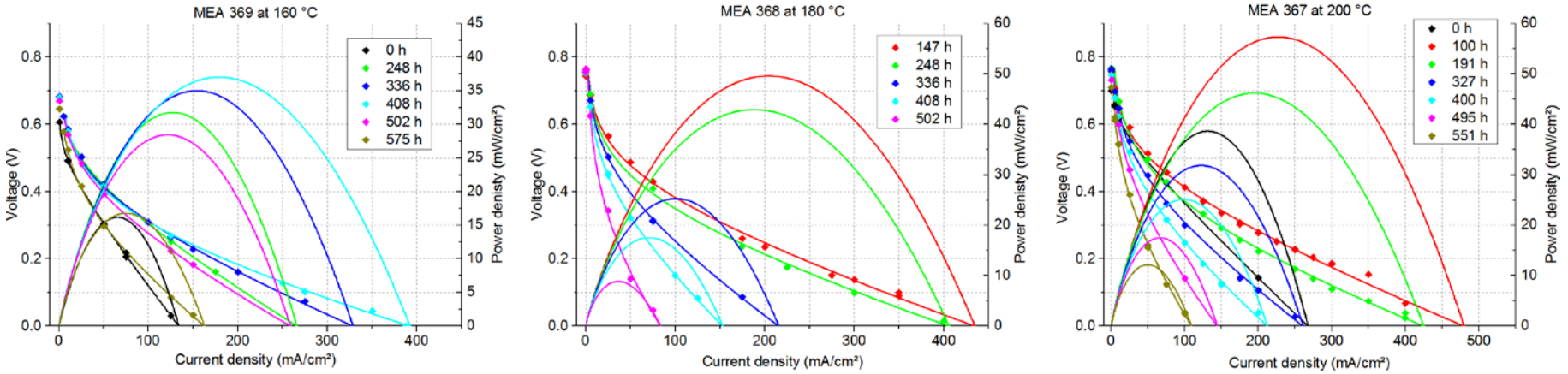

Figure 6.6: Polarisation curves for direct DME cells at different temperatures and operation times, H_2O/DME = 6. The points represent the instrumental readouts, while the lines are based on curve fittings according to equation 5.2.

together with the fitted curves are plotted in Figure 6.6. The trends described for the previous experiments were also observed for the increased water stoichiometry but at a decreased development rate, confirming that decreased DME partial pressure had a positive effect on durability of the cells

Despite the improved lifetimes at higher water stoichiometry the demonstrated 600 hours is still not enough to take direct DME HT-PEM FC into consideration for practical applications. While those relatively short lifetimes have been present in most studied MEAs, there was one which stood out, with the cell lifespan exceeding 1600 hours of operation with reasons unknown. The durability data are represented in Figure 6.7 below. There is also no explanation for the sudden improvement in the voltage at 700 h of operation time.

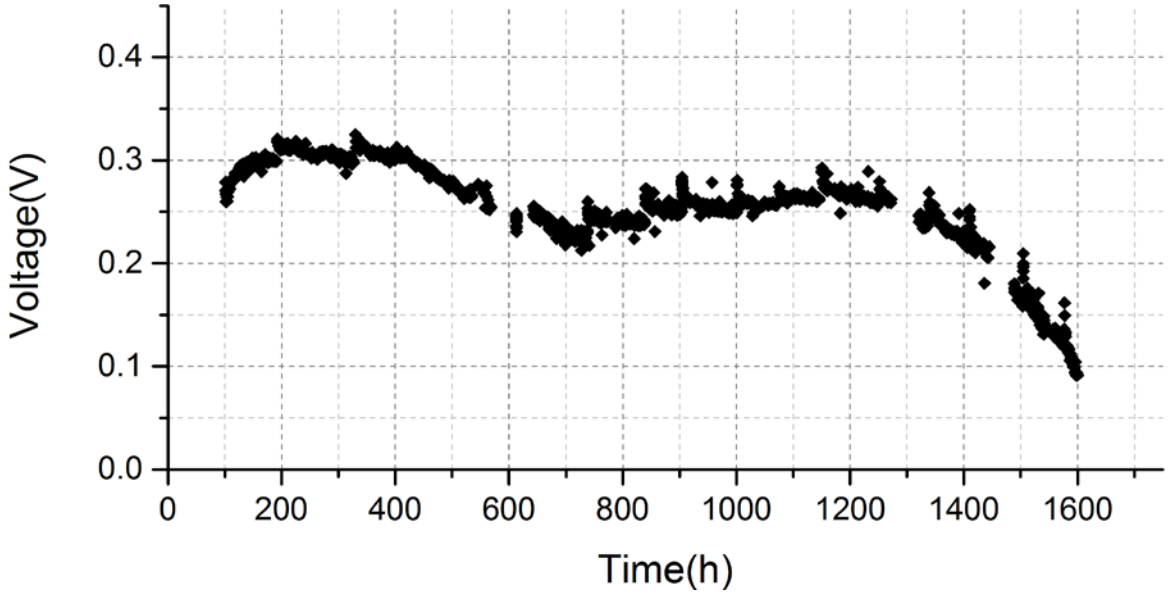

Figure 6.7: Cell running at 100 mA/cm² and 180 °C with water-to-DME ratio of 6 (double stoichiometry).

6.2 Post-mortem analysis by SEM

As a part of the durability study the cross-sections of the tested MEAs were examined post-mortem by scanning electron microscopy (SEM). The MEAs were cut with scalpel or scissors first and then the cut was etched in an ion mill for 8 hours to obtain a very plane surface. The images at 1000x magnification are given in Figure 6.8. Unfortunately it was not possible to avoid a certain degree of delamination, as the protective polysulfon film around the membrane outside the MEA structure was sticking to the Viton® O-rings providing gas sealing and thus were quite difficult to detach upon disassembly of the cell, partially ripping the electrode off from the membrane. Also, the sample preparation procedure with repeated evacuation of the samples and following exposure to the atmosphere must have had its effects. Therefore voids were present in most of the investigated MEAs, seen as black gaps running alongside the catalyst layers. Nonetheless the images give some clues to

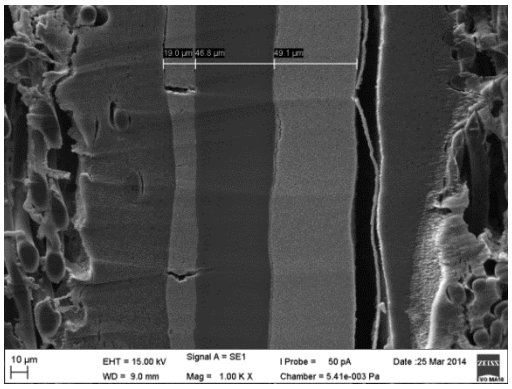

MEA-13-362, 375 h at 160 °C

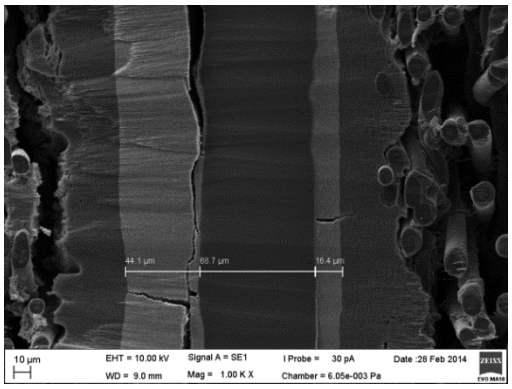

MEA-13-365, 425 h at 160 °C

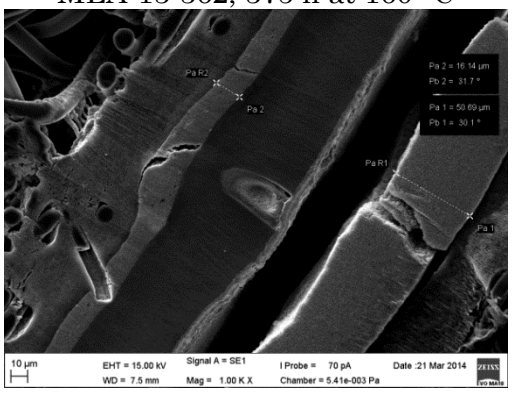

MEA-13-363, 430 h at 180 °C

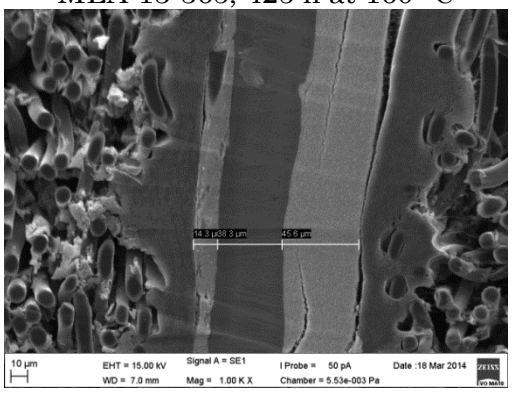

MEA-13-366, 1600 h at 180 °C

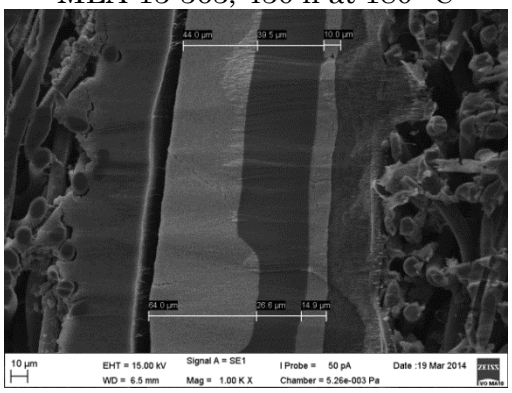

MEA-13-364, 290 h at 200 °C

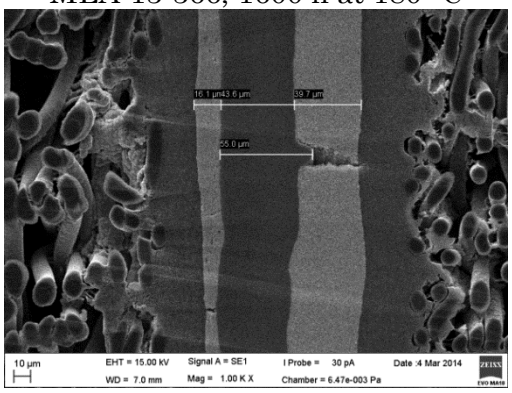

MEA-13-367, 575 h at 200 °C

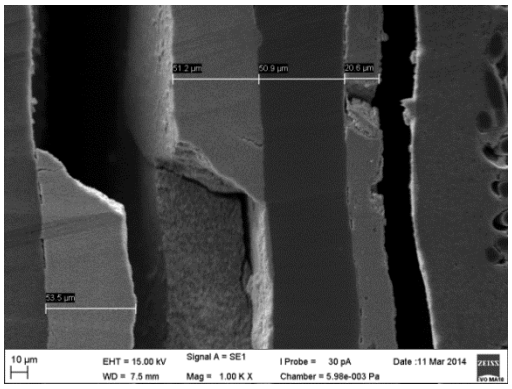

MEA-13-371, unused

Figure 6.8: Cross section SEM images of the MEAs used in the durability study prepared by means of ion milling. The measured thicknesses are given in Table 6.3.

degradation mechanisms. A summary of the tested MEAs and the thickness parameters of the membrane and catalyst layers on the anode and cathode are given in Table 6.3.

As can be seen from Table 6.3, there was no apparent correlation between the visible thicknesses and the lifetimes. With the spraying methods of the electrodes, described in section 4.6.1 and illustrated on Figure 4.8 a certain variation in the anode catalyst layer thickness was expected. From the manufacturer of the cathodes it was known that the thickness variation could be up to 30 %, which was reflected very well in the apparent measured thicknesses of the cathode catalyst layer.

Table 6.3: Durability parameters and component thicknesses of the tested MEAs obtained from SEM images on Figure 6.8.

MEA ID	Lifetime (h)	Operating temperature (°C)	Anode thickness (µm)	Membrane thickness (µm)	Cathode thickness (µm)
MEA-13-362	375	160	49	47	19
MEA-13-363	430	180	50	55	16
MEA-13-364	290	200	44 - 64	26 - 39	10 – 15
MEA-13-365	425 (sudden death)	160	44	69	16
MEA-13-366	1600	180	45	38	14
MEA-13-367	575	200	40	43 – 55	16
MEA-13-371	unused	NA	51	51	21

More interesting were the thicknesses of the membranes. Ideally, if DME was to have a dissolving effect on the PBI polymer, the membrane should be thinning throughout the operation at a certain rate, therefore the membranes ran for longer hours should be thinner. This appears not to be the case. From the manufacturer the thickness of the un-doped membranes was known, 41 ± 1 µm. Doped they are supposed to swell by up to 50 % and upon compression shrink again. The latter might explain the discrepancy in the measured data. The cross-sections represent only a very limited part of the MEAs and might therefore be non-representative. If a cross-section is taken from a part of the MEA which was in between the ribs of the gas flow field plates, the compression on that part would be limited and therefore the layers would be thicker, which might be the case with the MEA-13-365, showing the thickest membrane of the investigated samples.

If looking in closer detail on the SEM images presented on Figure 6.8 there is a number of interesting features, which can give clues to the nature of degradation mechanisms. When looking in the upper centre of the unused MEA-13-371 (lowest) a concave in the membrane filled with catalyst can be seen, also present in MEA-13-366. This is an indication of a pin hole in the membrane, a weakness that would most certainly propagate and grow during operation. A confirmation of this is the big concave feature found in the lower part of the MEA-13-364 image. It is interesting

that the concaves are filled with catalyst. Apparently the catalyst layer is not solid, but behaves more like a gel and probably flows into the cavity under the influence of gas and water supply and pressure from the cell assembly. It can be that this process is caught midway in the MEA-13-363, showing a very interesting feature in the centre of the image. The hollow in the membrane was covered by Pt-Ru catalyst, identified by EDX detector. The propagation and growth of the pinholes can be explained by formation of a hot spot from a simple consideration of Ohm's law. The voltage across the entire of the electrode should be the same as it has very good electronic conductivity. As the resistance in the thinner part is less than in the thicker parts, the local current at the pinhole must be higher, leading to excessive localised heating of the material and therefore increased rate of degradation.

Another type of imperfection is seen on MEA-13-367 image, where an app. 10 µm "bump" in the membrane disturbs the catalyst layer. This is probably a pre-operation feature, where the irregularity in the membrane was pressed onto the plane catalyst layer and caused it to crack. The effects can be both beneficial and negative. On one hand it might increase the active surface area of the electrode, but on the expense of higher ohmic resistance due to the longer proton conduction path. It might also have a negative effect on fuel crossover, as there is more direct contact between the gas and the membrane. The nature of the bump is unknown, but the polymer in the feature is probably stiffer than the rest of the membrane, as it would otherwise be flattened by a supposedly firmer catalyst layer upon hot-pressing of the MEA or assembly of the cell. In this case the local H_3PO_4 doping level must be less, having a negative impact on proton conductivity.

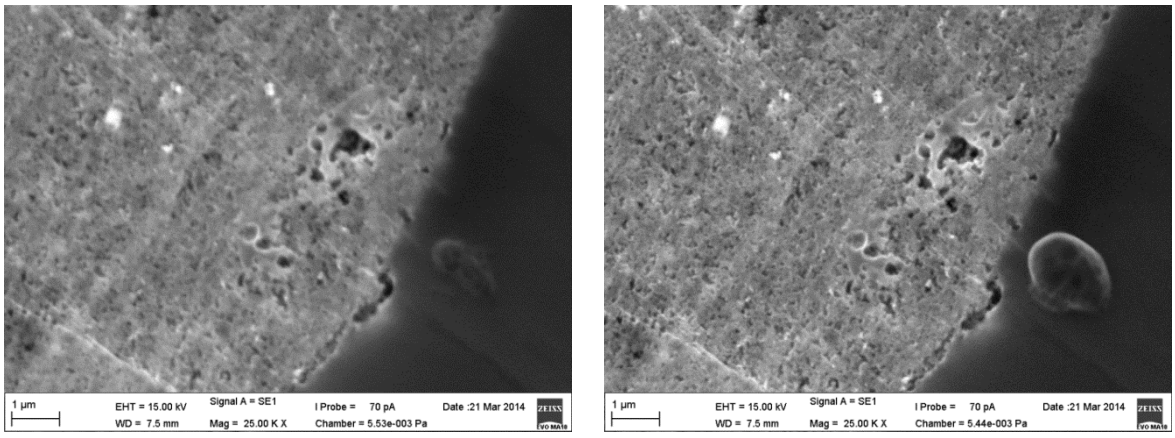

Figure 6.9: Appearance of matter on the cross section cut of the H_3PO_4-doped PBI membrane in MEA-13-368 under influence of electron beam in scanning electron microscope.

An interesting observation was made while trying to get high magnification, high resolution SEM images on MEA-13-363, seen on Figure 6.9. Under the influence of the electron beam emitted by the tungsten filament a droplet on the surface of the H_3PO_4-doped PBI membrane formed and grew in size. This can be water resulting from polymerisation of phosphoric acid due to the heat originating from the electron beam. No further investigation of the feature was made, as it was clearly formed

under the influence of the instrument and probably had no relation to or effect on the MEA performance.

From this chapter it is obvious that there are still many unanswered questions with regard to the operation and durability of the direct DME HT-PEM fuel cells. With the general short lifetimes of the MEAs there is no urge in trying to find an application niche, but if the conditions of the cell operating past 1600 hours can be identified, there might be an opportunity opening.

7 Conclusions and Outlook

This section gives a recapitulation of the conducted research and engineering work given in chapters 1, 1 and 1, and proposes directions for future work in order to obtain a more complete understanding of the direct dimethyl ether high temperature PEM fuel cell. It has been shown that direct fuelling of an HT-PEM fuel cell with DME and water mixture is indeed possible. The highest obtained power density was 80 mW/cm² on a 60 wt% $Pt_{50}Ru_{50}$ on 40 wt% C anode catalyst, using a non-pressurised system with athmospheric air as oxidant. Additionally, as an overall conclusion to the question whether direct dimethyl ether high temperature fuel cells are a possible alternative to the conventional hydrogen/air operation in practical applications the answer is negative. A much better efficiency is thought to be obtained by prior reforming to hydrogen and then use in HT-PEM FC, which can tolerate the CO, CO_2 and unreformed fuel impurities. It remains, however, a very interesting research topic, as can be seen from the following.

7.1 General conclusions

In order to test the performances of HT-PEM fuel cells operated on the organic fuels DME and methanol a complete single fuel cell testing station was designed and constructed, where a precise and reliable delivery of the vaporised fuel-water mixture was ensured by a novel design of the evaporator. Based on the gathered experience with the single cell setup a larger one for simultaneous and independent testing of 6 cells was proposed, designed and constructed, incorporating the novel evaporator design, but also ensuring great flexibility in terms of fuel and oxidant types and composition, allowing for operation with up to 3 different gasses and steam or methanol on one of the electrodes. Computer aided design facilitated by Autodesk Inventor 2013 proved to be a great tool in order to achieve this with a further benefit of greatly reducing the time required for the actual assembly of the setup.

The work on optimising membrane electrode assembly components showed that large amounts of PBI in the electrode catalyst layer are undesirable, as it leads to formation of holes and cracks in the layer by contraction upon drying, effectively blocking the catalyst particles with increased ohmic resistance and mass transport limitations as a consequence. In terms of catalyst ink preparation however, it proved to be advantageous for the employed ink formulation with formic acid as a solvent, with the inks containing too little PBI failing to achieve any kind of dispersion of catalyst particles.

The loading of the anode catalyst proved to have a tremendous effect on the direct DME operation, increasing the maximum observed power density from 25 mW/cm² for a 1 mg/cm² catalyst loading to 67 mW/cm² at 3.7 mg/cm², before falling again to 47

mW/cm² for an increased loading of 5.5 mg/cm². A similar effect was observed with methanol as fuel. The situation with hydrogen/air operation was different, where the maximum power density was observed for the MEA with the lowest anode catalyst loading, steadily decreasing with increasing loading due to increased ohmic resistance. Therefore on optimum exists between 3 and 4 mg/cm² for DME and methanol operation, where there the amount of active sites to facilitate rapid oxidation of the fuel counterweights the drawbacks connected to the increased thickness of the catalyst layer.

Anode catalysts with different Pt, Ru and Sn ratios were prepared and characterised, showing that a simple synthesis method with the simultaneous reduction of metal chloride salts with $NaBH_4$ yields in metal ratios according to theoretical composition. There was no apparent trend in performance of the MEAs with different fuels, which shows that other components of the MEAs have a tremendous effect on the performance. Polarisation curve fittings were also not able to provide a satisfactory explanation. Another method is thus required to test the activity of the synthesised catalysts towards DME and MeOH oxidation, but the conducted experiments show that optimisation of the catalyst activity will not necessarily lead to improved performance if other constituents of the MEA are not optimised.

It has been shown that increasing temperature has a positive effect on the performance of the MEAs with all the fuels tried - hydrogen, DME and MeOH, providing additional energy to overcome the kinetic barrier of the oxidation. Additionally, it has been found that the increased temperature also decreases ohmic resistance, until the point when critical temperature is reached beyond 200 °C and the resistance starts to increase rapidly due to membrane dryout and polymerisation of the phosphoric acid, thereby losing the proton conductivity.

An effect of the oxygen partial pressure increase from 0.21 to 1 bar was also investigated, showing improvement of the OCV and the overall performance of the MEA with all the three fuels tested. The peak power densities were increased by 25 and 35 % for DME and MeOH fuels respectively, with the higher increase of the latter indirectly confirming the effect of the larger fuel crossover being counteracted by increased oxygen partial pressure. It is thus more beneficial to operate a DMFC on pure oxygen than a direct DME HT-PEM FC.

Analysis of the anode exhaust gas at different current densities with DME and MeOH was also conducted by gas chromatography, showing that at 200 °C operating temperature a small fraction of the fuel is internally reformed to syngas when methanol is used as fuel, and a mixture of CO_2, methane and hydrogen if the cell is fed with DME-water mixture.

The findings by the GC analysis were partly confirmed by the performed electrochemical impedance spectroscopy analysis, where the best equivalent circuit fitting for methanol operation contained a Gerischer element usually indicating a preceding chemical reaction and a diffusion process, which could be an indication of

the internal fuel reforming. The same element did not give a satisfactory fitting when DME was used as fuel, but it could be that the effect was hidden by additional elements not identified and therefore not included in the equivalent circuit. An interesting finding on initial operation with hydrogen was that the resistance of the electrolyte was seemingly decreasing with increasing current density, showing that the conductivity is affected by the hydration effect to a small extent, but it proved to last over several hours. Overall it has been demonstrated that EIS is a powerful tool for MEA investigation, obviating the need for a reference electrode, but extensive preliminary knowledge about the cell together with a series of carefully planned and executed experiments are needed to ensure a correct interpretation.

Finally, durability studies showed that the lifetimes of the prepared cells operated with DME as fuel are in the range of 300 – 600 hours, increasing with increased water content and decreasing temperature. One particular MEA had a lifetime exceeding 1600 hours with the reasons unknown. As dimethyl ether is a known organic solvent, there was a suspicion that thinning of the membrane occurred, resulting in the short lifetimes. A post-mortem analysis by SEM showed that the reason for the MEA failure was formation of pinholes rather than an overall thinning.

7.2 Future work

The conducted work can more or less be divided into two parts, the first being an engineering task to provide a stable and reliable framework for the direct DME HT-PEM FC testing and the second was to actually make the MEAs and test them with the constructed equipment. The two tasks were not separate and consecutive, but rather simultaneous, with a number of problems and issues encountered, which were resolved on the go, leaving the mark on the quality of the obtained MEA results. With the gathered knowledge about the operation and testing the road is open to plan series of more detailed investigations, combining several methods described in the presented work. There is a great desire to couple the single cell testing setup exhaust to a gas chromatograph, such that the anode exhaust composition could be monitored online, detecting the gas composition changes as function of operating parameters.

More detailed electrochemical impedance spectroscopy experiments should be performed with variation of one parameter while holding the rest constant to identify and map the responses from various MEA components. The parameters could be reactant gas composition, partial pressure, catalyst type and loading, cell voltage, temperature, membrane electrolyte thickness, etc. Coupled with the online gas chromatograph this technique would indeed give a complete picture of the operation of the HT-PEM FC not only on dimethyl ether, but on any other organic fuel. Also, the effects of e.g. CO poisoning could be investigated to a great detail.

There is also a great desire to conduct more fundamental studies on DME electrooxidation at elevated conditions in phosphoric acid electrolyte on different catalysts by e.g. cyclic voltammetry in a 3 electrode cell or a half cell. Even though

there is some literature available on the DME electrooxidation, as described in section 3.2, none of this has been done at 200 °C. Making a working half-cell with H_3PO_4 operated at those temperatures can be quite difficult, but far from impossible, as has been proven by the author's co-workers.

In this temperature range other non-noble catalysts become more interesting, e.g. WC, which has shown activities for hydrogen evolution on par with the classical platinum catalyst. It is also known for not being strongly affected by CO-poisoning, making it a very interesting alternative for direct oxidation of organic fuels in an HT PEM FC. It should be noted that a crude attempt on an MEA with a low surface area WC as anode catalyst was attempted with the unfortunate outcome of the tungsten oxidizing to the blue WO_2 in the beginning of the MEA testing, showing that care must be taken during preparation, hot pressing mounting and run-in of the MEA, ensuring reducing conditions at all times to preserve the initial composition of the WC catalyst.

Finally, to make the direct DME HT-PEM FC more competitive to the DMFC the conditions for the extended life time of 1600 h must be identified and replicated. More durability tests using the setup constructed for that purpose during this work must be conducted, ideally coupled with EIS and post-mortem analysis by SEM to map the degradation processes.

8 Bibliography

1. BP, *Statistical Review of World Energy*, 2013.

2. U.S. Energy Information Administration (EIA), *Annual Energy Review*, 2012.

3. S. Trasatti, *Water electrolysis: who first?*, Journal of Electroanalytical Chemistry, 1999, **476** (1), p. 90-91.

4. R. de Levie, *The electrolysis of water*, Journal of Electroanalytical Chemistry, 1999, **476** (1), p. 92-93.

5. W.R. Grove, *On voltaic series and the combination of gases by platinum*, Philosophical Magazine Series 3, 1839, **14** (86), p. 127-130.

6. W.R. Grove, *On a gaseous voltaic battery*, Philosophical Magazine, 2012, **92** (31), p. 3753-3756.

7. W.R. Grove, *The correlation of physical forces by W.R. Grove*, 1874, London, Longmans, Green.

8. L. Mond and C. Langer, *A new form of gas battery*, Proceedings of the Royal Society of London, 1889, **46** (280-285), p. 296-304.

9. A.J. Appleby, *From Sir William Grove to today: fuel cells and the future*, Journal of Power Sources, 1990, **29** (1–2), p. 3-11.

10. F.W. Ostwald, *Zeitschrift für Elektrotechnik und Elektrochemie. Die Wissenschaftliche Elektrochemie der Gegenwart und die Technische der Zukunft*, Zeitschrift für Elektrotechnik und Elektrochemie, 1894, **1** (4), p. 122-125.

11. W.H. Nernst, *Die elektromotorische Wirksamkeit der Jonen*, Habil Thesis, Philosophischen Fakultät, Universität Leipzig, 1889, DOI: 10.3931/e-rara-10994.

12. W.H. Nernst, *Über die elektrolytische Leitung fester Körper bei sehr hohen Temperaturen*, Zeitschrift für Elektrochemie, 1899, **6** (2), p. 41-43.

13. E. Baur, *Über die Beziehung zwischen Elektrolytischer Dissociation und Dielektrizitätskonstante*, Zeitschrift fur Elektrochemie und Angewandte Physikalische Chemie, 1906, **12** (39), p. 725-726.

14. E. Baur, *The relation between electrolytic dissociation and dielectricity constants*, Zeitschrift fur Elektrochemie und Angewandte Physikalische Chemie, 1906, **12**, p. 725-732.

15. E. Baur, *Über die Rühr- und Körner-Elektrode*, Zeitschrift fur Elektrochemie und Angewandte Physikalische Chemie, 1933, **39** (3), p. 168-169.

16. E. Baur, *Über Ketten mit Luftelektroden*, Zeitschrift fur Elektrochemie und Angewandte Physikalische Chemie, 1934, **40** (5), p. 249-252.

17. E. Baur and J. Tobler, *Brennstoffketten*, Zeitschrift fur Elektrochemie und Angewandte Physikalische Chemie, 1933, **39** (3), p. 169-180.

18. E. Baur and H. Preis, *Über Brennstoff-Ketten mit Festleitern*, Zeitschrift fur Elektrochemie und Angewandte Physikalische Chemie, 1937, **43** (9), p. 727-732.

19. E. Baur and H. Preis, *Brennstoff-Ketten mit Festleitern*, Zeitschrift fur Elektrochemie und Angewandte Physikalische Chemie, 1938, **44** (9), p. 695-698.

20. J. Larminie and A. Dicks, *Fuel cell systems explained*, 2003, Wiley.

21. G.A. Olah, A. Goeppert and G.K.S. Prakash, *Beyond oil and gas: the methanol economy*, Second updated and enlarged edition ed., 2009, Wiley-VCH.

22. *Handbook of fuel cells : fundamentals, technology, and applications*, ed. W. Vielstich, A. Lamm and H.A. Gasteiger, Vol. 1, 2003, Wiley.

23. J.M. Andujar and F. Segura, *Fuel cells: History and updating. A walk along two centuries*, Renewable and Sustainable Energy Reviews, 2009, **13** (9), p. 2309-2322.

24. C. Stone and A.E. Morrison, *From curiosity to "power to change the world"*, Solid State Ionics, Diffusion and Reactions, 2002, **152-153**, p. 1-13.

25. H.K. Ihrig, *Fuel cell powerplant for electrically propelled earthmoving machinery*, Society of Automotive Engineers - Papers, 1960.

26. K.V. Kordesch, *Hydrogen-air/lead battery hybrid system for vehicle propulsion*, Journal of the Electrochemical Society, 1971, **118** (5), p. 812.

27. W. Mitchell, *Fuel cells*, 1963, Academic Press.

28. W.T. Grubb, *Ionic migration in ion-exchange membranes*, Journal of Physical Chemistry, 1959, **63** (1), p. 55-67.

29. W.T. Grubb and L.W. Niedrach, *Batteries with solid ion-exchange membrane electrolytes: II. Low-temperature hydrogen-oxygen fuel cells*, Journal of the Electrochemical Society, 1960, **107** (2), p. 131-135.

30. K. Prater, *The renaissance of the solid polymer fuel-cell*, Journal of Power Sources, 1990, **29** (1-2), p. 239-250.

31. P.F. Howard and C.J. Greenhill, *Ballard PEM fuel cell powered ZEV bus*, SAE Special Publications, 1993 (984), p. 113-119.

32. K.B. Prater, *Solid polymer fuel cells for transport and stationary applications*, Journal of Power Sources, 1996, **61** (1-2), p. 105-109.

33. M. Jacoby, *Fuel cells heading for sale*, Chemical & Engineering News, 1999, **77** (24), p. 31-37.

34. J.H. Wee, *Applications of proton exchange membrane fuel cell systems*, Renewable & Sustainable Energy Reviews, 2007, **11** (8), p. 1720-1738.

35. D. Ross, *Power struggle: power supplies for portable equipment*, IEE Review, 2003, **49** (7), p. 34-38.

36. X. Li, *Principles of Fuel Cells*, 2006, Taylor & Francis Group.

37. A. Boudghene Stambouli and E. Traversa, *Fuel cells, an alternative to standard sources of energy*, Renewable and Sustainable Energy Reviews, 2002, **6** (3), p. 297-306.

38. K. Strasser, *The design of alkaline fuel-cells*, Journal of Power Sources, 1990, **29** (1-2), p. 149-166.

39. *Handbook of fuel cells : fundamentals, technology, and applications*, ed. W. Vielstich, A. Lamm, and H.A. Gasteiger, Vol. 4, 2003, Wiley.

40. G.V. Elmore and H.A. Tanner, *Intermediate temperature fuel cells*, Journal of the Electrochemical Society, 1961, **108** (7), p. 669-671.

41. M. Sahibzada et al., *Evaluation of PEN structures incorporating supported thick film Ce0.9Gd0.1O1.95 electrolytes*, Proceedings of the Fifth International Symposium on Solid Oxide Fuel Cells, ed. U. Stimming, et al., Vol. 97. 1997, 244-253.

42. K.Q. Huang, M. Feng and J.B. Goodenough, *Bi2O3-Y2O3-CeO2 solid solution oxide-ion electrolyte*, Solid State Ionics, 1996, **89** (1-2), p. 17-24.

43. M. Feng et al., *Fuel cells with doped lanthanum gallate electrolyte*, Journal of Power Sources, 1996, **63** (1), p. 47-51.

44. W.L. Worell, *Electrical properties of mixed-conducting oxides having high oxygen-ion conductivity*, Solid State Ionics, 1992, **52** (1-3), p. 147-151.

45. H.E. Vollmar et al., *Innovative concepts for the coproduction of electricity and syngas with solid oxide fuel cells*, Journal of Power Sources, 2000, **86** (1–2), p. 90-97.

46. J. Mitteldorf and G. Wilemski, *Film thickness and distribution of electrolyte in porous fuel cell components*, Journal of the Electrochemical Society, 1984, **131** (8), p. 1784-1788.

47. M. Bischoff and G. Huppmann, *Operating experience with a 250 kW(el) molten carbonate fuel cell (MCFC) power plant*, Journal of Power Sources, 2002, **105** (2), p. 216-221.

48. A. Dicks and A. Siddle, *Assessment of commercial prospects of molten carbonate fuel cells*, Journal of Power Sources, 2000, **86** (1–2), p. 316-323.

49. B.D. McNicol, D.A.J. Rand and K.R. Williams, *Fuel cells for road transportation purposes - yes or no?*, Journal of Power Sources, 2001, **100** (1-2), p. 47-59.

50. A.J. Appleby and E.B. Yeager, *Solid polymer electrolyte fuel cells (SPEFCs)*, Energy, 1986, **11** (1-2), p. 137-152.

51. Y. Wang et al., *A review of polymer electrolyte membrane fuel cells: Technology, applications, and needs on fundamental research*, Applied Energy, 2011, **88** (4), p. 981-1007.

52. A. Kuver, I. Vogel and W. Vielstich, *Distinct performance evaluation of a direct methanol SPE fuel cell. A new method using a dynamic hydrogen reference electrode*, Journal of Power Sources, 1994, **52** (1), p. 77-80.

53. J.T. Wang, S. Wasmus and R.F. Savinell, *Real-time mass spectrometric study of the methanal crossover in a direct methanol fuel cell*, Journal of the Electrochemical Society, 1996, **143** (4), p. 1233-1239.

54. K.M. McGrath, G.K.S. Prakash and G.A. Olah, *Direct methanol fuel cells*, Journal of Industrial and Engineering Chemistry, 2004, **10** (7), p. 1063-1080.

55. J.S. Wainright et al., *Acid - doped polybenzimidazoles: A new polymer electrolyte*, Journal of the Electrochemical Society, 1995, **142** (7), p. L121-L123.

56. D. Weng et al., *Electro - osmotic drag coefficient of water and methanol in polymer electrolytes at elevated temperatures*, Journal of the Electrochemical Society, 1996, **143** (4), p. 1260-1263.

57. S.R. Samms, S. Wasmus and R.F. Savinell, *Thermal stability of proton conducting acid doped polybenzimidazole in simulated fuel cell environments*, Journal of the Electrochemical Society, 1996, **143** (4), p. 1225-1232.

58. J.T. Wang et al., *A H-2/O-2 fuel cell using acid doped polybenzimidazole as polymer electrolyte*, Electrochimica Acta, 1996, **41** (2), p. 193-197.

59. Q. Li et al., *High temperature proton exchange membranes based on polybenzimidazoles for fuel cells*, Progress in Polymer Science, 2009, **34** (5), p. 449-477.

60. T.J. Schmidt and J. Baurmeister, *Durability and reliability in high-temperature reformed hydrogen PEFCs*, ECS Transactions, 2006, **3** (1), p. 861-869.

61. R. Bartlett, *Peak Oil*, 2008, February 28, Congressional Record, U.S. Government Printing Office, p. H1172-1172.

62. G. Hoogers, *Fuel cell technology handbook*, 2003, CRC Press.

63. T.A. Semelsberger, R.L. Borup and H.L. Greene, *Dimethyl ether (DME) as an alternative fuel*, Journal of Power Sources, 2006, **156** (2), p. 497-511.

64. T.H. Fleisch et al., *Dimethyl ether: A fuel for the 21st century*, in *Studies in Surface Science and Catalysis*, ed. R.L.E.M. de Pontes, C. P. Nicolaides, J. H. Scholtz, and M.S. Scurrell, 1997, Elsevier, p. 117-125.

65. J.O.M. Bockris, *Is methanol using CO2 from the atmosphere a new fuel to replace gasoline?*, Smart grid and renewable energy, 2011, **2** (2), p. 152-157.

66. D.R. Lide et al., *CRC handbook of chemistry and physics. A ready-reference book of chemical and physical data*, 2006.

67. G.A. Olah, *After oil and gas: Methanol economy*, Catalysis Letters, 2004, **93** (1-2), p. 1-2.

68. E. Fiedler et al., *Methanol*, in *Ullmann's Encyclopedia of Industrial Chemistry*, 2000, Wiley-VCH.

69. G.K.S. Prakash, G. Olah and A. Goeppert, *Beyond oil and gas: The methanol economy*, ECS Transactions, 2011, **35** (11), p. 31-40.

70. Methanol Institute, *Applications for Methanol*, 2011, Available from: http://www.methanol.org/.

71. World Health Organisation, International Programme on Chemical Safety, *Methanol*, Health and Safety Guide No. 105, 1997, Geneva, Available from: http://www.inchem.org/documents/hsg/hsg/v105hsg.htm#SectionNumber:1.4

72. U.S. Environmental Protection Agency (EPA), Office of Mobile Sources, *Methanol Fuels and Fire Safety*, Fact Sheet OMS-8, EPA 400-F-92-010, 1994.

73. S.C. Sorenson, *Dimethyl ether in diesel engines: Progress and perspectives*, Journal of Engineering for Gas Turbines and Power, 2000, **123** (3), p. 652-658.

74. J.B. Hansen et al., *Large scale manufacture of dimethyl ether – a new alternative diesel fuel from natural gas*, in *SAE International Congress & Exposition*, 1995, Society of Automotive Engineers, Detroit, MI, USA.

75. I. Dybkjær and J.B. Hansen, *Large-scale production of alternative synthetic fuels from natural gas*, in *Studies in Surface Science and Catalysis*, R.L.E. M. de Pontes, C. P. Nicolaides, J. H. Scholtz, M. S. Scurrell, Editor, 1997, Elsevier, p. 99-116.

76. T. Shikada et al., *Direct synthesis of dimethyl ether form synthesis gas*, in *Studies in Surface Science and Catalysis*, D.S. A. Parmaliana, F. Frusteri, A. Vaccari, F. Arena, Editor, 1998, Elsevier, p. 515-520.

77. T. Ogawa et al., *Direct dimethyl ether (DME) synthesis from natural gas*, in *Studies in Surface Science and Catalysis*, B. Xinhe and X. Yide, Editors, 2004, Elsevier, p. 379-384.

78. C. Kidder, *DME value proposition*, in *International DME Association Alternative Fuel Executive Briefing*, 2013, September 27, Washington D.C.

79. M. Müller and U. Hübsch, *Dimethyl Ether*, in *Ullmann's Encyclopedia of Industrial Chemistry*, 2000, Wiley-VCH Verlag GmbH & Co. KGaA.

80. *A Pharmacist's Guide to OTC Therapy: OTC Treatments for Warts*, in *Pharmacy Times,* 2006, July 1.

81. S. Alt, *DME on the Road*. in *DME Associations' 2013 DME Alternative Fuel Executive Briefing*, 2013, September 27, Washington DC.

82. H.J.A. Lanz, C. Messer, *Hydrogen fuel cell engines and related technologies*, 2001, 43-500 Monterey Avenue, Palm Desert, CA 92260, College of the Desert, Palm Desert, CA, USA.

83. D.A. Good et al., *Lifetimes and global warming potentials for dimethyl ether and for fluorinated ethers: CH3OCF3 (E143a), CHF2OCHF2 (E134), CHF2OCF3 (E125)*, Journal of Geophysical Research: Atmospheres, 1998, **103** (D21), p. 28181-28186.

84. P. Atkins and J.d. Paula, *Atkins' physical chemistry*, 2002, Oxford University Press.

85. *NIST-JANAF Thermochemical Tables*. Monograph No.9 ed., ed. W.J. Chase, 1998, American Chemical Society.

86. A.J. Bard et al., *Electrochemical methods : fundamentals and applications*, 2001, Wiley.

87. G.R.D. Pletcher et al., *Instrumental Methods in Electrochemistry*, 2001, Horwood Publishing Limited.

88. S.E. Nam et al., *Preparation of Nafion/sulfonated poly(phenylsilsesquioxane) nanocomposite as high temperature proton exchange membranes*, Journal of Membrane Science, 2008, **322** (2), p. 466-474.

89. F. Barbir, *PEM fuel cells : theory and practice*, 2013, Academic Press.

90. J. Kim et al., *Modeling of proton exchange membrane fuel cell performance with an empirical equation*, Journal of the Electrochemical Society, 1995, **142** (8), p. 2670-2674.

91. S. Srinivasan et al., *Advances in solid polymer electrolyte fuel cell technology with low platinum loading electrodes*, Journal of Power Sources, 1988, **22** (3–4), p. 359-375.

92. P. Costamagna and S. Srinivasan, *Quantum jumps in the PEMFC science and technology from the 1960s to the year 2000 Part I. Fundamental scientific aspects*, Journal of Power Sources, 2001, **102** (1-2), p. 242-252.

93. A. Heinzel and V.M. Barragan, *A review of the state-of-the-art of the methanol crossover in direct methanol fuel cells*, Journal of Power Sources, 1999, **84** (1), p. 70-74.

94. Q. Li et al., *Approaches and recent development of polymer electrolyte membranes for fuel cells operating above 100 °C*, Chemistry of Materials, 2003, **15** (26), p. 4896-4915.

95. R. Bouchet and E. Siebert, *Proton conduction in acid doped polybenzimidazole*, Solid State Ionics, 1999, **118** (3-4), p. 287-299.

96. N. Agmon, *The Grotthuss mechanism*, Chemical Physics Letters, 1995, **244** (5–6), p. 456-462.

97. K.D. Kreuer, A. Rabenau and W. Weppner, *Vehicle mechanism, a new model for the interpretation of the conductivity of fast proton conductors*, Angewandte Chemie International Edition in English, 1982, **21** (3), p. 208-209.

98. K.D. Kreuer et al., *Transport in proton conductors for fuel-cell applications: Simulations, elementary reactions, and phenomenology*, Chemical Reviews, 2004, **104** (10), p. 4637-4678.

99. L. Gubler and G.G. Scherer, *Trends for fuel cell membrane development*, Desalination, 2010, **250** (3), p. 1034-1037.

100. O. Savadogo and B. Xing, *Hydrogen/oxygen polymer electrolyte membrane fuel cell (PEMFC) based on acid-doped polybenzimidazole (PBI)*, Journal of New Materials for Electrochemical Systems, 2000, **3** (4), p. 343-347.

101. S. Trasatti, *Work function, electronegativity, and electrochemical behaviour of metals - III. Electrolytic hydrogen evolution in acid solutions*, Journal of Electroanalytical Chemistry, 1972, **39** (1), p. 163-184.

102. J.K. Nørskov et al., *Origin of the overpotential for oxygen reduction at a fuel cell cathode*, J. Phys. Chem. B, 2004, **108**, p. 17886-17892.

103. K. Kinoshita, *Particle-size effects for oxygen reduction on highly dispersed platinum in acid electrolytes*, Journal of the Electrochemical Society, 1990, **137** (3), p. 845-848.

104. W. Sheng, H.A. Gasteiger and Y. Shao-Horn, *Hydrogen oxidation and evolution reaction kinetics on platinum: Acid vs alkaline electrolytes*, Journal of the Electrochemical Society, 2010, **157** (11), p. 1529-1536.

105. K.C. Neyerlin et al., *Study of the exchange current density for the hydrogen oxidation and evolution reactions*, Journal of the Electrochemical Society, 2007, **154** (7).

106. L. Formaro and S. Trasatti, *Capacitance measurements on platinum in H3PO4 solutions*, Electrochimica Acta, 1970, **15** (5), p. 729-736.

107. V. Stamenkovic et al., *Changing the activity of electrocatalysts for oxygen reduction by tuning the surface electronic structure*, Angewandte Chemie - International Edition, 2006, **45** (18), p. 2897-2901.

108. J. Greeley et al., *Alloys of platinum and early transition metals as oxygen reduction electrocatalysts*, Nature Chemistry, 2009, **1** (7), p. 552-556.

109. V.R. Stamenkovic et al., *Trends in electrocatalysis on extended and nanoscale Pt-bimetallic alloy surfaces*, Nature Materials, 2007, **6** (3), p. 241-247.

110. J. Zhang et al., *Platinum monolayer on nonnoble metal-noble metal core-shell nanoparticle electrocatalysts for O-2 reduction*, Journal of Physical Chemistry B, 2005, **109** (48), p. 22701-22704.

111. T. Ghosh et al., *Intermetallics as novel supports for pt monolayer o2 reduction electrocatalysts: potential for significantly improving properties*, Journal of the American Chemical Society, 2009, **132** (3), p. 906-907.

112. T. Toda et al., *Enhancement of the electroreduction of oxygen on Pt alloys with Fe, Ni, and Co*, Journal of the Electrochemical Society, 1999, **146** (10), p. 3750-3756.

113. H.R. Colon-Mercado, H. Kim and B.N. Popov, *Durability study of Pt3Ni1 catalysts as cathode in PEM fuel cells*, Electrochemistry Communications, 2004, **6** (8), p. 795-799.

114. A. Bonakdarpour et al., *Corrosion of transition metals in Pt1-xMx (M = Fe, Ni, Mn) Proton Exchange Membrane Fuel Cell (PEMFC) electrocatalysts*, Meeting Abstracts, 2004.

115. A. Bonakdarpour et al., *Studies of transition metal dissolution from combinatorially sputtered, nanostructured Pt1-xMx (M = Fe, Ni; 0 < x < 1) electrocatalysts for PEM fuel cells*, Journal of the Electrochemical Society, 2005, **152** (1).

116. Y. Shao-Horn et al., *Instability of supported platinum nanoparticles in low-temperature fuel cells*, Topics in Catalysis, 2007, **46** (3-4), p. 285-305.

117. *Handbook of fuel cells : fundamentals, technology, and applications*, ed. W. Vielstich, A. Lamm, and H.A. Gasteiger, Vol. 2. 2003, Wiley.

118. J.X. Wang et al., *Hydrogen oxidation reaction on Pt in acidic media: Adsorption isotherm and activation free energies*, Journal of Physical Chemistry C, 2007, **111** (33), p. 12425-12433.

119. A. Damjanovic and V. Brusic, *Electrode kinetics of oxygen reduction on oxide-free platinum electrodes*, Electrochimica Acta, 1967, **12** (6), p. 615-628.

120. E. Yeager, *Electrocatalysts for O2 reduction*, Electrochimica Acta, 1984, **29** (11), p. 1527-1537.

121. K.L. Hsueh, D.T. Chin and S. Srinivasan, *Electrode kinetics of oxygen reduction: A theoretical and experimental analysis of the rotating ring-disc electrode method*, Journal of Electroanalytical Chemistry and Interfacial Electrochemistry, 1983, **153** (1–2), p. 79-95.

122. W.E. Mustain and J. Prakash, *A model for the electroreduction of molecular oxygen*, Journal of the Electrochemical Society, 2007, **154** (7).

123. S.K. Kamarudin, F. Achmad and W.R.W. Daud, *Overview on the application of direct methanol fuel cell (DMFC) for portable electronic devices*, International Journal of Hydrogen Energy, 2009, **34** (16), p. 6902-6916.

124. J. Prabhuram and R. Manoharan, *Investigation of methanol oxidation on unsupported platinum electrodes in strong alkali and strong acid*, Journal of Power Sources, 1998, **74** (1), p. 54-61.

125. S. Wasmus, J.T. Wang and R.F. Savinell, *Real-time mass-spectrometric investigation of the methanol oxidation in a direct methanol fuel-cell*, Journal of the Electrochemical Society, 1995, **142** (11), p. 3825-3833.

126. V.S. Bagotzky, Y.B. Vassiliev and O.A. Khazova, *Generalized scheme of chemisorption, electrooxidation and electroreduction of simple organic compounds on platinum group metals*, Journal of Electroanalytical Chemistry, 1977, **81** (2), p. 229-238.

127. M.T. Reetz et al., *Methanol oxidation on Pt, PtRu, and colloidal Pt electrocatalysts: A DEMS study of product formation*, Journal of Electroanalytical Chemistry, 2001, **509** (2), p. 163-169.

128. T. Iwasita, *Electrocatalysis of methanol oxidation*, Electrochimica Acta, 2002, **47** (22-23), p. 3663-3674.

129. H.W. Buschmann, S. Wilhelm and W. Vielstich, *On the study of methanol oxidation by electrochemical sims*, Electrochimica Acta, 1986, **31** (8), p. 939-942.

130. P. Olivi et al., *The electrooxidation of formaldehyde on Pt(100) and Pt(110) electrodes in perchloric acid solutions*, Electrochimica Acta, 1996, **41** (6), p. 927-932.

131. M. Weber et al., *Formic acid oxidation in a polymer electrolyte fuel cell - A real-time mass-spectrometry study*, Journal of the Electrochemical Society, 1996, **143** (7).

132. J.M. Leger, B. Beden and C. Lamy, *Electrosorption and electrocatalytic oxidation of formic acid on platinum + rhodium alloys*, Journal of Electroanalytical Chemistry, 1982, **134** (1), p. 117-130.

133. S. Wasmus and W. Vielstich, *The electro-oxidation of formic acid, formamide and dimethylformamide in aqueous acid solution—a comparative study using on-line MS*, Electrochimica Acta, 1993, **38** (2–3), p. 185-189.

134. N.M. Markovic et al., *Electro-oxidation mechanisms of methanol and formic acid on Pt-Ru alloy surfaces*, Electrochimica Acta, 1993, **40** (1), p. 91-98.

135. R. Parsons and T. VanderNoot, *Oxidation of small organic molecules. A survey of recent fuel cell related research*, Journal of Electroanalytical Chemistry and Interfacial Electrochemistry, 1988, **257** (1-2), p. 9-45.

136. M.T.M. Koper et al., *Lattice gas model for CO electrooxidation on Pt-Ru bimetallic surfaces*, Journal of Physical Chemistry B, 1999, **103** (26), p. 5522-5529.

137. M. Watanabe and S. Motoo, *Electrocatalysis by ad-atoms: Part I. Enhancement of the oxidation of methanol on platinum and palladium by gold ad-atoms*, Journal of Electroanalytical Chemistry and Interfacial Electrochemistry, 1975, **60** (3), p. 259-266.

138. M.M.P. Janssen and J. Moolhuysen, *State and action of the tin atoms in platinum-tin catalysts for methanol fuel cells*, Journal of Catalysis, 1977, **46** (3), p. 289-296.

139. S. Mukerjee and J. McBreen, *An in situ X-ray absorption spectroscopy investigation of the effect of Sn additions to carbon-supported Pt electrocatalysts - Part I*, Journal of the Electrochemical Society, 1999, **146** (2), p. 600-606.

140. Honma and Toda, *Temperature dependence of kinetics of methanol electro-oxidation on PtSn alloys*, Journal of the Electrochemical Society, 2003, **150** (12).

141. K. Wang et al., *On the reaction pathway for methanol and carbon monoxide electrooxidation on Pt-Sn alloy versus Pt-Ru alloy surfaces*, Electrochimica Acta, 1996, **41** (16), p. 2587-2593.

142. L.X. Yang et al., *A comparative study of PtRu and PtRuSn thermally formed on titanium mesh for methanol electro-oxidation*, Journal of Power Sources, 2004, **137** (2), p. 257-263.

143. D. Chu and S. Gilman, *The influence of methanol on O(2) Electroreduction at a rotating Pt disk electrode in acid electrolyte,* Journal of the Electrochemical Society, 1994, **141** (7), p. 1770-1773.

144. E. Skou and P.S. Kauranen, *Mixed methanol oxidation/oxygen reduction currents on a carbon supported Pt catalyst*, Journal of Electroanalytical Chemistry, 1996, **408** (1-2), p. 189-198.

145. S. Gupta et al., *Methanol-tolerant electrocatalysts for oxygen reduction in a polymer electrolyte membrane fuel cell*, Journal of Applied Electrochemistry, 1998, **28** (7), p. 673-682.

146. K. Scott et al., *A mixed-reactants solid-polymer-electrolyte direct methanol fuel cell*, Journal of Power Sources, 2004, **126** (1-2), p. 67-75.

147. H. Tributsch et al., *Methanol-resistant cathodic oxygen reduction catalysts for methanol fuel cells*, Journal of Applied Electrochemistry, 1999, **31** (NO 7), p. 739-748.

148. M. Mamlouk, K. Scott and N. Hidayati, *High temperature direct methanol fuel cell based on phosphoric acid PBI membrane*, Journal of Fuel Cell Science and Technology, 2011, **8** (6).

149. A.S. Arico et al., *Performance analysis of polymer electrolyte membranes for direct methanol fuel cells*, Journal of Power Sources, 2013, **243**, p. 519-534.

150. J. Lobato et al., *Performance of a vapor-fed polybenzimidazole (PBI)-based direct methanol fuel cell*, Energy & Fuels, 2008, **22** (5), p. 3335-3345.

151. J.-M. Kwon, Y.-J. Kim and H.-J. Cho, *High-efficiency active DMFC system for portable applications*, IEEE Transactions on Power Electronics, 2011, **26** (8), p. 2201-2209.

152. R. Rashidi et al., *Performance evaluation of direct methanol fuel cells for portable applications*, Journal of Power Sources, 2009, **187** (2), p. 509-516.

153. Toshiba, [cited 10.12.2013], Available from: http://www3.toshiba.co.jp/ddc/eng/dmfc/develop.htm.

154. J.V. Larsen et al., *Characterisation of micro direct methanol fuel cells with silicon plate supported integrated ionomer membranes*, 2013, p. 2265-2267.

155. M. Stage, *Brændselscelle med tankstation gør høreapparater batteriløse*, Ingeniøren, 2013, 2 March.

156. Y. Tsutsumi, T. Sato and A. Yosizawa, *Feasibility of fuel cell using dimethyl ether fuel*, Advances of Alcohol Fuels in the World, ed. Q.M. Zhuing, et al., 1998, 403-408.

157. A. Serov and C. Kwak, *Progress in development of direct dimethyl ether fuel cells*, Applied Catalysis B-Environmental, 2009, **91** (1-2), p. 1-10.

158. J.T. Müller et al., *Electro-oxidation of dimethyl ether in a polymer-electrolyte-membrane fuel cell*, Journal of the Electrochemical Society, 2000, **147** (11), p. 4058-4060.

159. J.T. Müller et al., *Direct dimethyl ether fuel cells*, 2004, Google Patents.

160. Y. Tsutsumi et al., *Direct type polymer electrolyte fuel cells using methoxy fuel*, Electrochemistry, 2002, **70** (12), p. 984-987.

161. T. Murakami et al., *Progress on direct dimethyl-ether fuel cell*, 2002, p. 216-219.

162. G. Kerangueven et al., *Mechanism of di(methyl)ether (DME) electrooxidation at platinum electrodes in acid medium*, Journal of Applied Electrochemistry, 2006, **36** (4), p. 441-448.

163. M.H. Shao et al., *In situ ATR-SEIRAS study of electro oxidation of dimethyl ether on a Pt electrode in acid solutions*, Electrochemistry Communications, 2005, **7** (5), p. 459-465.

164. I. Mizutani et al., *Anode reaction mechanism and crossover in direct dimethyl ether fuel cell*, Journal of Power Sources, 2006, **156** (2), p. 183-189.

165. Q. Zhang et al., *The electro-oxidation of dimethyl ether on platinum-based catalyst*, Electrochimica Acta, 2008, **53** (28), p. 8298-8304.

166. Y. Liu et al., *Electro-oxidation of dimethyl ether on Pt/C and PtMe/C catalysts in sulfuric acid*, Electrochimica Acta, 2006, **51** (28), p. 6503-6509.

167. Y. Liu et al., *Electrochemical and ATR-FTIR study of dimethyl ether and methanol electro-oxidation on sputtered Pt electrode*, Electrochimica Acta, 2007, **52** (19), p. 5781-5788.

168. L.L. Lu et al., *Electrochemical behaviors of dimethyl ether on platinum single crystal electrodes. Part I: Pt(111)*, Journal of Electroanalytical Chemistry, 2008, **619**, p. 143-151.

169. L.L. Lu et al., *Electrochemical behaviors of dimethyl ether on platinum single crystal electrodes. Part II: Pt(100)*, Journal of Electroanalytical Chemistry, 2010, **642** (1), p. 82-91.

170. Y. Tong et al., *Surface structure dependent electro-oxidation of dimethyl ether on platinum single-crystal electrodes*, Journal of Physical Chemistry C, 2007, **111** (51), p. 18836-18838.

171. Y. Zhang et al., *Electrochemical and infrared study of electro-oxidation of dimethyl ether (DME) on platinum polycrystalline electrode in acid solutions*, Electrochimica Acta, 2008, **53** (21), p. 6093-6103.

172. L. Lu et al., *Electrocatalytic oxidation of dimethyl ether on ruthenium modified platinum single crystal electrodes*, Catalysis Communications, 2009, **10** (6), p. 971-974.

173. Y. Zhang et al., *DME dissociation reaction on platinum electrode surface: A quantitative kinetic analysis by in situ IR spectroscopy*, Journal of the Electrochemical Society, 2010, **157** (1), p. F10-F15.

174. K.D. Cai et al., *Investigation of an anode catalyst for a direct dimethyl ether fuel cell*, Energy & Fuels, 2009, **23** (1), p. 903-907.

175. L. Lu et al., *Electro-oxidation of dimethyl ether on platinum nanocubes with preferential {100} surfaces*, Electrochemistry Communications, 2009, **11** (8), p. 1596-1598.

176. A. Cuesta, *At least three contiguous atoms are necessary for CO formation during methanol electrooxidation on platinum*, Journal of the American Chemical Society, 2006, **128** (41), p. 13332-13333.

177. L. Pan et al., *Electrochemical and in situ FTIR studies of adsorption and oxidation of dimethyl ether on platinum electrode*, Acta Physico-Chimica Sinica, 2008, **24** (10), p. 1739-1744.

178. E.Y. Votchenko et al., *Adsorption and electrooxidation of dimethyl ether on platinized platinum electrode in sulfuric acid solution*, Russian Journal of Electrochemistry, 2010, **46** (2), p. 212-217.

179. H. Li et al., *Why (1 0 0) terraces break and make bonds: Oxidation of dimethyl ether on platinum single-crystal electrodes*, Journal of the American Chemical Society, 2013, **135** (38), p. 14329-14338.

180. M. Watanabe and S. Motoo, *Electrocatalysis by ad-atoms - Part III. Enhancement of the oxidation of carbon monoxide on platinum by ruthenium ad-atoms*, Journal of Electroanalytical Chemistry, 1975, **60** (3), p. 275-283.

181. M. Watanabe and S. Motoo, *Electrocatalysis by ad-atoms part II. Enhancement of the oxidation of methanol on platinum by ruthenium ad-atoms*, Journal of Electroanalytical Chemistry, 1975, **60** (3), p. 267-273.

182. T. Yajima et al., *Adsorbed water for the electro-oxidation of methanol at Pt-Ru alloy*, Chemical Communications, 2003 (7), p. 828-829.

183. Y.Y. Tong et al., *An NMR investigation of CO tolerance in a Pt/Ru fuel cell catalyst*, Journal of the American Chemical Society, 2002, **124** (3), p. 468-473.

184. M. Krausa and W. Vielstich, *Study of the electrocatalytic influence of Pt/Ru and Ru on the oxidation of residues of small organic-molecules*, Journal of Electroanalytical Chemistry, 1994, **379** (1-2), p. 307-314.

185. T. Frelink, W. Visscher and J.A.R. Vanveen, *On the role of Ru and Sn as promoters of methanol electro-oxidation over Pt*, SURFACE SCIENCE, 1995, **335** (1-3), p. 353-360.

186. G. Kerangueven et al., *Methoxy methane (dimethyl ether) as an alternative fuel for direct fuel cells*, Journal of Power Sources, 2006, **157** (1), p. 318-324.

187. R.H. Yu, H.G. Choi and S.M. Cho, *Performance of direct dimethyl ether fuel cells at low temperature*, Electrochemistry Communications, 2005, **7** (12), p. 1385-1388.

188. J.H. Yoo et al., *Fuel cells using dimethyl ether*, Journal of Power Sources, 2006, **163** (1), p. 103-106.

189. Y.M. Zhu, Z. Khan and R.I. Masel, *The behavior of palladium catalysts in direct formic acid fuel cells*, Journal of Power Sources, 2005, **139** (1-2), p. 15-20.

190. Q. Li et al., *A ternary catalyst for dimethyl ether electrooxidation*, ECS Transactions, 2013, **50** (2), p. 1933-1941.

191. S. Ueda et al., *Electrochemical characteristics of direct dimethyl ether fuel cells*, Solid State Ionics, 2006, **177** (19-25), p. 2175-2178.

192. T. Haraguchi et al., *Performance of dimethyl ether fuel cells using a Pt-Ru catalyst*, Electrical Engineering in Japan, 2005, **150** (3), p. 19-25.

193. F. Si et al., *Pt/C anodic catalysts with controlled morphology for direct dimethyl ether fuel cell: The role of consecutive surface*, Electrochimica Acta, 2011, **56** (17), p. 5966-5971.

194. J.R. Ferrell, J.A. Turner and A.M. Herring, *Using heteropolyacids in the anode catalyst layer of dimethyl ether PEM fuel cells*, in *Proton Exchange Membrane Fuel Cells 8, Pts 1 and 2*, T. Fuller, et al., editors, 2008, p. 1801-1809.

195. J.R. Ferrell, M.C. Kuo and A.M. Herring, *Direct dimethyl-ether proton exchange membrane fuel cells and the use of heteropolyacids in the anode catalyst layer for enhanced dimethyl ether oxidation*, Journal of Power Sources, 2010, **195** (1), p. 39-45.

196. M.M. Mench, H.M. Chance and C.Y. Wang, *Direct dimethyl ether polymer electrolyte fuel cells for portable applications*, Journal of the Electrochemical Society, 2004, **151** (1), p. A144-A150.

197. K.D. Cai and G.P. Yin, *Optimum compositions of membrane electrode assemblies (MEAs) for direct dimethyl ether fuel cell*, International Journal of Energy Research, 2010, **34** (8), p. 695-701.

198. K.D. Cai et al., *Investigation of a novel MEA for direct dimethyl ether fuel cell*, Electrochemistry Communications, 2008, **10** (2), p. 238-241.

199. K. Cai et al., *Investigation of anode flow field for direct dimethyl ether fuel cell*, International Journal of Hydrogen Energy, 2012, **37** (17), p. 12605-12608.

200. J.Y. Im et al., *Effect of pressure for direct fuel cells using DME-based fuels*, Journal of Power Sources, 2008, **179** (1), p. 301-304.

201. K.D. Cai et al., *Comparative investigation of dimethyl ether gas and solution as fuel under direct fuel cells*, Electrochemical and Solid State Letters, 2008, **11** (11), p. B205-B207.

202. Q. Li et al., *Anode catalysts for the direct dimethyl ether fuel cell*, Polymer Electrolyte Fuel Cells 11, 2011, **41** (1), p. 1969-1977.

203. L.H. Xing et al., *Investigation on the durability of direct dimethyl ether fuel cell. Part I: Anode degradation*, Journal of Power Sources, 2012, **198**, p. 170-175.

204. H. Holldorff and H. Knapp, *Binary vapor-liquid-liquid equilibrium of dimethyl ether - water and mutual solubilities of methyl-chloride and water - experimental results and data reduction*, Fluid Phase Equilibria, 1988, **44** (2), p. 195-209.

205. W. Gerrard, *Solubility of hydrogen sulfide, dimethyl ether, methyl chloride and sulfur-dioxide in liquids - prediction of solubility of all gases*, Journal of Applied Chemistry and Biotechnology, 1972, **22** (5), p. 623-&.

206. M.E. Pozo and W.B. Streett, *Fluid Phase-equilibria for the system dimethyl ether water from 50-degrees-C to 220-degrees-C and pressures to 50.9 MPa*, Journal of Chemical and Engineering Data, 1984, **29** (3), p. 324-329.

207. J.O. Jensen et al., *Method of operating a direct dme fuel cell system*, 2011, WO 2011/035784 A1.

208. J.O. Jensen et al., *Direct dimethyl ether fueling of a high temperature polymer fuel cell*, Journal of Power Sources, 2012, **211**, p. 173-176.

209. J. Neutzler et al., *Performance of vapor-fed direct dimethyl ether fuel cell utilizing high temperature polybenzimidazole polymer electrolyte membrane*, Journal of Power Sources, 2012, **216**, p. 471-474.

210. C. Noack, J. Kallo and A.K. Friedrich, *Direct conversion of dimethyl ether in high-temperature polymer electrolyte fuel cells under stationary and dynamic conditions*, Journal of Applied Electrochemistry, 2012, **42** (10), p. 833-841.

211. A. Vassiliev et al., *A direct DME high temperature PEM fuel cell*, E C S Transactions, 2012, **50**.

212. Q. Li et al., *Direct dimethyl ether fuel cell with much improved performance*, Electrocatalysis, 2014, **5** (3), p. 310-317.

213. L.E. Smart and E.A. Moore, *Solid state chemistry, an introduction*, 2005, CRC Press.

214. P.J. Goodhew, J. Humphreys and R. Beanland, *Electron microscopy and analysis*, 2001, Taylor & Francis.

215. *How does a SEM work*, [cited 24.01.2014], Available from: http://www.purdue.edu/rem/rs/sem.htm.

216. JEOL Ltd., *SEM A to Z light*, 2009, [cited 24.01.2014], Available from: http://www.jeolusa.com/RESOURCES/ElectronOptics/DocumentsDownloads/tabid/320/Default.aspx?EntryId=598.

217. W.S. He and T. Van Nguyen, *Edge effects on reference electrode measurements in PEM fuel cells*, Journal of the Electrochemical Society, 2004, **151** (2).

218. Z.Y. Liu et al., *Positioning the reference electrode in proton exchange membrane fuel cells: calculations of primary and secondary current distribution*, Electrochimica Acta, 2004, **49** (6), p. 923-935.

219. G.C. Li and P.G. Pickup, *Dependence of electrode overpotentials in PEM fuel cells on the placement of the reference electrode - Measurement of local overpotentials*, Electrochemical and Solid State Letters, 2006, **9** (5).

220. R. Dross and B. Maynard, *In-situ reference electrode testing for cathode carbon corrosion*, ECS Transactions, 2007, **11** (1), p. 1059-1068.

221. O.E. Herrera, W. Merida and D.P. Wilkinson, *New reference electrode approach for fuel cell performance evaluation*, Proton Exchange Membrane Fuel Cells 8, Pts 1 And 2, 2008, **16** (2), p. 1915-1926.

222. F.M. Sapountzi et al., *Enhanced performance of CO poisoned proton exchange membrane fuel cells via triode operation*, Electrochimica Acta, 2011, **56** (20), p. 6966-6975.

223. M. Mamlouk and K. Scott, *Analysis of high temperature polymer electrolyte membrane fuel cell electrodes using electrochemical impedance spectroscopy*, Electrochimica Acta, 2011, **56** (16), p. 5493-5512.

224. X.-Z. Yuan et al., *Electrochemical impedance spectroscopy in PEM fuel cells : fundamentals and applications*, 2010, Springer.

225. Gamry Instruments, *Basics of Electrochemical Impedance Spectroscopy*, *Application Note*.

226. Sono-Tek Corporation, [cited 30.01.2014], Available from: http://www.sono-tek.com/accumist/.

227. M.K. Hansen, *PEM Water electrolysis at elevated temperatures*, Ph.D. Thesis, Department of Energy Conversion and Storage 2012, Technical University of Denmark, Kgs. Lyngby, Denmark.

228. balticFuelCells, [cited 05.02.2014], Available from: http://www.balticfuelcells.de/qcf.html.

229. Brooks Instruments, [cited 07.02.2014], Available from: http://www.brooksinstrument.com/.

230. J. Lobato et al., *Study of the catalytic layer in polybenzimidazole-based high temperature PEMFC: Effect of platinum content on the carbon support*, Fuel Cells, 2010, **10** (2), p. 312-319.

231. J.-H. Kim et al., *Dependence of the performance of a high-temperature polymer electrolyte fuel cell on phosphoric acid-doped polybenzimidazole ionomer content in cathode catalyst layer*, Journal of Power Sources, 2007, **170** (2), p. 275-280.

232. A. Su et al., *Experimental and numerical investigations of the effects of PBI loading and operating temperature on a high-temperature PEMFC*, International Journal of Hydrogen Energy, 2012, **37** (9), p. 7710-7718.

233. C. Coutanceau et al., *Review of different methods for developing nanoelectrocatalysts for the oxidation of organic compounds*, Electrochimica Acta, 2008, **53** (23), p. 6865-6880.

234. Antolini and Cardellini, *Formation of carbon supported PtRu alloys: an XRD analysis*, Journal of Alloys and Compounds, 2001, **315**, p. 118-122.

235. V. Radmilovic, H.A. Gasteiger and P.N. Ross, *Structure and chemical composition of a supported Pt-Ru electrocatalyst for methanol oxidation*, Journal of Catalysis, 1995, **154** (1), p. 98-106.

236. H. Li et al., *Impacts of operating conditions on the effects of chloride contamination on PEM fuel cell performance and durability*, Journal of Power Sources, 2012, **218** (0), p. 375-382.

237. J.C. Chaston, *Oxidation of the platinum metals*, Platinum Met Rev, 1975, **19** (4), p. 135-140.

238. A. Watson, L.A. Cornish and R. Süss, *Building a thermodynamic database for platinum-based superalloys: Part II*, Platinum Metals Review, 2007, **51** (4), p. 189-198.

239. V.A. Sethuraman et al., *Hydrogen peroxide formation rates in a PEMFC anode and cathode - Effect of humidity and temperature*, Journal of the Electrochemical Society, 2008, **155** (1).

240. *Handbook of fuel cells : fundamentals, technology, and applications*, ed. W. Vielstich, A. Lamm and H.A. Gasteiger, Vol. 3, 2003, Wiley.

241. B.A. Boukamp, *A linear kronig-kramers transform test for immittance data validation*, Journal of the Electrochemical Society, 1995, **142** (6), p. 1885-1894.

242. B.A. Boukamp, *Electrochemical impedance spectroscopy in solid state ionics: recent advances*, Solid State Ionics, 2004, **169** (1-4), p. 65-73.

243. D. Chakraborty, I. Chorkendoff and T. Johannessen, *Electrochemical impedance spectroscopy study of methanol oxidation on nanoparticulate PtRu direct methanol fuel cell anodes: Kinetics and performance evaluation*, Journal of Power Sources, 2006, **162** (2), p. 1010-1022.

244. J.R. Ferrell et al., *The use of the heteropoly acids, H3PMo12O40 and H3PW12O40, for the enhanced electrochemical oxidation of methanol for direct methanol fuel cells*, Electrochimica Acta, 2008, **53** (14), p. 4927-4933.

245. B.A. Boukamp and H.J.M. Bouwmeester, *Interpretation of the Gerischer impedance in solid state ionics*, Solid State Ionics, 2003, **157** (1–4), p. 29-33.

246. A.-K. Meland, D. Bedeaux and S. Kjelstrup, *A Gerischer phase element in the impedance diagram of the polymer electrolyte membrane fuel cell anode*, The Journal of Physical Chemistry B, 2005, **109** (45), p. 21380-21388.

247. C. Wannek et al., *Redistribution of phosphoric acid in membrane electrode assemblies for high-temperature polymer electrolyte fuel cells*, International Journal of Hydrogen Energy, 2009, **34** (23), p. 9479-9485.

248. J. Lobato et al., *PBI-based polymer electrolyte membranes fuel cells - Temperature effects on cell performance and catalyst stability*, Electrochimica Acta, 2007, **52** (12), p. 3910-3920.

249. T. Tingelof and J.K. Ihonen, *A rapid break-in procedure for PBI fuel cells*, International Journal of Hydrogen Energy, 2009, **34** (15), p. 6452-6456.

250. T.J. Schmidt and J. Baurmeister, *Properties of high-temperature PEFC Celtec (R)-P 1000 MEAs in start/stop operation mode*, Journal of Power Sources, 2008, **176** (2), p. 428-434.

9 Appendix

9.1 Exploded view of the evaporator and fittings

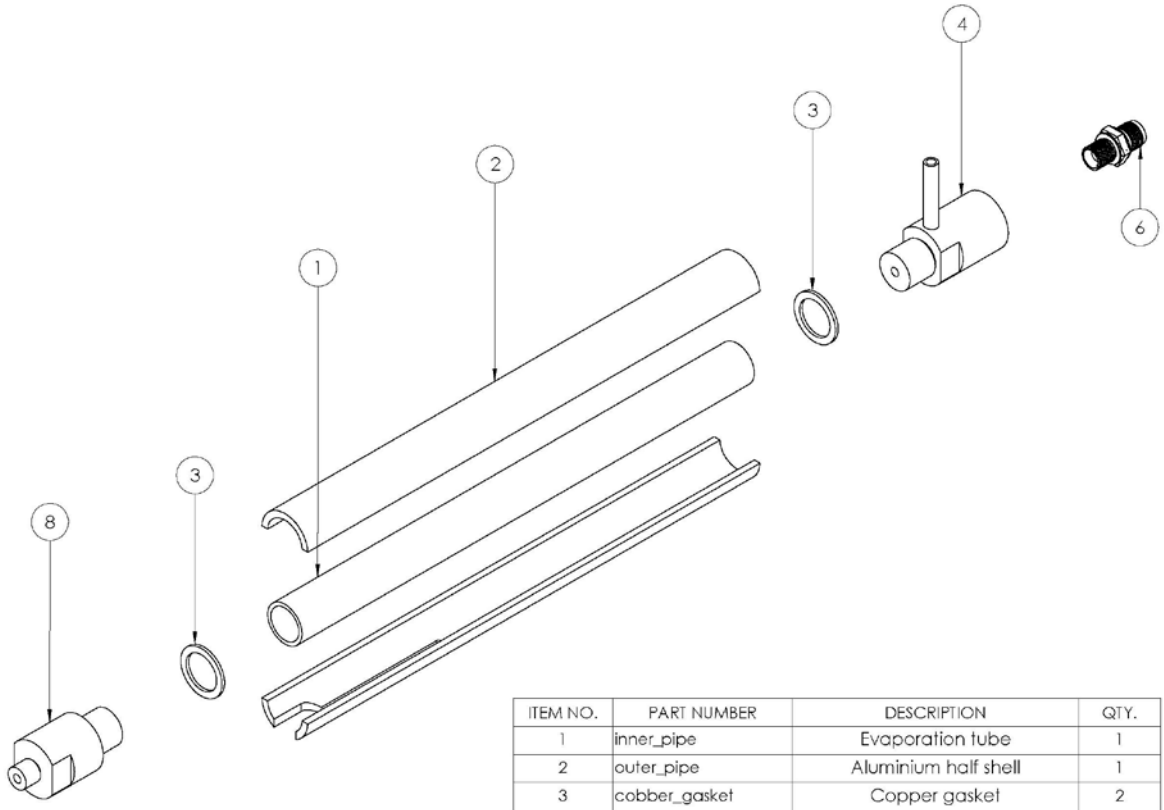

ITEM NO.	PART NUMBER	DESCRIPTION	QTY.
1	inner_pipe	Evaporation tube	1
2	outer_pipe	Aluminium half shell	1
3	cobber_gasket	Copper gasket	2
4	end_fitting_2	Inlet fitting	1
6	transition	Swagelock fitting	1
8	end_fitting_3	Outlet fitting	1

9.2 Control box wiring overview

	Wire					
Cell 1	1 - black	2 - brown	5 - yellow	8 - purple	9 - gray	10 - white
Flowmeters	i-7024	i-7017		i-7017		i-7024
1.1	11(0B) AGND	01(01) V0+	PSU+ (live)	11(0B) V0	PSU- (neut)	01(01) V0-
1.2	11(0B) AGND	01(01) V1+	PSU+ (live)	11(0B) V1	PSU- (neut)	01(01) V1-
1.3	11(0B) AGND	01(01) V2+	PSU+ (live)	11(0B) V2	PSU- (neut)	01(01) V2-
1.4	11(0B) AGND	01(01) V3+	PSU+ (live)	11(0B) V3	PSU- (neut)	01(01) V3-
	Wire					
Cell 2	1 - black	2 - brown	5 - yellow	8 - purple	9 - gray	10 - white
Flowmeters	i-7024	i-7017		i-7017		i-7024
2.1	12(0C) AGND	02(02) V0+	PSU+ (live)	12(0C) V0	PSU- (neut)	02(02) V0-
2.2	12(0C) AGND	02(02) V1+	PSU+ (live)	12(0C) V1	PSU- (neut)	02(02) V1-
2.3	12(0C) AGND	02(02) V2+	PSU+ (live)	12(0C) V2	PSU- (neut)	02(02) V2-
2.4	12(0C) AGND	02(02) V3+	PSU+ (live)	12(0C) V3	PSU- (neut)	02(02) V3-
	Wire					
Cell 3	1 - black	2 - brown	5 - yellow	8 - purple	9 - gray	10 - white
Flowmeters	i-7024	i-7017		i-7017		i-7024
3.1	13(0D) AGND	03(03) V0+	PSU+ (live)	13(0D) V0	PSU- (neut)	03(03) V0-
3.2	13(0D) AGND	03(03) V1+	PSU+ (live)	13(0D) V1	PSU- (neut)	03(03) V1-
3.3	13(0D) AGND	03(03) V2+	PSU+ (live)	13(0D) V2	PSU- (neut)	03(03) V2-
3.4	13(0D) AGND	03(03) V3+	PSU+ (live)	13(0D) V3	PSU- (neut)	03(03) V3-
	Wire					
Cell 4	1 - black	2 - brown	5 - yellow	8 - purple	9 - gray	10 - white
Flowmeters	i-7024	i-7017		i-7017		i-7024
4.1	14(0E) AGND	04(04) V0+	PSU+ (live)	14(0E) V0	PSU- (neut)	04(04) V0-
4.2	14(0E) AGND	04(04) V1+	PSU+ (live)	14(0E) V1	PSU- (neut)	04(04) V1-
4.3	14(0E) AGND	04(04) V2+	PSU+ (live)	14(0E) V2	PSU- (neut)	04(04) V2-
4.4	14(0E) AGND	04(04) V3+	PSU+ (live)	14(0E) V3	PSU- (neut)	04(04) V3-
	Wire					
Cell 5	1 - black	2 - brown	5 - yellow	8 - purple	9 - gray	10 - white
Flowmeters	i-7024	i-7017		i-7017		i-7024
5.1	15(0F) AGND	05(05) V0+	PSU+ (live)	15(0F) V0	PSU- (neut)	05(05) V0-
5.2	15(0F) AGND	05(05) V1+	PSU+ (live)	15(0F) V1	PSU- (neut)	05(05) V1-
5.3	15(0F) AGND	05(05) V2+	PSU+ (live)	15(0F) V2	PSU- (neut)	05(05) V2-
5.4	15(0F) AGND	05(05) V3+	PSU+ (live)	15(0F) V3	PSU- (neut)	05(05) V3-
	Wire					
Cell 6	1 - black	2 - brown	5 - yellow	8 - purple	9 - gray	10 - white
Flowmeters	i-7024	i-7017		i-7017		i-7024
6.1	16(10) AGND	06(06) V0+	PSU+ (live)	16(10) V0	PSU- (neut)	06(06) V0-
6.2	16(10) AGND	06(06) V1+	PSU+ (live)	16(10) V1	PSU- (neut)	06(06) V1-
6.3	16(10) AGND	06(06) V2+	PSU+ (live)	16(10) V2	PSU- (neut)	06(06) V2-
6.4	16(10) AGND	06(06) V3+	PSU+ (live)	16(10) V3	PSU- (neut)	06(06) V3-

	Wire					
	1 - black	2 - brown	5 - yellow	8 - purple	9 - gray	10 - white
BPV	i-7024	i-7017		i-7017		i-7024
BP 1.1	21(15) AGND	01(01) V4+	PSU+ (live)	21(15) V0	PSU- (neut)	01(01) V4
BP 1.2	21(15) AGND	01(01) V5+	PSU+ (live)	21(15) V1	PSU- (neut)	01(01) V5-
BP 4.1	21(15) AGND	04(04) V4+	PSU+ (live)	21(15) V2	PSU- (neut)	04(04) V4-
BP 4.2	21(15) AGND	04(04) V5+	PSU+ (live)	21(15) V3	PSU- (neut)	04(04) V5-
BP 2.1	22(16) AGND	02(02) V4+	PSU+ (live)	22(16) V0	PSU- (neut)	02(02) V4-
BP 2.2	22(16) AGND	02(02) V5+	PSU+ (live)	22(16) V1	PSU- (neut)	02(02) V5-
BP 5.1	22(16) AGND	05(05) V4+	PSU+ (live)	22(16) V2	PSU- (neut)	05(05) V4-
BP 5.2	22(16) AGND	05(05) V5+	PSU+ (live)	22(16) V3	PSU- (neut)	05(05) V5-
BP 3.1	23(17) AGND	03(03) V4+	PSU+ (live)	23(17) V0	PSU- (neut)	03(03) V4-
BP 3.2	23(17) AGND	03(03) V5+	PSU+ (live)	23(17) V1	PSU- (neut)	03(03) V5-
BP 6.1	23(17) AGND	06(06) V4+	PSU+ (live)	23(17) V2	PSU- (neut)	06(06) V4-
BP 6.2	23(17) AGND	06(06) V5+	PSU+ (live)	23(17) V3	PSU- (neut)	06(06) V5-

10 Publications

This section gives a chronologic overview of publications in peer-reviewed journals and communications to conferences and workshops that are a direct outcome of the presented work.

1. Poster at "Progress MEA 2010" conference, La Grande Motte, France, 2010.
   "A direct DME fuel cell based on acid doped PBI", J.O. Jensen, M. I. Olsen, Q. Li, A. Vassiliev, C. Pan, T. Steenberg, and N.J. Bjerrum.

2. Oral presentation at "World Hydrogen + Fuel Cells 2011" conference, Vancouver, Canada, May 2011.
   "Direct DME HT PEMFC", A. Vassiliev, J.O. Jensen, Q. Li, C. Pan and N.J. Bjerrum.

3. Poster at "3rd Carisma 2012 International Conference", Copenhagen, Denmark, 2012.
   "Direct dimethyl ether high temperature polymer electrolyte membrane fuel cells with improved performance", A. Vassiliev, J.O. Jensen, Q. Li, C. Pan and N.J. Bjerrum.

4. Peer-reviewed article in Journal of Power Sources, 2012.
   "Direct dimethyl ether fuelling of a high temperature polymer fuel cell", J.O. Jensen, A. Vassiliev, M. I. Olsen, Q. Li, C. Pan, L.N. Cleemann, T. Steenberg, H.A. Hjuler and N.J. Bjerrum, *Journal of Power Sources*, Vol. 211, 2012, p. 173-176.

5. Oral presentation at "Honolulu PRiME 2012" ECS meeting, Honolulu, October 2012.
   "A Direct DME High Temperature PEM Fuel Cell", A. Vassiliev, J.O. Jensen, Q. Li, C. Pan, L.N. Cleemann, T. Steenberg, H.A. Hjuler and N.J. Bjerrum.

6. Poster at "Energieffektivisering for fremtiden"conference, Kgs. Lyngby, Denmark, November 2012.
   "Direct dimethyl ether high temperature polymer electrolyte membrane fuel cells", A. Vassiliev, J.O. Jensen, Q. Li and N.J. Bjerrum.

7. Peer-reviewed article in ECS Transactions, 2012.
   "A Direct DME High Temperature PEM Fuel Cell", A. Vassiliev, J.O. Jensen, Q. Li, C. Pan, L.N. Cleemann, T. Steenberg, H.A. Hjuler and N.J. Bjerrum, *ECS Transactions*, Vol. 50, 2012, p. 869-876.

8. Oral presentation at "Grøn omstilling giver nye forretningsmuligheder", Taastrup, Denmark, October 2013.
   "HT PEM brændselsceller og organiske brændsler", A. Vassiliev, J.O. Jensen, Q. Li and N.J. Bjerrum.

9. Oral presentation at "Challenges in HT PEFCs" workshop, Kgs. Lyngby, Denmark, January 2014.
   "Direct dimethyl ether high temperature PEM fuel cells", A. Vassiliev, J.O. Jensen, Q. Li and N.J. Bjerrum.

10. Oral presentation at "BIT's 1st Emerging Industry Forum 2014" conference, Dalian, China, June 2014 (invited speaker).
    "Direct dimethyl ether high temperature fuel cells", A. Vassiliev, J.O. Jensen, Q. Li and N.J. Bjerrum.

11. Peer-reviewed article in Journal of Power Sources, 2014.
    "Determining the platinum loading and distribution of industrial scale polymer electrolyte membrane fuel cell electrodes using low energy X-ray imaging", T. Holst, A. Vassiliev, R. Kerr, Q. Li, T. Steenberg, C. Terkelsen and H.A. Hjuler, *Journal of Power Sources*, Vol. 270, 2014, p. 208-2012.

Modern way of life demands enormous amounts of energy, which so far has been mainly produced by combustion of fossil fuels, leading to massive climate changes. There is a need to make the energy production sustainable and break the dependency on fossil fuels.

Dimethyl ether has already been identified as an excellent renewable fuel and a diesel substitute. With its predicted widespread, there is an interest in harvesting electricity from dimethyl ether directly, rather than using it solely for combustion. High temperature proton exchange membrane (PEM) fuel cells provide such an opportunity.

The presented work describes a way to operate a high temperature PEM fuel cell directly on dimethyl ether and sheds some light on the nature of the processes occurring in the cell. Influence of experimental conditions and cell components on the performance and durability are also investigated.

Thermoelectrical Generators / Superconducting Components
High Temperature Polymer Electrolyte Membrane Fuel Cells
Energy Conversion
Magnetism
Electrochemistry
Defect Chemistry
Colloidal Chemistry / Electrochemistry
Polymer Solar Cells
Solid State Physics
Electron Microscopy
Ceramic Membranes
Solid Oxide Fuel Cells
Shaping Processes / Electron Microscopy / Solid State Physics / Computational Materials Design
Modelling / Heterostructures
Solid Oxide Electrolysis Cells
Computational Materials Design
X-Ray and Neutron Scattering
High Temperature Polymer Electrolyte Membrane Electrolysis Cells
Fuel Cells and Hydrogen Test Center
Shaping Processes / Defect Chemistry
Electrochemical Flue Gas Purification
Batteries / Hydrogen Storage
Synthesis / Colloidal Chemistry / Heterostructures / X-Ray and Neutron Scattering
Magnetic Refrigeration
Energy Storage
Sintering
Synthetic Fuels
Fuel Cells
Magnetism
Synthesis
Modelling
Sintering

Department of Energy Conversion and Storage
Technical University of Denmark
Lyngby Campus
Kemitorvet 207
2800 Kgs. Lyngby
Denmark
www.ecs.dtu.dk
ISBN 978-87-92986-18-4